Université de Paris

UNIVERSITÉ DE PARIS

ÉCOLE DOCTORALE N^{O}560: STEP'UP

LABORATOIRE ASTROPHYSIQUE INSTRUMENTATION MODÉLISATION (AIM)

Relativistic jets from stellar mass accreting black holes

FRANCESCO CAROTENUTO

THÈSE DE DOCTORAT EN ASTROPHYSIQUE

dirigée par STÉPHANE CORBEL

Date de soutenance: 21 janvier 2022

Membre du jury	
Fabien Casse	Président du jury
Stéphane Corbel	Directeur de thèse
Guillaume Dubus	Rapporteur
Jörn Wilms	Rapporteur
Susanna Vergani	Examinatrice
Piergiorgio Casella	Examinateur
Mickael Coriat	Examinateur

Except where otherwise noted, this is work licensed under
https://creativecommons.org/licenses/by-nc-nd/3.0/fr/

Dedicated to the memory of Giuseppe "Peppe" Ungaretti

Summary

Relativistic jets are outflows powered by accreting compact objects, including stellar mass black holes (BH). In black hole low mass X-ray binaries (BH LMXBs), the BH accretes matter from a companion star through an accretion disk. In this configuration, the system is able to channel a fraction of the accreted mass and energy into two types of powerful jets: compact jets at small scales and moving, discrete plasmons at parsec scales. BH LMXBs spend most of the time in quiescence and enter into sporadic outburst phases, during which they cycle through different accretion states with very different X-ray spectral properties, allowing us to study the same object over the full range of accretion regimes on human timescales.

Nowadays, several major problems remain open, including the intimate connection between the disk and the jets, the jet launching mechanism and the feedback of these jets on the interstellar medium (ISM). The goal of my thesis is to provide new observational insights into the jet properties, and progress can be made by targeting a single object and focusing on a dense monitoring campaign, covering the entire outburst.

During this thesis, I performed the radio and X-ray monitoring campaign of the discovery outburst of the BH LMXB MAXI J1348−630. The monitoring campaign was conducted with MeerKAT, ATCA, *Swift* and MAXI, totaling more than 200 observations as part of the ThunderKAT collaboration. During the outburst, the source transitioned through all the X-ray spectral states typical of LMXBs and we detected the presence of evolving radio compact jets, which quenched and re-activated during the different accretion states. We studied the correlation in the hard state between the radio (compact jets) and X-ray luminosities (inner accretion flow). Our results, with the addition of the detection in quiescence of MAXI J1348−630 in radio and X-rays, span more than seven orders of magnitude in X-ray luminosity, allowing us to probe the accretion/ejection coupling down to very low levels of activity of a BH LMXB, which are still unexplored. We find that MAXI J1348−630 belongs to the population of outliers and displays a hybrid radio/X-ray correlation, and we discuss its behavior in light of the currently proposed scenarios.

We detected two rare and subsequent relativistic discrete ejecta that displayed the highest proper motion ever measured for this kind of objects. The first was launched at the hard-to-soft state transition, while the second was launched during a short excursion from the soft to the intermediate state. After traveling with constant speed, the first component underwent a strong deceleration, which was covered with unprecedented details.

Observing the full trajectory of these ejecta allows to model their motion with great accuracy, and this is essential for measuring their physical properties. We successfully modelled the jet motion with an external shock model, which allowed us to constrain the jet initial Lorentz factor, inclination angle and ejection date. One of the major finding is that the jet is accelerated with a very large initial kinetic energy of 10^{46} erg, which is far greater than what is commonly measured for LMXBs based solely on the jet's synchrotron emission. This implies that discrete ejecta only radiate away a small fraction of their total energy, which is instead fully transferred to the BH environment. The estimate on the jet power is larger than the simultaneous available accretion power, and we present several options to mitigate this discrepancy. We infer that

MAXI J1348−630 is likely embedded in a 0.6 pc low-density ISM cavity, which could have possibly been produced by the previous activity of the system.

Our dense monitoring campaign, our interpretation of the data and our modelling allowed us to obtain key information on the properties of the two types of BH LMXB jets and on the environment in which these systems are living.

Keywords: X-ray binaries – Black holes – Microquasars – Accretion – Relativistic jets

Résumé

Les jets relativistes sont des éjections produites par des objets compacts, dont les trous noirs de masse stellaire. Dans les binaires X de faible masse (BH LMXB en anglais), le trou noir accrète la matière d'une étoile compagnon à travers un disque d'accrétion. Dans cette configuration, le système canalise une fraction de la masse et de l'énergie accrétée dans deux types des jets puissants: jets compacts à petite échelle et plasmons discrets à grandes échelles. Les BH LMXB passent la plupart du temps en quiescence et entrent dans des phases de sursaut sporadiques, au cours desquelles ils parcourent différents états d'accrétion avec des propriétés spectrales de rayons X très différentes, ce qui nous permet d'étudier le même objet sur toute la gamme des régimes d'accrétion à des échelles de temps humaines. Plusieurs problèmes majeurs restent ouverts, dont la connexion entre le disque et les jets, le mécanisme de lancement des jets et la rétroaction de ces jets sur le milieu interstellaire. L'objectif de ma thèse est de fournir de nouvelles informations sur les propriétés des jets, et des progrès peuvent être réalisés en ciblant un seul objet et en se concentrant sur une campagne de surveillance dense, couvrant l'ensemble du sursaut.

Au cours de cette thèse, j'ai réalisé la campagne des observations radio et X du sursaut du BH LMXB MAXI J1348−630. La campagne d'observations a été menée avec MeerKAT, ATCA, *Swift* et MAXI, totalisant plus de 200 observations dans le cadre de la collaboration ThunderKAT. Au cours du sursaut, la source a traversé tous les états spectraux X typiques des BH LMXB et nous avons détecté de jets compacts en évolution, qui se sont éteints et réactivés au cours des différents états d'accrétion. Nous avons étudié la corrélation à l'état dur entre les luminosités radio (jets compacts) et X (flux d'accrétion interne). Nos résultats, avec l'ajout de la détection en quiescence du MAXI J1348−630 en radio et X, couvrent plus de sept ordres de grandeur en luminosité X, ce qui nous permet de sonder le couplage accrétion-éjection jusqu'à des niveaux d'activité très faibles, encore inexplorés. Nous constatons que MAXI J1348−630 appartient à la population des *outliers* et affiche une corrélation hybride radio/X, et nous discutons de son comportement in relation à des scénarios actuellement proposés.

Nous avons détecté deux rares éjections discrètes relativistes qui ont affiché le mouvement propre le plus élevé jamais mesuré pour ce type d'objets. La première éjection s'est produite lors de la transition d'état dur à mou, tandis que la seconde a été lancée lors d'une courte excursion de l'état mou à l'état intermédiaire. Après avoir voyagé à vitesse constante, la première composante a subi une forte décélération, qui a été observée de façon très détaillée.

L'observation de la trajectoire complète du jets permet de modéliser précisément leur mouvement, ce qui est essentiel pour mesurer leurs propriétés physiques. Nous avons réussi à modéliser le mouvement du jet avec un modèle de choc externe, nous permettant ainsi de contraindre le facteur de Lorentz initial du jet, l'angle d'inclinaison et la date d'éjection. L'une des principales conclusions est que le jet est accéléré avec une très grande énergie cinétique initiale (10^{46} erg), bien supérieur à ce qui est mesuré avec l'émission synchrotron du jet. Cela implique que les éjections discrètes rayonnent une petite fraction de leur énergie totale, qui est entièrement transférée à l'environnement. L'estimation de la puissance du jet est supérieure à la puissance d'accrétion disponible, et nous présentons plusieurs options pour atténuer cet

écart. Aussi, MAXI J1348−630 est probablement dans une cavité à basse densité de 0.6 pc, qui pourrait avoir été produite par l'activité précédente du système.

Nos observations, notre interprétation des données et notre modélisation nous ont permis d'obtenir des informations clés sur les propriétés des deux types de jets des BH LMXB et sur l'environnement dans lequel évoluent ces systèmes.

Mots-clés: Binaires X – Trous noirs – Microquasars – Accrétion – Jets relativistes

Résumé détaillé

Les jets relativistes sont des éjections produites par des objets compacts, dont les trous noirs de masse stellaire. Dans les binaires X de faible masse (LMXB en anglais), le trou noir accrète la matière d'une étoile compagnon à travers un disque d'accrétion. Dans cette configuration, le système canalise une fraction de la masse et de l'énergie accrétée dans deux types des jets puissants: jets compacts à petite échelle et ejectas discrets à grandes échelles. Les binaires X de faible masse à trou noir passent la plupart du temps en quiescence et entrent dans des phases de sursaut sporadiques, au cours desquelles ils parcourent différents états d'accrétion avec des propriétés spectrales de rayons X très différentes, ce qui nous permet d'étudier le même objet sur toute la gamme des régimes d'accrétion à des échelles de temps humaines.

Malgré les progrès fondamentaux réalisés dans le domaine au cours des 50 dernières années, nous n'avons toujours pas une compréhension complète de toutes les propriétés observationnelles présentées par les binaires X de faible masse à trou noir et sur la physique associée, et nous manquons d'un modèle précis regroupant toutes les signatures observationnelles et l'interaction entre les différents composants du système. Au cours des $\sim$25 dernières années, des jets ont été observés, résolus et identifiés dans un grand nombre de sources et des résultats importants ont été obtenus concernant notre connaissance de ces éjections relativistes. Cependant, plusieurs questions fondamentales restent aujourd'hui sans réponse. Par exemple, le mécanisme d'accélération des jets fait encore l'objet d'un débat, et il n'est pas clair s'il consiste à extraire l'énergie de rotation d'un trou noir en rotation ou en captant l'énergie du disque d'accrétion. Cela concerne la connexion fondamentale entre les jets et le disque et, pour cette raison, la nature du couplage entre l'accrétion et l'éjection dans les objets compacts accrétants a été largement étudiée au cours des dernières décennies et est aujourd'hui l'une des questions les plus importantes dans le domaine d'astrophysique des hautes énergies. Étonnamment, la surveillance radio et X de plusieurs binaires X de faible masse à trou noir au cours des deux dernières décennies a conduit à la découverte de deux populations distinctes de trous noirs, qui présentent des comportements différents dans le diagramme radio/X global de trou noirs accrétants de masse stellaire. Ce diagramme compare les luminosités des jets et du flux d'accrétion central. Ceci peut suggérer l'existence de deux couplages fondamentaux différents entre les jets compacts et le flux d'accrétion central, dont l'origine est encore mal comprise. De plus, il existe des indications de sources qui pourraient passer d'un groupe à l'autre, affichant un comportement hybride, compliquant davantage la situation. La composition du jet est encore inconnue, et il n'y a pas d'indication claire vers un scénario baryonique ou leptonique, ou un mélange des deux, comme par exemple proposé pour les noyaux galactiques actifs (AGN). De plus, nous ne pouvons toujours pas contraindre avec précision les paramètres physiques des éjectas discrets. En particulier, l'énergie des jets est un paramètre clé, car aujourd'hui le contenu énergétique total de ces jets est inconnu. Alors que les limites inférieures de l'énergie sont généralement obtenues en considérant l'émission synchrotron du jet, une telle méthode est susceptible de largement sous-estimer le contenu énergétique total du jet. De plus, il existe une grande incertitude sur la masse du jet, et une estimation fiable de la masse et de l'énergie du jet peut être particulièrement utile pour comprendre la composition du jet lui-même. Enfin, nous ne

sommes pas en mesure d'identifier avec précision la séquence de signatures observationnelles qui précèdent une éjection discrète, y compris les transitions d'état spectral, les flares et la présence variable de différents types d'oscillations quasi-périodiques (QPO) observées dans les rayons X.

L'objectif de cette thèse est de fournir de nouvelles informations sur les propriétés des jets compacts et des éjectas discrets des binaires X de faible masse à trous noir grâce à des campagnes observationelles intensives. Chaque source présente des propriétés particulières liées à la formation du jets compacts, à leur évolution et à leur connexion avec le flux d'accrétion, ainsi qu'au lancement et au mouvement d'éjectas discrets. Dans cette thèse, plutôt que de viser des études de population, notre approche a consisté à cibler un seul objet et à effectuer une campagne d'observations multi-longueurs d'onde très dense, car nous pensons que des progrès dans ce domaine peuvent être réalisés en améliorant la qualité des données et le détail avec dont chaque source est observée.

La physique des jets des binaires X à trou noir est incroyablement complexe, et une seule thèse n'est certainement pas suffisante pour répondre aux nombreuses questions ouvertes dont nous avons discuté avant. Je résumerai ici les principaux résultats de cette la thèse, dans laquelle j'ai présenté le monitoring radio et X de MAXI J1348−630 lors de son sursaut 2019/2020. MAXI J1348−630 est un nouveau candidat trou noir dans un système binaire X de faible masse qui s'intègre très bien dans le scénario générale adoptée pour les binaires X. Grâce à notre monitoring avec MAXI et *Swift* en rayons X, nous avons pu suivre l'ensemble du sursaut, dans laquelle la source affichait une évolution au rayons X assez typique dans la première partie, complétant tout un cycle dans le Diagramme Dureté-Intensité, puis présentait une séquence complexe de phases de réactivation uniquement à l'état dur dans la deuxième partie.

Deux éjectas discrets subséquent, approchants et avec un seul composant ont été suivis alors qu'ils s'éloignaient du trou noir dans la même direction, avec le mouvement propre le plus élevé ($\gtrsim$ 100 mas day^{-1}) observé jusqu'à présent parmi les binaires X. Nous avons pu placer des contraintes similaires pour les deux éjectas sur la vitesse intrinsèque $\beta \geq 0.7$ et l'angle d'inclinaison de l'axe du jet $\theta \leq 45°$. Le premier ejecta ayant été suivi pendant 11 mois, nous avons pu contraindre son angle de demi-ouverture à $\leq 3°$. Nous avons caractérisé précisément son mouvement, composé d'une première partie de mouvement balistique suivie d'une forte décélération survenant après que l'éjecta ait parcouru au moins 0.3 pc. Cette décélération est en accord avec le scénario de microquasars noyés dans des cavités de faible densité à l'échelle du parsec dans le milieu interstellaire. A partir d'une première modélisation phénoménologique simple du mouvement des deux éjectas, on peut en déduire que l'éjection du premier composant s'est produite avant une forte flare radio, alors que le système était dans l'état intermédiaire. De plus, les contraintes sur l'énergie et la puissance minimales requises pour produire le flare radio observée sont en accord avec les valeurs généralement mesurées pour les éjectas discrets.

La trajectoire du premier éjecta étant observée avec une grande précision, cela nous a permis modéliser le mouvement du jet et contraindre certains paramètres physiques importants. En fait, nous avons modélisé avec succès le mouvement du jet avec un modèle dynamique de choc externe, avec un approche Bayésien et en utilisant les Monte Carlo Markov Chains. Cela nous a permis de contraindre le facteur de Lorentz initial du jet $\Gamma_0 = 1.85^{+0.15}_{-0.12}$, l'angle d'inclinaison $\theta = 29.27°^{+2.71°}_{-3.23°}$ et la date d'éjection $t_{\rm ej} = 21.45^{+1.88}_{-3.19}$ (MJD – 58500). Sous des hypothèses simples sur l'angle d'ouverture du jet et sur la densité du milieu interstellaire externe, on constate que le jet a une grande énergie cinétique initiale $E_0 = 4.6^{+20.0}_{-3.4} \times 10^{46}$ erg, bien supérieur à ce qui est couramment mesuré pour les binaires X à trou noir à partir de l'émission synchrotron du jets. Cela implique que les éjectas discrets ne rayonnent qu'une

petite fraction de leur énergie totale, qui est plutôt transférée à l'environnement via leur énergie cinétique seul. L'estimation de la puissance du jet est supérieure à la puissance d'accrétion disponible, et nous avons présenté plusieurs options pour atténuer cet écart. Nous en déduisons que MAXI J1348−630 est probablement noyé dans une cavité du milieu interstellaire avec une densité interne $n = 0.0010^{+0.0005}_{-0.0003}$ cm^{-3} et rayon $R_{\rm c} = 0.61^{+0.11}_{-0.09}$, qui aurait pu être produit par l'activité précédente du système, comme proposé pour d'autres binaires X de faible masse à trous noirs. Dans l'ensemble, notre travail fournit des résultats importants sur les éjectas discrets des binaires X de faible masse à trous noirs. Grâce à notre stratégie de surveillance, nous avons pu couvrir toute la "vie" du jet, ce qui nous a permis de contraindre les propriétés physiques du jet, notamment son énergie cinétique initiale, ce qui a rarement été possible pour ce type de jets. Nos résultats confirment que l'énergie totale de ces jets est plus importante qu'on ne le pensait auparavant, et qu'elle n'est pas bien retracée par l'émission électromagnétique observée. Cela pourrait avoir des implications importantes pour les mécanismes proposés de production de jets, et l'estimation du contenu énergétique réel de ces jets est actuellement une question ouverte importante. Le temps d'éjection est aussi particulièrement important, puisqu'il permet de relier le lancement du jet à l'état du disque d'accrétion et donc d'obtenir des informations sur la façon dont le jet est produit. La richesse des informations physiques obtenues pour les jets de MAXI J1348−630 n'était pas accessible pour la majorité des éjectas discrets observés jusqu'à présent, et il est important de remarquer que les observations de la décélération du jet étaient essentielles pour contraindre les paramètres physiques du jet et de l'environnement entourant MAXI J1348−630. Le deuxième éjecta de MAXI J1348−630 a probablement été lancé lors d'une courte excursion du système de l'état mou à l'état intermédiaire, un comportement observé dans quelques binaires X, mais qui est encore aujourd'hui largement inexploré. Le lien entre les éjectas discrets et les propriétés spectrales et temporelles de l'émission X est un sujet central des efforts de recherche actuels, et les futures campagnes observationelles multi-longueurs d'onde à cadence élevée des binaires X à trous noirs aux transitions d'état (et dans l'état mou) seront nécessaires pour caractériser la séquence causale des événements conduisant au lancement d'éjectas discrets.

Grâce à nos observations radio menées avec MeerKAT et ATCA, nous avons observée la montée, l'extinction et la réactivation des jets compacts dans différentes phases du sursaut, en limitant spécifiquement le facteur d'extinction du jet à 3.5 ordres de grandeur dans l'état mou. Notre campagne d'observations radio et X nous a également permis d'étudier la corrélation entre les luminosités radio et X à l'état dur qui sont produites respectivement par les jets compacts et par le flux d'accrétion central. Nos résultats couvrent près de 6 ordres de grandeur de luminosité aux rayons X au sein d'une même sursaut (très rare pour une seule source), ce qui nous permet de sonder le couplage accrétion-éjection depuis les phases brillantes du sursaut jusqu'à de très faibles niveaux d'activité de un binaire X à trou noir, encore largement inexploré. Nous constatons que MAXI J1348−630 appartient à la population croissante de *outliers* aux luminosités observées les plus élevées. Fait intéressant,MAXI J1348−630 dévie de la trajectoire de les *outliers* à $L_{\rm X} \lesssim 7 \times 10^{35} (D/2.2\,{\rm kpc})^2$ erg s^{-1} et rejoint finalement la trajectoire standard à $L_{\rm X} \simeq 10^{33} (D/2.2\,{\rm kpc})^2$ erg s^{-1}, affichant une corrélation radio/X hybride, partiellement observée dans seulement une poignée de sources. Cependant, pour MAXI J1348−630 ces transitions se produisent à des luminosités bien inférieures à celles observées pour des sources similaires (au moins un ordre de grandeur). Nous avons discuté du comportement de MAXI J1348−630 à la lumière des scénarios actuellement proposés, constatant que nos données ne sont pas cohérentes avec quelques explications proposées pour la dichotomie observée. De plus, nos observations *Chandra* et ATCA dédiées, sensibles et simultanées nous ont permis d'obtenir

une détection en radio et rayons X de MAXI J1348−630 en quiescence, à $\sim 10^{-8.3} L_{\rm Edd}$, ce qui a rarement été fait pour les binaires X à trou noir et il est sans précédent pour les sources de corrélation hybride. Nos observations nous ont conduit à découvrir une nouvelle source de corrélation hybride, et nous remarquons qu'à ce moment-là MAXI J1348−630 est la seule source de ce groupe qui a été observée sur toute la gamme de luminosités au sein d'une seul sursaut et jusqu'à la phase de quiescence. De plus, MAXI J1348−630 a la luminosité de transition du groupe des *outliers* au groupe *standard* la plus faible parmi les sources hybrides connues. Grâce aux observations en régime de basse luminosité, et à la détection en quiescence, nous confirmons qu'après H1743−322, les sources hybrides rejoignent le groupe standard en régime bas flux. Alors que plusieurs explications proposées ont été discutées, le mécanisme physique responsable de ce changement dans le couplage disque/jet est encore inconnu et c'est une question clé ouverte dans l'étude de la connexion entre le disque et les jets dans le binaires X à trou noir. Le comportement hybride pourrait résulter d'un changement dans les propriétés du flux d'accrétion à différentes luminosités, ou d'un changement dans l'émission du jet à différents taux d'accrétion. Cet ensemble de données sera d'une grande importance pour les études futures de la connexion entre les jets et le disque dans les binaires X, et il permettra de placer des contraintes sur les mécanismes d'émission des jets et de exclure les dégénérescences entre les différents modèles. Pour conclure, ce travail a montré comment des observations multi-longueurs d'onde (radio et rayons X) et une modélisation physique détaillée peuvent être utilisées pour sonder l'évolution des jets produits par l'accrétion de trous noirs, à partir de la connexion des jets compacts avec le disque d'accrétion, au lancement, au mouvement et à l'impact des éjectas discrets. Les informations clés sur les jets que nous avons obtenues dans cette thèse permettront à terme de comprendre comment ces types de jets puissants sont produits et lancés à partir d'objets compacts en accrétion, potentiellement à toutes les échelles physiques.

Acknowledgements

I write these acknowledgments after defending my thesis and obtaining my PhD in High Energy Astrophysics. This is, so far, the most important achievement of my life, and it would have never been possible without the help and support of many people during these exciting and demanding three years.

First and foremost, I would like to thank my supervisor, Prof. Stéphane Corbel. As mentioned during the defense, you have been an amazing supervisor. You not only introduced me to the amazing science of jets launched by accreting black holes, but you also taught me so much about the world of astronomy in general, so that I owe you really a lot in terms of my growth as a scientist. You have been always very available for me, even during the dramatic years of the pandemic, supporting and encouraging me when I needed it the most. And you also pushed me when it was the right time, as I would have never started my work on MAXI J1348–630 if it wasn't for your initiative. Above all, I enjoyed a lot all our scientific discussions, from which I always learned something, and also our everyday chats and drinks after work. These past three years have been exciting but also very demanding, and in this period I realized how lucky I was to have you as a supervisor. For this reason, I will be forever grateful for the time that I have spent working with you.

The second person that I absolutely need to thank is Dr. Lilia Tremou. At the beginning of my PhD, you taught me everything about radio-interferometry and, year after year, you became a true friend for me. Entering in the office in the morning and seeing you at your desk always put me in a better mood to start the day. I will never forget our chats, our beers, our *pomodoro* sessions during the lockdown and the time spent discussing and trying to solve problems at 2 AM!

I want to thank Mathilde Espinasse, my PhD adventure companion: it has been a pleasure to work with you during these three years. We helped and supported each other a lot, and this has been so important for me. Thanks for always been available, for being so nice and fast whenever I needed some help, and for our lunches and chats together.

I would also like to thank Prof. Rob Fender and Prof. James Miller-Jones. Within the *relativistic accretion* working group of the ThunderKAT collaboration, you effectively allowed me to observe MAXI J1348–630 with MeerKAT for more than one year, providing extremely valuable suggestions throughout the work. I am also really grateful for the fact that you supported all my postdoc applications, that greatly benefited from your recommendations.

A big thanks to Dr. Alex Tetarenko! Your help with MCMCs was fundamental for the work on the modeling of the jet kinematics, which is the one I am most proud of. You were always available and nice, and your contributions both on the code side and on the physical interpretation of the results has been essential for obtaining some of the most interesting conclusions of this thesis. I have to say that you really represent the scientist I would like to become.

Next, I wish to offer a special thanks to Dr. Tasso Tzioumis. Thank you Tasso for all the observations you performed. You spent nights awake to observe MAXI J1348–630 with ATCA, and these observations turned out be nothing less than fundamental for the results presented in this thesis. I want to thank you also for teaching me how to operate ATCA. What an emotion

it has been to control and use an entire radio-interferometer! I hope to be able one day to visit you in Australia and to operate the Compact Array from its control room.

A big thanks also to Dr. Tom Russell. You shared with me your ATCA observations of MAXI J1348–630, you provided some useful comments that really improved my publications, and we started a nice collaboration that I am sure will produce great results.

Thanks to Dr. Sara Motta for her help in the reduction and analysis of X-ray observations, and also for setting up a significant part *Swift* monitoring of MAXI J1348–630 linked to ThunderKAT. Thanks also to Dr. Ian Heywood for his crucial comment about positional offsets in MeerKAT images, which allowed me to solve an important problem during the data analysis.

I would like also to thank the whole ThunderKAT collaboration, since working in this international community of experts has been a privilege. Having so much MeerKAT time available has been a real advantage, and I did not immediately realize how powerful this telescope is. Your support and your expertise have been important for the success of this work.

Thanks to Dr. Jerome Rodriguez, who is leading the High Energy group in Saclay, for your help. You were always very available for a chat whenever i needed it, you regularly checked on me during the worst months of the pandemic, and you provided very good advice, both on the PhD life and on the X-ray data analysis.

Thanks also to Dr. Vianney Lebouteiller and Prof. Fabien Casse for the PhD follow-up during these years as part of my *comité de suivi de thèse*, as they provided very useful help and insights.

Beyond work, I am incredibly happy for having met so many wonderful people during these three years of my life in Paris. First, thank you Luca for having become one of my closest friends. You made everything better, and I simply wouldn't have made it during these complicated years without you. Your friendship is the best thing that I bring with me as I move away from Paris. Thanks also to Virginia for the many nice memories that we have of this adventure. You are one of the best people that I have ever met, and your sensitivity, generosity and strength are qualities that I profoundly admire in you. Thanks also to my group of friends that I will greatly miss: Federico, Victor, Vicky, Theo, Matteo, Denise, Ester, Pippo, Michela, and the volleyball team at CEA/Saclay, including Thomas, Eric and Michel.

I would like also to thank Nicole Louisnard for allowing me to live in one of the best places on Earth: the *Quartier Latin* in Paris.

A special thanks to Prof. Daniele Cialdella, my professor of math and physics in high-school. You taught me so much, and over the years you became a very close friend. I would have never been able to accomplish this without the math that I studied with you during my high-school years in Rome. You were the first to make me really understand what I was doing, opening my mind and giving me a strong foundation of method and knowledge, which resulted extremely useful for everything that I learned afterwards.

Thanks to Giuseppe Cruciani, David Parenzo and Alberto Gottardo, the hosts of the radio show *La Zanzara* on Radio24. Your voices have been a constant, reliable, warm and funny presence in my house during these three years. You will never know how important you have been for my mental health.

Thanks to my family: Mom, Dad, Agata, Davide, Matteo and Eleonora. Thanks for your unconditional love and for always being there for me. During these very difficult years, I hope to have given you good news, reasons to joy and something to be proud of.

And the final thanks goes to Giuseppe "Peppe" Ungaretti, to whom this thesis is dedicated. For me, you simply define generosity. You cared for me, you invested in my formation, and you personally bought all the books for my university courses during the 5 years of university.

This help has been fundamental for me during some difficult years. I also greatly enjoyed our coffees and dinners in Rome. Your passing away in 2019 has been a terrible surprise, and it is hard to realize that I will never be able to properly give back what I received. For this, and for everything you did for me, this thesis is dedicated to your memory.

Contents

Summary v

Résumé vii

Résumé détaillé ix

Acknowledgements xiii

List of Figures xxi

List of Tables xxiii

List of Abbreviations xxv

Introduction xxvii

1 X-ray binaries 1
- 1.1 Accreting compact objects . . . 2
  - 1.1.1 The birth of compact objects . . . 2
  - 1.1.2 Compactness . . . 3
  - 1.1.3 Accretion efficiency and Eddington limit . . . 4
- 1.2 Accretion in a binary system . . . 6
  - 1.2.1 Roche lobe overflow . . . 6
  - 1.2.2 Accretion disk formation and emission . . . 8
- 1.3 Black hole X-ray binaries . . . 10
  - 1.3.1 Population . . . 10
  - 1.3.2 Main components . . . 13
- 1.4 The outburst phase . . . 17
  - 1.4.1 The disk instability model . . . 18
  - 1.4.2 Spectral states and outburst evolution . . . 20

2 Compact jets and disk/jet coupling 25
- 2.1 Flat spectra from compact jets . . . 26
  - 2.1.1 Emission from a single segment . . . 26
  - 2.1.2 The full spectrum . . . 28
- 2.2 Powering mechanism . . . 31
- 2.3 Recent progresses . . . 32
  - 2.3.1 Evolution of the break frequency . . . 32
  - 2.3.2 Insights from fast variability . . . 34
- 2.4 The radio/X-ray correlation . . . 35
- 2.5 Proposed explanations . . . 37

2.5.1 Geometry . . . 37
2.5.2 Radiative efficiency of the accretion flow . . . 38
2.5.3 Jet properties . . . 40
2.6 The fundamental plane of black hole activity . . . 41

3 Discrete ejecta from black hole X-ray binaries 43
3.1 Superluminal jets from galactic black holes . . . 44
3.1.1 Observations . . . 44
3.1.2 Proper motion . . . 45
3.1.3 Composition . . . 47
3.1.4 Production . . . 48
3.2 The ejection . . . 48
3.2.1 Radio flaring . . . 49
3.2.2 Minimum associated energy . . . 49
3.2.3 Ejection time and connection with X-ray variability . . . 51
3.3 Interaction with the interstellar medium . . . 52
3.3.1 Decelerating jets . . . 53
3.3.2 X-ray detections . . . 54
3.3.3 Jet feedback . . . 55

4 Instruments and data analysis 59
4.1 Radio-interferometry . . . 60
4.1.1 Aperture synthesis . . . 60
4.1.2 Calibration . . . 62
4.1.3 Imaging and deconvolution . . . 63
4.2 Radio-interferometers . . . 65
4.2.1 MeerKAT . . . 65
4.2.2 ATCA . . . 67
4.3 X-ray observatories . . . 67
4.3.1 *Swift* . . . 68
4.3.2 MAXI . . . 69
4.4 Statistical techniques . . . 70
4.4.1 Bayesian statistics . . . 70
4.4.2 The MCMC technique . . . 72

5 The new black hole X-ray binary MAXI J1348–630 77
5.1 Introducing MAXI J1348−630 . . . 78
5.2 Description of the campaign . . . 79
5.2.1 MeerKAT observations . . . 79
5.2.2 ATCA observations . . . 80
5.2.3 *Swift* observations . . . 80
5.2.4 MAXI observations . . . 82
5.3 Outburst presentation . . . 82
5.3.1 X-ray light curve . . . 84
5.3.2 Radio light curve . . . 84
5.3.3 X-ray spectral evolution . . . 88
5.3.4 Evolution of the compact jets . . . 90
5.4 The distance to MAXI J1348−630 . . . 91

5.4.1 H I absorption . . . 91
5.4.2 X-ray light echoes . . . 93
5.5 Tabulated data . . . 94
5.5.1 Radio data . . . 94
5.5.2 X-ray data . . . 98

6 The hybrid disk/jet connection of MAXI J1348–630 101
6.1 Radio and X-ray observations in the hard state . . . 102
6.2 Hybrid correlation . . . 106
6.3 Radio quiet hypothesis . . . 107
6.4 X-ray loud hypothesis . . . 108
6.5 MAXI J1348-630 in quiescence . . . 110

7 The discrete ejecta of MAXI J1348–630 115
7.1 Observations of the first discrete ejecta . . . 116
7.1.1 Light curve evolution . . . 117
7.2 Observations of the second discrete ejecta . . . 119
7.2.1 Light curve evolution . . . 119
7.3 Ejecta motion . . . 121
7.3.1 Astrometry correction . . . 121
7.3.2 Motion of the first discrete ejecta . . . 125
7.3.3 Motion of the second discrete ejecta . . . 126
7.4 Constraints from the jet motion . . . 128
7.4.1 Jet opening angle . . . 129
7.5 Ejection of the first component . . . 130
7.5.1 Link with X-ray observations . . . 130
7.5.2 Multiple radio flares . . . 130
7.5.3 Flare energetics . . . 131
7.6 Late time behaviour of the first discrete ejecta . . . 133
7.6.1 Cavity scenario . . . 133
7.6.2 Alternative hypotheses . . . 134
7.7 Considerations on the second discrete ejecta . . . 135
7.7.1 Ejection . . . 135
7.7.2 Late time behaviour . . . 136
7.8 Radio flux densities of the first ejecta . . . 137

8 Modeling the kinematics of the decelerating jets from MAXI J1348–630 141
8.1 The external shock model . . . 142
8.2 Bayesian analysis . . . 144
8.2.1 Data and setup . . . 145
8.2.2 The uniform density case . . . 146
8.2.3 Motion in a low-density ISM cavity . . . 146
8.3 Discussion on the jet properties . . . 151
8.3.1 Initial Lorentz factor . . . 151
8.3.2 Inclination angle . . . 152
8.3.3 Ejection time . . . 152
8.3.4 A large kinetic energy . . . 153
8.3.5 Jet power . . . 154

8.3.6 Jet mass . . . 155
8.3.7 Jet composition . . . 157
8.4 The environment of MAXI J1348−630 . . . 159
8.4.1 Alternative explanations . . . 160
8.4.2 Predictions for the receding component . . . 160
8.5 Conclusions . . . 161

Conclusions and perspectives **167**

Bibliography **167**

A Research paper: "Measuring the distance to the black hole candidate X-ray binary MAXI J1348−630 using H I absorption" **203**

B Observing proposals **209**

List of Figures

1.1 The shadow of the supermassive black hole at the center of M87 3
1.2 Equipotential lines of the Roche potential for a binary system and artistic representation of an accreting black hole 7
1.3 Temperature profile and spectrum of an accretion disk 9
1.4 Scale drawings of 16 X-ray binaries in the Milky Way with a dynamically confirmed stellar-mass black hole 11
1.5 Artistic impression of a microquasar 14
1.6 Scheme of the disk/corona configuration 15
1.7 Radio images of the two main types of microquasar jets 16
1.8 Schematic representation of the broadband spectral energy distribution of a BH LMXB 17
1.9 RXTE/All Sky Monitor soft X-ray (1.5–12 keV) light curve of GX 339−4 . . . 18
1.10 Σ–T plane for the relation between temperature and surface density in each ring of the accretion disk 19
1.11 Example of Hardness-intensity diagram 22

2.1 Emitted spectrum from a segment of the compact jet 28
2.2 Schematic representation of a total jet spectrum 29
2.3 SED modelling of MAXI J1535–571 and jet break frequency evolution 33
2.4 Cross-correlation functions (CCFs) between the X-ray and radio emission from Cyg X-1 34
2.5 Radio/X-ray diagram 36
2.6 A scheme of the radio/X-ray diagram for Galactic black holes 40
2.7 Fundamental plane of black hole activity 42

3.1 Examples of discrete ejecta from galactic BH LMXBs 45
3.2 Geometry of a symmetric double-sided ejection and the apparent transverse velocity of a relativistic source as a function of the viewing angle, for different intrinsic speeds 46
3.3 AMI-LA radio light curve of MAXI J1820+070 52
3.4 Angular separation of the decelerating discrete ejecta from XTE J1550–564 . . 53
3.5 X-ray *Chandra* detections of the jets of XTE J1550−564 and broadband jet spectrum 54
3.6 *Herschel* PACS map of the region surrounding the GRS 1915+105 56

4.1 Illustrative scheme of a two-antenna interferometer 60
4.2 The MeerKAT radio interferometer 66
4.3 The Australia Telescope Compact Array (ATCA) 67
4.4 Artistic representation of the *Swift* spacecraft 69
4.5 The MAXI all-sky monitor 70

4.6 Intuitive illustration of the Bayes theorem . . . 71
4.7 Schematic illustration of the Metropolis-Hastings algorithm . . . 74

5.1 Hardness-Intensity Diagram (HID) of MAXI J1348−630 . . . 83
5.2 X-ray and radio light curves of MAXI J1348−630 during its 2019/2020 outburst 85
5.3 MeerKAT large scale radio image at 1.28 GHz of the MAXI J1348−630 field . 86
5.4 Radio spectra of MAXI J1348−630 of four epochs in the hard state . . . 87
5.5 First part of the radio light curve at the core location of MAXI J1348−630 . . . 90
5.6 The H I absorption complex observed with ASKAP in the direction of MAXI J1348−630 and the variation of the predicted velocity of the local standard of rest ($V_{\rm LSR}$) as a function of distance from the Sun (D) . . . 92
5.7 False-colour $3° \times 3°$ image of the eROSITA All-Sky Survey observation . . . 94

6.1 HID of MAXI J1348−630 with the times of the radio observations used for the radio/X-ray correlation . . . 102
6.2 MAXI J1348−630 radio/X-ray diagram during its 2019/2020 outburst . . . 106
6.3 Radio/X-ray diagram of GX 339−4, V404 Cyg and H1743−322 with the results of the application of the *accretion-jet* model . . . 109
6.4 ATCA and *Chandra* detections of MAXI J1348−630 in quiescence . . . 111
6.5 Radio/X-ray diagram of MAXI J1348−630, with the addition of its detection in quiescence . . . 112
6.6 Radio/X-ray diagram with the known BH LMXBs detected in quiescence . . . 113

7.1 MeerKAT images of MAXI J1348−630 – First part . . . 116
7.2 MeerKAT images of MAXI J1348−630 – Second part . . . 117
7.3 Radio light curve of RK1 . . . 118
7.4 ATCA 9 GHz image of the discrete ejecta RK1 and RK2 . . . 120
7.5 Radio light curve of RK2 . . . 120
7.6 Positional offset of a stable background point source observed with MeerKAT . 122
7.7 Angular separation in arcsec between RK1 and MAXI J1348−630 . . . 124
7.8 Angular separation in arcsec between RK2 and MAXI J1348−630 . . . 127
7.9 Constraints on the jet speed and inclination for RK1 and RK2 . . . 129

8.1 Schematic representation of the observed jet behaviour and proposed scenario for MAXI J1348−630 . . . 144
8.2 Angular separation between the discrete ejecta and MAXI J1348−630 – External shock model fit with uniform density . . . 147
8.3 Angular separation between the discrete ejecta and MAXI J1348−630 – External shock model fit with cavity scenario . . . 148
8.4 Corner plots showing the results of the external shock model fit with MCMC . 149
8.5 Angular separation between the discrete ejecta and MAXI J1348−630 – External shock model fit with distance prior centered at 3.39 kpc . . . 150
8.6 Posterior distribution for the ejecta mass . . . 156
8.7 Predicted proper motion of the unseen receding component of the discrete ejecta from MAXI J1348−630 . . . 161

List of Tables

1.1 Average values of mass, radius, density and compactness for different classes of compact objects 4

5.1 Summary of the X-ray spectral state evolution of MAXI J1348−630 during the 2019/2020 major outburst 82
5.2 Radio flux densities S_ν of MAXI J1348−630 94
5.3 X-ray spectral parameters of MAXI J1348−630 obtained from *Swift*/XRT observations 98

6.1 Radio flux densities and unabsorbed X-ray fluxes selected for the radio/X-ray diagram of MAXI J1348−630 103

7.1 Radio flux densities S_ν of the second radio knot RK2 121
7.2 Measured positions of RK1 and its angular separation from MAXI J1348−630 122
7.3 Parameters obtained from the fitting of the motion of RK1 and RK2 126
7.4 Measured positions of RK2 and its angular separation from MAXI J1348−630 127
7.5 Radio flux densities S_ν of the first radio knot RK1 137

8.1 Parameters of the external shock model applied in this work and chosen prior distributions 146
8.2 Fit results of the application of the external shock model to MAXI J1348−630 . 148

List of Abbreviations

ADAF	Advection Dominated Accretion Flow
ADIOS	Advection Dominated Inflow-Outflow Solutions
AGN	Active Galactic Nuclei
ATCA	Australia Telescope Compact Array
AU	Astronomical Units
BAT	Burst Alert Telescope on board *Swift*
BH	Black Hole
CASA	Common Astronomy Software Application
CCD	Charge-Coupled Device
DDT	Director's Discretionary Time
DEC	Declination
ESA	European Space Agency
EVN	European VLBI Network
FWHM	Full Width at Half Maximum
GRB	Gamma-Ray Burst
GSC	Gas Slit Camera
HEASARC	High Energy Astrophysics Science Archive Research Center
HID	Hardness-Intensity Diagram
HIMS	Hard-Intermediate State
HMXB	High-mass X-ray binary
IMBH	Intermediate-mass black hole
INTEGRAL	International Gamma-Ray Astrophysics Laboratory
IR	Infrared
ISCO	Innermost Stable Circular Orbit
ISS	International Space Station
LMXB	Low-Mass X-ray binary
MAXI	Monitor of All-sky X-ray Image
MERLIN	Multi-Element Radio Linked Interferometer Network
MJD	Modified Julian Date
MRI	Magnetic Rotational Instability
NASA	National Aeronautics and Space Administration
NIR	Near-Infrared
NuSTAR	Nuclear Spectroscopic Telescope Array
PC	Photon-Counting
QPO	Quasi-Periodic Oscillations
PI	Principal Investigator
PSF	Point Spread Function
RA	Right Ascension
RFI	Radio frequency interference
rms	Root Mean Square

RXTE	Rossi X-ray Timing Explorer
SIMS	Soft-Intermediate State
SKA	Square Kilometer Array
SMBH	Supermassive Black Hole
SNR	Signal-to-noise ratio
SSC	Synchrotron Self-Compton
SVOM	Space-based multi-band astronomical Variable Objects Monitor
2MASS	Two Micron All Sky Survey
ToO	Target of Opportunity
UV	Ultraviolet
UVOT	Ultraviolet/Optical Telescope on board *Swift*
VLA	Karl G. Jansky Very Large Array
VLBI	Very Long Baseline Interferometry
WT	Windowed-Timing
XRT	X-ray Telescope on board Swift
XSPEC	X-Ray Spectral Fitting Package

Introduction

Astrophysical jets are a fascinating phenomenon observed across a wide range of galactic and extra-galactic objects. The first evidence for the existence of large scale, collimated jets dates back to Curtis (1918), who found an elongated jet-like feature of unknown origin in optical observations of the galaxy M87 in the Virgo cluster. It was later realized through radio observations that such jets were associated with rapid plasma ejection (Baade and Minkowski, 1954), and synchrotron from electrons accelerated at relativistic speeds in a magnetic field was identified as the emission mechanism responsible for the observed radiation, requiring a huge amount of energy (Burbidge, 1956).

Subsequently, similar jet features were observed in other radio-galaxies, quasars and active galactic nuclei (AGNs), and jets were found to share distinctive properties, being collimated, energetic, extended at large scales and constituted of matter accelerated at extremely high velocities, close to the speed of light. Such outflows are therefore often called *relativistic jets*. Jets were later found also in galactic objects, including protostars (Herbig-Haro objects), and, most importantly for this thesis, X-ray binaries (XRBs). X-ray binaries were first discovered with the birth of X-ray astronomy around sixty years ago (Giacconi et al., 1962), when it was rapidly understood that the observed intense X-ray emission was produced by the accretion of stellar material onto compact objects (e.g. Salpeter 1964). At the same time, the development of radio astronomy allowed the first detections of radio emission from XRBs (e.g. Sco X-1, Cyg X-1 and Cyg X-3, Hjellming and Wade 1971a; Hjellming and Wade 1971b; Gregory and Kronberg 1972). Jets were then resolved in radio for the first time in SS 433 (Spencer, 1979; Hjellming and Johnston, 1981), and superluminal discrete ejecta were detected in the galactic XRB GRS 1915+105 (Mirabel and Rodríguez, 1994). For their striking similarities with AGNs, XRBs displaying jets were also called *microquasars*. It then became clear that collimated ejection phenomena are universal among a large variety of objects and across all physical scales, from stellar objects to supermassive black holes. It was also realised that all sources of jets were sharing a fundamental physical mechanism, which is the accretion of matter. Jets are, in fact, indissolubly linked to accretion, and this fundamental connection is valid for all size and energy scales in the Universe. Understanding the nature of this intimate connection is crucial for improving our understanding of the processes that occur around compact objects, including black holes.

In this thesis, I focus on black hole low mass X-ray binaries (BH LMXBs) to investigate the properties of their jets and to study their coupling with the accretion flow. Black hole low mass X-ray binaries represent astrophysical laboratories of key importance, as they enable us to study the accretion/ejection connection, to investigate the influence of compact objects up to the galactic scale and to test General Relativity in the strong field regime. In BH LMXBs, a stellar mass black hole accretes matter from the companion star and is able to channel a fraction of the accreted mass and liberated (potential) gravitational energy into powerful jets. These systems occasionally enter outburst phases during which they cycle through different accretion states with distinct spectral and timing signatures (Homan and Belloni, 2005), allowing us to study the full range of accretion states in the same object on human timescales, and how these

states connect to the properties of their relativistic ejections (e.g. Remillard and McClintock 2006). Very significant progress has been achieved in the past decades, which led to a "standard picture" of BH LMXBs in outburst (Corbel et al., 2004a; Fender, Belloni, and Gallo, 2004).

Jets from BH LMXBs can have different forms on very different scales: from compact, collimated jets at small scales (∼tens of AU), to moving, discrete jet components at pc scales (e.g. Fender 2006). These discrete ejecta are in fact one of the most interesting features of BH LMXBs, and consist of bipolar plasmons that move away from the core at relativistic speeds, often displaying apparent superluminal motion. At ejection, these objects produce strong flares and emit synchrotron radiation at radio wavelengths (e.g. Fender, Belloni, and Gallo 2004). After a first phase, in some cases these jets can travel undetected for long periods, before being detected again at large (parsec) scales, with the emission coming from their interaction with the surrounding interstellar medium. The energy released through the jets can have a strong impact on the interstellar medium (ISM) and, similarly to AGNs, BH LMXBs can be important sources of feedback, up to galactic scales.

Despite the fundamental progress achieved in the field over the past 50 years, we still do not have a complete understanding of all the observational properties exhibited by BH LMXBs and on the physics associated, and we lack a precise model bringing together all the observational signatures and the interplay between the different components of the system. In the last ∼25 years, jets have been observed, resolved and identified in a large number of sources (e.g. Mirabel et al. 1992; Mirabel and Rodríguez 1994; Corbel et al. 2000) and important results were achieved concerning our knowledge of these relativistic outflows. However, several fundamental questions remain today unanswered. For instance, the powering mechanism of the jets is still subject of debate, and it is not clear whether it consists of extracting rotational energy from a spinning black hole (Blandford and Znajek, 1977) or by tapping energy from the accretion disk (Blandford and Payne, 1982). This involves the fundamental connection between the jets and the disk and, for this reason, the nature of the coupling between accretion and ejection in accreting compact objects has been studied extensively over the past decades and is today one of the most important questions in the field of high-energy astrophysics. Surprisingly, the radio and X-ray monitoring of multiple BH LMXBs over the last two decades has led to the discovery of two distinct populations of black holes, that display different behaviours in the global radio/X-ray diagram of stellar-mass accreting BH, which compares the luminosities of the jets and of the accretion flow (Hannikainen et al., 1998; Corbel et al., 2000; Coriat et al., 2011; Corbel et al., 2013b). This may suggest the existence of two different fundamental couplings between the compact jets and the inner accretion flow, whose origin is still poorly understood. Moreover, there are hints of sources that might switch from one group to the other, displaying a *hybrid* behaviour, further complicating the picture.

The jet composition is still unknown, and there is no clear indication towards a baryonic or leptonic scenario, or a mixture of the two, as for instance proposed for AGNs (e.g. Vuillaume, Henri, and Petrucci 2018). Moreover, we still cannot accurately constrain the physical parameters of the discrete ejecta. In particular, the jet energy is a key parameter, as today the total energy content of these jets is unknown. While lower limits on the energy are generally obtained by considering the jet's synchrotron emission (e.g. Longair 2011), such a method is likely to largely underestimate the total energy content of the jet (Steiner and McClintock, 2012; Bright et al., 2020). In addition, there is large uncertainty on the jet mass loading, and a reliable estimation of the jet's mass and energy can be particularly useful for understanding the jet composition. Finally, we are not able to precisely identify the sequence of observational signatures that precede a discrete ejection, including the spectral state transitions, the flaring

activity and the variable presence of different types of quasi-periodic oscillations (QPOs) seen in the X-rays (van der Klis, 2006; Ingram and Motta, 2019).

The goal of my thesis is to provide new observational insights into the jet properties, trying to address some of the open problems listed above, both on compact jets and discrete ejecta. Progress can be made by focusing on a single object (every source shows peculiar properties) and performing a dense monitoring campaign, covering the entire outburst and obtaining high-quality observations of the jets during their entire evolution. Then, such information can be linked to what is currently known on the entire source population to obtain a global context. Therefore, my work has been focused in the interpretation of the results concerning both compact jets and discrete ejecta observed in a new source: the black hole X-ray binary MAXI J1348−630, and in this thesis I present the results of our dense multi-wavelength monitoring campaign of this new source during its 2019/2020 discovery outburst. We have observed MAXI J1348−630 in the radio band with MeerKAT and with the Australia Telescope Compact Array (ATCA), and in the X-rays with MAXI, *Swift*/XRT and *Chandra*, collecting in total more than 200 observations.

In the first part of the manuscript, I present what is currently known on the physics of accreting black holes and on their jets. Specifically, in Chapter 1 I discuss the accretion onto compact objects and our current knowledge of XRBs, including their classification, their components and their outburst phenomenology. Then, in Chapter 2 I discuss in detail the compact jets and their connection with the accretion flow, presenting the above-mentioned radio/X-ray diagram and its possible interpretations. Discrete ejecta are the subject of Chapter 3, and I will discuss their observation, their ejection phenomenology and their interaction with the ISM. In the following Chapter (4), I present the tools used for our data analysis, including the telescopes (MeerKAT, ATCA, *Swift*/XRT and MAXI), the radio-interferometry technique and an introduction on Bayesian statistics and Monte Carlo Markov Chains.

The results of my work are presented in the second part of the manuscript, starting with a broad presentation of the outburst of MAXI J1348−630 in Chapter 5. Then, in Chapter 6 I present the study of the disk/jet coupling in MAXI J1348−630 and a discussion of its behaviour in light of the currently proposed scenarios, with the addition of its recent detection in quiescence. In Chapter 7 I present the observations of the two discrete ejecta launched by MAXI J1348−630, and I discuss their ejection, motion, and late-time behaviour. The final Chapter (8) is dedicated to a discussion of the results of the application of an external shock model to the motion of the first ejecta, showing how such modeling allowed us to constrain a large number of physical parameters of the jets and to obtain information on the environment surrounding MAXI J1348−630.

I finish the manuscript with the conclusions on this work and with the perspectives for its future continuation. The work presented in this thesis has been the subject of three research papers, which have been recently published. Our data also contributed to the results of a fourth paper, that is included in Appendix A.

Chapter 1

X-ray binaries

Contents

1.1 Accreting compact objects . . . 2
1.1.1 The birth of compact objects . . . 2
1.1.2 Compactness . . . 3
1.1.3 Accretion efficiency and Eddington limit . . . 4
1.2 Accretion in a binary system . . . 6
1.2.1 Roche lobe overflow . . . 6
1.2.2 Accretion disk formation and emission . . . 8
1.3 Black hole X-ray binaries . . . 10
1.3.1 Population . . . 10
1.3.2 Main components . . . 13
1.4 The outburst phase . . . 17
1.4.1 The disk instability model . . . 18
1.4.2 Spectral states and outburst evolution . . . 20

This first chapter outlines the main characteristics and our current understanding of accreting black hole X-ray binaries (XRBs), which are the objects studied in the thesis work. In particular, I am interested in the properties of their spectacular relativistic outflows, taking the form of different types of relativistic jets. However, ejection appears to be common wherever mass accretion onto a central object occurs, and hence it is fundamental to first introduce the accretion process. Without the scope of being exhaustive, this discussion aims at providing a general idea of our current knowledge of XRBs, including their phenomenology, their components and their classification. In Section 1.1 I introduce compact objects and some useful equations linked to the energetics of accretion, while in Section 1.2 I discuss the dominant process through which stellar mass black holes accrete: Roche lobe overflow, and I outline the main characteristics of the resulting accretion disk. In the following, I present the different classification of XRBs (Section 1.3), along with their main components (jets, disk, corona), and the currently known

population. These sources are mostly observed during bright outburst phases, hence I present the outburst phenomenology and the observed spectral state transitions in Section 1.4. The primary bibliographic source for this chapter is Frank, King, and Raine (2002).

1.1 Accreting compact objects

An accreting object accumulates matter through gravitational attraction. As accreting material falls onto a gravitationally attracting body, its gravitational potential energy is converted into kinetic energy. The phenomenon of accretion is universal among a large variety of astrophysical objects, from the accumulation of material in protoplanetary disks to the feeding of galactic and supermassive black holes through hot plasma accretion disks. Here I discuss accretion onto compact objects, which have the property of having an extremely strong gravitational field, to the extent that relativistic effects have to be taken into account in their physical description (e.g. Longair 2011).

1.1.1 The birth of compact objects

Compact objects, which include white dwarfs, neutron stars and black holes in order of increasing compactness, are the final products of stellar evolution. The type of remnant object which is left after the end of thermonuclear reactions inside the star's core depends on the mass and on the metallicity of the progenitor star itself. In a first approximation, the more massive the star is, and the lowest the metallicity, the more compact the remnant object will be (e.g. Woosley, Heger, and Weaver 2002).

After the end of the internal nuclear reactions, the radiation pressure dramatically decreases and the star is not anymore able to compensate for the auto-gravitation, and therefore collapses on itself. Such collapse continues until the density reaches a value high enough for new sources of pressure to sustain the object. For stars with mass $M \lesssim 8M_\odot$, the collapse will result in the birth of a *white dwarf*, which is sustained by the electron degeneracy pressure originating from the Pauli exclusion principle of quantum mechanics. The maximum mass of a white dwarf allowed by this mechanism is roughly $1.4M_\odot$ (the Chandrasekhar mass). If the progenitor star is part of a binary system, the white dwarf might accrete from the companion star and the system will become a cataclysmic variable (CV, Warner 2003).

More massive stars ($M \gtrsim 8M_\odot$) will produce an iron core at the end of their life with a mass above the Chandrasekhar limit. Their collapse will cause the disintegration of the atomic nuclei, causing the electrons and protons to combine to form neutrons in a even denser compact object, called *neutron star*. Such object is not supported by the electron degeneracy pressure, but it is sustained by the neutron degeneracy pressure and by short-range repulsive neutron-neutron strong-force interactions. The limiting value for a neutron star mass, analogous to the Chandrasekhar limit, is known as the Tolman-Oppenheimer-Volkoff limit, and its current estimate is $\sim 2.3\ M_\odot$ (Kalogera and Baym, 1996; Shibata et al., 2019), corresponding to a progenitor star in the mass interval $10 \sim 25\ M_\odot$.

Above this limit, nothing can stop the gravitational collapse, and a stellar mass *black hole* will be formed. These stellar mass black holes are the sites of the highest gravitational curvature available today in the universe, and represents the best tests of general relativity available to us in the strong field regime (Psaltis, 2008). Black holes do not form only through gravitational collapse, but also through mergers of compact objects, as recently confirmed by the repeated LIGO and Virgo detections of gravitational waves from the coalescence of pairs of stellar-mass



Figure 1.1: The shadow of the supermassive black hole at the center of M87 in a radio-interferometric image made by the Event Horizon Telescope. This is the first observation to ever resolve the shadow and the photon capture radius of a black hole, which is around ∼2.5 times the Schwarzschild radius $R_{\rm S}$. Credits: Event Horizon Telescope Collaboration et al. (2019).

black holes, that merge and form new, more massive, black holes (e.g. Abbott et al. 2016 and other publications from the LIGO-Virgo collaboration).

On the other side of the mass spectrum we have supermassive black holes (SMBHs). These objects are located at the centres of most of the large galaxies, including the Milky Way, and have masses of $10^6 \sim 10^9 M_\odot$. It is not yet clear how SMBHs can be formed, and there are nowadays multiple viable scenarios, which include the accretion of large amounts of mass onto a pre-existing stellar-mass black hole, the direct gravitational collapse of a dense cluster of stars, or the merger of many stellar-mass black holes (e.g. Shapiro and Teukolsky 1985; Shibata and Shapiro 2002; Begelman, Volonteri, and Rees 2006). A first, historical, radio-interferometric picture of a SMBH is shown in Figure 1.1, which displays the SMBH M87* that has been imaged by the Event Horizon Telescope in 2019 (Event Horizon Telescope Collaboration et al., 2019).

1.1.2 Compactness

It is possible to define a parameter linking the gravitational and rest-mass energy of an astrophysical object to obtain a quantitative estimate of how much such an object deforms the surrounding space-time. An homogeneous sphere with mass M and radius R has a total gravitational energy

$$E_{\rm grav} = -\frac{3}{5}\frac{GM^2}{R} \tag{1.1}$$

where G is the gravitational constant. At the same time, the rest-mass energy is Mc^2, and the ratio between the two energies is

$$\frac{E_{\rm grav}}{Mc^2} = -\frac{3}{5}\frac{GM}{Rc^2} \tag{1.2}$$

Table 1.1: Average values of mass, radius, density and compactness for different classes of compact objects. For black holes, the average density is computed as the ratio between the mass and the volume inside the event horizon. In the last row, the highest density corresponds to the least massive black holes. Adapted from Coriat (2010) and Cangemi (2020).

Object	Mass [$M_\odot$]	Radius [km]	Density [kg m^{-3}]	Compactness
White dwarf	0.1-1.4	$\sim 10^4$	$\sim 10^{10}$	10^{-4}–10^{-3}
Neutron star	1–3	~ 10	$\sim 10^{18}$	~ 0.2
Non-rotating stellar mass black hole	$\gtrsim 3$	9^a	$\sim 10^{18}$	0.5
Rotating stellar mass black hole^b	$\gtrsim 3$	4.5^a	$\sim 10^{19}$	1
Rotating supermassive black hole	10^6–10^9	10^6–10^9	10^2–10^8	1

^{a}for $M = 3M_\odot$.

^{b}Assuming maximal rotation (spin $a = 1$).

From this ratio, we can define the adimensional *compactness* parameter Ξ (e.g. Shibata 2015) as

$$\Xi = \frac{GM}{Rc^2} = \frac{R_\mathrm{G}}{R} \tag{1.3}$$

which can also be expressed in terms of the gravitational radius $R_\mathrm{G} = GM/c^2$, which is a typical length scale for compact objects and its value is $1/2$ of the Schwarzschild radius R_S (i.e. the radius around an object at which the escape velocity equals c). The compactness allows us to quantify how strong the gravitational field of a given object is, and how important general relativistic effects will be for its description. An object is defined as *compact* if it has $\Xi > 10^{-4}$. I present in Table 1.1 the values of Ξ for the compact objects discussed in the previous section. The maximum compactness in the universe is attained by rotating black holes, described by the Kerr metric in General Relativity, for which $R = R_\mathrm{G}$, implying $\Xi = 1$.

1.1.3 Accretion efficiency and Eddington limit

As mentioned in Section 1.1, accreting compact objects are able to convert gravitational potential energy into kinetic energy and then radiation, by tapping into the large energy reservoir created by their strong gravitational field. Accretion is one of the most effective ways in the whole Universe (surpassed only by matter-antimatter annihilation) for the extraction of energy from matter. For this reason, accretion is always involved in the most energetic events known today, such as gamma-ray bursts, supernovae, ejections from active galactic nuclei (AGNs) and tidal disruption events (TDEs).

If we consider a compact object with mass M and radius R, the available potential energy from the accretion of a mass m is

$$\Delta E_\mathrm{acc} = \frac{GMm}{R} = \Xi mc^2 \tag{1.4}$$

from which we can directly see that, the more compact the accreting object is, the higher is the extracted energy. For compact objects, the compactness is high enough that a significant fraction of the rest-mass energy of accreted matter can be released: around 20% for neutron stars and 100% for black holes (but not in practice). This is way higher than another efficient

way of producing energy: nuclear fusion. In fact, the fusion of the same mass of hydrogen m into helium can provide "only" a value $\Delta E_{\rm nuc} \simeq 0.007mc^2$.

If the extracted gravitational energy is fully converted into radiation, for an accretion rate $\dot{M}$ the corresponding accretion luminosity can be written as

$$L_{\rm acc} = \Xi \dot{M} c^2 \tag{1.5}$$

This equation needs to be corrected for black holes, that, without a hard surface, will advect most of the energy through the event horizon, increasing their mass instead of radiating. Therefore, the accretion luminosity needs to be parameterised by an efficiency η

$$L_{\rm acc} = \eta \dot{M} c^2 \tag{1.6}$$

η corresponds to the radiative efficiency of the accretion flow, or, in other words, the efficiency in converting the rest-mass energy of the accreted matter in radiation. While hard to measure, one can place upper limits on its value by considering that the matter cannot be advected unless it dissipates its gravitational energy. We can then estimate η as the available potential energy per unit mass at the innermost stable circular orbit (called ISCO, Misner, Thorne, and Wheeler 1973; Steiner et al. 2010). Theoretical calculations estimate $\eta_{\rm max} \sim 6\%$ for Schwarzschild (non-rotating) black holes and $\eta_{\rm max} \sim 40\%$ for a Kerr (maximally rotating) black hole (e.g. Bardeen, Press, and Teukolsky 1972; Page and Thorne 1974; Frank, King, and Raine 2002).

Despite the high accretion efficiency of compact objects, there is a theoretical limit to the luminosity derived by accretion, referred to as the Eddington luminosity. This is because accretion is only possible as long as the gravitational attraction is stronger than the radiation pressure produced by photons from the internal regions of the accretion flow. When the radiation pressure exceeds the gravitational pull, the in-falling matter is expelled and the accretion is halted. The Eddington limit can be derived if we consider the accretion of plasma at distance r from the compact object. An electron-proton pair will be subject to a gravitational force

$$F_{\rm grav} = \frac{GM(m_{\rm p} + m_{\rm e})}{r^2} \tag{1.7}$$

Each emitted photon transfers his momentum $p = h\nu/c$ (where h is the Planck constant) to an electron through Thomson scattering, hence with a cross section $\sigma_{\rm T} \propto m^{-2}$, which is larger for electrons than for protons. The number of photons per unit time and surface is $N_{\rm ph} = L/4\pi r^2 h\nu$. The force applied to each electron then corresponds to the rate of momentum transfer from the photons to the electron itself, and can be written as

$$F_{\rm rad} = \sigma_{\rm T} N_{\rm ph} p = \frac{\sigma_{\rm T} L}{4\pi r^2 c} \tag{1.8}$$

Equating the two previous quantities, we obtain the maximum possible luminosity for a stable accretion, namely the Eddington luminosity

$$L_{\rm Edd} = \frac{4\pi M G m_{\rm p} c}{\sigma_{\rm T}} \simeq 1.26 \times 10^{38} \left(\frac{M}{M_\odot}\right) {\rm erg\ s^{-1}} \tag{1.9}$$

from which, with Equation 1.6, we can obtain the limit on the corresponding accretion rate, which is fundamentally capped at

$$\dot{M}_{\rm Edd} = \frac{4\pi M G m_{\rm p} c}{\eta c \sigma_{\rm T}} \simeq 2.2 \times 10^{-9} \left(\frac{M}{M_\odot}\right) {\rm M}_\odot \ {\rm yr}^{-1} \tag{1.10}$$

It is important to remark that the Eddington limit is valid for spherically symmetric accretion, while often accretion is highly asymmetrical, as in XRBs. Thus, super-Eddington accretion is indeed possible, and it could be the case for the so-called ultraluminous X-ray sources, a part of which is composed of neutron stars that can accrete at rates over 100 times $\dot{M}_{\rm Edd}$ (see for instance Kaaret, Feng, and Roberts 2017).

1.2 Accretion in a binary system

In my thesis, I am interested in accretion and ejection in binary systems. In the Universe, binary systems are suprisingly common, as the majority of stars in our galaxy are found to live in binary systems (e.g. Duquennoy and Mayor 1991). An *X-ray binary* (XRB) is a system composed by a compact object, which is a black hole or a neutron star, and a second star, called *companion star*. The two components of the system will satisfy the third Kepler law

$$4\pi^2 a^3 = G(M_{\rm a} + M_{\rm d}) T_{\rm orb}^2 \tag{1.11}$$

where a is the orbital separation of the two objects, $M_{\rm a}$ is the mass of the "accreting" compact object, $M_{\rm d}$ is the mass of the "donor" companion star and $T_{\rm orb}$ is the orbital period, which generally is of the order of hours to days (e.g. Tetarenko et al. 2016). From Equation 1.11, we can get an estimate of the orbital separation (and hence the size) of the binary system

$$a = 3.5 \times 10^{10} \left(\frac{M_{\rm a}}{M_\odot}\right)^{\frac{1}{3}} \left(1 + \frac{M_{\rm a}}{M_{\rm d}}\right)^{\frac{1}{3}} \left(\frac{T_{\rm orb}}{\rm h}\right)^{\frac{2}{3}} \ {\rm cm} \tag{1.12}$$

which depends on the orbital period and on the mass ratio of the two components.

In this configuration, the energy extraction happens thanks to the accretion of mass transferred from the companion star to the compact object. In X-ray binaries, accretion generally occurs in two different ways: Roche-lobe overflow and wind accretion. The first way is dominant in the so-called low mass X-ray binaries (LMXBs), while the second is important for high mass X-ray binaries (HMXBs). This distinction depends on the type of companion star, and the two classes of sources are discussed in Section 1.3. Since in this work I deal with LMXBs, I will discuss more in detail the mechanism of accretion through Roche lobe overflow, while for wind accretion one can see for instance Frank, King, and Raine (2002).

1.2.1 Roche lobe overflow

For understanding the accretion process in a binary system, one needs to consider the gravitational potential in the reference frame rotating with the angular velocity of the system Ω. In such frame, where the reference point is the center of mass of the system, we can write the gravitational potential at a point $\vec{r}$, called Roche potential, by taking into account the gravitational

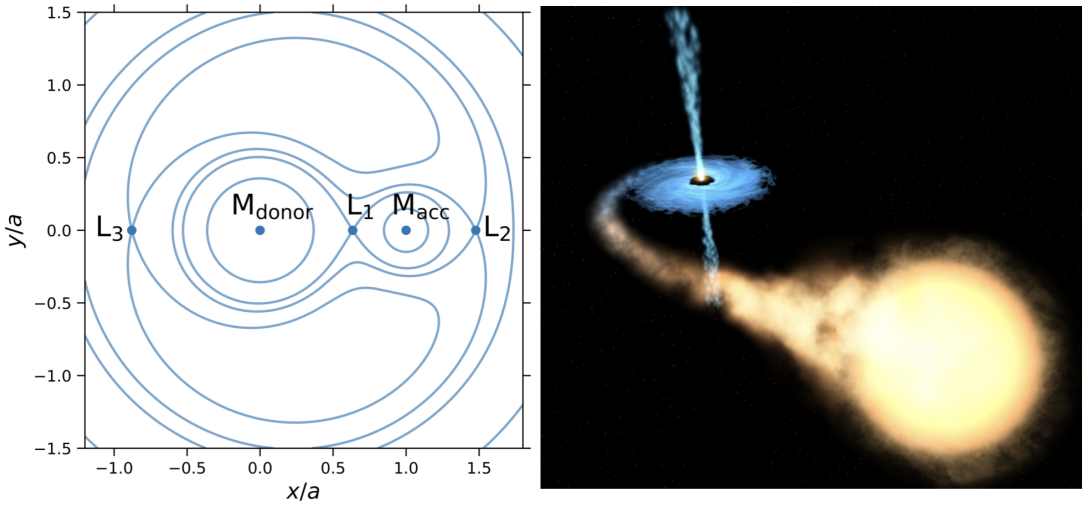

Figure 1.2: *Left*: Equipotential lines of the Roche potential for a binary system with binary separation a and mass ratio $M_{\rm a}/M_{\rm d} = 0.26$, from Misra et al. (2020). The equipotential lines passing through Lagrangian points L_1, L_2 , and L_3 are also shown. *Right:* Artistic representation of a black hole accreting matter from a companion star through Roche lobe overflow. The mass from the companion star is gravitationally attracted towards the black hole, forming an accretion disk. *Credits*: NASA.

attraction of the two objects and the centrifugal force. We have:

$$\Phi_{\rm R}(\vec{r}) = -\frac{GM_{\rm d}}{|\vec{r}-\vec{r}_{\rm d}|} - \frac{GM_{\rm a}}{|\vec{r}-\vec{r}_{\rm a}|} - \frac{1}{2}(\vec{\Omega}\times\vec{r})^2 \tag{1.13}$$

where $\vec{r}_{\rm d}$ and $\vec{r}_{\rm a}$ are the distances to the accreting compact object and to the companion star, respectively. The equipotential surfaces for the donor and the accretor are shown in Figure 1.2. In a binary system, we can then identify five points in which the net gravitational attraction vanishes, called *Lagrangian* points, representing points of stable or unstable gravitational equilibrium. In this context, the point that is of interest for us is L_1, which is the saddle point in common between two specific equipotential surfaces (called *Roche lobes*) of the objects (see Figure 1.2). The reason is that gravitationally bound matter passing by L_1 can be transferred from one object to the other. The mass transfer from the donor to the accretor is possible when the companion star expands and fills entirely its Roche lobe, in general due to stellar evolution, up to the point for which a part of its outer layers is close to L_1. In this situation, a simple perturbation can trigger the mass transfer into the gravitational well of the compact object. The first stream of matter flowing through L_1 traces an elliptical trajectory (at a first approximation) around the compact object, before colliding with the following material and dissipating energy through shocks, without losing its angular momentum (Frank, King, and Raine, 2002). This causes the accreted matter to settle into a circular orbit around the compact object, at a radius determined by the conservation of angular momentum J of the incoming gas at L_1

$$R_{\rm circ} = \frac{J^2}{GM_a} = \frac{\Omega^2 b^4}{GM_a} \tag{1.14}$$

where b is the distance between the compact object and L_1.

1.2.2 Accretion disk formation and emission

After the in-flowing matter circularised at a given $R_{\rm circ}$, energy dissipation occurs through viscous friction. The dissipation causes the conversion of gravitational and kinetic energy into internal energy, which will heat the orbiting material and will be radiated away. Such energy loss means that the gas will move to a lower orbit, that implies also a lower angular momentum, which has to be redistributed outwards. Since the timescale for such redistribution is larger than the rotation period and than the timescale for energy loss by radiation (Frank, King, and Raine, 2002), the matter will slowly spiral inwards in a succession of circular orbits, creating a so-called *accretion disk* (Frank, King, and Raine, 2002). Such a disk can extend down to the ISCO, after which the matter is finally accreted, and, in case of a black hole, crosses the event horizon. Neglecting the auto-gravity of the disk, since its mass is way smaller than the one of the accretor, the orbits will be Keplerian and the in-falling matter will have an angular velocity

$$\omega = \sqrt{\frac{GM_{\rm a}}{R^3}} \tag{1.15}$$

where R is the distance from the accretor, and hereafter we will refer to M as the mass of the accreting object. Hence, the disk will be characterized by differential rotation. In a standard accretion disk, as the matter slowly approaches the accretor, the angular momentum is transported outwards to the layers with higher energy and at higher orbits. In the disk plasma, viscosity is responsible for the systematic transport of the angular momentum (Frank, King, and Raine, 2002). Such viscosity is thought to be produced in turbulent conditions, but its origin is not completely understood. The most promising explanation today is the so-called *magneto-rotational instability* (MRI, Velikhov 1959; Chandrasekhar 1960; Balbus and Hawley 1998), for which the disk magnetic field has a key role. In a disk threaded by a magnetic field, the field itself acts as a spring that counteracts any possible displacement perpendicular to a field line. Without entering in details, if the disk has differential rotation, this effect will make the motion of particles in the different orbits unstable, creating turbulence and ultimately producing viscosity in the disk.

The accretion disk radiates with a multi-temperature thermal spectrum peaking in the X-rays, and we can derive here the emission for geometrically thin, optically thick, radiatively efficient disk. If the disk rotation is Keplerian, then the viscous dissipation per unit area per unit time at radius R is

$$D(R) = \frac{3GM\dot{M}}{4\pi R^3}\left[1 - \left(\frac{R_*}{R}\right)^{\frac{1}{2}}\right] \tag{1.16}$$

where R_* is the radius of the compact object (Pringle, 1981).

The total radiated power can be obtained by integrating $D(R)$ from the ISCO radius $R_{\rm int}$ to infinity

$$L_{\rm disk} = \int_{R_{\rm in}}^{\infty} D(R) 2\pi R dR = \frac{GM\dot{M}}{2R_{\rm in}} \tag{1.17}$$

from which we can see that the disk can radiate up to $1/2$ of the accretion power $\dot{M}c^2$ for a maximally rotating black hole, for which $R_{\rm int} = GM/c^2$ (but see discussion in Section 1.1.3). Since the disk is optically thick, each layer at radius R of the disk surface emits as a blackbody

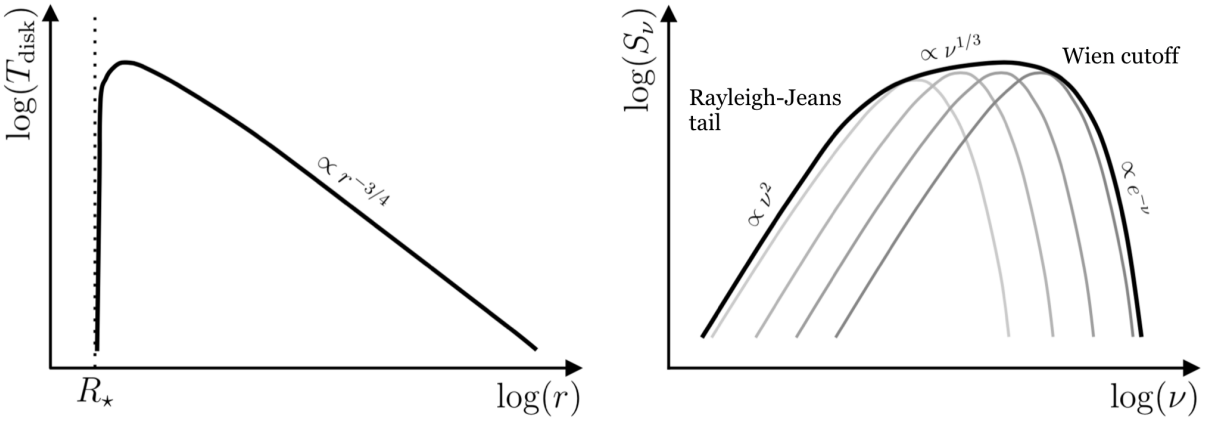

Figure 1.3: *Left*: Temperature profile of an accretion disk. The maximum temperature is reached close to the compact object, up to $\sim 10^7$ K for a stellar mass black hole (Shakura and Sunyaev, 1973). *Right*: Spectrum of a multi-color accretion disk. The spectrum results from the superposition of blackbody emissions from layers of the disk at different distances from the center. Adapted from Loh (2016).

with temperature

$$T(R) = \left[\frac{3GM\dot{M}}{8\pi R^3\sigma}\left(1 - \left[\frac{R_*}{R}\right]^{\frac{1}{2}}\right)\right]^{\frac{1}{4}} \tag{1.18}$$

where σ is the Stefan-Boltzmann constant, (Frank, King, and Raine, 2002). The temperature profile of a typical accretion disk is shown in the left panel of Figure 1.3.

The blackbody spectrum reads

$$B_\nu(T) = \frac{2h\nu^3}{c^2}\left[\exp\left(\frac{h\nu}{k_\mathrm{B}T}\right) - 1\right]^{-1} \tag{1.19}$$

where k_B is the Boltzmann constant. If the disk plane has an inclination i with the line of sight of an observer at distance D, the resulting observable spectrum from the disk will be

$$S_\nu = \frac{4\pi h\nu^3\cos i}{c^2 D^2}\int_{R_*}^{R_\mathrm{out}} \frac{RdR}{\exp\left(\frac{h\nu}{k_\mathrm{B}T(R)}\right) - 1} \tag{1.20}$$

where R_out is the radius of the outer edge of the disk (Frank, King, and Raine, 2002). Such a spectrum is the direct result of the superposition of multiple layers of the disk that are located at different distances from the compact object and have different temperatures. For this reason, it is also called a *multi-color* disk spectrum (Mitsuda et al., 1984). The spectrum is shown in the right panel of Figure 1.3. It is remarkable to notice that the emitted spectrum is independent of the disk viscosity. For frequencies $\nu \ll k_\mathrm{B}T(R_\mathrm{out})/h$ the spectrum has the typical Rayleigh-Jeans tail where $S_\nu \propto \nu^2$. At intermediate frequencies, the spectrum goes as $S_\nu \propto \nu^{1/3}$, while for $\nu \gg k_\mathrm{B}T(R_\mathrm{out})/h$ we have the well-known Wien cutoff. The inner layer of the disk is characterized by the highest temperature, and emits around 1 keV for typical black hole low mass X-ray binaries, while the cooler, outer layers contribute to the emission at lower energies, around 0.1 keV.

1.3 Black hole X-ray binaries

The discussion presented above is valid for every compact object. From now on, I will focus on the population of objects studied in this thesis, X-ray binaries containing stellar mass ($\sim$10 $M_\odot$) black holes. I present here the classification, the known population and main properties of black hole X-ray binaries.

1.3.1 Population

X-ray binaries (XRBs) are binary systems that, as the name says, radiate most of their energy in the X-ray band. To identify the nature of the accreting compact object, discriminating between a neutron star and a black hole, the preferred method is to measure its mass in a model independent way. This can be done by measuring an important observational quantity, called the binary mass function, which is given by

$$f(M) = \frac{P_{\rm orb}}{2\pi G}(K_{\rm d})^3 = \frac{M_{\rm a}^3 \sin^3 i}{(M_{\rm a} + M_{\rm d})^2} \tag{1.21}$$

where $K_{\rm d}$ is the radial velocity of the companion star, $P_{\rm orb}$ is the orbital period, i it the orbital inclination of the system, and the last equality is due to the third Kepler's law. Since $\sin^3 i < 1$, this implies $M_{\rm a} > f(M)$, which can provide us with a direct lower limit on the mass of the compact object. If $M_{\rm a}$ turns out to be higher than what is possible for a neutron star (see Section 1.1.1), then it has to be a black hole. Such method requires optical/infrared (or X-rays) observations to measure the orbital period of the system from its light curve and the radial velocity (Doppler spectroscopy of spectral lines) of the star. This method allowed so far to identify at least 20 stellar-mass *dynamically confirmed black holes* in our Galaxy (e.g. Orosz et al. 2002; Remillard and McClintock 2006; Orosz et al. 2011; Miller-Jones et al. 2021), and a part of them is shown in Figure 1.4. However, due to the faintness of the stellar emission, such observations are not always possible. In this case, we can rely on the measurements of the spectral and timing properties of the systems, that can be consistent with the presence of a black hole, and will be discussed in Section 1.4. In this way, nowadays $\sim$50 black hole *candidates* in XRBs have been identified (e.g. Fender and Muñoz-Darias 2016), bringing the total number of potentially observed galactic stellar-mass black holes to $\sim$70. Those sources have been mostly discovered thanks to the presence of all-sky monitors on board X-ray satellites, susch as *Ginga* (from 1987 to 1991), the Rossi X-ray Timing Explorer (RXTE, from 1996 to 2012), *Swift* (since 2004) and MAXI (since 2009).

However, this is just a tiny fraction of the total number of black hole XRBs that might be present in our Galaxy ($\sim 10^4$, from population synthesis studies, Yungelson et al. 2006), which is in turn just a negligible fraction of the estimated total number of black holes in our Galaxy, around $10^8 - 10^9$, from stellar evolution models (Brown and Bethe, 1994). The low number of black hole binary systems discovered so far is mostly due to the low outburst rate of these sources (e.g. Corral-Santana et al. 2016, but see Section 1.4), or due to their possible faint peak X-ray luminosities.

X-ray binaries are generally classified in two groups with very different accreting properties, depending on the mass of the companion star. Low mass X-ray binaries (LMXBs) have in general companion stars with $M \lesssim 3M_\odot$, while high mass X-ray binaries (HMXBs) have companion stars with $M \gtrsim 10M_\odot$ (e.g. Tetarenko et al. 2016. I discuss the main properties of the two groups here, starting with HMXBs.

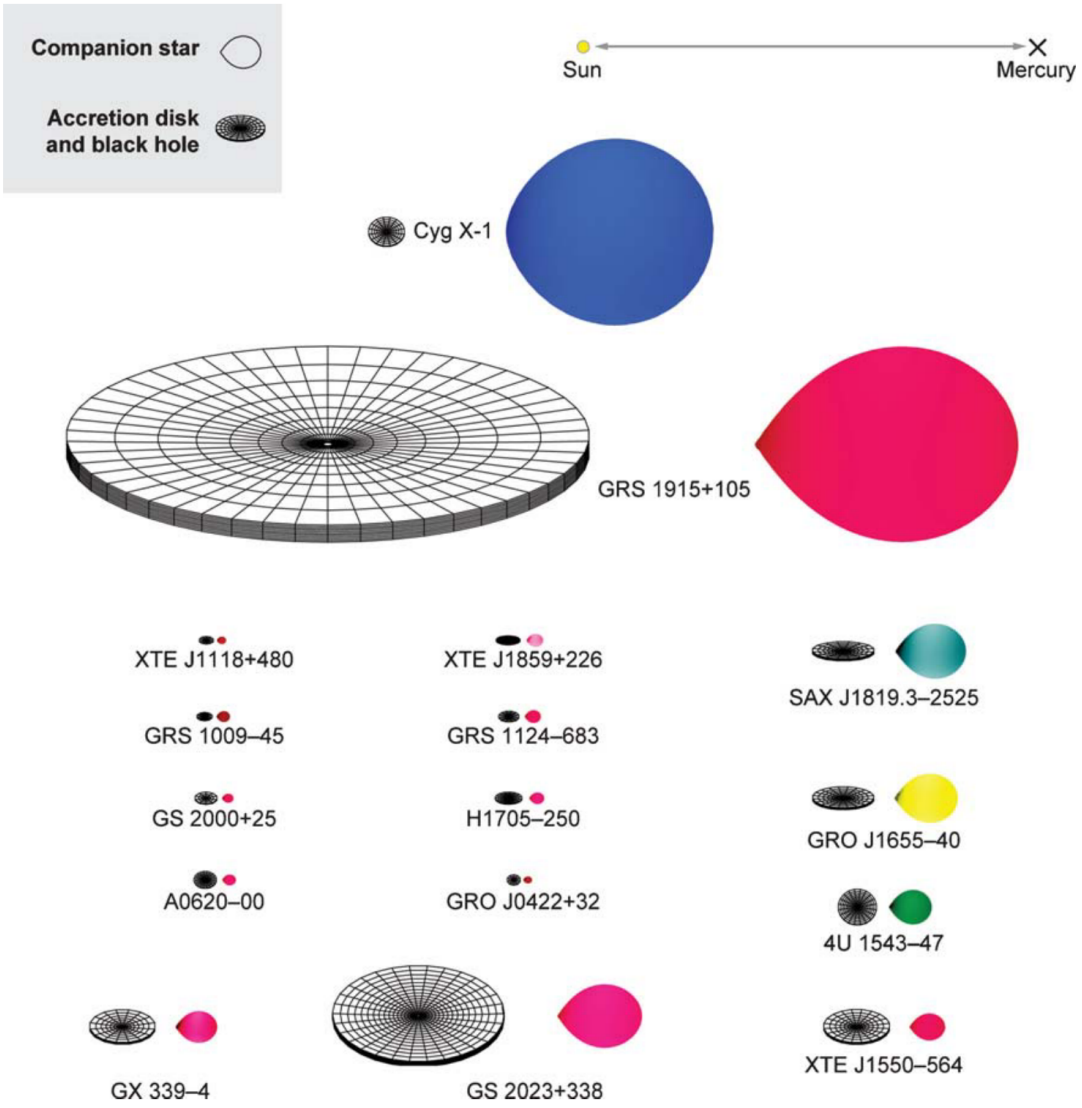

Figure 1.4: Scale drawings of 16 X-ray binaries in the Milky Way with a dynamically confirmed stellar-mass black hole, from Remillard and McClintock (2006). The Sun–Mercury distance (0.4 AU) is shown in the top-right corner. The tilt of the accretion disk is proportional to the estimated binary inclination, and the color of the companion star is related to its surface temperature.

High mass X-ray binaries (HMXB)

The companions in HXMBs are young and massive stars on the main sequence (blue giants, type O, B, or Wolf-Rayet). These systems are mostly located in the galactic plane. Due to the large mass of the companion star, the size of its Roche lobe is also large, hence accretion via Roche lobe overflow is unlikely to happen. The star loses mass isotropically through strong winds, and the black hole can instead accrete part of the encountered stellar material (e.g. Negueruela 2010). Typically, HMXB are long-term persistent sources (with the exception of the Be/X-ray binaries, Reig 2011), that spend most of their time in an X-ray bright state (see Section 1.4). The long-term mass transfer rates due to the stellar wind can be as high as $10^{-6}\ M_\odot\ \mathrm{yr}^{-1}$ (Lewin, van Paradijs, and van den Heuvel, 1997). These winds have a small circularisation radius R_{circ} (from Equation 1.14), and as a consequence the outer edge of the accretion disk is always ionized, allowing these systems to remain in a bright outburst state for long periods (see Section 1.4.1 and Tetarenko et al. 2016).

One of the most famous high-mass X-ray binaries is Cyg X-1, which hosts a supergiant O-type star and the first dynamically confirmed black hole (Webster and Murdin, 1972; Gies and Bolton, 1986; Orosz et al., 2011; Miller-Jones et al., 2021).

Low mass X-ray binaries (LMXBs)

In LMXBs, the companion is a rather old and faint solar type or red dwarf star (type G, K or M) and its mass is rarely larger than 1 $M_\odot$ (Lewin, van Paradijs, and van den Heuvel, 1997). These systems are mostly found in the galactic bulge and in globular clusters. Since the black hole is more massive than the companion star, its Roche lobe is comparatively larger than the star's one, and accretion can easily and steadily happen through Roche lobe overflow (see Section 1.2.1). However, opposite to HXMBs, while the accretion rate is stable, the emission from LMXBs displays a high degree of variability on timescales that range from milliseconds to years (Remillard and McClintock, 2006; Ingram and Motta, 2019).

Depending on the mass accretion rate $\dot{M}$, which has strong implications on the observational properties of these systems, a sub-classification is possible among LMXBs. Sources with high accretion rates ($\sim 10^{-8}\ M_\odot\ \mathrm{yr}^{-1}$, such as LMC X–3 or GRS 1915+105, Remillard and McClintock 2006; Deegan, Combet, and Wynn 2009) and X-ray luminosities close to the Eddington limit display a roughly persistent emission (Tanaka and Shibazaki, 1996). The high luminosity of the accretion disk extends down the optical band, effectively outshining the emission from the companion star.

On the other hand, sources with low accretion rates ($\lesssim 10^{-9}\ M_\odot\ \mathrm{yr}^{-1}$, Tanaka and Shibazaki 1996) display a transient behaviour, spending most of the time in long quiescent states and entering sporadic outburst phases during which the brightness of the system rises by several orders of magnitude, up to luminosities similar to those found in the persistent sources. The mechanism for the production of these outburst is outlined in Section 1.4. The typical recurrence timescale between outbursts span from years to centuries (McClintock and Remillard, 2006).

Microquasars

An X-ray binary (either LMXB or HMXB) which displays, in addition to the observational properties due to the accretion, also collimated ejection phenomena, is called a *microquasar*. The term comes from the comparison to AGNs, of which these sources resemble stellar-size versions. After the first detections of radio emission produced by XRBs (Hjellming and Wade,

1971a; Hjellming and Wade, 1971b) and the first evidence of the presence of jets in SS 433 (Spencer, 1979; Hjellming and Johnston, 1981), 1E 1740.7–2942 was the first source to be classified as microquasar (Mirabel et al., 1992). Soon after that, apparently superluminal discrete jets were seen for the fist time in the BH XRB GRS 1915+105 (Mirabel and Rodríguez, 1994). It is not currently known if jets are a universal feature among XRBs, but jets, both transient and persistent, have been detected since then in dozens of XRBs, such that, in principle, all could produce jets. Since the first period of discovery, detailed investigations of the jets from X-ray binaries, both in the radio band and at shorter wavelengths, have revealed a rich phenomenology (which I will discuss in Chapters 2 and 3) and opened up the field of investigation into the connection between accretion and ejection in compact objects (e.g. Hannikainen et al. 1998; Corbel et al. 2000; Fender 2003; Remillard and McClintock 2006; Fender and Muñoz-Darias 2016; Tetarenko et al. 2016). Jets in microquasars are relativistic, and estimations of their bulk Lorentz factors Γ are of the order $2 \lesssim \Gamma \lesssim 5$ (Fender, 2003; Miller-Jones, Fender, and Nakar, 2006; Saikia et al., 2019), implying bulk speeds close to the speed of light. As the goal of this work is to improve our current understanding of the different types of relativistic jets in relation to black holes, microquasars will be the focus of this entire thesis, and hereafter all our discussion will be centered on BH LMXBs that display powerful relativistic jets. This is because, of all the systems that launch jets, XRBs are ideal laboratories for their study, with this being due to their relative proximity and the fact that such jets evolve on rapid (human) timescales.

Before moving forward in the discussion on microquasars hosting black holes, it is important to mention that these systems can also host neutron stars, both in LXMBs and HMXBs. These compact objects make up an important fraction of microquasars, as such systems are also able to accelerate persistent and transient jets (Fomalont, Geldzahler, and Bradshaw, 2001; Fender, 2003; Motta and Fender, 2019; van den Eijnden et al., 2021). However, due their rich phenomenology and due to the marked differences with respect to black holes (starting with the presence of a hard surface), a complete treatment of NS XRBs is beyond the scope of this thesis, and the term microquasar will denote only systems containing black holes.

1.3.2 Main components

I present in this section the main components of a BH LMXB. Four components will be discussed in the following: the accretion disk, the corona and the two types of jets (compact jets and discrete ejecta). An artistic rendition of a microquasar is shown in Figure 1.5. The combination of the emission of these part of the system covers almost the entire electromagnetic spectrum, from radio to hard X-rays.

Disk

The main characteristics of the accretion disk have been already presented in Section 1.2.2. Basically, BH LMXBs accrete mostly through Roche lobe overflow, and viscous friction within the accreted plasma causes the material to spread into an accretion disk. In this structure, angular momentum is transported outwards, while the plasma inside the accretion disk slowly spirals towards the black hole radiating away part of its gravitational energy. The accretion disk produces a multi-temperature black-body spectrum peaking in the soft X-rays (Frank, King, and Raine, 2002).

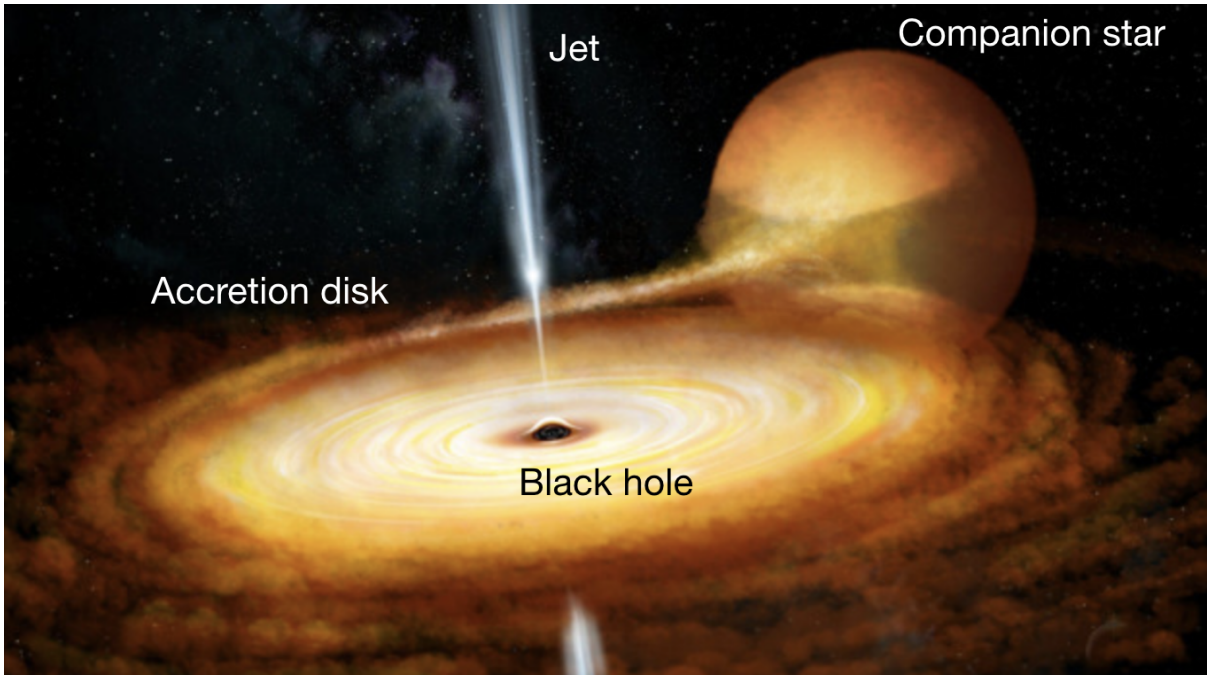

Figure 1.5: An artistic impression of a microquasar, including the main components of the system: companion star, accretion disk and collimated jets. *Credits*: J. Paice.

In BH LMXBs during outburst, the standard model of a geometrically thin, optically-thick accretion disk can explain the soft X-ray emission that is observed at the highest luminosities (Shakura and Sunyaev, 1973). In this state, the inner edge of the disk is thought to extend down to the ISCO (Steiner et al., 2010), which is

$$R_{\rm ISCO} = \phi \frac{6GM}{c^2} \tag{1.22}$$

where ϕ is a function of the black hole spin that is equal to 1 for a Schwarzschild black hole (corresponding to $R_{\rm ISCO} \simeq 60$ km for $10 M_\odot$ black hole) and to $1/6$ for an maximally rotating Kerr black hole (Soria, 2007). The inner edge and the optical depth of the accretion disk are believed to vary during an outburst (Esin, McClintock, and Narayan, 1997), and this will be discussed more in detail in the following section.

Inner accretion flow / Corona

Emission from BH LMXBs is detected up to the hard X-rays ($\gtrsim$100 keV). The accretion disk cannot account for the non-thermal, hard X-rays that are observed in these systems. The spectrum of such emission can be modeled with a power law, with the addition of an exponential cutoff around $\sim$100 keV. The nature and the geometry of the component of the system responsible for such non-thermal emission is highly debated, and today there is not universal consensus on it. It has been proposed that such hard X-ray emission can be explained by the presence of a new component: a cloud/corona of hot electrons which inverse-Compton scatter the soft photons from the disk, producing the observed power law (e.g. Sunyaev and Titarchuk 1980; Zdziarski and Gierliński 2004; Poutanen, Veledina, and Revnivtsev 2014). This corona is thought to be located close to the black hole, where most of the gravitational energy is released, and to be

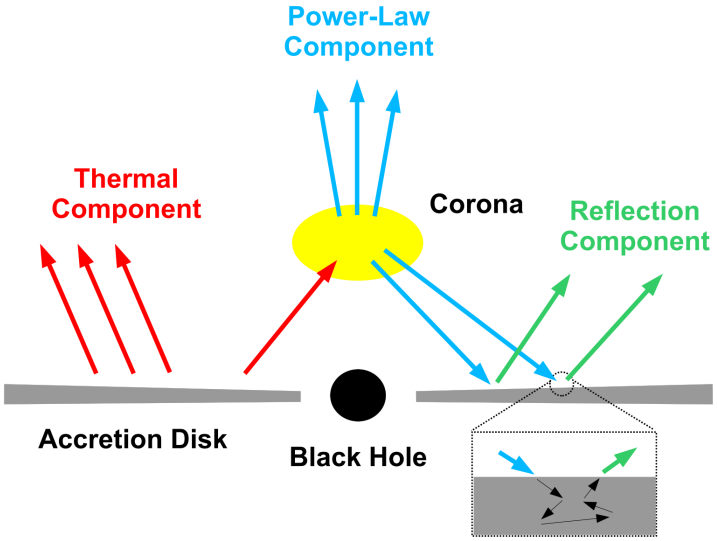

Figure 1.6: Scheme of the disk/corona configuration. The red arrows mark the black-body emission from the accretion disk surrounding the black hole. Photons from the disk are scattered through inverse Compton by the hot electrons in the corona, producing non-thermal emission in the hard X-rays (blue arrows). The reflection component, produced by the disk re-processing of the coronal emission, is marked with green arrows. From Bambi (2018).

made up of quasi-thermal electrons of energy $k_{\rm B}T_{\rm e} = 50$–100 keV. However, the exact geometry of the corona is unknown. In the so-called *lamppost* geometry, the corona is a point-like source on the black hole spin axis (Dauser et al., 2013), while in the *sandwich* geometry the corona is assumed to be the atmosphere above the accretion disk (Haardt and Maraschi, 1993). The hard X-rays emission from the corona illuminates also the accretion disk. Such emission is re-processed in the disk and this results in a reflection component (as shown in Figure 1.6) with fluorescent emission lines (García et al., 2013). The strongest reflection feature is the fluorescent iron Kα line at 6.4 keV.

In alternative to the corona hypothesis, the hard X-ray emission might also be produced by the jets (Markoff, Nowak, and Wilms, 2005) or by a highly magnetized inner part of the accretion disk (Ferreira et al., 2006).

Compact Jets

Jets are a fundamental component and a distinctive feature of microquasars. In fact, in the Universe, basically every accretion process appears to be accompanied by a collimated ejection process (excluding uncollimated winds). I discuss here the so-called compact jets. These energetic outflows consist of continuous and collimated ejections of plasma at relativistic speeds, on the relatively small scale of tens of AUs (e.g. Dhawan, Goss, and Rodríguez 2000; Stirling et al. 2001). A high-resolution radio image of the resolved jet of Cyg X-1 is shown in the left panel of Figure 1.7. Such jets are mostly present in the *hard* state (see Section 1.4.2), emitting self-absorbed synchrotron radiation (Corbel et al., 2000; Fender, 2001). This results in a flat or slightly inverted radio spectrum ($\alpha \gtrsim 0$, where the radio flux density follows $S_\nu \propto \nu^\alpha$) up to a break frequency $\nu_{\rm break}$ located in the IR (Markoff, Falcke, and Fender, 2001; Corbel and Fender, 2002; Russell et al., 2013a; Russell et al., 2014; Russell et al., 2020), after which the jet becomes optically thin ($\alpha \simeq -0.6$). This type of spectrum, which has been already observed

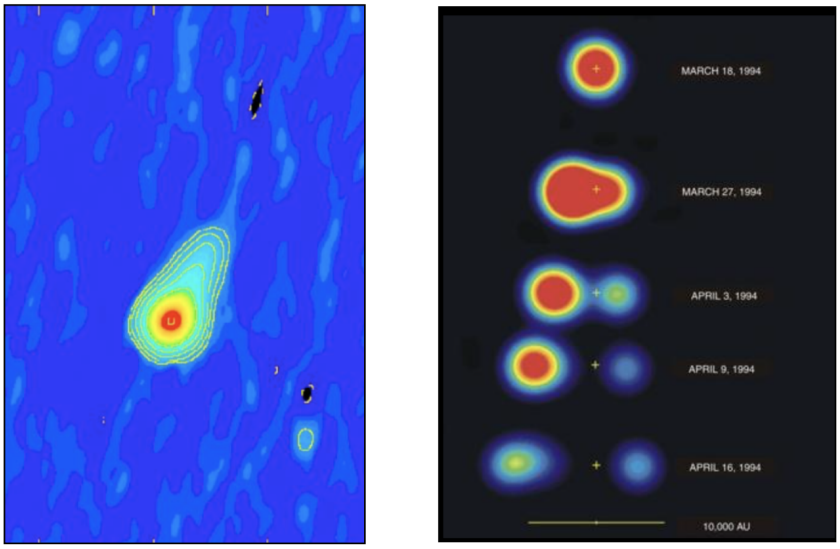

Figure 1.7: Radio images of the two main types of microquasar jets, for illustrative purposes. *Left:* Resolved compact jets in a VLBI observation of Cyg X-1. From Stirling et al. (2001). *Right*: VLA image of discrete ejecta moving away with time from the core of GRS 1915+105, showing apparent superluminal motion. From Mirabel and Rodríguez (1994).

in the compact cores of AGNs, is explained as the superposition of self-absorbed synchrotron radiation from different layers or "slices" of the jets, at different distances from the black hole (Blandford and Königl, 1979; Hjellming and Johnston, 1988). Such aspect of compact jets, as well as their connection with the accretion disk, is discussed more in detail in Chapter 2.

Synchrotron radiation from compact jets can also contribute to the hard X-ray emission (e.g. Markoff, Nowak, and Wilms 2005). There are indications that matter in compact jets could be accelerated up to bulk Lorentz factors $\Gamma_j \lesssim 3.5$ (e.g. Ribó, Dhawan, and Mirabel 2004; Russell et al. 2015; Tetarenko et al. 2019; Saikia et al. 2019; Péault et al. 2019).

Transient Jets / Discrete ejecta

Perhaps the most spectacular feature of BH LMXBs is the launch of discrete ejecta, which are bipolar blobs of plasma moving away from the core, often displaying apparent superluminal motion, similarly to what is observed in AGNs (e.g. Marscher et al. 2002; Gómez et al. 2008). The first discrete ejecta from a microquasar were resolved for GRS 1915+105 and are shown in the right panel of Figure 1.7. While all BH LMXBs are thought to produce jets, resolved discrete ejecta have been observed in radio in a dozen of sources so far (e.g. Mirabel and Rodríguez 1994; Hjellming and Rupen 1995; Fender et al. 1999; Mioduszewski et al. 2001; Gallo et al. 2004; Yang et al. 2010; Rushton et al. 2017; Russell et al. 2019c; Miller-Jones et al. 2019; Bright et al. 2020). For some of them, both the approaching and receding components have been detected, while for a large fraction of sources only one component (usually the approaching one, due to Doppler boosting, see Chapter 3) was observed. Discrete ejecta have been observed also in neutron star LMXBs (Fomalont, Geldzahler, and Bradshaw, 2001; Calvelo et al., 2012).

Observationally, these ejecta display an optically thin spectrum at radio frequencies ($\alpha \simeq -0.6$, Corbel et al. 2002) and are often accompanied by bright, multi-frequency flaring activity. Such ejection events, when not resolved, are also called *transient jets* and are believed to be the result of the rapid launch of an adiabatically expanding plasma threaded by a magnetic field

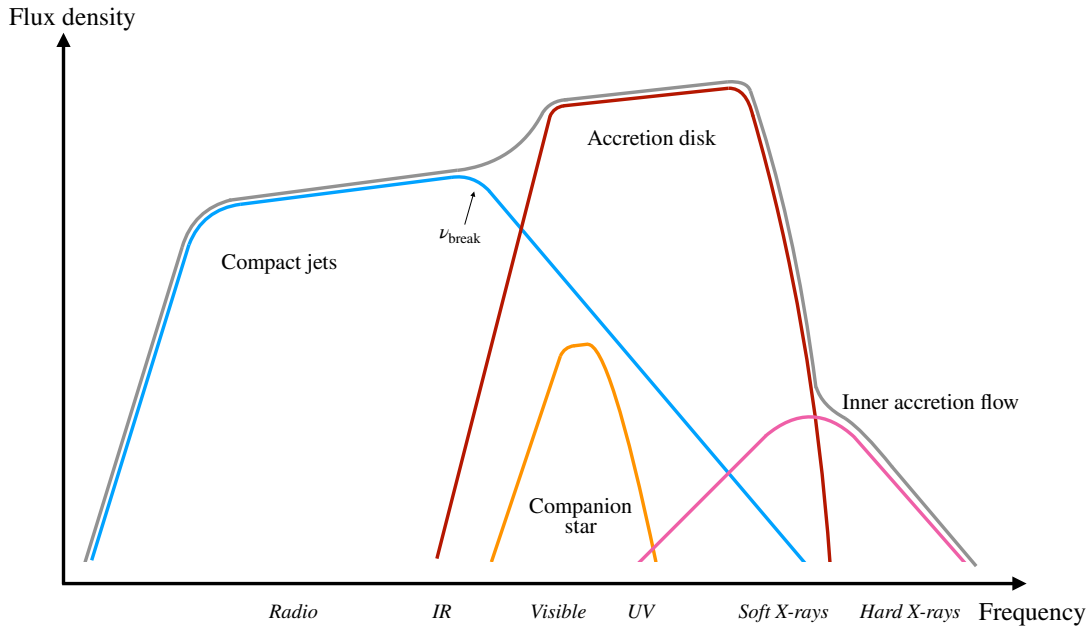

Figure 1.8: Schematic representation of the broadband spectral energy distribution of a BH LMXB in outburst, in the hard state (see Section 1.4.2). The grey continuous line represents the total observed emission. $\nu_{\rm break}$ is the jet spectral break discussed in Section 1.3.2 and Chapter 2. Figure inspired by Coriat (2010).

(e.g. van der Laan 1966; Hjellming and Johnston 1988). While a definitive sequence of events leading to these ejections has not yet been identified, the ejection time has been tentatively linked to X-ray timing signatures (e.g. Miller-Jones et al. 2012; Russell et al. 2019c; Homan et al. 2020). I refer to Chapter 3 for a complete discussion on this type of episodic outflows.

Spectral energy distribution

The individual and total contributions of the components outlined in the previous section, including compact jets, accretion disk and inner accretion flow, are shown in Figure 1.8, where we plot the typical broadband spectra for a BH LMXB in the hard state (see Section 1.4.2). In this plot, called spectral-energy distribution (SED) it is possible to notice how the emission from the different components overlap in given frequency intervals, such as the infrared band, where we have the jet spectral break and the emission from the outer edge of the disk. Moreover, different emissions overlap also in the X-ray band. During an outburst, often the spectral contribution from the companion star is completely covered by the brighter disk emission.

1.4 The outburst phase

A striking and fundamental aspect of the majority of BH LMXBs is their transient nature. These systems evolve from periods of inactivity into a sporadic bright outburst phases that can last from weeks to months. During an outburst the X-ray luminosity increases dramatically, by several orders of magnitude, and can reach levels close to the Eddington limit (Remillard and

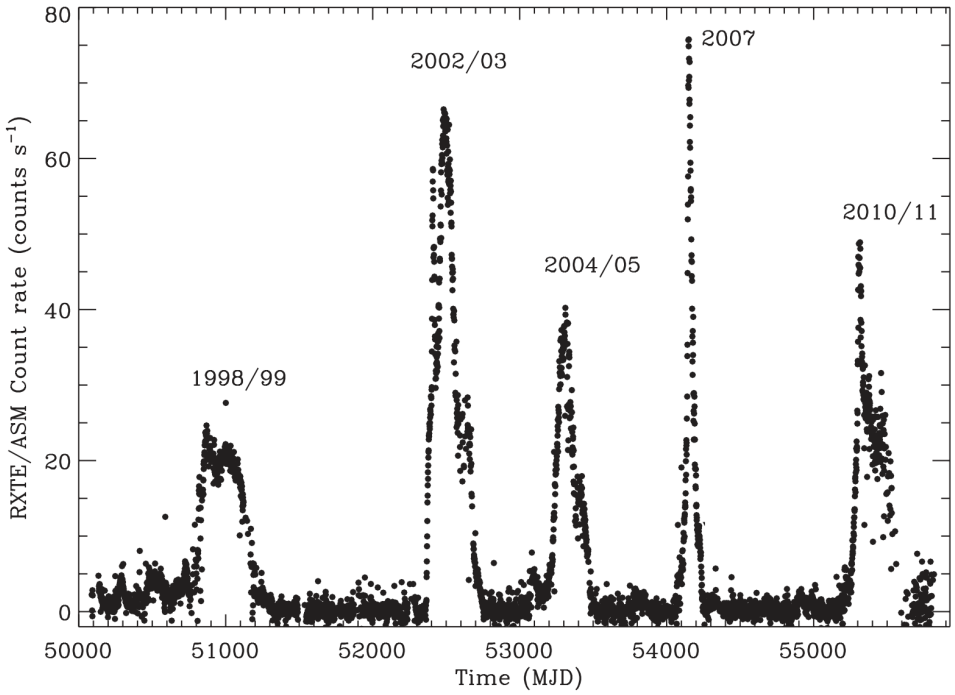

Figure 1.9: RXTE/All Sky Monitor soft X-ray (1.5–12 keV) light curve of GX 339−4 for the entire RXTE lifetime (1996 January to 2011 December), clearly showing the transient nature of the source. From Corbel et al. (2013b).

McClintock, 2006). A clear example is shown in Figure 1.9. During an outburst, the system cycles through different accretion states that are characterized by distinct spectral and timing signatures (e.g. Homan and Belloni 2005; Remillard and McClintock 2006; Belloni 2010; Belloni and Motta 2016a; Ingram and Motta 2019).

1.4.1 The disk instability model

The best explanation that we have today for the outbursting behaviour of BH LMXBs is, in short, that the outburst is caused by an increased accretion rate onto the compact object as consequence of thermal-viscous disk instabilities, which allow matter to move inwards and produce rapid and large increases in the X-ray luminosity (Frank, King, and Raine, 2002). Such instabilities are believed to be produced when the disk temperature is close to 10^4 K, which leads to the partial ionization of the hydrogen present in the disk and to a large increase in the disk opacity (Meyer and Meyer-Hofmeister, 1981). In this framework, a physical model, called the Disk Instability Model (DIM), has been developed to explain the causal link between thermal instabilities and outbursts (see Lasota 2001). While first developed to explain the outbursts of cataclysmic variables (Meyer and Meyer-Hofmeister, 1981; Cannizzo, Ghosh, and Wheeler, 1982), the DIM has been shown to be able to explain (with some adjustments) the behaviour of LMXBs in outburst (van Paradijs, 1996; Lasota, 2001; Coriat, Fender, and Dubus, 2012).

I present here the main assumptions and concepts of the model. Assuming an optically thick and geometrically thin disk, its equilibrium depends on the compensation between the heating and cooling mechanisms. At equilibrium, for each disk ring a relation is present between the ring temperature T and the surface density Σ, which is obtained by the vertical integration along the disk of the mass density ρ (Done, Gierliński, and Kubota, 2007; Latter and Papaloizou,

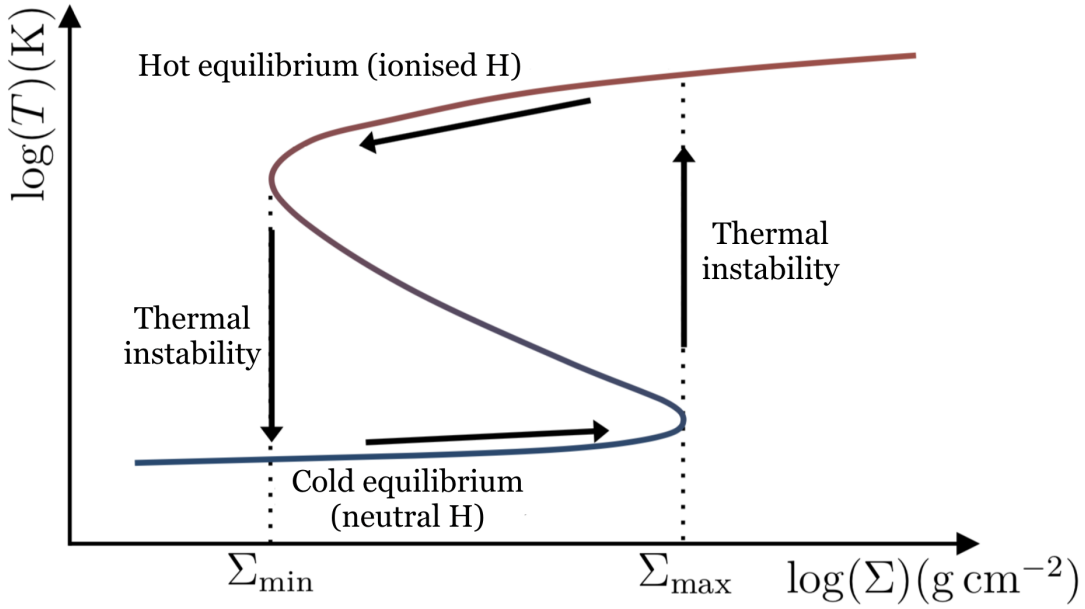

Figure 1.10: Σ–T plane for the relation between temperature and surface density in each ring of the accretion disk. The two stable equilibrium branches (hot and cold) are marked respectively in red and blue and are, again respectively, above and below the hydrogen ionization temperature ($\sim 10^4$ K). Between outburst and quiescence, the system perform a sort of hysteris cycle in the Σ–T plane, where the passage between the two branches is caused by thermal-viscous instabilities. Adapted from Loh (2016).

2012). This can be represented as an "S" curve on the Σ–T plane, shown in Figure 1.10. On this curve, the equilibrium is stable on two branches, a cold one and a hot one, both marked with colors in Figure 1.10 and, respectively, above and below the hydrogen ionization temperature $\sim 10^4$ K, while the central branch is characterized by an unstable equilibrium. (Done, Gierliński, and Kubota, 2007).

In quiescence, the system starts in the cold branch, as the temperature is low and the hydrogen is neutral. While the accretion rate in this phase is rather low, the steady matter accumulation leads to a progressive increase of the disk temperature and surface density. When the maximum surface density $\Sigma_{\rm max}$ is reached, the hydrogen starts to be ionised and the opacity dramatically increases. This causes the photons radiated from the disk to be re-absorbed locally, contributing to the temperature increase and causing the disk to enter in a loop with positive feedback, creating a thermal instability. The local temperature increase produces then a local increase of the accretion rate which is transported to the whole disk through the MRI mechanism (see Section 1.2.2). A this point, the system lies on the hot branch and the outburst begins, as the matter is accreted and the release of gravitational energy causes the dramatic increase in the X-ray luminosity of the source. Subsequently, the high accretion rate greatly reduces the matter stored in the disk, and the temperature progressively decreases, until reaching the conditions on the Σ–T plane for which the hydrogen recombines and the opacity drops. Cooling dominates over heating in this phase, and the temperature largely decreases, down to move the system back to the cold equilibrium branch, in quiescence. Sources undergo multiple outburst phases with very different recurring timescales (e.g. Remillard and McClintock 2006), during which they repeatedly perform the type of hysteresis cycle in the Σ–T plane that we just discussed.

As briefly mentioned in Section 1.3.1, sources with persistent bright emissions are also observed (Tanaka and Shibazaki, 1996). In this context, such behaviour can be explained by

the disk constantly having an equilibrium temperature above the hydrogen ionization threshold, so that the system spend all of its time on the hot branch in the Σ–T plane (Done, Gierliński, and Kubota, 2007).

However, the DIM alone cannot explain a variety of observational properties of BH LMXB outbursts, such as the presence of slow decay phases and subsequent short re-brightenings (Coriat, Fender, and Dubus, 2012). Therefore, numerous additions to the base model have been added over the years. The most important one in the case of black holes is the inclusion of irradiation when considering the radiation properties in the disk. In fact, the X-ray irradiation from the inner regions illuminates the disk and increases the duration of the outburst by contributing to the disk ionization, prolonging the time that a transient system spends on the hot branch (Dubus, Hameury, and Lasota, 2001). This results in a different profile in the X-ray light curve (Tetarenko et al., 2018c). In this context, an irradiation geometry that varies in space or in time could possibly explain the re-flaring episodes observed after the main outburst in many sources (Tetarenko et al., 2018c; Tetarenko et al., 2020b; Parikh et al., 2019).

1.4.2 Spectral states and outburst evolution

During an outburst, BH LMXBs display a very rich phenomenology as they cycle through different accretion states with very different spectral and timing properties, but whose origin is not completely understood (e.g. Homan and Belloni 2005; Remillard and McClintock 2006; Belloni 2010; Belloni and Motta 2016a; Ingram and Motta 2019). I present here the different spectral states of and then I discuss their evolution during a given outburst.

Hard state

In the so-called hard state, the X-ray spectrum is dominated by a hard non-thermal power law that is thought to be the result of inverse-Compton scattering by a corona of hot electrons close to the compact object (see Section 1.3.2, e.g. Zdziarski and Gierliński 2004; Poutanen, Veledina, and Revnivtsev 2014). The power law photon index Γ (where $N(E) \propto E^{-\Gamma}$, in which $N(E)$ is the number of photons with energy E per second per unit area) is in general contained in the interval $1.4 < \Gamma < 2.0$ and often displays an exponential cut-off around 100 keV (McClintock and Remillard 2006). In addition, a subdominant thermal emission may also be present. Such emission is produced by the accretion disk, which is likely to be truncated, geometrically thick and optically thin in this phase (e.g. Done, Gierliński, and Kubota 2007), although the discussion of this particular aspect is beyond the scope of this work. The variability of the X-ray emission is high in the hard state, with a rms variability of up to 30% (Remillard and McClintock, 2006; Belloni, 2010; Belloni and Motta, 2016b).

In the hard state, compact jets are present and are observed in the radio band, emitting self-absorbed synchrotron radiation (Corbel et al., 2000; Fender, 2001), resulting in the flat/inverted radio spectrum presented in Section 1.3.2. Such jets are strongly coupled to the accretion flow, as their radio luminosity is correlated to the X-ray luminosity (Hannikainen et al., 1998; Corbel et al., 2000; Corbel et al., 2013b). A detailed discussion of compact jets and their connection with the disk will be presented in Chapter 2.

Soft state

In the so-called soft state, the X-ray emission is characterised by a drop in the rms variability, and it is completely dominated by the thermal emission from the accretion disk, which reaches

temperatures of $k_{\rm B}T \sim 1$ keV, as already discussed in Section 1.2.2. The disk is optically thick and geometrically thin (Shakura and Sunyaev, 1973), and its inner radius is thought to reach the ISCO (e.g. Steiner et al. 2010). The spectrum also displays a fainter non-thermal component that can be described with a softer power law ($\Gamma > 2.4$) with respect to the hard state. Strong disk winds are observed in this state (e.g. Díaz Trigo and Boirin 2016; Fender and Muñoz-Darias 2016). No radio emission is usually detected during the soft state, as compact jets are strongly quenched (Fender et al., 1999; Corbel et al., 2000), by at least 3.5 orders of magnitude (Coriat et al., 2011; Russell et al., 2019c; Maccarone et al., 2020).

Intermediate state

Between the hard and soft state, we have also intermediate states, that are displayed by the system when transitioning between the two main states. Observationally, intermediate states present an almost equal contribution between the thermal disk emission and the non-thermal contribution from the corona. Their classification is still subject of debate, but the currently accepted distinction included two intermediate states, called respectively soft-intermediate state (SIMS) and hard-intermediate state (HIMS) (Homan and Belloni, 2005; Remillard and McClintock, 2006). Their difference depends on the presence of a specific timing signature, a quasi-periodic oscillation (QPOs) of the Type-B (e.g. Zhang et al. 2020a). BH and NS XRBs commonly display QPOs in their X-ray emission, both at low and high frequencies (LFQPO, $1 \sim 10$ Hz, and HFQPO at $\sim$1 kHz). Despite the large number of detections, their physical origin is still far from being completely understood. In the specific, the presence of Type-B QPOs defines the SIMS with respect to the HIMS, and these QPOs are tentatively linked to the launch of discrete ejecta (e.g. Homan et al. 2020), but see Chapter 3 and Ingram and Motta (2019) for a review on QPOs.

Interestingly, during intermediate states, when the system transitions between the hard and the soft state (as discussed in the following) strong radio flares are observed in an important fraction of sources (e.g. Brocksopp et al. 2007; McClintock et al. 2009; Xie, Yan, and Wu 2020; Russell et al. 2019c; Bright et al. 2020). Such flares are produced by the ejection of transient jets, that are discrete plasmons launched by the system at relativistic speeds. See Chapter 3 for a complete discussion on discrete ejecta.

Outburst evolution

After the presentation of the different spectral states displayed by BH LMXBs, I discuss here how a typical outburst proceeds and how the system evolves over time. As the spectral properties of the system change dramatically within an outburst, the main tool to follow the evolution of the source is a diagram that compares the source brightness with its spectral "hardness", which is the ratio between the flux in the soft and hard X-rays. This phenomenological tool is called Hardness Intensity Diagram (HID), and allows us to completely describe the outburst cycle of a BH LMXB in a model-independent way. An example of an HID is shown in Figure 1.11, where the typical SEDs for the hard and the soft states are shown, along with disk properties and the ejections observed in each spectral state. As can be seen from Figure 1.11, the source traces a sort of Q-shaped cycle on the HID (also called *turtle-head* diagram), and I present in the following the system evolution.

As the outburst begins, these systems are typically observed in a rising hard X-ray state, at the bottom-right corner of the HID. As detailed above, in the hard state the X-ray spectrum, with high rms variability, is dominated by a non-thermal power law resulting of inverse-Compton

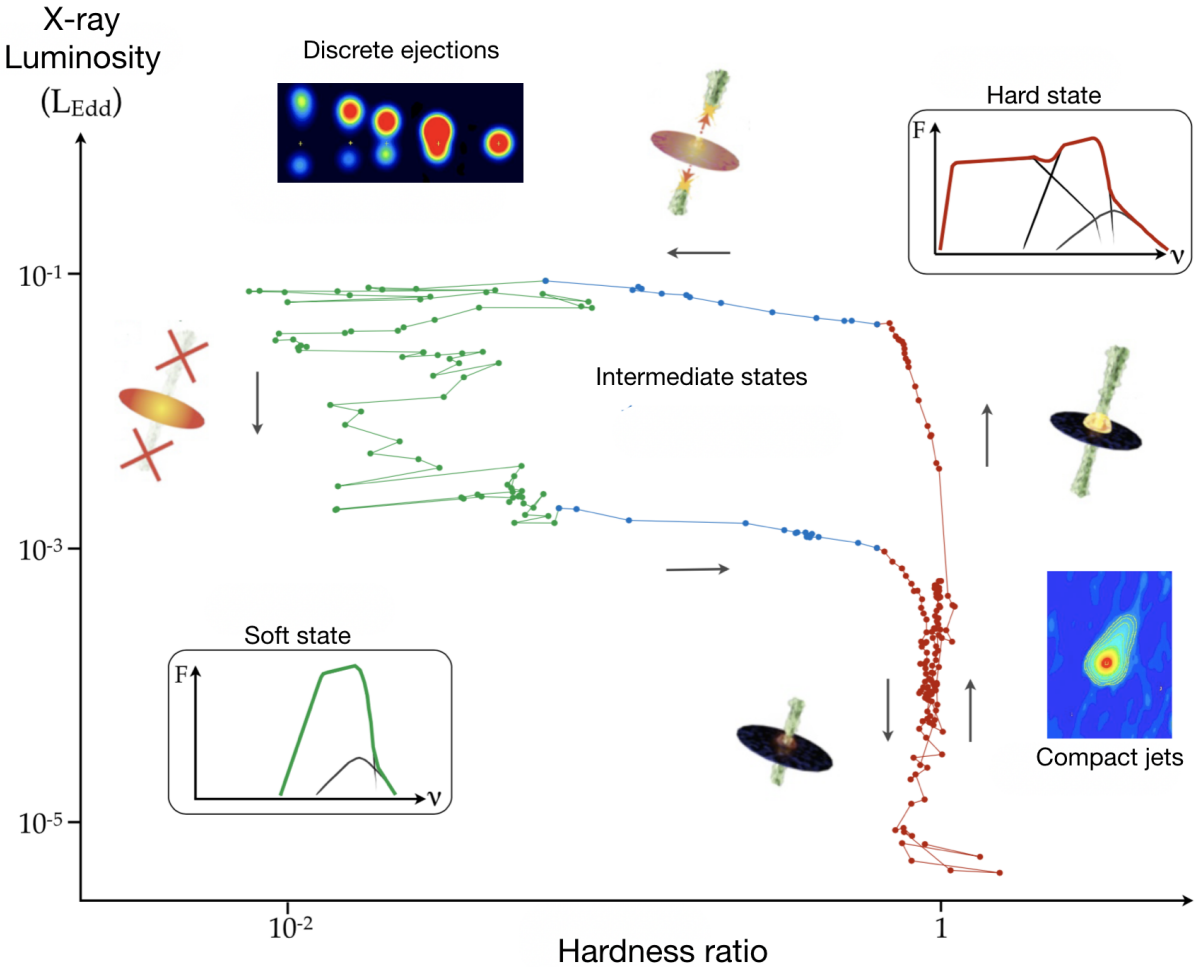

Figure 1.11: Hardness-intensity diagram with the associated spectral properties (SED) and different types of ejections, discussed in Section 1.4. The data used in this case are from the 2007 outburst of the BH LMXB GX 339−4 (Coriat et al., 2009). Red, green and blue points mark, respectively, the hard, soft and intermediate states. Adapted from Coriat (2010).

scattering by a corona of hot electrons close to the compact object (e.g. Sunyaev and Titarchuk 1980; Zdziarski and Gierliński 2004; Poutanen, Veledina, and Revnivtsev 2014). Rising compact jets are routinely detected in radio (Corbel et al., 2000; Fender, 2001; Corbel et al., 2013b). While in the hard state, both the radio and X-ray luminosities greatly increase, and the source will move upwards along the right hand vertical line in Figure 1.11.

As the outburst progresses, the accretion rate increases and the system transitions to the intermediate state, first in the HIMS and then in the SIMS, during which the X-ray spectrum becomes progressively softer as the thermal emission from the accretion disk increases and the rms variability decreases. Dramatic changes to the jet emission are observed in this phase, as the compact jets switch off and radio flaring is present, marking the launching of discrete, bright, ejecta moving at relativistic speeds (Corbel et al., 2004a; Fender, Belloni, and Gallo, 2004).

The system subsequently enters the soft state, which is characterized by a drop in the rms variability and in which the thermal X-ray spectrum is produced by the optically thick, geometrically thin accretion disk, whose inner radius shrinks down to reach the ISCO (Steiner et al., 2010). X-ray binaries may oscillate between the soft state and the intermediate state, producing flares at each hard-to-soft transition (Brocksopp et al., 2001; Homan et al., 2001; Fender, Belloni, and Gallo, 2004).

Some weeks to months later, the luminosity decreases and, at some point, the system re-enters a lower luminosity IMS. Compact jets are then gradually re-activated as the systems transition back to the final hard state, which precedes quiescence (Miller-Jones et al., 2012; Kalemci et al., 2013; Corbel et al., 2013a; Russell et al., 2014). The cycle is then closed and the system re-enters an often long-lived quiescence phase.

It is interesting to remark that the transition luminosity in the hard-to-soft state transition is much higher than the luminosity for the reverse transition. This implies that such transitions, whose origin is not understood today, cannot depend simply on a single parameter such as the accretion rate, but it is possible that multiple parameters govern the evolution of the system and produce the observed hysteresis cycle on the HID (e.g. Homan et al. 2001). For example, the global evolution of the X-ray spectrum might be consistent with a truncated disk model (e.g. Done, Gierliński, and Kubota 2007). According to this model, the standard optically thick and geometrically thin disk is truncated at a given radius, where the coronal region starts (Esin, McClintock, and Narayan, 1997). At low luminosities, the truncation radius is large, hence the thermal contribution from the disk is negligible and the non-thermal coronal emission dominates. Then, as the luminosity increases, the truncation radius decreases and the inner edge of the thin disk approached the ISCO, producing a bright thermal spectrum. Therefore, taking into account the independent parameter of the disk truncation radius, in addition the accretion rate, might be important in the context of the hysteresis cycle (e.g. Ferreira et al. 2006; Marcel et al. 2018a; Marcel et al. 2018b; Marcel et al. 2019).

The quiescent phase

The quiescence phase is one of the less explored and less understood states in which a BH LMXB can be found, and this is of course due to the increased difficulty in detecting sources at their minimum levels of emission. However, this state is one of the most important, as it is the condition in which BH LMXBs spend most of their time (Remillard and McClintock, 2006). When in quiescence, BH LMXBs are weakly accreting, and the IR and optical emission from these systems is dominated by the companion star. The current picture of the quiescence state considers it as a low-luminosity version of the hard state, with the same physical and

observational properties (e.g. Gallo et al. 2019). In this state, a large fraction of the radiative power of the accretion flow appears to be emitted by the compact jets in the radio band (Plotkin et al., 2019), which is still present from the decaying, second hard state that precedes the end of an outburst. The dominance of the jet at these low luminosities is also believed to be responsible for the observed progressive X-ray spectral softening (up to $\Gamma \simeq 2.2$, e.g. Corbel, Tomsick, and Kaaret 2006; Plotkin, Gallo, and Jonker 2013; Reynolds et al. 2014). However, the jet properties and the cause of the softening (possibly also linked to the physics of the accretion flow) remain unclear at the moment, as observations with the sensitivities required to accurately measure the radio and X-ray spectra of BH-LMXBs in quiescence are rare.

Chapter 2

Compact jets and disk/jet coupling

Contents

2.1 Flat spectra from compact jets . . . 26
2.1.1 Emission from a single segment . . . 26
2.1.2 The full spectrum . . . 28
2.2 Powering mechanism . . . 31
2.3 Recent progresses . . . 32
2.3.1 Evolution of the break frequency . . . 32
2.3.2 Insights from fast variability . . . 34
2.4 The radio/X-ray correlation . . . 35
2.5 Proposed explanations . . . 37
2.5.1 Geometry . . . 37
2.5.2 Radiative efficiency of the accretion flow . . . 38
2.5.3 Jet properties . . . 40
2.6 The fundamental plane of black hole activity . . . 41

Astrophysical jets are collimated, relativistic outflows produced by accreting compact objects over a wide range of physical scales, from stellar-mass to supermassive black holes. These jets, accelerated from the inner regions of the accretion flow, are thought to be the main channel for the transfer of accretion energy to the surrounding environment, possibly having an important feedback effect, up to galactic scales.

This chapter is dedicated to the discussion of compact jets from BH LMXBs. I have already presented this particular type of jets in Section 1.3.2. Jets are systematically detected during the hard state phases of outbursts from BH LMXBs, displaying a flat or slightly inverted spectrum from radio to the NIR. In analogy with flat-spectrum jets observed in AGNs, such jets can be successfully described by the model proposed by Blandford and Königl (1979), which is now the standard model for relativistic, collimated jets and that I will present in a basic version in Section 2.1. Along with the main equations used to describe the jet emission from the properties

of the synchrotron emitting plasma, I will briefly mention the current extensions of the model. In Section 2.3, I will outline some of the newest results on our understanding, including what can be learned by studying the jet fast variability (Tetarenko et al., 2019), and insights on how the jet quenches at the transition from the hard to the soft state (Russell et al., 2020). Subsequently, in Section 2.2 I will discuss the fundamental aspect of the jet powering mechanism. The second part of the chapter is dedicated the important topic of the connection between the jets and disk. I will discuss the observational proof of such connection: the radio/X-ray correlation in Section 2.4, some proposed explanations from the behaviour observed on the radio/X-ray diagram (2.5), and how such connection has been extended from stellar-mass to supermassive black holes in 2.6.

2.1 Flat spectra from compact jets

I present in this section the basics of the standard model for compact jets, as proposed by Blandford and Königl (1979), adopting the formulation of Kaiser (2006). This model considers the synchrotron emission from the compact jets as the sum of the emissions from different adjacent shells of plasma along the flow.

In order to introduce the concept behind the model, we consider a plasma threaded with magnetic fields containing relativistic electrons characterized by a power law energy distribution. Above a given critical frequency, this plasma will produce an optically thin power law spectrum, but below such critical frequency the emitted photons will be re-absorbed by the radiating electrons, producing an optically thick spectrum with slope $\alpha = 5/2$ (Rybicki and Lightman, 1979), where the flux density follows $S_\nu \propto \nu^\alpha$ and α is the spectral index. This phenomenon is called synchrotron self-absorption and, given the two different behaviours at high and low frequencies, the spectrum emitted by the plasma will show a significant peak. The central concept of the Blandford-Königl model is that the plasma conditions are changing along the jet, from the base to the terminal zone, and hence the peaks of the self-absorbed spectra from different shells of plasma will be located at different frequencies. If the individual spectra peak roughly at the same level (determined by the plasma conditions), the un-resolved compact jets will display a flat spectrum.

2.1.1 Emission from a single segment

In the Blandford-Königl model, the jet is assumed to be conical, without any external confinement, and the bulk speed of the jet plasma along the jet axis is assumed to be constant, with velocity $\beta = v/c$ and Lorentz factor $\Gamma = (1-\beta^2)^{-1/2}$. We consider that the jet axis (x-axis) has an angle θ with the line of sight. The magnetic field is assumed to be perpendicular to the jet axis and 'frozen' into the jet plasma. Therefore, we can start by writing the expressions for the jet radius r and the magnetic field B. From the conservation of the magnetic flux, we have that $B \propto r^{-1}$ (Kaiser, 2006), hence we can write

$$r(x) = r_0 \left(\frac{x}{x_0}\right), \qquad B = B_0 \left(\frac{r}{r_0}\right)^{-1} = B_0 \left(\frac{x}{x_0}\right)^{-1} \tag{2.1}$$

where x_0 and r_0 are the position and radius of the jet base.

The observed synchrotron emission is produced by a population of relativistic electrons, for which we assume a typical power law energy distribution with index p

$$N(E)dE = kE^{-p}dE \tag{2.2}$$

where $E = \gamma m_e c^2$ is the energy of electrons with individual Lorentz factor γ, $N(E)$ the number of electrons per unit volume and k the normalization, which goes as $k \propto r^{-2} \propto x^{-2}$, from energy and particle conservation in a conical geometry (Kaiser, 2006). The particle energy distribution ranges between $\gamma_{\rm min}$ and $\gamma_{\rm max}$ and it is assumed to be the result of an unknown acceleration mechanism, which provides energy to the electrons throughout their motion in the jet flow. Such mechanism is required to compensate for the energy losses of the electrons due to radiation and to the adiabatic expansion of the jet, which are not included in the original Blandford-Königl model.

To build a model for the emission, we can now divide the jet in segments of length dx along the jet axis. The segments are moving with constant speed $v = \beta c$. Taking into account absorption and assuming that each photon travels on average a distance $r(x)$ in the jet, the observable monochromatic intensity of a single segment can be written as

$$I_\nu = \delta_\mp^3 \frac{J_\nu}{4\pi\chi_\nu}\left(1 - e^{-\chi_\nu r(x)}\right) \tag{2.3}$$

where J_ν is the emissivity per unit volume, χ_ν is the absorption coefficient and δ is the Doppler factor

$$\delta_\mp = \frac{1}{\Gamma(1 \mp \beta\cos\theta)} \tag{2.4}$$

for the approaching (–) and receding (+) jet. Using that, the observed frequency is linked to the frequency ν measured in the rest frame of the jet by $\nu_{\rm obs} = \delta_\mp \nu$. A scheme of the considered jet segment is shown in Figure 2.1.

The segment has an area $2\pi r(x)dx$, and hence its observed flux density is

$$dF_\nu = \delta_\mp^3 \frac{r(x)}{2D^2}\frac{J_\nu}{\chi_\nu}\left(1 - e^{-\tau_\nu}\right)dx \tag{2.5}$$

where D is the source distance and $\tau_\nu(x) = \chi_\nu r(x)$ the optical depth (Kaiser, 2006). For synchrotron emission, the emissivity J_ν and the absorption coefficient χ_ν can be written as:

$$J_\nu = J_* k B^{\frac{p+1}{2}} \nu^{\frac{1-p}{2}} \tag{2.6}$$

$$\chi_\nu = \chi_* k B^{\frac{p+2}{2}} \nu^{-\frac{(p+4)}{2}} \tag{2.7}$$

where J_* and χ_* are coefficients depending on the fundamental constants e, m_e, ϵ_0 and c, and only weakly on p. Their full expression can be found, for instance, in Rybicki and Lightman (1979). With the equations listed above, and by substituting $l = x/x_0$, we can then write the flux density from the jet segment as

$$dF_\nu = \delta_\mp^3 \frac{r_0 x_0 B^{-\frac{1}{2}}}{2D^2}\frac{J_*}{\chi_*}\nu^{\frac{5}{2}} l^{\frac{3}{2}}\left(1 - e^{-\tau_\nu}\right)dl \tag{2.8}$$

from which we can obtain the peaked morphology of the spectrum from the jet segment at distance l from the jet base. In the optically thick, self-absorbed regime, we have that $\tau_\nu \gg 1$,

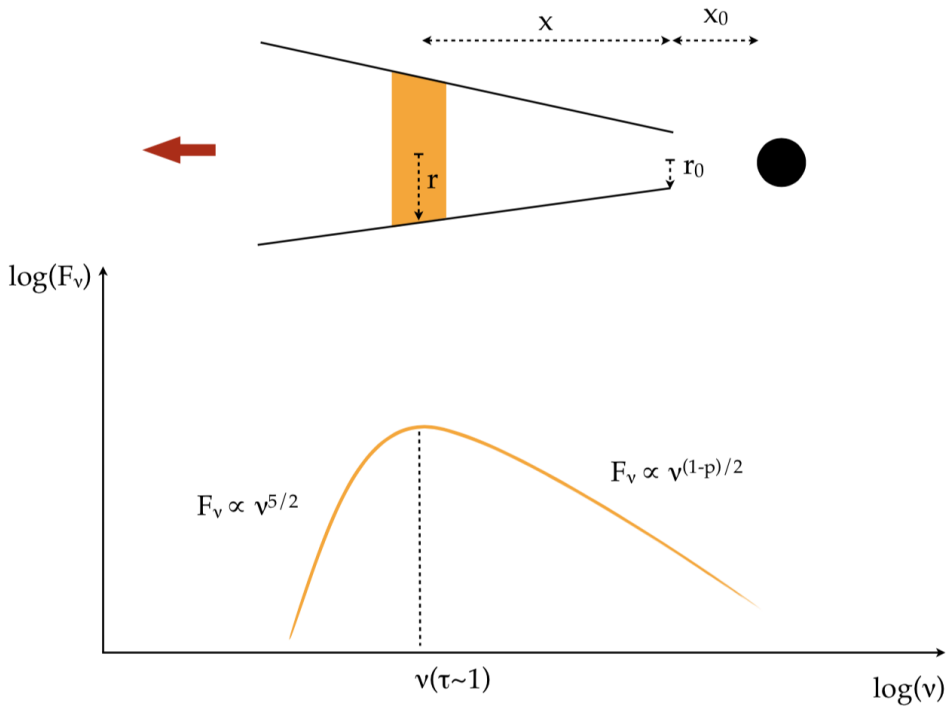

Figure 2.1: Emitted spectrum from a segment of the compact jet, at radius r from the axis and distance x from the base. Taken from Coriat (2010).

hence $dF_\nu \propto \nu^{5/2}$. On the other hand, in the optically thin regime $\tau_\nu \ll 1$ we have that $dF_\nu \propto \tau_\nu \nu^{5/2}$. To obtain the spectral behavior in such regime, we use Equation 2.7 for the expression of the optical depth

$$\tau_\nu(l) = \chi_* k_0 r_0 B_0^{\frac{p+2}{2}} \nu^{-\frac{(p+4)}{2}} l^{-\frac{(p+4)}{2}} = \tau_* \nu^{-\frac{(p+4)}{2}} l^{-\frac{(p+4)}{2}} \tag{2.9}$$

where we set $\tau_* = \chi_* k_0 r_0 B_0^{\frac{p+2}{2}}$. Therefore, at a fixed l, $\tau_\nu \propto \nu^{-\frac{(p+4)}{2}}$, and hence the spectrum in the optically thin regime will go as $dF_\nu \propto \nu^{\frac{1-p}{2}}$. At this point, the two different behaviors will cause the spectrum to peak at $\tau_\nu \simeq 1$, as shown in Figure 2.1.

2.1.2 The full spectrum

We can obtain the expression for the full spectrum of jet by integrating Equation 2.8 over the entire length of the jet

$$F_\nu = \delta_\mp^3 \frac{r_0 x_0 B_0^{-\frac{1}{2}}}{2D^2} \frac{J_\nu}{\chi_\nu} \nu^{\frac{5}{2}} \int_1^{l_{\max}} l^{\frac{3}{2}} \left(1 - e^{-\tau_\nu(l)}\right) dl \tag{2.10}$$

where $l_{\max}$ is the terminal point of the jet. Equation 2.10 can be rewritten using the optical depth τ_ν from Equation 2.9

$$F_\nu = \delta_\mp^3 \frac{r_0 x_0 B_0^{-\frac{1}{2}}}{(p+4)D^2} \frac{J_*}{\chi_*} \tau_*^{\frac{5}{p+4}} \int_{\tau_{\min}}^{\tau_{\max}} \tau_\nu^{-\frac{5}{p+4}-1} \left(1 - e^{-\tau_\nu}\right) d\tau \tag{2.11}$$

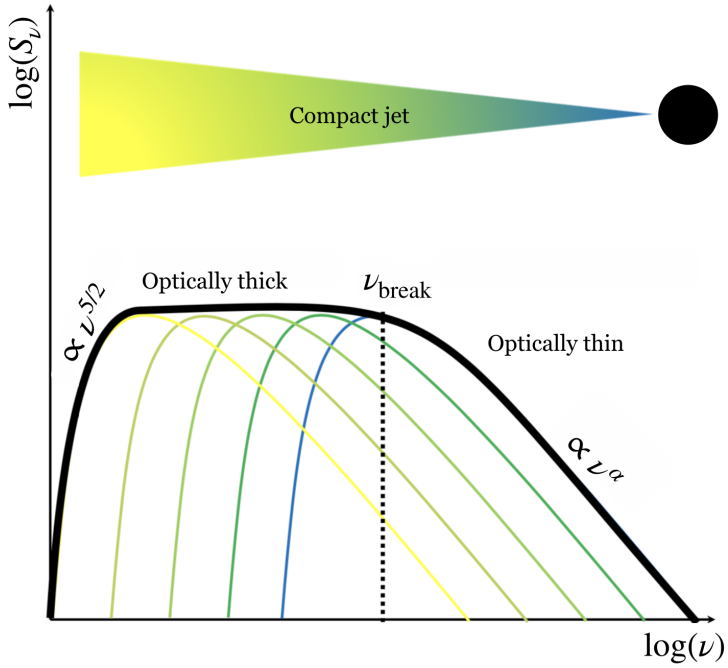

Figure 2.2: Schematic representation of a total jet spectrum. The overall emission results from the superposition of multiple segments of the jet, each producing self-absorbed synchrotron radiation peaking at different frequencies. The spectrum goes as $\propto \nu^{5/2}$ at low radio frequencies, it is flat between the radio and the NIR bands, up to a critical frequency $\nu_{\rm break}$ located in the NIR, and it is steep above $\nu_{\rm break}$. Adapted from Cangemi (2020).

where the maximum optical depth is reached at the base of the jet, hence $\tau_{\rm max} = \tau_\nu(l = 1)$, and the minimum optical depth is reached at the terminal zone of the jet, thus $\tau_{\rm min} = \tau_\nu(l_{\rm max})$ (Kaiser, 2006). It is important to note that F_ν depends on the frequency only through the limits of the integral $\tau_{\rm min}$ and $\tau_{\rm max}$. If the jet is sufficiently extended in length, it is reasonable to assume that in a given frequency range we will have $\tau_{\rm max} \to \infty$ and $\tau_{\rm min} \to 0$. With such assumption, the integral in Equation 2.11 can be evaluated as $-\hat{\Gamma}(\frac{-5}{p+4})$, where $\hat{\Gamma}$ is the Gamma function. The consequence of such argument is that F_ν is independent of the frequency, and the resulting spectrum is flat.

To link such argument with the initial line of reasoning put forward by Blandford and Königl (1979), we can see from Equation 2.9 that the spectral peak of each jet segment ($\tau_\nu \simeq 1$) is reached at lower frequencies for increasing distances from the jet base. Hence, segments at larger distances from the base will produce emission peaking at lower frequencies. The global, resulting jet emission will be a superposition of the individual spectra from the jet segments, and the observed flat spectrum will be a direct consequence of the change of physical conditions of the electrons throughout the propagation along the jet. A schematic representation of the jet is shown in Figure 2.2.

The flat spectrum is limited between two characteristic frequencies where we have the emission from the jet segments which are respectively closest and farthest from the jet base. Far from the jet base, the global spectrum will display the optically thick, self-absorbed emission from the last segment at low frequencies, while at the jet base the first segment will peak at a frequency $\nu_{\rm break}$ (shown in Figure 2.2). Such frequency, located in the NIR, is particularly interesting and has been thoroughly investigated in the recent years, as it is a direct manifestation of the physical conditions close to the compact object (Markoff, Falcke, and Fender, 2001;

Corbel and Fender, 2002; Russell et al., 2013a; Russell et al., 2014; Russell et al., 2020). At frequencies higher than $\nu_{\rm break}$, the spectrum will be optically thin, with a slope $(1-p)/2$, as discussed in Section 2.1.1.

Extensions of the model

While this model is able to reproduce successfully the observed spectra from jets launched by BH LMXBs, it presents an important energetic problem that needs to be addressed. As mentioned at the beginning of this section, the energy losses due to radiation and adiabatic expansion are assumed to be completely replenished by an undetermined re-acceleration mechanism that should continuously act along the jet. Without a re-energization mechanism, and conserving the initial standard hypotheses on the jet configuration, the observed spectrum would not be flat anymore (e.g. Kaiser 2006). Many works have tried to solve this issue, starting with a possible candidate mechanism for the continuous energy supply for the jet particles. Internal shocks within the jet plasma have been consistently proposed as a viable mechanism for compensating the energy losses (e.g. Kaiser, Sunyaev, and Spruit 2000; Spada et al. 2001; Jamil, Fender, and Kaiser 2010; Malzac 2013). Internal shock models assume that the jet can be composed of a large number of discrete ejecta. In analogy with gamma-ray bursts (e.g. Mészáros 2006), those ejecta are launched by the central "engine" with slightly different velocities and then propagate along the jet. When the faster plasma shells start catching up and colliding with the slower ones, internal shocks are produced. In those shocks, a fraction of the bulk kinetic energy of the ejecta is converted into internal energy of the particles, which are efficiently re-accelerated (e.g. Malzac 2013).

Other possible extensions of the Blandford-Königl model proposed to take into account energy losses include a modification of the initial hypotheses, such as the possibility of a non-conical jet geometry or a hybrid thermal/non-thermal electron distribution (e.g. Hjellming and Johnston 1988; Kaiser 2006; Pe'er and Casella 2009).

A possible jet contribution in the X-rays?

The optically thin part of the full jet spectrum might extend up to frequencies higher than the NIR band, even up the hard X-rays. In fact, the power law spectrum observed in the hard X-rays appears compatible with an extrapolation of the optically thin synchrotron emission from the radio and IR to the X-rays (Corbel and Fender, 2002). This could be a straightforward explanation for the origin of the hard X-ray emission observed in BH LMXBs. The idea of an X-ray emission from the jets has been developed in detail by Markoff, Falcke, and Fender (2001) and Markoff and Nowak (2004). According to these works, the jet can contribute in a dominant way to the hard X-rays through the synchrotron emission of the most energetic electrons at the base of the jet, and through the inverse-Compton emission from the same population of electrons. The photon field for the Compton upscattering might be the soft emission from the accretion disk, or could consist of the jet synchrotron photons (synchrotron self-Compton). A jet contribution to the hard X-rays might be possibly supported by high polarization fraction (expected for synchrotron radiation, e.g. Rybicki and Lightman 1979) detected in the high-energy tail of Cyg X-1 with the INTEGRAL satellite (Rodriguez et al., 2015; Cangemi, 2020).

2.2 Powering mechanism

A fundamental and still open question regarding jets from BH LMXBs is how these relativistic outflows are powered by the system. Current models for the jet formation and powering require the accretion of plasma, the presence of magnetic fields and the extraction of energy from the central system. This last point is what differentiates the two main proposed models: according to the Blandford-Payne model, the energy is extracted from the accretion disk (Blandford and Payne, 1982), while according to the Blandford-Znajek model such energy is provided by the rotational energy of the black hole itself (Blandford and Znajek, 1977). I present here in a very qualitative way the two models, without entering into the details, that can be very complex and their treatment is beyond the scope of this work.

In the Blandford-Znajek model, jets are directly powered by the rotation of the ergosphere of a spinning Kerr black hole. In the disk, matter will be accreted towards the black hole carrying magnetic fields, so that the matter density will greatly rise close to the compact jets and strong magnetic field lines will be produced in this region. As matter is advected through the event horizon, the magnetic field lines remain threaded through the event horizon. Space-time rotation will produce a twisting of these lines in the inner region, and charged plasma will be accelerated along the rotation axis, producing a highly relativistic Poynting flux jet (Blandford and Znajek, 1977).

In the second model, Blandford and Payne (1982) proposed that the strong magnetic fields responsible for the jet acceleration and collimation are produced by the accretion disk. The jet has then a magneto-hydrodynamic (MHD) origin. The magnetic field is considered to have a poloidal configuration and to be anchored in the rotating accretion disk. It has been shown that if the magnetic field lines have an inclination angle larger than 30° with respect to the rotation axis, it is more energetically convenient for the particles to escape the disk by following the poloidal lines (Blandford and Payne, 1982). The angular velocity of the rotating field lines is assumed to be constant. Hence, the more the particles depart from the disk, the more are subject of a centrifugal force that accelerates them (like "beads on a wire", and this mechanism is also called *magneto-centrifugal acceleration*, e.g. Jafari 2019). At some point, due to the MHD process, the rotating accelerated particles are able to deform the field lines and to produce a toroidal component of the magnetic field. This field component is then responsible for the collimation of the plasma in the form of jets, and the whole process effectively extracts energy and angular momentum from the disk (Blandford and Payne, 1982).

We have to remark that the Blandford-Znajek model requires the presence of a black hole, and therefore cannot be applied to jets launched by other accreting objects (such as neutron stars or white dwarfs), while the Blandford-Payne model requires only the presence of an accretion disk, regardless of the central compact object.

While it is extremely difficult to observationally distinguish between the two mechanisms, in the recent years general relativistic magneto-hydrodynamic (GRMHD) simulations have tried to contribute to the solution of this problem. From simulations, it appears that for black holes both mechanism might be at play (McKinney, 2006; Mościbrodzka and Falcke, 2013; Chatterjee et al., 2019). A consequence of this dichotomy might be the formation of a structured or stratified jet, in which a highly relativistic, Poynting-flux dominated jet (from the Blandford-Znajek mechanism) is surrounded by a slower, mass-loaded MHD jet from the Blandford-Payne mechanism (e.g. Ghisellini, Tavecchio, and Chiaberge 2005; Vuillaume, Henri, and Petrucci 2018).

2.3 Recent progresses

Before discussing the fundamental connection between the jets and the accretion flow, which is the core of the second part of this chapter, I present two recent results on compact jets: one on the evolution of the break frequency (Russell et al., 2020) and one on the jet fast variability (Tetarenko et al., 2019), that show how the field is progressing thanks to new observing strategies and new approaches to the data analysis.

2.3.1 Evolution of the break frequency

As discussed in Section 2.1, the compact jet spectrum extends up to a break frequency $\nu_{\rm break}$ located in the infrared band, around $\sim 10^{13}$ Hz (e.g. Corbel and Fender 2002; Russell et al. 2013a), and this spectral break corresponds to the region in the jet closest to the black hole, where particle acceleration begins (Blandford and Königl, 1979).

During a typical outburst, as the source transitions from the hard to the soft state and spends a short amount of time in the intermediate states, the compact jet is observed to quench (by at least 3.5 orders of magnitude Coriat et al. 2011; Russell et al. 2019c, see Section 1.4.2). During the quenching process, the frequency of the jet break is believed to gradually shift from the infrared to the radio band. The inverse is instead observed for the compact jet re-activation during the reverse (soft-to-hard) transition (e.g. Corbel et al. 2013a). Since the properties of the jet spectral break (frequency and flux density) depend on the internal jet plasma properties close to the compact object, determining the break's location and studying its evolution during the outburst has a great discovery potential and can help us to reveal key properties of the jets (e.g. Heinz and Sunyaev 2003a; Chaty, Dubus, and Raichoor 2011; Russell et al. 2014).

While there have been numerous attempts in the past to track the break frequency evolution, both during the quenching and re-activation phases, the behaviour of the break frequency has not been yet observed in detail. The first evidence of such evolution is the observation of the radio spectrum changing from flat to steep as the break frequency moves inside the radio band (e.g. Corbel et al. 2013a; van der Horst et al. 2013). Such break frequency evolution has also been inferred in the neutron star XRB Aquila X-1 (Díaz Trigo et al., 2018).

For tracking the evolution of the break frequency, it is important to have a high-cadence multi-wavelength observing campaign. This, when possible, allows to fit the SED of each epoch with simple models corresponding to the main components of the system, including a broken power law for the compact jets, and to follow in detail the decrease of the break frequency during the hard-to-soft state transition. A first demonstration of the importance of such approach was provided with the 2011 outburst of the BH LMXB MAXI J1836–194 (Russell et al., 2013a; Russell et al., 2014).

Subsequently, good progress has been achieved with the recent observation of the 2017 outburst of the BH LMXB MAXI J1535–571, presented in Russell et al. (2019c) and Russell et al. (2020). These authors present six quasi-simultaneous multi-wavelength observations, from radio to X-rays using the Australian Telescope Compact Array (ATCA), the Atacama Large Millimeter/sub-millimeter Array (ALMA), the Las Cumbres Observatory and *Swift*/XRT (see Chapter 4).

The observations, taken in September 2017 at the hard-to-soft state transition (specifically from the HIMS to the SIMS, Russell et al. 2019c), show how the jet contribution to the global SED changed dramatically over a very short timescale, as the jet was strongly quenched. The data and the SED fit for each epoch are shown in Figure 2.3, taken from Russell et al. (2020).

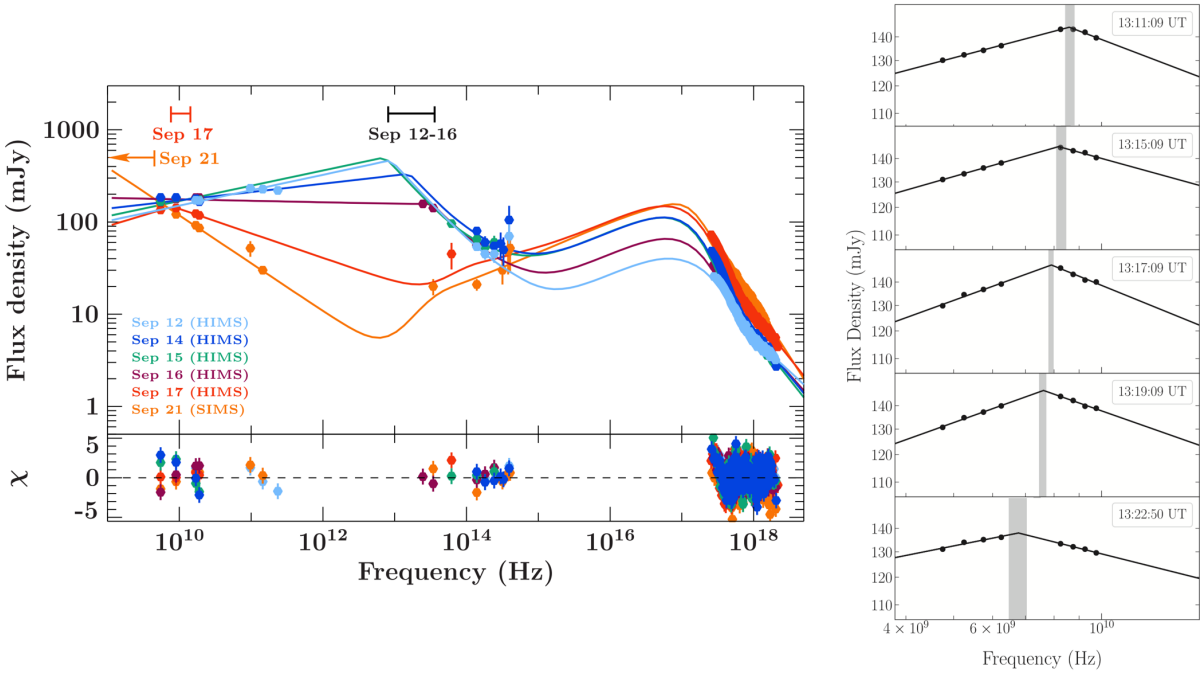

Figure 2.3: *Left*: SED modelling of MAXI J1535–571 in its 2017 outburst, during the source transition between the HIMS to the SIMS, from Russell et al. (2020). Solid lines represent the broad-band models for each epoch, where different colours depict different observational epochs. The jet contribution is modeled as a broken power law. The top horizontal bars show the confidence interval for the location of $\nu_{\rm break}$ in each epoch. Fit residuals are shown in the lower panel. After being relatively steady for the first five days of the monitoring, the break frequency rapidly decreased by roughly 3 orders of magnitude, entering in the radio band. *Right:* Rapid decrease of $\nu_{\rm break}$ within the radio band on the observation of September 17 2017. Adapted from Russell et al. (2020).

From the global fits, the break frequency is identified at each epoch, and it is clearly observed to move, after a first steady phase, from the infrared to the radio band (decreasing by $\sim$3 orders of magnitude) in a very short timescale, of less than a day. The quick evolution was captured in the short subsequent radio observations of September 17 2017, as can be seen in Figure 2.3 (plot on the right). From the values of the break frequency and flux density at the break for each epoch, for the first time it has been possible to estimate the time evolution of the magnetic field and of size of the particle acceleration region at the base of the jet (Russell et al., 2020). The results show that the rapid decrease of the jet emission during the quenching was not consistent with radiative cooling timescales, but with dynamical timescales. The favored interpretation is that the particle acceleration region might be moving away from the black hole on roughly dynamical timescales. Hence, the main conclusion is that the compact jet quenching is not caused by local phenomena, such as changes in the way particle are accelerated, but instead it is more likely that the quenching results from global changes in the jet properties. More in detail, it might be caused by the first acceleration region that moves away from the black hole system on adiabatic/dynamical timescales (Russell et al., 2020). This is an important step in our understanding of the jet's evolution in relation to the major changes in the accretion flow observed during state transitions.

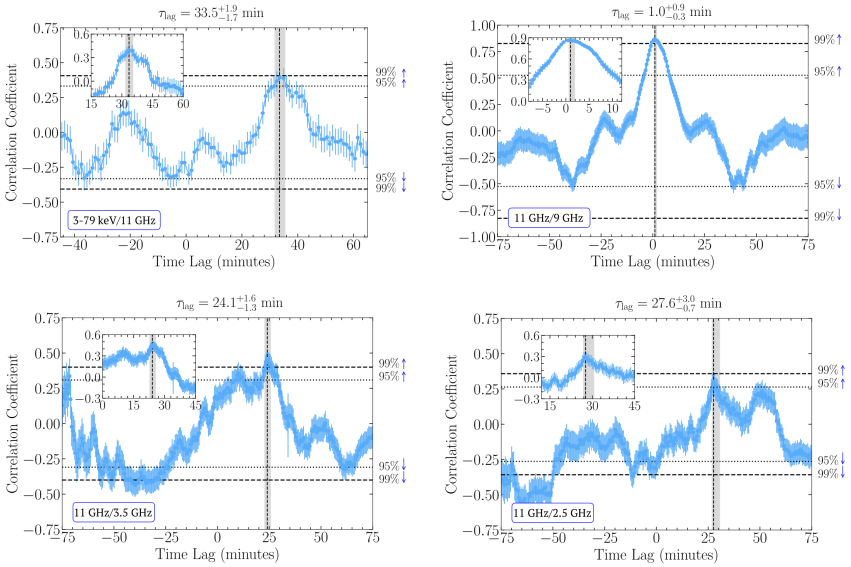

Figure 2.4: Cross-correlation functions (CCFs) between the X-ray and radio emission from Cyg X-1, from Tetarenko et al. (2019). On the four panels we have the CCF between the pair 3-79 keV/11 GHz (top left), 11/9 GHz (top right), 11/3.5 GHz (bottom left), and 11/2.5 GHz (bottom right). The peak of each CCF represents the best estimate of a potential time lag between the light curves from different bands, and it is shown with the black dotted line, along with the 1σ confidence interval on $\tau_{\rm lag}$. The horizontal dotted and dashed lines represents, respectively, the 1σ and 2σ confidence intervals for the significance of the CCF peaks (see Tetarenko et al. (2019) for details). The peaks can be better visualized in the insets on each panel. Positive time lags indicate that lower frequencies lags behind the higher frequencies band. Negative lags are considered unphysical in the Bayesian analysis adopted to estimate the lags (Tetarenko et al., 2019).

2.3.2 Insights from fast variability

Fast variability of the jet emission is observed at multiple wavelengths, and its detailed study can represent a new powerful way to access the jet physics (Casella et al., 2010; Uttley and Casella, 2014; Gandhi et al., 2017). Analysing the jet's emission in the Fourier space can effectively probe physical scales that are absolutely not observable with the current imaging capabilities (10–100 $R_{\rm g}$ at kpc distances, far below the mas scale). With timing studies of the jet emission, it is possible to map out the jet structure and to obtain estimations of the jet cross-section and opening angle. Due to optical depth effects (see Section 2.1), it is expected for the jet emission to display a distinct observational signature, consisting of signals at lower frequencies to lag behind signals at higher frequencies (Blandford and Königl, 1979; Hjellming and Johnston, 1988). Through the combination of size scale constraints at different frequencies and time-lag measurements, it is possible to place constraints on the jet power and speed (e.g. Uttley and Casella 2014). Moreover, with timing studies is it possible to directly link changes in the accretion flow with changes in jet emission at different scales, having an additional way to look into the sequence of events that leads to jet launching and acceleration. Evidences of correlations between optical/infrared (jets) and X-ray (accretion flow) variability have been found on second and sub-second timescales, implying that variations in the accretion flow could drive variability in the jet emission (Casella et al., 2010; Gandhi et al., 2017; Vincentelli et al., 2018; Malzac et al., 2018).

While timing analysis already existed for the X-ray and optical/infrared bands, recently

Tetarenko et al. (2019) applied these new powerful techniques in the radio band, with simultaneous radio and X-ray observations of the BH HMXB Cyg X-1. The monitoring campaign was performed in 2016, during a phase of hard state for Cyg X-1, and consisted of simultaneous multi-band and high time resolution radio and X-ray observations using the Very Large Array (VLA) and the Nuclear Spectroscopic Telescope Array (NuSTAR). For the first time, this work was able to obtain insights on the jet physics from the rapid variability of radio light curves. Evidences of correlations between the different light curves of Cyg X-1 were found, both within the radio band and between radio and X-rays (see Tetarenko et al. 2019), and cross-correlation functions were computed between the different bands to estimate the value of the time lags, which are shown in Figure 2.4. In particular, the radio emission was found to lag the X-ray emission by tens of minutes, and similar lags were found within the radio band. The lags were then used to solve for the compact jet speed $\beta = 0.92^{+0.03}_{-0.06}$ and corresponding Lorentz factor $\Gamma = 2.59^{+0.79}_{-0.61}$, finding that the Cyg X–1 jet is slightly more relativistic than what assumed for compact jets (Tetarenko et al., 2019). This is one of the rare constraints (even if model dependent) on the compact jet Lorentz factor of a microquasar. Moreover, the analysis in the Fourier domain (see details in Tetarenko et al. 2019) allows to constrain how the size of the jet x scales with frequency, obtaining $x \propto 1/\nu^{0.4}$, which seems to deviate from the standard jet models ($x \propto 1/\nu$, Blandford and Königl 1979). The jet opening angle was estimated to be $\phi = 0.4°$–$1.8°$.

Such approach, rich of return in physical information, was then also applied to another important source of the recent years: MAXI J1820+070, which displayed powerful evolving radio jets (Bright et al., 2020). A similar observational campaign was performed on the 2018/2019 outburst of MAXI J1820+070, with the inclusion of the sub-mm, infrared, and optical bands. Also in this case, the jet opening angle ($1.5° \pm 1°$), Lorentz factor (1.5–4.5) and overall power ($2\text{–}5 \times 10^{38}$ erg s^{-1}) were estimated (Tetarenko et al., 2021; Zdziarski, Tetarenko, and Sikora, 2021), further validating the power of the timing approach in the study of compact jets.

2.4 The radio/X-ray correlation

Until now, we have focused on the compact jets, without considering their fundamental connection with the accretion flow. Such connection, which is not currently understood (beside the models for the jet powering mechanisms discussed in Section 2.2), is vitally important to discover and then predict how these ejections from compact objects depend on the accretion state of the system. Nowadays, the relationship between the radio luminosity, determined by the jets, and the X-ray luminosity, linked to the accretion flow, is one of the main observational tools used for studying the connection between inflows and outflows in accreting black holes.

A strong correlation of the form

$$L_{\rm R} \propto L_{\rm X}^{\beta} \tag{2.12}$$

has been observed between the radio and X-ray luminosities in the hard state phases of BH LMXBs (Hannikainen et al., 1998; Corbel et al., 2000). Since, as we will see below, $\beta > 0$, this connection implies that an increase in the accretion rate onto the black hole during an outburst, that is observed as an increase in $L_{\rm X}$, causes an increase in the mass loading of the jet, which in turn increases its emission ($L_{\rm R}$)[1]. The coupling of Equation 2.12 has been found to exist

[1]On the other hand, discrete ejecta do not appear to be physically connected to the black hole, and hence do not depend anymore on the accretion activity after the ejection, thus are not included in the correlation.

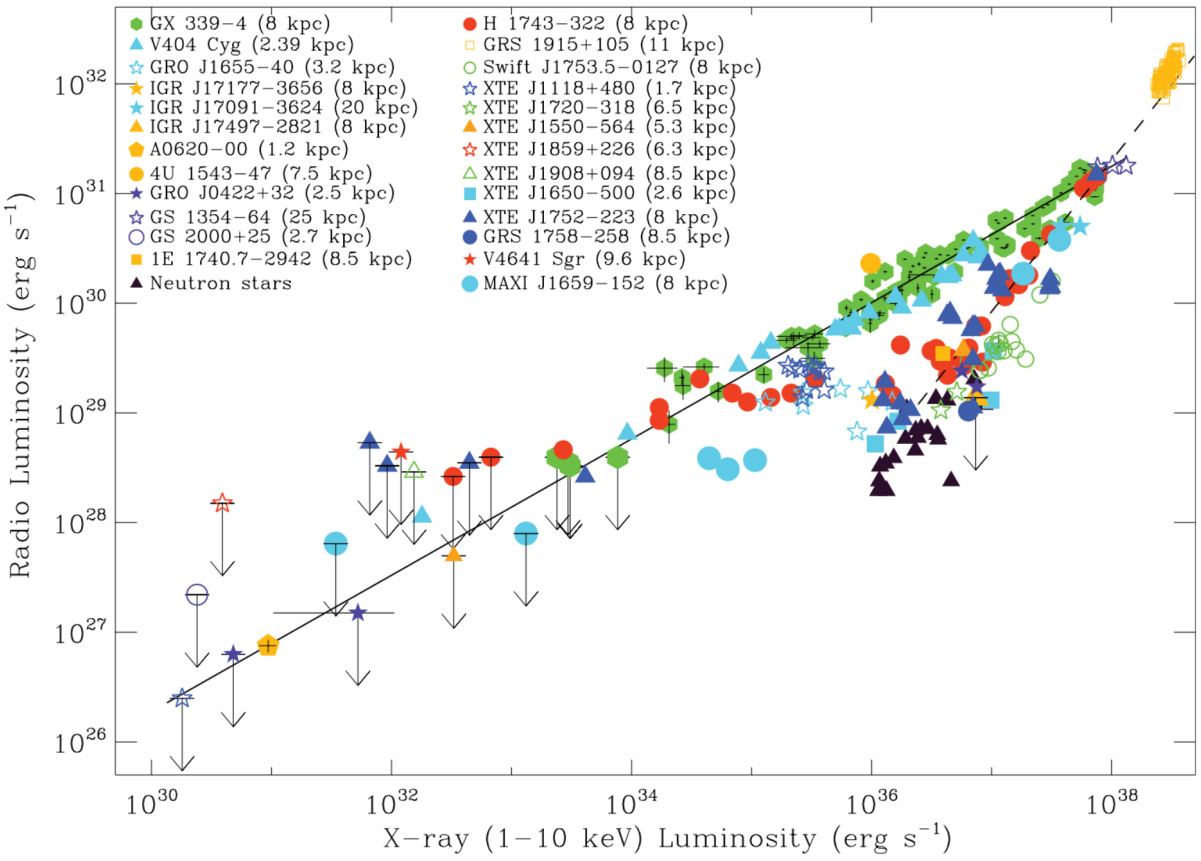

Figure 2.5: The radio and X-ray (1–10 keV) luminosities for galactic BH LMXBs in the hard and quiescence states, with their known or unknown distances, taken from Corbel et al. (2013b). The standard track (with GX 339−4 and V404 Cyg, with index $\beta \simeq 0.6$) and the outlier track (with H1743−322 and Swift J1753.5−0127, with index $\beta \simeq 1.4$) are shown. The solid line represents the fit to the whole sample of GX 339−4 (Corbel et al., 2013b), while the dashed line corresponds to the fit to the data for H1743−322 (Coriat et al., 2011).

over several orders magnitude of both $L_{\rm X}$ and $L_{\rm R}$, and can be visualized on the well-known radio/X-ray diagram, which is shown in Figure 2.5 and includes the known population of BH XRB observed simultaneously in radio and X-rays in the hard state.

Originally, the few "historical" black hole XRBs were found to lie on a track labeled as *standard*, with a power law index $\beta \simeq 0.6$ (such as GX 339−4, V404 Cyg and now also MAXI J1820+070, Corbel et al. 2000; Corbel et al. 2003; Corbel et al. 2013b; Gallo, Fender, and Pooley 2003; Bright et al. 2020; Shaw et al. 2021). Based on scale-invariant properties of black hole accretion and jet production, this correlation has also been extended to AGNs by including the mass as an additional parameter (Merloni, Heinz, and di Matteo, 2003; Falcke, Körding, and Markoff, 2004; Plotkin et al., 2012), and this is discussed in Section 2.6.

As new observations accumulated, more and more sources (labeled *outliers*) were found to lie on a different branch, well below the standard track, with a steeper slope $\beta \gtrsim 1$ (see Figure 2.5, Coriat et al. 2011). We note that in some works the two populations are referred to as *radio-loud* and *radio-quiet*, one of the two ways to interpret the data (see Coriat et al., 2011 and Section 2.5.3 for more details). While multiple explanations have been proposed (see Section 2.5) the reasons for the existence of such dichotomy on the diagram are not yet understood. Outliers could be characterized by more negative radio spectral indices (Espinasse

and Fender, 2018) and lower rms variability (Dinçer et al., 2014; Motta, Casella, and Fender, 2018) with respect to standard track sources, which may be indications for understanding the nature of the two different tracks. The existence of the two tracks may suggest the existence of two different fundamental couplings between the compact jets and the inner accretion flow, whose origin is still poorly understood (e.g. Soleri and Fender 2011; Gallo et al. 2014; Espinasse and Fender 2018).

The above-mentioned two populations of sources tentatively display a very different behaviour in the low flux regime, when re-approaching quiescence. Standard track sources, as for example the well-monitored GX 339−4, appear to maintain the correlation even below $\sim 10^{-5} L_{\rm Edd}$, down to the quiescent level (Corbel et al., 2013b; Gallo et al., 2019; Tremou et al., 2020), while the outliers seem to deviate from their correlation and may re-join the standard track below a transition luminosity of $\sim 10^{-5}$–$10^{-3} L_{\rm Edd}$, through a sort of *hybrid*, flat branch, a behaviour observed for the first time in H1743−322 (Coriat et al., 2011). This supports the idea of a significant change in the coupling between the jets and the accretion disk as the accretion rate decreases. While the phenomenon is not yet understood, several explanations and models have been proposed for this scenario, as we will see in the next section. Currently, tracking sources in their path on the radio/X-ray diagram is important, as it can place constraints on the jet emission mechanisms, and measuring their radio/X-ray correlation is crucial for potentially breaking degeneracies between different models (e.g. Plotkin et al. 2017a).

Finally, a similar radio/X-ray correlation was also found for microquasars containing neutron stars (a part of them is shown in Figure 2.5), with a steep correlation index $\beta \simeq 1.4$ and fainter $L_{\rm R}$ for a given $L_{\rm X}$ with respect to black holes (Migliari and Fender, 2006a; Tudor et al., 2017; van den Eijnden et al., 2021). However, the global situation of NS XRBs on the radio/X-ray diagram is rather complex and a full treatment of these systems is beyond the scope of this work.

2.5 Proposed explanations

The existence of the two tracks on the diagram is still not explained today, and it constitutes an important open problem in the physics of accreting black holes. While the attempts to identify the physical origin of the dichotomy on the diagram have been unsuccessful so far, several explanations for the observed scenario have been proposed, and I present them in this section. First, a physical difference in the disk-jet coupling may be responsible for the two groups. This could originate from the structure of the inner accretion flow or alternatively the properties of jets might differ between the two tracks, causing different levels of radio emission. I present below the description of both alternatives. The existence of the two tracks has also been questioned statistically (e.g. Gallo et al. 2014; Gallo, Degenaar, and van den Eijnden 2018) if one considers the whole sample of sources. However, it is particularly important to precisely track the behaviour of specific sources, such as H1743−322 (Coriat et al., 2011; Williams et al., 2020) or MAXI J1348−630 (this thesis), for which the path on the diagram is very clear, to pinpoint the overall behaviour which may be masked in the whole sample due to overlap of sources and possible transition between the two tracks.

2.5.1 Geometry

As a first approach, the two populations on the diagram might originate from geometric effects, rather than intrinsic physical differences between sources. Evidence has accumulated in recent studies about the inclination angle of the disk affecting X-ray timing and spectral observations.

High inclination sources (close to the *edge-on* configuration) appear to show harder X-ray spectra in the hard state (Heil, Uttley, and Klein-Wolt, 2015) and a modified shape of the HID (see Section 1.4.2 and Muñoz-Darias et al. 2013)

On the other hand, the inclination is expected to play a role also in the jet radio synchrotron emission due to Doppler boosting (see Equation 2.4). Therefore it has been proposed that the low inclination sources might be more radio-bright, and hence the standard track could group sources with generally low inclinations (Motta, Casella, and Fender, 2018). As it appears today that most of the observed BH LMXBs are outliers, this could be the "normal-mode" for their behaviour, and the inclination of the X-ray binary might be the main factor responsible for the observed radio-loudness of a small number of sources. This has been tested in Motta, Casella, and Fender (2018) with the available inclination angles measurements and it did not lead to firm conclusions on whether the dichotomy on the diagram is indeed due to geometric effects.

In addition, Doppler boosting was taken into account in Soleri and Fender (2011), where a toy model for the jet emission was used. Assuming that $L_{\rm R} \propto L_{\rm X}\delta^2$, where δ is the Doppler factor (the factor 2 comes from Doppler boosting of a continuous jet, Fender 2003), and considering a uniform distribution of inclination angles, the model can qualitatively reproduce the observed distribution of sources on the radio/X-ray diagram. However, this interpretation suffers from several problems. First, it cannot explain the *hybrid* behaviour observed in several sources and discussed the previous section, as there would be no obvious reason for the source to change track at a given luminosity. Moreover, it is not certain whether the orbital inclination corresponds to the jet inclination, and several cases of disk/jet misalignment have been found (e.g. Maccarone 2002; Poutanen et al. 2021), further complicating this picture.

2.5.2 Radiative efficiency of the accretion flow

An alternative approach for a tentative explanation of the observed dichotomy on the diagram is to invoke differences in the X-ray emission produced by the accretion flow between the two groups. One proposed explanation in Coriat et al. (2011) is that the two groups of sources might be characterized by accretion flows with different radiative efficiencies. In this context, outliers might be considered *X-ray bright* and not *radio-quiet* with respect to standard track sources. We discuss in the following the basic concepts behind this possibility.

Two classes of accretion flow exist, and the distinction depends on how important is the release through radiation of the gravitational energy of the accreted matter. In *radiatively efficient* accretion flows, the energy is preferentially radiated away, while in *radiatively inefficient* accretion flows the energy is stored in the accreted matter and it is advected into the event horizon of the black hole. Examples of radiatively efficient accretion flows are the standard geometrically thin, optically thick accretion disk model (Shakura and Sunyaev, 1973), some models of accretion disc coronae (ADC, e.g. Haardt and Maraschi 1991) and the luminous hot accretion flow (LHAF, Yuan and Zdziarski 2004). For radiatively inefficient flows, the advected energy can either cross the event horizon in the well-known *advection-dominated accretion flow* model (ADAF, Ichimaru 1977; Narayan and Yi 1994; Abramowicz et al. 1995), or be expelled from the system through outflows, in the so-called *advection-dominated inflow-outflow solution* (ADIOS, Blandford and Begelman 1999).

While we do not enter into details for specific properties of each accretion flow model listed above, we discuss briefly the characteristics of the ADAF model, which are particularly interesting and appear to be important for explaining the standard track.

Advection-dominated accretion flows

While at high accretion rates (0.01–$1\dot{M}_{\rm Edd}$) the thin disk model is thought to be a good approximation and the plasma radiates efficiently, at lower accretion rates the gas density is low and the disk might be unable to radiate energy efficiently. In such case, the energy in the disk, generated though viscosity caused by the MRI-induced turbulence (see Section 1.2.2), will remain stored in the accreting plasma and the disk will become hot, since the cooling by radiation is not efficient (Frank, King, and Raine, 2002). This motivated the development of an accretion flow model suitable for the low-accretion rate phases of the outburst, called advection-dominated accretion flow or ADAF (Ichimaru, 1977; Narayan and Yi, 1994; Abramowicz et al., 1995).

At low accretion rates, electron and ions are strongly decoupled since the Coulomb interactions occur on a longer timescale than the accretion timescale (Esin, McClintock, and Narayan, 1997), and the disk gas can be described as a two-temperature plasma. The electrons are still able to radiate efficiently and hence are much cooler than the ions, which in turn contain most of the viscous energy, which will be advected. The ion heating leads to an expansion of the disk, that appears "puffed-up". Therefore, the properties of a disk described by an ADAF are dramatically different from the ones of a standard thin disk (e.g. Shakura and Sunyaev 1973): at low accretion rates the disk is believed to be geometrically thick, optically thin, hot and radiatively inefficient (Narayan and Yi, 1994).

Dependence on the accretion rate and "hybrid" behaviour

A key difference between the two types of accretion flow is the dependence of the X-ray luminosity on the accretion rate. For a radiatively efficient accretion flow, where a significant fraction of the thermal energy is radiated away before being advected, the X-ray luminosity is expected to be proportional to the mass accretion rate, as $L_{\rm X} \propto \dot{M}$ (Shakura and Sunyaev 1973), while for a radiatively inefficient flow we have $L_{\rm X} \propto \dot{M}^{2-3}$ (Narayan and Yi, 1994). We note that a dependence on the accretion rate similar to the radiatively inefficient case is also obtained for models that consider the hard X-rays to be produced at the base of the jets as optically thin synchrotron emission and/or inverse Compton (see Section 2.1, Markoff et al. 2003; Markoff, Nowak, and Wilms 2005). For a microquasar, since the ejection results from accretion, we can consider the total power of the jet to be a fraction ϵ of the accretion power, $P_{\rm jet} = \epsilon P_{\rm acc} \propto \dot{M}$. Moreover, it has been shown by Heinz and Sunyaev (2003a) that, considering the jet synchrotron emission, the jet luminosity scales with the jets power as

$$L_{\rm jet} \propto P_{\rm jet}^{\xi} = P_{\rm jet}^{\frac{2p-(p+6)\alpha+13}{2(p+4)}} \tag{2.13}$$

where α is the spectral index of the jet synchrotron emission and p the index of the power law distribution of electrons. The index ξ has a characteristic value of $\sim$1.4 (but see Coriat et al. (2011) for details). With these equations, we then have a relation between the jet's radio luminosity and the disk X-ray luminosity. For a radiatively efficient accretion flow, we obtain $L_{\rm jet} \propto L_{\rm X}^{\sim 1.4}$, which is consistent with the outlier track, while for a radiatively inefficient accretion flow the scaling is instead $L_{\rm jet} \propto L_{\rm X}^{0.5-0.7}$, consistent with the standard track (Coriat et al., 2011). This is completely compatible with the two tracks observed on the diagram, and might be a valid explanation for their existence. A schematic representation of the diagram with the radiatively efficient/inefficient tracks is shown in Figure 2.6. This scenario is also supported by the detection of hard X-ray cut-offs in the spectra of outliers, implying an effective cooling of

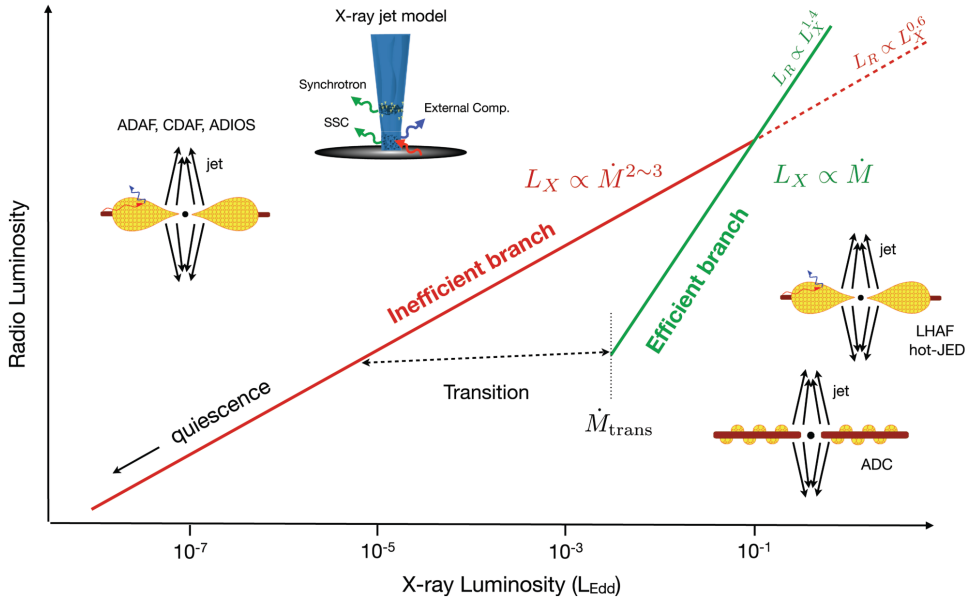

Figure 2.6: A scheme of the radio/X-ray diagram for Galactic black holes, from Coriat et al. (2011). The X-ray luminosity is expressed in units of $L_{\rm Edd}$ for a 10 $M_\odot$ black hole. The two main branches are distinguished according to the radiative efficiency of the accretion flow and to the corresponding proportionality between the X-ray luminosity and the mass accretion rate. For each branch, several models for the radiatively efficient/inefficient accretion flows are shown (see text and Coriat et al. 2011 for details). The transitional branch linked to the *hybrid* correlation is also shown.

the electrons responsible for the Comptonization of disk photons, consistent with a radiatively efficient accretion flow (Koljonen and Russell, 2019).

The behaviour of hybrid sources, which appear to transition between the two tracks at a given X-ray luminosity, has not been explored in depth and it represents an important open problem. There exist today some interesting explanations, and we mention here one of them, which also involves the radiative efficiency of the accretion flow. It has been shown that the radiative efficiency might increase non linearly with the mass accretion rate (and hence $L_{\rm X}$, Narayan and Yi 1995), up to a critical value where the accretion flow changes from an ADAF to different types of LHAF (Coriat et al., 2011; Xie and Yuan, 2012; Xie and Yuan, 2016). Close to the critical luminosity $L_{\rm C}$, as the morphology of the accretion flows changes, there is a sharp increase of radiative efficiency with little change in the mass accretion rate. Hence, hybrid sources might reach the critical luminosity and transition to an X-ray bright branch. Standard track sources and outliers would then simply be characterized by different critical luminosities (Xie and Yuan 2016, and see Chapter 6 for details).

2.5.3 Jet properties

The other main line of investigation for understanding the existence of the two tracks on the diagram involves the possibility that outliers and standard track sources have fundamentally different jet properties. The distribution of radio spectral indices among sources on the radio/X-ray correlation seems to show a difference between outliers and standard track sources, with the first presenting steeper spectra than the second (Espinasse and Fender, 2018). This might suggest the presence of a distinct physical difference between the jets (in the structure and/or particle acceleration) of the two groups of sources. Espinasse and Fender (2018) also found

that the behaviour of a source on the diagram does not seem to depend on the spin of the black hole. However, this scenario does not seem consistent with the hybrid sources, which should display a shift in the radio spectral index when transitioning between the two tracks. While it is difficult to test such hypothesis, as multi-frequency observations are difficult to perform during the transition, there seems to be no evidence of that (Shaposhnikov et al., 2007).

Another possible explanation might involve the strength of the magnetic field threaded in the jet plasma, that will have an important influence on the jet synchrotron emission. According to Pe'er and Casella (2009), the radio flux depends on the value of the magnetic field in a complex way. Above a critical value of the magnetic field , the electrons at the jet base would be rapidly cooled, strongly quenching the radio emission. Therefore, it was proposed that the outliers are sources with stronger magnetic fields, above the critical value (Pe'er and Casella, 2009). In this context, an evolution of the magnetic field throughout the outburst, possibly increasing with the accretion rate, could also explain the observed hybrid correlation.

2.6 The fundamental plane of black hole activity

After the discovery of the standard track on the radio/X-ray diagram for galactic stellar-mass black holes, it began to be investigated whether such correlation between the radio and X-ray luminosities was valid also for other black holes, especially the supermassive black holes in AGNs. Such approach had the aim of testing the self-similarity of the accretion disk and of the compact jets, and to see if all black holes are characterized by the same connection between the disk and the jets.

Such approach was successful, as Merloni, Heinz, and di Matteo (2003) and Falcke, Körding, and Markoff (2004) found that AGNs follow a correlation very similar to the one displayed by the standard track sources in a tri-dimensional hyper-plane, including the X-ray and radio luminosities and the black hole mass. From Merloni, Heinz, and di Matteo (2003), adding a term for the mass correction, the relation was originally written as

$$L_{\rm R} \propto L_{\rm X}^{0.6} M_{\rm BH}^{0.8} \tag{2.14}$$

This $L_{\rm X} - L_{\rm R} - M_{\rm BH}$ relation is also called the *fundamental plane of black hole activity*, since it groups all the accreting black holes known today (with the important exception of outlier sources) and appears to depend on universal properties of black hole accretion and jet launching. A projection in mass of the $L_{\rm X} - L_{\rm R} - M_{\rm BH}$ relation is shown in Figure 2.7.

The existence of such correlation on the fundamental plane might have important implications about the physics of accretion onto black holes and can open up a new line of research to study the disk/jet coupling in compact objects (Falcke, Körding, and Markoff, 2004; Plotkin et al., 2012). The fundamental plane could result from the scale invariance of the disk/jet coupling, which links the jet power, probed by radio, and the mass accretion rate, probed by X-rays (Merloni, Heinz, and di Matteo, 2003). This implies that, under certain conditions, our knowledge of BH LMXBs can be applied to the study of AGNs, and vice versa. The scale invariance implies also that black hole accretion can be studied in two ways. First, we can observe how fundamental quantities, such as the accretion rate, vary over time during outburst of BH XRBs (with constant black hole mass, spin and inclination angle). Alternatively, we can study the large sample of AGNs, which are characterized by a constant accretion rate and by a wide range of black hole masses, spin and inclination angles.

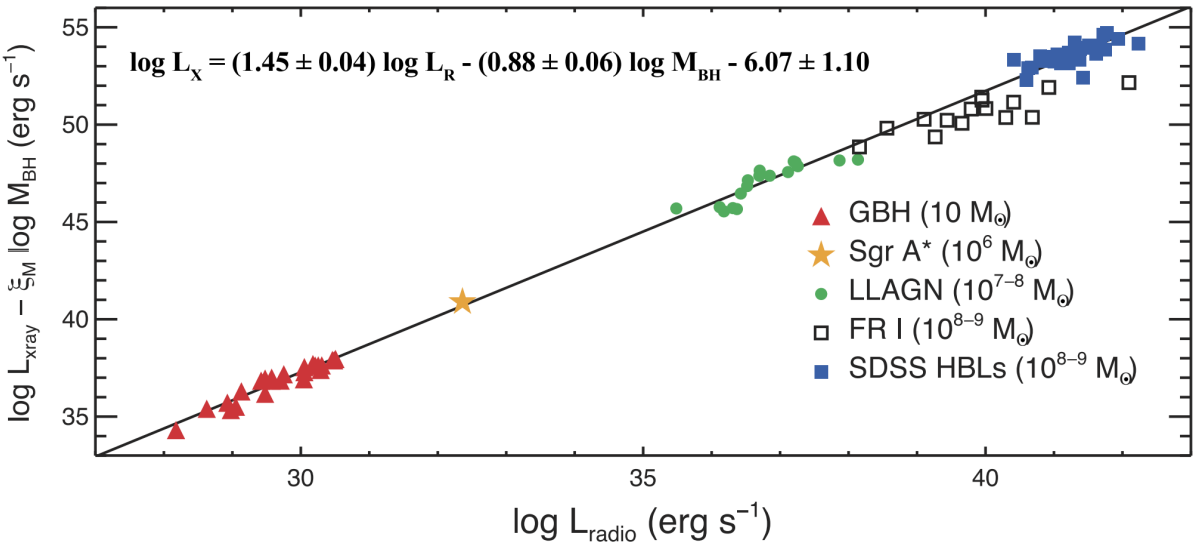

Figure 2.7: A projection in mass of the fundamental plane of black hole activity onto the radio and X-ray luminosity plane (note that here the axes are inverted with respect to the diagram in Figure 2.5), from Plotkin et al. (2012). The data shown on the plane include a sample of hard state BH LMXBs and different types of sub-Eddington AGNs. The best fit is shown as a black line, with the obtained full $L_{\rm X} - L_{\rm R} - M_{\rm BH}$ relation shown on top. This particular plot contains only relatively low accretion rate sources, but the correlation is still valid (with more scatter), when all types of AGNs are included (Merloni, Heinz, and di Matteo, 2003).

Chapter 3

Discrete ejecta from black hole X-ray binaries

Contents

3.1 Superluminal jets from galactic black holes . . . 44
3.1.1 Observations . . . 44
3.1.2 Proper motion . . . 45
3.1.3 Composition . . . 47
3.1.4 Production . . . 48
3.2 The ejection . . . 48
3.2.1 Radio flaring . . . 49
3.2.2 Minimum associated energy . . . 49
3.2.3 Ejection time and connection with X-ray variability . . . 51
3.3 Interaction with the interstellar medium . . . 52
3.3.1 Decelerating jets . . . 53
3.3.2 X-ray detections . . . 54
3.3.3 Jet feedback . . . 55

One of the most interesting properties of BH LMXBs is the capability of launching transient jets, which are bipolar, discrete blobs of plasma ejected from the system at relativistic speeds. Discrete ejecta from BH LMXBs are one of the core topics of my thesis and have been studied extensively in my work. After a short mention in Chapter 1, I present in this chapter what is currently known on these relativistic outflows, starting from an introduction on their observations, kinematics and discussing their unknown composition (Section 3.1). Then I discuss their ejection period in Section 3.2, considering the strong radio flares associated with the launch of these transient jets, the associated minimum energy required to produce such flares, and I present the ejection in relation with additional observables at higher frequencies (X-rays). The last section (3.3) is dedicated to a discussion of the interaction between the ejecta

and the interstellar medium (ISM), including the jet deceleration, the X-ray detections of ejecta at large scales and the feedback that these ejections have on the surrounding environment.

3.1 Superluminal jets from galactic black holes

3.1.1 Observations

The first discrete ejecta from a black hole X-ray binary were discovered in 1994 with VLA radio observations of GRS 1915+105 (Mirabel and Rodríguez, 1994). While discrete ejecta were already routinely observed in AGNs (e.g. Pearson and Zensus 1987), the observations of moving radio components from GRS 1915+105 demonstrated that also X-ray binaries could produce highly relativistic jets (see also Mirabel and Rodríguez 1999; Fender et al. 1999 for GRS 1915+105), opening a entirely new chapter in the study of jets from X-ray binaries. The two ejecta, which are shown in Figure 3.1, displayed the first superluminal motion observed in our Galaxy (Mirabel and Rodríguez, 1994), with apparent velocity $\beta_{\rm obs} > 1$. Shortly after that, superluminal jets were observed in a second galactic source, GRO J1655–40 (Tingay et al., 1995; Hjellming and Rupen, 1995).

Projected speeds of more than $10c$ have been observed in discrete ejecta from AGNs for decades before the discovery of microquasars (Pearson and Zensus, 1987; Zensus, 1997), and superluminal motions were rapidly understood to be only an effect of relativistic aberration (Rees, 1966), without violating special relativity. In fact, the apparent superluminal motion is a geometric effect resulting from the emitting source travelling with a radial component of the velocity that is a significant fraction of the speed of light. Therefore, it was understood that ejecta from X-ray binaries are intrinsically relativistic, with Lorentz factors $\Gamma \gtrsim 2$, even if it was later shown that the bulk Lorentz factors of the jets cannot be constrained from observations of their proper motion alone (Fender, 2003), and hence it is difficult to assess exactly how relativistic these jets are.

While all BH LMXBs are thought to produce jets, resolved discrete ejecta have been observed in radio in only a dozen of sources so far (e.g. Mirabel and Rodríguez 1994; Hjellming and Rupen 1995; Fender et al. 1999; Corbel et al. 2002; Mioduszewski et al. 2001; Gallo et al. 2004; Miller-Jones et al. 2012; Yang et al. 2010; Rushton et al. 2017; Russell et al. 2019c; Miller-Jones et al. 2019; Bright et al. 2020; Carotenuto et al. 2021a). For some of them both the approaching and receding components have been detected, while for a large fraction of sources only one component (usually the approaching one, due to Doppler boosting) was observed. Examples of radio observations of discrete ejecta are shown in Figure 3.1. When the ejecta are not resolved in radio, this type of jet is also called *transient jet*. Discrete ejecta have been observed also in neutron star LMXBs (e.g. Sco X-1, Fomalont, Geldzahler, and Bradshaw 2001; Fender et al. 2006).

Observationally, after launch, the ejecta display a first phase of adiabatic expansion, producing strong radio flares and appearing to leave the system at constant, relativistic velocities. Throughout their evolution, the plasma bubbles emit synchrotron radiation at radio wavelengths and their optical depth decreases as the physical size increases (see Section 3.2.1 and van der Laan 1966; Fender and Bright 2019), up to displaying an optically thin spectrum, with a spectral index $\alpha \simeq -0.6$ (e.g. Corbel et al. 2002), where the radio flux density follows $S_\nu \propto \nu^\alpha$.

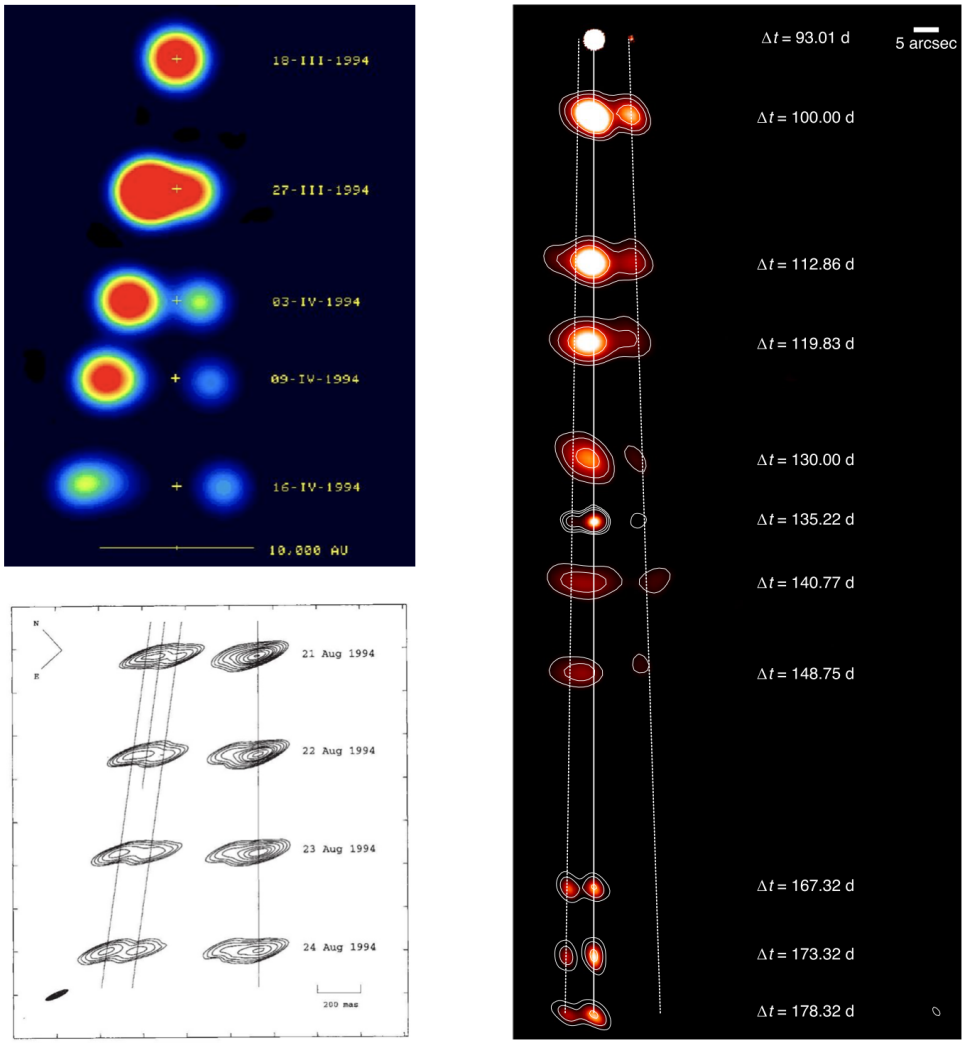

Figure 3.1: Examples of discrete ejecta from galactic BH LMXBs. *Top left:* The first superluminal jets ever observed from a BH LMXB (Mirabel and Rodríguez, 1994). The bipolar ejecta of GRS 1915+105 were observed with the VLA. *Bottom left:* VLBI observations of superluminal jets from GRO 1655–40 (Tingay et al., 1995). *Right:* Bipolar jets from MAXI J1820+070 observed with MeerKAT, VLA and the Multi-Element Radio Linked Interferometer Network (eMERLIN, Bright et al. 2020).

3.1.2 Proper motion

One of the most important observables of discrete ejecta is their proper motion, which can be measured and linked to the intrinsic properties of the jets (e.g. Fender 2006). We consider the simultaneous and symmetric ejection of a pair of twin plasma bubbles moving at velocity $\beta_{\rm obs}$ (projected on the plane of the sky, see Figure 3.2), which is linked to the observed proper motion by $\beta_{\rm obs} \sim \mu D$, where D is the source distance.

The apparent velocity is related to the intrinsic velocity $\beta_{\rm int}$ by

$$\beta_{\rm obs} = \frac{\beta_{\rm int} \sin\theta}{1 \mp \beta_{\rm int} \cos\theta} \tag{3.1}$$

where θ is the inclination angle of the jet axis and $\mp$ refer to the approaching and receding components, respectively (Mirabel and Rodríguez, 1994). From Equation 3.1, we can see that

in order to have apparent superluminal motion (i.e. $\beta_{\rm obs} > 1$), the emitting source needs to be moving with a mildly relativistic speed $\beta_{\rm int} \geq 0.7$ (Fender, 2006). This can also be seen from Figure 3.2,

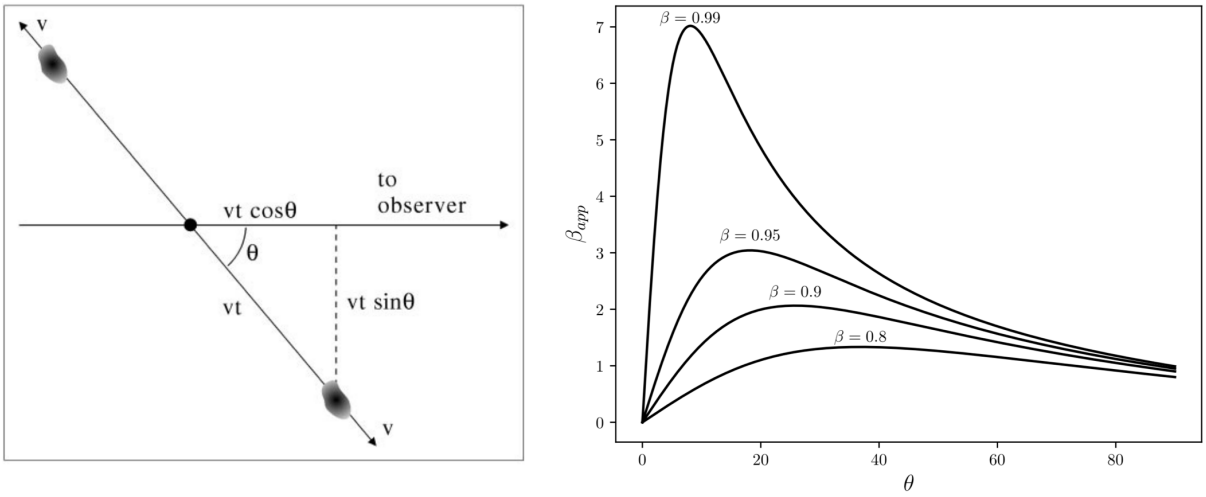

Figure 3.2: *Left*: Geometry of a symmetric double-sided ejection, with a velocity $v = \beta_{\rm int} c$ and an angle θ to the line of sight. Taken from Mirabel and Rodríguez (1999). *Right*: The apparent transverse velocity (called $\beta_{\rm app}$ in the plot) of a relativistic source as a function of the inclination angle θ, for different intrinsic velocities $\beta_{\rm int}$, taken from Bright (2020).

With the measurements of the proper motion $\mu_{\rm app}$ and $\mu_{\rm rec}$ of the approaching and receding components, the two different equations above can be re-arranged to obtain the following product:

$$\beta_{\rm int} \cos\theta = \frac{\mu_{\rm app} - \mu_{\rm rec}}{\mu_{\rm app} + \mu_{\rm rec}} \tag{3.2}$$

Hence, $\beta_{\rm int}$ can be obtained if a precise measurement of the inclination angle is available. This in turn can be determined for every source distance

$$\tan\theta = \frac{2D}{c}\left(\frac{\mu_{\rm app}\mu_{\rm rec}}{\mu_{\rm app} - \mu_{\rm rec}}\right) \tag{3.3}$$

given that the product $\beta_{\rm int} \cos\theta$ is already known (Mirabel and Rodríguez, 1999). If the distance is not known, an upper limit on it (corresponding to $\beta_{\rm int} = 1$) can be placed with the simple measurement of $\mu_{\rm app}$ and $\mu_{\rm rec}$

$$D_{\rm max} = \frac{c}{\sqrt{\mu_{\rm app}\mu_{\rm rec}}} \tag{3.4}$$

The $D_{\rm max}$ constraint can be of significant interest when a precise, model-independent distance measurement of a BH LMXB is not available. For example, in the case GRS 1915+105, the proper motion of the two ejecta $\mu_{\rm app} = 17.6 \pm 0.4$ mas and $\mu_{\rm rec} = 9.0 \pm 0.1$ mas (Mirabel and Rodríguez, 1994) allowed to derive an upper limit on the distance of $D \leq 13.7$ kpc, confirming the galactic nature of the source.

At a distance $D_{\rm max}$ one can also obtain the maximum angle of the jet to the line of sight (Fender, 2006):

$$\theta_{\rm max} = \cos^{-1}\frac{\mu_{\rm app} - \mu_{\rm rec}}{\mu_{\rm app} + \mu_{\rm rec}} \tag{3.5}$$

Since the motion of the ejecta is relativistic, Doppler beaming will play an important role in the emission received from these objects. In fact, objects moving at relativistic speeds have an observed surface brightness that is a factor $\delta^{k-\alpha}$ brighter (or fainter), where δ is the Doppler factor presented in Equation 2.4 and α is the spectral index of the jet emission. Here $2 < k < 3$, and in this context $k = 2$ is for continuous jets, as it corresponds to the average of multiple events, while $k = 3$ is for discrete ejecta, as it corresponds to emission produced by a single evolving source (e.g. Blandford, McKee, and Rees 1977). Hence, the flux ratio between the approaching and receding components can be written as

$$\frac{S_{\rm app}}{S_{\rm rec}} = \left(\frac{\delta_{\rm app}}{\delta_{\rm rec}}\right)^{k-\alpha} \tag{3.6}$$

It is important to note that, in order for Equation 3.6 to be valid, the fluxes of the two jets must be measured at the same angular separation from the core, to observe the two jets at the same time in their evolution. This is relevant because light travel time also plays a role in the observations of ejecta, and the two components will appear at the same angular separation at different times. In fact, for relativistic, symmetric jets, an observation will show the receding component at an earlier stage of its evolution with respect to the approaching jet (Fender, 2006). Due to this effect, at a given time the ratio between the observed travelled distances $l_{\rm app}$ and $l_{\rm rec}$ of the two jets will be

$$\frac{l_{\rm app}}{l_{\rm rec}} = \frac{1 + \beta_{\rm int}\cos\theta}{1 - \beta_{\rm int}\cos\theta} \tag{3.7}$$

Therefore, at the time of the observation, the approaching component will always appear to have travelled further from the core than the receding component.

Orientation

The orientation of the jet axis has generally been assumed to be perpendicular to the orbital plane of the system (and hence of the accretion disk). While this is expected to be the case for the majority of the systems, few cases of disk/jet misalignment have been reported. Significant misalignment has been found in V4641 Sgr and GRO J1655–40 (Maccarone, 2002), and possibly in MAXI J1820+070 (Poutanen et al., 2021). Such misalignment might be responsible for a certain degree of warping of the disk, referred to as the Bardeen-Petterson effect (Bardeen and Petterson, 1975). Precessing jets were found in the microquasar SS 433 (e.g. Eikenberry et al. 2001), and the jet precession period of $\sim$162 days was linked to the precession period of the accretion disk (Ogilvie and Dubus, 2001). Recently, Miller-Jones et al. (2019) found an exceptionally fast-changing jet orientation in the BH XRB V404 Cyg, with Very Long Baseline Interferometry radio observations (see Chapter 4). The jet inclination axis appeared to evolve on timescale of minutes and hours, while several discrete ejecta were launched in rapid succession (as reported in Tetarenko et al. 2017). Such evolution was tentatively linked to the precession of a slim inner disk that could be responsible for redirecting the jets at small scales (hundred of $R_{\rm g}$) through Lense–Thirring precession (Miller-Jones et al., 2019).

3.1.3 Composition

The composition of discrete ejecta is a long-standing open problem. So far, the observed synchrotron emission from jets in BH LMXBs is produced by their leptonic component, both electrons and/or positrons (Fender, 2006). Evidences for a baryonic content have been found

in the jets of a single source: SS 433, with the detection of Doppler-shifted iron line emission (Kotani et al., 1996; Migliari, Fender, and Méndez, 2002), and additional lines at lower frequencies. It is not clear at the moment why only SS 433 has such properties. Other jets have been detected in the X-rays (see Section 3.3.2), but displayed simple power law spectra without any feature, consistent with an extrapolation from radio to the X-rays of the jet synchrotron emission (Corbel et al., 2002; Corbel et al., 2005; Espinasse et al., 2020). Since these jets are relativistic, atomic emission lines could be almost impossible to detect due to strong Doppler broadening (Mirabel et al., 1997), or because the lines are Doppler-shifted too far in frequency to be identified, due to the largely unconstrained Lorentz factors of the ejecta (Fender, 2003). One possibility is that the baryonic component of the jets from SS 433 is due to mass-entrainment in the supernova remnant W50, and this might be consistent with the low bulk speed of the jet ($\simeq 0.26c$, Margon 1984) compared to other relativistic ejecta.

In this case, the preferred scenario would be that jets from XRBs are mainly of leptonic composition. But it is also possible that the potential baryonic component of jets (expected in case the ejection taps material from the accretion disk) does not contribute significantly to the observed emission. Hence, jets might essentially contain a population of "cold" protons that would carry most of the energy without radiating it. This question remains open, and more observations of ejecta are needed to constrain the jet physical properties and obtain insights on the jet composition (which is also unknown for jets from AGNs).

3.1.4 Production

Despite the progress made so far, the mechanism responsible for the jet launching has not yet been identified. In many systems, strong radio flares are observed to happen close to the transition between the hard and the soft state and are believed to be the signature of the ejection of transient jets (Corbel et al., 2004b; Fender, Belloni, and Gallo, 2004), even in the cases for which the presence of extended jets cannot be confirmed by imaging. Discrete ejections could originate within compact jets due to internal shocks produced by a change in the accretion flow and a subsequent sharp increase in the Lorentz factor (Kaiser, Sunyaev, and Spruit, 2000; Fender, Belloni, and Gallo, 2004). In alternative, the transient jet could be the result of the ejection of the coronal material at state transitions (Rodriguez, Corbel, and Tomsick, 2003; Vadawale et al., 2003), although this scenario could imply an abrupt change in the coronal spectral properties that is not observed. To make progress in this line of research, it is of first importance to accurately model the jet motion. With such models, we can precisely infer the jet ejection date and possibly identify, along with other observational features, the causal relation that leads to a discrete ejection, which will have important implications for the jet production mechanism. It was proposed that transient jets are associated with a change in the X-ray variability and with the presence of Type-B Quasi Periodic Oscillations (QPOs; Soleri, Belloni, and Casella 2008; Fender, Homan, and Belloni 2009). The moment of ejection and the observational signatures of an ejection that are currently known are discussed in the next section.

3.2 The ejection

I discuss in this section what is currently known on the ejection of these relativistic components. As mentioned above, studying the first phases of launch and evolution of discrete ejecta is crucial for the understanding on how jets are produced and accelerated.

3.2.1 Radio flaring

As already mentioned in Section 1.3.2, phases of strong synchrotron radio flaring are generally observed among BH LMXBs at the transition from the hard to the soft state (see Section 1.4.2 and 3.2.3), and there is convincing evidence that such flares are produced by the launch of discrete ejecta, that can sometimes be resolved from the core of the system and whose motion can be used to track down the moment of ejection (e.g. Fender, Belloni, and Gallo 2004; Tetarenko et al. 2017). What triggers the ejection is currently unknown, but is is likely that these flares are associated with dramatic changes in the properties of the accretion flow (Fender, 2006).

The temporal and spectral properties of these radio flares, and their evolution, provide insights on the physical conditions of the emitting region. Most of the flares observed from BH LMXBs (and not only) show a typical spectral evolution displaying an optically thick spectrum (spectral index $\alpha > 0$) during the rise phase, and a transition to an optically thin spectrum ($\alpha \lesssim -0.5$) in the decay phase, after the peak. Such evolution has been explained in the context of the first models for variable radio sources, like the "synchrotron bubble" model from van der Laan (1966). In the context of this model, the ejecta are considered as expanding plasma bubbles and the rising, optically thick, phase of the flare is produced by an increasing surface area, during which the optical depth continuously decreases at frequencies that are initially in a synchrotron self-absorbed regime (van der Laan, 1966; Hjellming and Johnston, 1988; Hjellming and Rupen, 1995; Tetarenko et al., 2017). Then, at a given frequency the light curve peaks when its corresponding optical depth reaches unity ($\tau \simeq 1$), and the decay phase results from adiabatic expansion losses that dominate in the optically thin regime.

Fully optically thin flares are also observed, and in this case the optical depth evolution of the synchrotron bubble model cannot explain the flare morphology. Such flares are believed to result from periods of short-term particles injection into an optically thin expanding plasma cloud (Fender, 2006), and the peak is reached when the injection ceases.

However, the full temporal and spectral coverage of these flaring periods is rather hard to achieve, and this is mostly due to the the unpredictability of state transitions during which radio flaring occurs and to the short timescales of these flares (especially the rising phase), which complicates the organization of observations.

3.2.2 Minimum associated energy

One of the most important physical measurements that is possible to obtain from the strong radio flares observed in X-ray binaries is an estimate of the minimum kinetic energy associated with the synchrotron flare, and consequently with the ejection (Burbidge, 1956; Pacholczyk, 1970). Remarkably, such estimation is possible even in the case (the majority) in which the radio emission is not spatially resolved and the ejecta are not followed in their motion. The basic assumption behind this estimation is that the energies in electrons and magnetic field inside the plasma bubble are comparable, so that the system is close to "equipartition" (Longair, 2011). If this condition is not satisfied in reality, nevertheless such estimation provides a lower limit on the energy.

A full derivation of the minimum energy calculation can be found in Longair (2011). From a single measurement of the synchrotron monochromatic luminosity L_ν at a given frequency ν and in a given volume V, we can compute the minimum energy required for the observed

synchrotron emission

$$E_{\rm min} \simeq 8 \times 10^6 \eta^{\frac{4}{7}} \left(\frac{V}{\rm cm^3}\right)^{\frac{3}{7}} \left(\frac{\nu}{\rm GHz}\right)^{\frac{2}{7}} \left(\frac{L_\nu}{\rm erg\ s^{-1}\ Hz^{-1}}\right)^{\frac{4}{7}} {\rm erg} \tag{3.8}$$

where $\eta = (1 + \hat{\beta})$ and $\hat{\beta} = \epsilon_{\rm p}/\epsilon_{\rm e}$ is the ratio of energy in protons to that in electrons. It is generally assumed that $\hat{\beta} \simeq 0$ and hence $\eta \simeq 1$. The volume of the emitting region is a key parameter in the above equation. In case the emission is spatially resolved, the size of the emitting region can be obtained directly. Alternatively, if the flaring source is not resolved (the majority of cases), an upper limit on its size can be obtained by $v\Delta t$, where v is the expansion speed of the plasma bubble and Δt the variability timescale of the radio light curve, estimated from the rising timescale of the flare. An absolute upper limit on the expansions speed is c, and hence a spherical expanding bubble will have a volume smaller than $V = (4/3)\pi(c\Delta t)^3$, and Equation 3.8 can be rewritten as

$$E_{\rm min} \simeq 3 \times 10^{33} \eta^{\frac{4}{7}} \left(\frac{\Delta t}{\rm s}\right)^{\frac{9}{7}} \left(\frac{\nu}{\rm GHz}\right)^{\frac{2}{7}} \left(\frac{S_\nu}{\rm mJy}\right)^{\frac{4}{7}} \left(\frac{D}{\rm kpc}\right)^{\frac{8}{7}} {\rm erg} \tag{3.9}$$

where S_ν is the flux density and D the source distance (Longair, 2011; Fender, 2006). However, from recent works it appears that discrete ejecta expand at speeds much lower than the speed of light (0.01–$0.1c$, Fender and Bright 2019). Typical values of minimum energy constraints for discrete ejecta range appproximately from 10^{39} to 10^{42} erg (e.g. Rushton et al. 2017; Russell et al. 2019c; Espinasse et al. 2020; Carotenuto et al. 2021a). I will discuss in Sections 3.3.1 and 8.3.4 why this is likely to be a large underestimation of the total energy contained in the ejecta. Using the variability timescale, the minimum average power of the ejection event is

$$P_{\rm min} = \frac{E_{\rm min}}{\Delta t} \simeq 3 \times 10^{33} \eta^{\frac{4}{7}} \left(\frac{\Delta t}{\rm s}\right)^{\frac{2}{7}} \left(\frac{\nu}{\rm GHz}\right)^{\frac{2}{7}} \left(\frac{S_\nu}{\rm mJy}\right)^{\frac{4}{7}} \left(\frac{D}{\rm kpc}\right)^{\frac{8}{7}} {\rm erg\ s^{-1}} \tag{3.10}$$

At equipartition conditions (Longair, 2011), the corresponding (and not minimum) magnetic field is

$$B_{\rm eq} \simeq 30 \eta^{\frac{2}{7}} \left(\frac{\Delta t}{\rm s}\right)^{-\frac{6}{7}} \left(\frac{\nu}{\rm GHz}\right)^{\frac{1}{7}} \left(\frac{S_\nu}{\rm mJy}\right)^{\frac{2}{7}} \left(\frac{D}{\rm kpc}\right)^{\frac{4}{7}} {\rm G} \tag{3.11}$$

and the individual Lorentz factor of the electrons emitting synchrotron radiation at a given frequency ν is:

$$\gamma_{\rm e} \simeq 30 \left(\frac{\nu}{\rm GHz}\right)^{\frac{1}{2}} \left(\frac{B_{\rm eq}}{\rm G}\right)^{-\frac{1}{2}} \tag{3.12}$$

Since discrete ejecta are moving at relativistic speeds, their Doppler factor δ is significantly different from 1. Hence the quantities mentioned above (such as the flux density, the frequency and the rising timescale of the flare), must be corrected from the observer's frame to the comoving frame of the ejecta in order to obtain a reliable estimation. Moreover, the kinetic energy associated to the ejecta bulk motion needs to be taken into account. Such energy can be written as

$$E_{\rm kin} = (\Gamma - 1) E_{\rm min} \tag{3.13}$$

where Γ is the bulk Lorentz factor of the ejecta. We note that for $\Gamma > 2$ such kinetic energy represents the dominant term in the total energy of the ejecta (Fender, 2006).

3.2.3 Ejection time and connection with X-ray variability

Constraining the time of ejection is fundamental to put the launch of discrete ejecta in context with the other multi-wavelength observational signatures and to have a comprehensive view of the source evolution during the state transition. In this context, modeling the jet motion is also of prime importance to precisely constrain the time of ejection (e.g. Miller-Jones et al. 2012; Russell et al. 2019c; Bright et al. 2020; Espinasse et al. 2020). The ejection time can already be roughly inferred from the radio flaring behaviour, which is the prominent signature of an ejection, but the unknown delay between the effective ejection and the subsequent flare, opacity effects, and the eventually sparse observational sampling, can limit the accuracy on the estimation of the ejection time (e.g. Russell et al. 2019c). Radio flares are usually observed at the transition between the hard and soft intermediate states (HIMS to SIMS) on the top branch of the HID (Corbel et al., 2004a; Fender, Belloni, and Gallo, 2004), but it is still not clear what triggers (and powers) the ejection and if there is a unique time-ordered combination of observational signatures associated with discrete ejections. The onset of the transient jet might be a direct consequence of the compact jet quenching in the HIMS (Russell et al., 2020), but other explanations are possible (e.g. Kaiser, Sunyaev, and Spruit 2000; Vadawale et al. 2003; Rodriguez, Corbel, and Tomsick 2003). A significant change in the X-ray emission properties is generally observed during the IMS, consisting of a sharp decrease in the fractional rms variability (e.g. Belloni et al. 2005) and the sudden appearance of Type-B Quasi Periodic Oscillations (QPOs, Soleri, Belloni, and Casella 2008 and see Ingram and Motta (2019) for a review on QPOs). While of unknown origin, Type-B QPOs seem to depend on the viewing angle, to be stronger in face-on systems (Motta et al., 2015), and to be detected close in time to jet ejections. Hence, it appears likely for them to be linked to the jet production, even though we still lack a physical model capable of explaining how they are generated. A physical connection would also be consistent with jet models that predict a jet contribution to the X-ray emission (Markoff, Falcke, and Fender, 2001; Markoff, Nowak, and Wilms, 2005). Detailed studies of X-ray variability and radio flares in many sources, including XTE J1550−564, GX 339−4, XTE J1859+226, H1743−322 and MAXI J1535−571 did not lead to a firm conclusion on whether such connection exists and it is universal among BH LMXBs (Fender, Homan, and Belloni, 2009; Miller-Jones et al., 2012; Russell et al., 2019c; Wood et al., 2021; Zhang et al., 2021).

A particularly interesting case has been recently presented for MAXI J1820+070 in Homan et al. (2020), with simultaneous radio and X-ray observations performed with the Neutron Star Interior Composition Explorer (NICER) and the Arcminute Microkelvin Imager Large Array (AMI-LA) during the rapid hard-to-soft state transition in the 2018 outburst of the BH LMXB MAXI J1820+070. During the transition, QPOs were detected, and in particular it was obseved a switch from Type-C to Type-B QPOs simultaneously with a drop in the X-ray variability, just $\sim$2 hours before the detection of a strong radio flare produced by the launch of discrete ejecta (Bright et al., 2020). The beginning of the radio flare was inferred from an accurate fitting of the radio light curve including the baseline emission and the rising and decay phases of the radio flare. The AMI-LA light curve of MAXI J1820+070 from Homan et al. (2020) is shown in Figure 3.3, along with the times of the detections of Type-B QPOs. While, as mentioned above, results for other BH XRBs do not appear to support this claim, these observations are today the strongest observational evidence for a connection between the discrete ejections and Type-B QPOs (Homan et al., 2020).

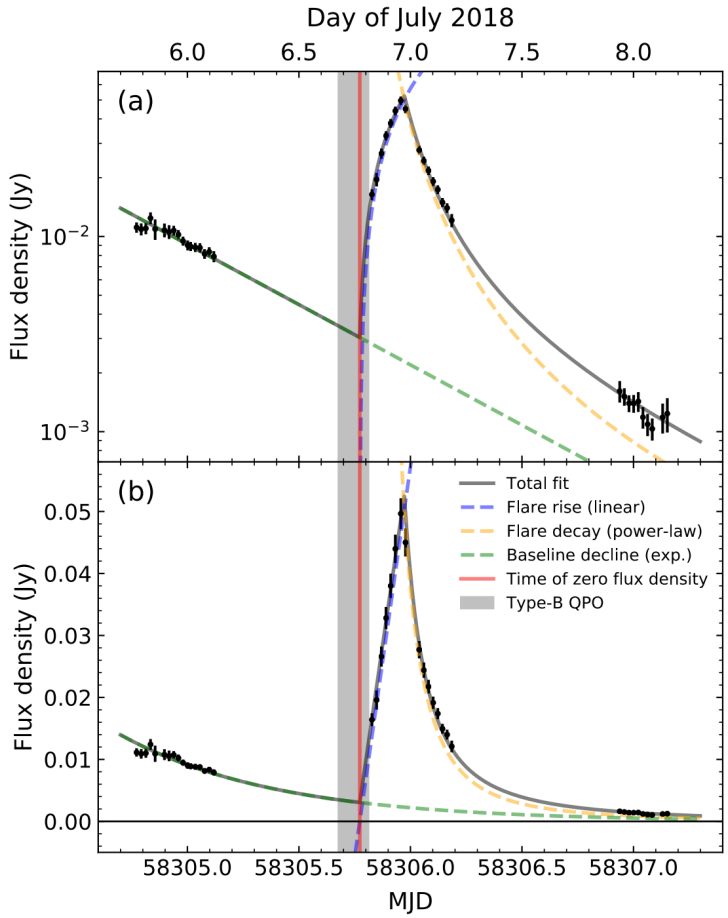

Figure 3.3: AMI-LA radio light curve (15.5 GHz) of MAXI J1820+070 (black dots) from Bright et al. (2020). this plot compares the inferred ejection date of the jets from MAXI J1820+070 with the appearance of Type-B QPOs observed with NICER. The gray shaded areas mark the times in which Type-B QPOs were detected. To infer the start of the radio flare, the radio data were fitted with a model for the whole light curve, including the baseline decay and the rise and decay phases of the flare. The scale on the y-axis is different between the two panels, which show the same data.

3.3 Interaction with the interstellar medium

As mentioned in the previous section, discrete ejecta produce strong radio flares at their launch and emit synchrotron radiation as they adiabatically expand and travel away from the central black hole (e.g. Corbel et al. 2002). After a first phase of usually ballistic motion, in some cases these components can travel unseen for months to years, before being detected again at large (parsecs) scales, with the emission coming from their interaction with the surrounding ISM, which causes the jets to strongly decelerate.

Studying the jet/ISM interaction is fundamental, as it is a unique way to obtain physical information on the properties of the jets that are not accessible otherwise. I discuss in this section what is currently known on the jet deceleration in the ISM and on why it is useful to observe them at late times. Moreover, I discuss the detection at high energies of these components and the feedback that these jets can have on the environment surrounding BH LMXBs.

For the sake of completeness, jet/ISM interaction has been found also in sources that display persistent jets at parsec scales, that take the form of extended hot-spots and radio lobes, such as GRS 1758–258, 1E 1740.7–2942 (Mirabel et al., 1992; Martí et al., 2002), or extended X-ray

jets in 4U 1755–33 (Angelini and White, 2003; Kaaret et al., 2006).

3.3.1 Decelerating jets

While all discrete ejecta decelerate at some point, for most of them their motion has only been partially observed, with observations focusing on the initial phase after the ejection, in which we usually resolve at small scales (i.e. close to the BH) the ejecta travelling at constant speeds. But after this first phase, jets may travel unseen for years after the outburst in which they were ejected, before being revealed through the interaction with the ambient medium. Such interaction causes the jets to strongly decelerate and produces broadband (from radio to X-rays) synchrotron radiation from *in-situ* particle acceleration, up to TeV energies (see Section 3.3.2, e.g. Corbel et al. 2002; Espinasse et al. 2020). An example of decelerating ejecta from XTE J1550−564 (Migliori et al., 2017) is shown in Figure 3.4.

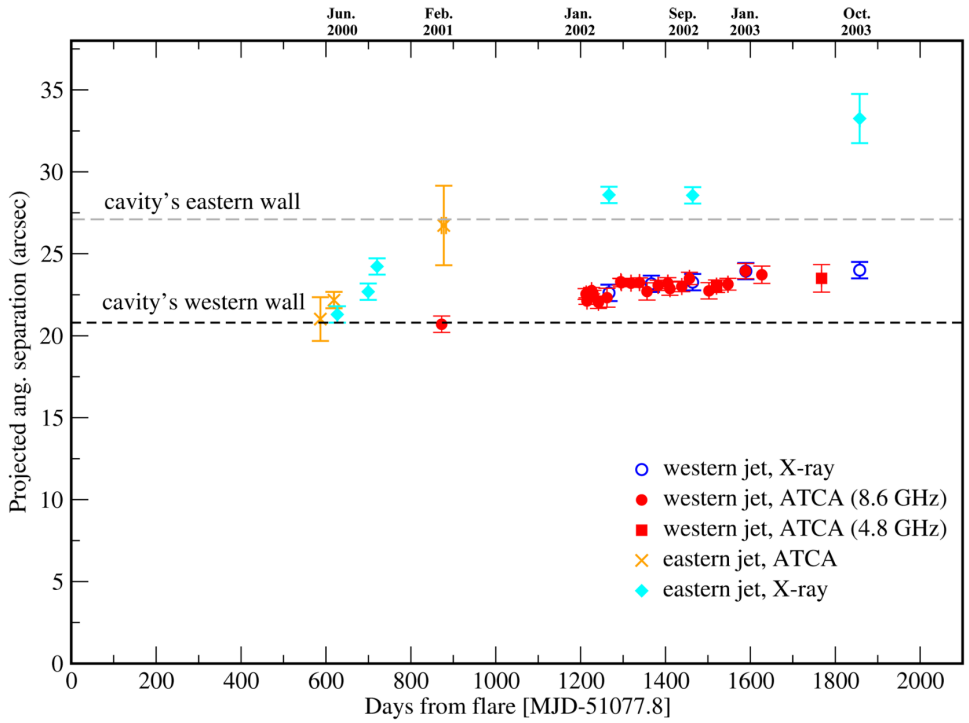

Figure 3.4: Angular separation of the decelerating bipolar discrete ejecta jet from the BH LMXB XTE J1550–564 as a function of time, from Migliori et al. (2017). The horizontal dashed lines mark the borders of the low-density ISM cavity as obtained by Steiner and McClintock (2012).

Decelerating discrete ejecta at large scales have been so far only detected in a handful of sources (Tomsick et al., 2003; Kaaret et al., 2003; Corbel et al., 2005; Miller-Jones et al., 2007; Yang et al., 2010; Miller-Jones et al., 2011b; Russell et al., 2019c; Espinasse et al., 2020; Carotenuto et al., 2021a). However, following the jet deceleration phase is turning out to be particularly important to improve our understanding of their production, energetics, dynamics and impact on the surrounding environment. Covering the last phase of the jets evolution allows us to obtain a complete picture of their motion, and this in turn enables us to fully model their evolution with physical models (e.g. Steiner and McClintock 2012). This is particularly useful for estimating the jet initial energy, which is a key parameter in this context, as today the total energy budget of these jets is unknown. I discussed in Section 3.2.2 how constraints on the

minimum energy can be obtained by considering the synchrotron emission at the initial radio flares (Longair, 2011; Fender and Bright, 2019). However, such estimates (often between 10^{39} and 10^{42} erg) are likely to largely underestimate the total energy content of the jet (Steiner and McClintock, 2012; Bright et al., 2020). In addition, there is large uncertainty on the jet matter content (see Section 3.1.3, e.g. Romero et al. 2017), and the knowledge of the jet mass and energy can be particularly useful for understanding the jet composition.

The jet deceleration also encodes information on the environment surrounding the black hole, including the presence of under-dense ISM cavities possibly produced by previous activity of the system. Such cavities were inferred to exist for the majority of BH LMXBs (Heinz, 2002; Hao and Zhang, 2009) and their borders are assumed to be sites of significant jet/ISM interaction. Under several assumptions, modeling the jet motion can allow us to obtain hints on the local density and on the cavity geometry, as done for XTE J1550–564 (Steiner and McClintock, 2012) and H1743−322 (Hao and Zhang, 2009; Steiner, McClintock, and Reid, 2012). Since it is not known *a priori* when the jet will start its deceleration phase, a complete coverage of its motion requires dense and uniform radio monitoring campaigns, with a constant (∼weekly) cadence and on timescales of months to years (e.g. Migliori et al. 2017; Bright et al. 2020).

3.3.2 X-ray detections

Emission from discrete ejecta launched by BH LMXBs has been detected at large scales not only in radio, but also in X-rays. This has been possible thanks to the extraordinary sub-arc second resolution of the *Chandra* X-ray observatory, along with its high sensitivity. Over the past two decades, *Chandra* observations allowed the detection of X-ray jets in several BH LMXB, namely XTE J1550−564, H1743−322 and MAXI J1820+070 (Corbel et al., 2002; Tomsick et al., 2003; Corbel et al., 2005; Migliori et al., 2017; Espinasse et al., 2020). An example of discrete ejecta detected in the X-rays is shown in the left panel of Figure 3.5.

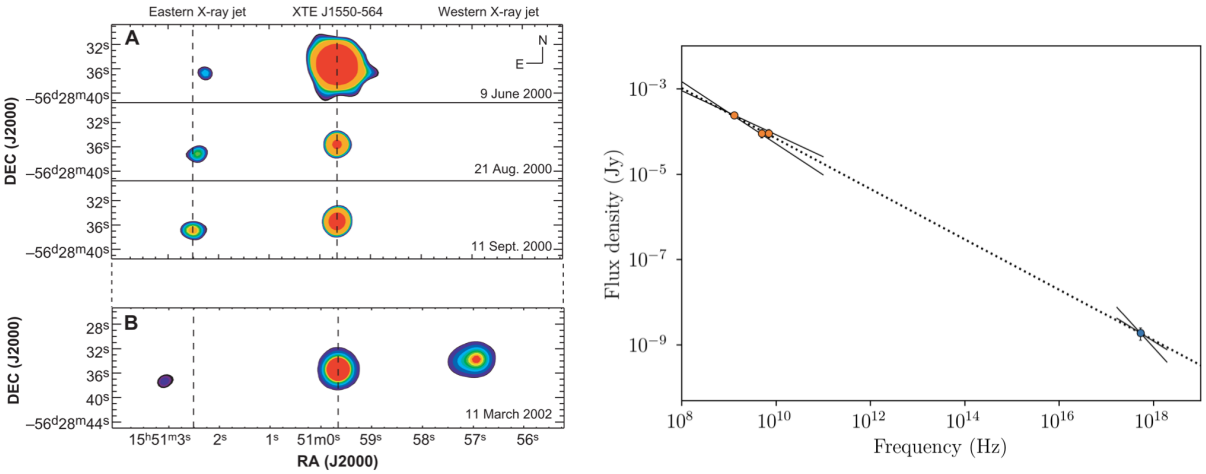

Figure 3.5: *Left: Chandra* 0.3–8 keV detections of the BH XRB XTE J1550−564 with the presence of the core and of decelerating bipolar ejecta, from Corbel et al. (2002). *Right:* Radio to X-ray spectral energy distribution (SED) of the discrete ejecta from MAXI J1820+070 launched in 2018, from Espinasse et al. (2020). The emission is consistent with synchrotron radiation from radio to X-rays, and a power law fit to the whole spectrum is shown as a dashed line. The full lines represent the uncertainties on the spectral indices obtained by fitting each wavelength domain alone.

In all cases, the X-ray spectrum was featureless and could be fitted with a single power law with index $\simeq -0.6$. Such a spectrum is fully consistent with an extrapolation of the radio emission to the soft X-rays, pointing to a scenario in which the broadband ejecta emission is synchrotron radiation from high energy particles (Corbel et al., 2002). An example of the jet's broadband spectrum is shown in the right panel of Figure 3.5. Detecting synchrotron radiation in the X-rays implies that, under the equipartition assumption, the particles responsible for the emission are accelerated to extremely large Lorentz factors, up to $\gamma_e \sim 10^7$, corresponding to an energy of $\sim$10 TeV (Corbel et al., 2002; Tomsick et al., 2003; Espinasse et al., 2020). The detection of X-ray synchrotron emission implies that BH XRB can accelerate electrons up to extremely high energies, and it also implies the presence of a mechanism capable of efficiently accelerate those particles at large distances from the black hole.

Acceleration in shocks is the most plausible explanation for the energies required to produce the observed radiation. External shocks are produced when the ejecta move at relativistic speeds and interact with the ISM, which also causes the jets to decelerate, converting bulk kinetic energy into internal energy. Inhomogeneities in the ISM, such as the presence of cavities (Hao and Zhang, 2009) or overdensities, might explain the detection of the approaching and receding components at different distances from the core (Hao and Zhang, 2009; Steiner and McClintock, 2012; Migliori et al., 2017). Alternatively, internal shocks between subsequent shells of plasma ejected at slightly different speeds might explain the ejecta re-brightening at large scales (Kaiser, Sunyaev, and Spruit, 2000; Jamil, Fender, and Kaiser, 2010; Malzac, 2013).

Interestingly, a jet tail was observed in the discrete ejecta launched by XTE J1550−564 (Corbel et al., 2002; Migliori et al., 2017). The jet was spatially resolved, and appeared to be expanding backwards along the direction of propagation, with an apparent velocity of $\sim -0.1c$. Such tail could be originated from the plasma of the jet itself, and its X-ray emission might be produced by particles accelerated in reverse shocks (Wang, Dai, and Lu, 2003; Hao and Zhang, 2009). In this context, a receding tail could be the signature of shock moving backwards through the jet plasma layers (Migliori et al., 2017).

3.3.3 Jet feedback

As the jets decelerate in the ISM, they transfer large amounts of energy and matter into their surrounding environment, and thus they represent an important source of feedback. Most jets BH LMXBs are thought to propagate in low density and low pressure environments (Heinz, 2002), possibly carved out by the activity of the jet itself (e.g. Hao and Zhang 2009). Jet-blown lobes in the interaction region can be inflated from sources with low peculiar velocities (Miller-Jones et al., 2008), while trails of radio plasma can be produced by sources with high peculiar velocities ($\sim$100 km s^{-1}, Heinz et al. 2008). In addition to possibly carving out under-dense cavities and thus shaping the ISM distribution, it is speculated that jets from galactic XRBs could inject roughly 1% average supernovae luminosity into the environment (Fender, Maccarone, and van Kesteren, 2005), heating and shocking the surrounding ISM. Their feedback might be so important that they could effectively stimulate star formation (Mirabel et al., 2015).

Important information on the jet properties, as for instance the total jet power, speed, and composition can be inferred from the characteristics of the jet/ISM interaction sites (e.g. Heinz 2006). As an example, the total time-averaged power of the compact jets of Cyg X-1, between 10^{36} and 10^{37} erg s^{-1}, has been estimated by Gallo et al. (2005) using the observed jet-blown cavity as a calorimeter and modelling the emission from the shocked gas.

However, the identification of such jet/ISM interaction sites is rather difficult at present, and so far we have only a few cases where jet/ISM interaction has been directly observed. Tracking the ejecta motion and looking for evidence of deceleration can be a way to identify systems that are possibly embedded in cavities, which are promising jet-ISM interaction sites. Moreover, the jet feedback on the ISM can be studied and characterized at higher frequencies, as the altered local chemistry and the distribution of excited gas can be probed through the observation and mapping of molecular line emission, as for instance recently done with ALMA in the sub-mm band for GRS 1915+105 (Tetarenko et al., 2018a), GRS 1758–258 and 1E 1740.7–2942 (Tetarenko et al. 2020a, although these two sources display persistent jets). To illustrate what has been possible to achieve in the recent years concerning the jet/ISM interaction sites, I briefly discuss here the ALMA observations performed by Tetarenko et al. (2018a) of the regions IRAS 19132+1035 and IRAS 19132+1035, that were first identified by Mirabel et al. (1998) and studied by Chaty et al. (2001) as potential sites for the interaction between the ejecta from GRS 1915+105 and the ISM. Such potential identification was based on the location of the region on the direction on the jet's axis and on the source morphology, which is shown in Figure 3.6. In a model proposed by Kaiser et al. (2004), IRAS 19132+1035 is composed of shock-heated ISM material close to the jet impact zone. Despite several observing campaigns, there is today no consensus on whether these emission regions are effectively associated with the jets of GRS 1915+105.

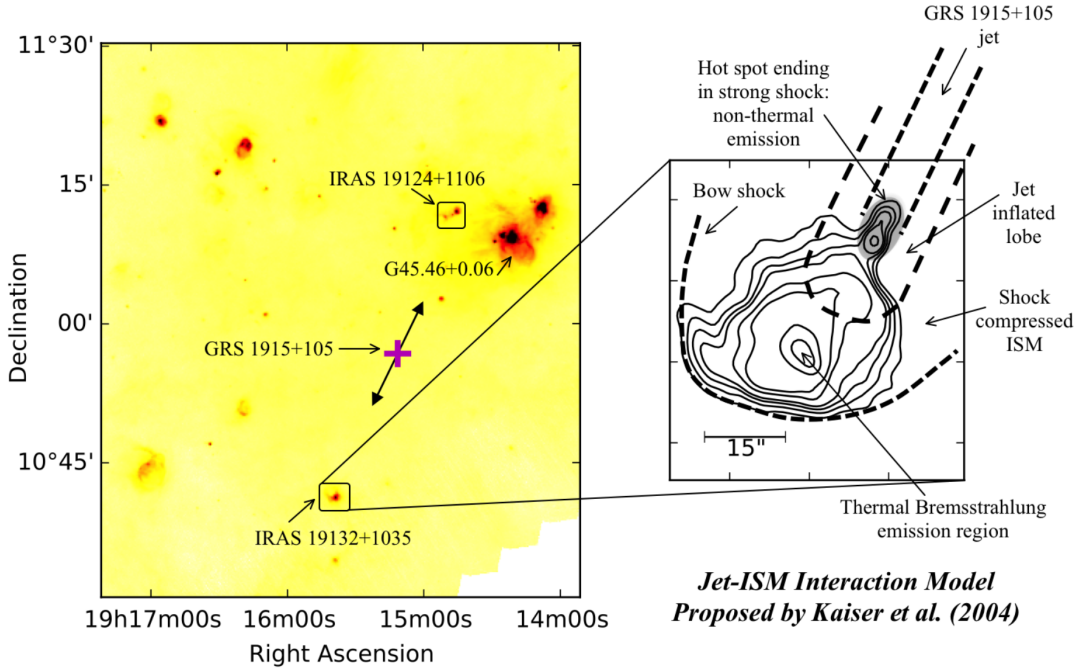

Figure 3.6: A map of the region surrounding GRS 1915+105, taken with the *Herschel* PACS instrument at 70 μm, from Tetarenko et al. (2018a). This map includes GRS 1915+105 and the two candidate jet/ISM interaction zones IRAS 19132+1035 and IRAS 19124+1106 (Mirabel et al., 1998). The inset on the right shows the VLA radio continuum map of IRAS 19132+1035 in the 4-8 GHz band, with contour levels between 0.2 and 3 mJy beam^{-1}. A schematic model of the jet/ISM interaction from Kaiser et al. (2004) is overlaid. Dashed lines mark features of the model which are not observed in the radio image.

New evidence supporting this connection were found with ALMA observations of molecular line emission. For instance, CO line emission tracks the location of most of the molecular gas, and, in the ALMA observations, the regions with highest CO column densities were found

to surround the low frequency radio emission, possibly tracing the borders of a jet-inflated cavity. Moreover, a gas over-density was found with CO line ratios at the suspected jet impact zone, and CO lines showed double peaked profiles, consistent with the presence of multiple gas components with different velocities, possibly resulting from a collision between the jet and the ISM in this region (Tetarenko et al., 2018a). Tracing molecular line emission appears to be a new interesting way of identifying and studying jet/ISM interaction sites, and such observables can provide important hints of the physical properties of the jet and of the ISM surrounding BH LMXBs.

Chapter 4

Instruments and data analysis

Contents

4.1 Radio-interferometry 60
4.1.1 Aperture synthesis 60
4.1.2 Calibration 62
4.1.3 Imaging and deconvolution 63
4.2 Radio-interferometers 65
4.2.1 MeerKAT 65
4.2.2 ATCA 67
4.3 X-ray observatories 67
4.3.1 *Swift* 68
4.3.2 MAXI 69
4.4 Statistical techniques 70
4.4.1 Bayesian statistics 70
4.4.2 The MCMC technique 72

The enormous progress achieved in the last decades in the understanding of XRBs has been possible so far thanks to the constantly-improving multi-wavelength observations. As discussed in the previous chapters, two fundamental electromagnetic bands for the study of XRBs are the radio and the X-ray ones, in which we have most of the emission coming from, respectively, the jets and the accretion disk. Therefore, most of our work consisted in conducting observations in radio and X-rays. In this Chapter I will present the concepts, the instruments and the data analysis tools that allowed us to obtain the results presented in the following chapters. In the first part, I outline the technique of radio-interferometry and aperture synthesis, discussing its basics, the calibration of the data, and the imaging part, as long as presenting the MeerKAT and ATCA interferometers used in our work. Then, I discuss the two X-ray observatories *Swift*/XRT and MAXI/GSC used in our monitoring programs. The last part of the chapter is dedicated to

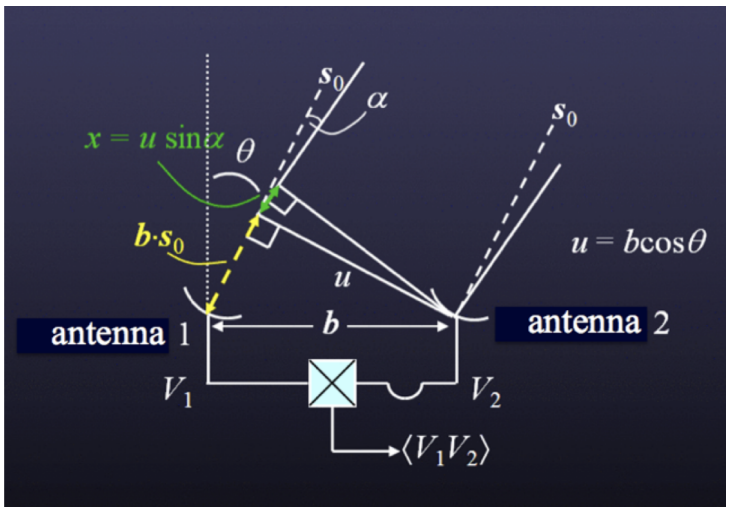

Figure 4.1: Illustrative scheme of a two-antenna interferometer, from Remijan et al. (2019). The two antennas are at a distance b and point at a sky position s_0, at an angle θ with respect to the zenit. The signals from both antennas are sent to the correlator which combines them to provide a *visibility* measurement

Bayesian statistics and Monte-Carlo Markov Chains, which are at the basis of the work on the modeling of the jet motion presented in Chapter 8.

4.1 Radio-interferometry

The resolution $\theta_{\rm min}$ of a single-dish telescope observing at a wavelength λ is limited by diffraction at $\theta_{\rm min} \simeq \lambda/D$, where D is the telescope's reflector diameter. Such resolution, corresponding to ∼arcminutes at low radio frequencies for the largest telescopes in the world, would not allow to resolve jets from XRBs. To obtain a much higher angular resolution images in radio, it is possible to combine signals from physically separated antennas scattered around a larger area (even at the global level) through interferometry. This powerful technique, called *aperture synthesis*, makes it possible to achieve a resolution which would correspond to that of a radio telescope with an extremely large diameter. For its invention, the 1974 Nobel Prize in Physics was partly awarded to Sir Martin Ryle. I present the basics of aperture synthesis in the next section, mostly following the complete treatment of Remijan et al. (2019), while other important resources for this topic are Wilson, Rohlfs, and Hüttemeister (2009) and Condon and Ransom (2016).

4.1.1 Aperture synthesis

To introduce the principle behind aperture synthesis, I first briefly discuss the example of a two-antenna interferometer, with the two components located at a distance D (or $b = D/\lambda$ in wavelength units) and part of a so-called *baseline*. A scheme of this simple interferometer is shown in Figure 4.1. The two antennas point to a position s_0 in the sky, at an angle θ from the zenith. The projected separation of the two antennas from the point of view of the source at s_0 is $u = b\cos\theta$. The geometrical delay $b\sin\theta$ that the emission from the source experiences between antenna 1 and 2 can be compensated electronically by inserting an artificial delay $\tau = b \cdot s_0/c$ in the signal path of antenna 2, so that both signals have the same phase when are

correlated afterwards. Aperture synthesis is possible only if both the amplitude and phase of an incoming signal are measured by each antenna, which, with the current electronics, is only achievable at radio/mm frequencies.

For off-axis positions, namely at a small angle α from s_0, we can use the direction cosine $l = \sin\alpha$. Here, in addition to the geometrical delay discussed above, the emission has to travel a longer path with respect to the on-axis position, which can be written as $x = u\sin\alpha = ul$ in wavelength units. Depending sinusoidally on the angle α, fringes will be produced as a result of the correlation and subsequent interference of the two incoming signals. Extending to two dimensions (with v and m corresponding, respectively, to u and l for the new dimension), the voltage measured on antenna 2 V_2 can be expressed as a function of the voltage of antenna 1 V_1 and a phase delay factor depending on the direction the sky

$$V_2 = V_1 e^{2\pi i(ul+vm)} \tag{4.1}$$

Here u and v are the projected antenna separations from the point of view of the source at the time of observing, but they can also be considered as spatial frequencies of the sinusoidal variation of V_2 with respect to V_1. The two signals are then sent to the *correlator*, which multiplies and averages them in time (to remove incoherent signals from different sky directions). Considering the whole sky, we integrate over all the (l, m) directions, and we can express the output of the correlator as

$$\langle V_1 V_2\rangle = \mathcal{V}(u,v) = \iint I(l,m) e^{2\pi i(ul+vm)} dl dm \tag{4.2}$$

where $I(l, m)$ is the intensity distribution of the sky, since $V^2 \propto P \propto I_\nu$, and where $\mathcal{V}(u, v)$ is called *complex visibility*, which is the two-dimensional Fourier transform of the sky brightness distribution in the image plane. Therefore, Equation 4.2 can be inverted, and hence the sky intensity distribution is the inverse Fourier transform of the visibility distribution

$$I(l,m) = \iint \mathcal{V}(u,v) e^{-2\pi i(ul+vm)} du dv \tag{4.3}$$

This fundamental relation is also known as the *van Cittert-Zernike theorem* and it is the core of aperture synthesis. This means that we can recover the sky brightness distribution, which is our goal, by measuring the complex visibilities $\mathcal{V}(u, v)$ in the conjugate plane, called also u-v *plane*, with every sample of $\mathcal{V}(u, v)$, corresponding to each baseline or antenna pair, which contains information on the spatial frequencies u and v across the whole image. $\mathcal{V}(u, v)$ is complex, and its amplitude is linked to the source brightness at the spatial frequencies u and v, while its phase is related to the location of the source with respect to the phase center ($l = 0, m = 0$). The fidelity of the reconstructed image depends on the goodness of the coverage of all the relevant spatial frequencies in the u-v plane. To maximize the coverage, one needs to have the largest possible number of antennas distributed in order to avoid baseline redundancy: a well-designed radio-interferometer array of N antennas has $N(N-1)/2$ independent baselines, each sampling a point (and its complex conjugate) in the u-v plane. Moreover, since in this context what matters is the projected baseline, one can use Earth's rotation to observe the same target over a longer period of time, so that, with respect to the target position, each baseline will have different projected distances, sampling multiple points in the u-v plane.

The resolution of the image will depend on the highest spatial frequency sampled, which corresponds to the longest baseline in the array, as follows

$$\theta_{\min} \simeq \frac{\lambda}{D_{\max}} \tag{4.4}$$

where the exact value depends on the weighting scheme chosen for the different visibilities in the u-v plane during the imaging process (discussed in the following). Since the antennas do not need to be physically close for their signals to be correlated effectively, it is possible to create arrays with baselines spanning from several meters up to tens or hundreds of km, allowing to achieve extremely good angular resolutions, down to the arcsec level for standard interferometers in the radio band, or even mas level for the so-called Very Long Baseline Radio Interferometry (VLBI), in which the antennas are not part of the same instrument and their signals are not correlated in real time, but *a-posteriori*. The best angular resolution ever achieved in astronomy was also obtained with VLBI, in particular by the Event Horizon Telescope, which observed M87* (shown in Figure 1.1) at 230 GHz with a combination of antennas scattered around the whole planet and a longest baseline of $\sim$10000 km (e.g. Event Horizon Telescope Collaboration et al. 2019).

On the other hand, it is not possible to sample spatial frequencies smaller than the shortest baseline, and this results in low sensitivity to diffuse emission at large scales, which can be completely "resolved out" in some cases. So, we can conclude that the incomplete sampling of the u-v plane results in the spatial filtering of the real sky brightness distribution, and a drawback of this powerful method, which allows such a high angular resolution, is that it is completely blind to the un-sampled sky spatial frequencies. This implies that interferometry is most effective for compact sources, which are characterized by a constant emission at all angular scales.

4.1.2 Calibration

When observing with radio interferometers, data calibration is an essential step required for a proper reconstruction of the true sky brightness. All the sources of noise in the measurements (except for radio frequency interference, RFI) are expected to provide a contribution to the visibilities that should combine linearly with the true value, so that (neglecting additive stochastic terms) the measured visibility $\mathcal{V}^{\rm obs}$ for the baseline ij can be written as

$$\mathcal{V}_{ij}^{\rm obs}(t) = G_{ij}(t)\mathcal{V}_{ij}(t) = g_i(t)g_j^*(t)\mathcal{V}_{ij}(t) \tag{4.5}$$

where the proportionality factor $G_{ij}(t)$ is called the complex *gain* for the ij-th baseline, and can be separated in the gains of the individual antennas $g(t)$. The gain of each antenna can be expressed as

$$g(t) = G_0(t)B_0(\nu)e^{2\pi i\tau(t)(\nu-\nu_0)} \tag{4.6}$$

where the function $G_0(t)$ models the time variability of the gain during the observation, which is mostly due to the atmosphere and does not depend on the frequency. $B_0(\nu)$ models instead the different response in frequency of the antenna, which is instrumental and it is supposed to vary on timescales much larger than the typical observing time. In addition, $\tau(t)$ is a factor for the delay between the time at which the signal is received by the antenna and the time at which it is received by another antenna chosen as reference. Such delay is computed at a reference frequency ν_0 and its variations are of instrumental and atmospheric origin.

Calibration sources

The goal of the calibration process is to measure and constrain the individual antenna gain functions from the observations of reference sources. During a typical observation, two calibrations sources are observed. The first one, called *primary calibrator*, is a stable, bright and compact source, such as a radio-galaxy, for which the flux and spectrum are well known and characterised over the years. This source is observed at beginning or at the end of each observing session in order to obtain the $B_0(\nu)$ gain and the absolute flux scaling. The second source is called *secondary* or *phase calibrator* and it is used to measure the gain variations throughout the whole observation. It is usually another stable (on short timescales) and bright compact source, which has to be located close to the target in the sky in order for its emission to travel through the same atmosphere as the target, but for which a detailed knowledge of the intrinsic flux density is not required. During a typical observation, short (1–2 min) observations of the phase calibrator are interleaved with longer target scans (10–20 min), and the whole cycle is repeated multiple times in order to obtain enough gain corrections for the whole observation. The gain solutions obtained for the phase calibrator are interpolated to obtain corrections for the target, which are then applied as calibration tables to the raw data.

Self-calibration

We stress that for a standard calibration procedure, it is possible to calibrate individually each antenna, hence the problem of determining the gains $g(t)$ for N antennas is largely over-constrained, given the fact that we have $N(N-1)/2$ visibility samples of the calibrator source at every time step and at each frequency. Even after the initial calibration using the two aforementioned calibrator sources, it is still possible to have residual phase or amplitude errors in the data. If the target is sufficiently bright, an additional calibration procedure, called *self-calibration* might be applied. This consists of the use of a model obtained from the target itself to obtain more accurate time-dependent corrections of the complex antenna gains. However, a detailed discussion of this topic is beyond the scope of this thesis. A much more complete discussion of self-calibration can be found, for instance, in Brogan, Hunter, and Fomalont (2018).

4.1.3 Imaging and deconvolution

After calibration, the following step is to perform the inverse Fourier transform of the data, following Equation 4.3. However, the incomplete sampling of the visibility plane needs to be taken into account. For M samples in the u-v plane, we can define a sampling function as a sum of $2M$ Dirac delta functions

$$S(u,v) = \sum_{k=1}^{2M} \delta(u-u_k, v-v_k) \tag{4.7}$$

Moreover, since the antennas have a finite diameter, the field of view of the instrument must be considered, and the Airy function $\mathcal{A}(l,m)$, also called *primary beam*, must be also included in the double integral of Equation 4.2.

Hence, Equation 4.3 then becomes

$$I^{\mathrm{D}}(l,m) = FT^{-1}\{S(u,v)\mathcal{V}(u,v)\} \tag{4.8}$$

where $S(u,v)$ and $\mathcal{V}(u,v)$ are convoluted in the Fourier transform. Since the Fourier transform of a convolution of two functions is the product of the Fourier Transforms of those functions, we can rewrite Equation 4.8 as

$$I^{\mathrm{D}}(l,m) = b(l,m) * I(l,m)\mathcal{A}(l,m) \tag{4.9}$$

where $b(l,m) = FT^{-1}\{S(u,v)\}$ is the point spread function (PSF) of the instrument, also called *synthesized beam*, and its size can be obtained from Equation 4.4. The resulting image $I^{\mathrm{D}}(l,m)$ is called *dirty image* and, since it is obtained through an incomplete sampling of the u-v plane and it is still convoluted with the instrument's PSF, it can be affected by significant artifacts and might not be ready for scientific use. To improve its quality, many deconvolution algorithms have been developed through the years, and one of the most important is the CLEAN algorithm (Högbom, 1974), which is optimized for small field-of-view interferometers and fields dominated by point sources. We used it for the deconvolution of our ATCA observations as part the Common Astronomy Software Applications (CASA, McMullin et al. 2007) package (see Section 5.2.2 and the following chapters), and I briefly outline its procedure here. The algorithm considers the dirty image as an ensemble of point sources. It identifies the highest peak in the image and subtracts iteratively a small fraction of it, convoluted with the PSF, until a pre-defined threshold is reached. Then the removed components are convoluted with a gaussian elliptical beam and added back to the "cleaned" image , creating the so-called *restored image*.

Weighting

A very important factor governing the result of imaging process is the weighting scheme applied to the the visibilities in the u-v plane. This weighting can be used to correct for differences in the density of sampling in different region of the u-v plane, which is common for interferometers. By applying different weighting schemes, it is possible to obtain very different restored images by playing on the relative importance of short and long baselines, depending if the goal is the minimization of the PSF sidelobes or the image sensitivity. A first weighting scheme, called *natural*, assigns constant weights to all visibilities, providing the best point-source sensitivity, but the worst angular resolution as the sidelobe levels are usually high. On the other hand, the *uniform* weighting assigns a weight inversely proportional to the u-v plane sampling density, boosting the contribution of the long baselines, minimizing the sidelobe levels and thus providing the best possible angular resolution (but with poorer sensitivity). A trade-off between the boosting of resolution and sensitivity was achieved by Briggs (1995), who defined a continuous weighting scheme that depends on the *robustness* parameter R. In this context $R = 0$ is exactly in the middle between natural and uniform weighting, while the extremes $R = 2$ and $R = -2$ are close, respectively, to the natural and uniform weighting schemes.

Source fitting

Once the imaging process is completed, the properties of the source, if detected, have to be determined. For most of our observations, the source studied was point-like or presented multiple components (compact jets and discrete ejecta from XRBs, see Chapters 2, 3, 5 and 7). Since the restored, deconvolved image for each observation is composed of Dirac functions convolved with gaussians, to obtain the flux density and the coordinates of each source, we fit elliptical gaussians in the image plane with the CASA task `imfit`. When the source was not

resolved, we fit a single gaussian with the size of the synthetized beam, while when the source was resolved and extended, possibly due to the presence of compact jets and discrete ejecta, we fit simultaneously multiple components in the image to obtain their fluxes and positions.

Advanced tools

The calibration process and the imaging steps outlined in the previous sections are, however, not completely adequate for the current and future state-of-the-art instruments. The new generation of radio interferometers (such as the precursors of the Square Kilometre Array or the upcoming upgrade of the Very Large Array) are characterized by large fields of view and large fractional bandwidth, as well as being much more sensitive than before.

These improvements are leading to a new wealth of scientific discoveries, but are also introducing new problems for calibration and imaging, which consists of effects that were previously negligible. The large field of view (up to more than a degree) makes the emission from different sky directions to travel through different parts of the atmosphere, preventing a single gain calibration to be valid for the entire field. This effect is part of the so-called Direction Dependent Effects (DDEs), which require new software in order to be accounted for. Moreover, a large field is more likely to include extremely bright sources, which can increase the overall noise level and can corrupt the image with deconvolution artifacts. Another important issue is the large fractional bandwidth of today radio interferometers, especially at low, GHz frequencies. Here the deconvolution algorithms need to take into account the continuum spectral properties of the observed sources.

Therefore, for observations conducted with the new radio interferometer MeerKAT (discussed in the next Section), we relied on the new wide-band, wide-field spectral deconvolution software DDFacet, coupled to the new calibration software killMS (Tasse et al., 2018). The DDFacet imager is based on a co-planar faceting scheme, whose purpose is to split a large field of view with multiple narrow-field images, each one with a different phase-center. In each direction, a different set of gain correction matrices is computed by killMS and is taken into account by DDFacet during the deconvolution process. Such an approach has been successfully applied in many recent works with different instruments, such as MeerKAT, ATCA and LOFAR, and at different frequencies (e.g. Coriat et al. 2019; Tremou et al. 2020; Tasse et al. 2021).

4.2 Radio-interferometers

After having introduced the basics of radio-interferometry, I present here the two radio-interferometers MeerKAT and ATCA that I used in my work. Both located in the southern hemisphere, the two instruments were both essential in the observing campaign that I present in the following chapters. I discuss their characteristics and technical specifics, starting with the new, powerful MeerKAT interferometer.

4.2.1 MeerKAT

The MeerKAT radio telescope is a precursor of the Square Kilometre Array (SKA) mid-frequency telescope and is located in the Karoo desert in the Northern Cape Province in South Africa. Inaugurated in 2018, MeerKAT consists of 64 antennas of 13.5 m diameter, currently equipped with L-band (0.86 – 1.71 GHz) and UHF (580 – 1015 MHz) receivers (Jonas and



Figure 4.2: The core of the MeerKAT radio interferometer in the Karoo desert. *Credit*: SARAO.

MeerKAT Team, 2016; Camilo et al., 2018). Characterized by a dense core and with a longest baseline of 8 km, the array has a large field of view ($\simeq$1.69 deg^2) and offers a very good snap-shot *uv*-coverage, achieving a resolution of $\simeq$5 arcsec in L-band. The core of the array is shown in Figure 4.2. MeerKAT will be integrated into the SKA1-MID component of the SKA in the next years, when the SKA1-MID array will be extended to around 200 antennas spread over a maximum baseline of 150 km.

The MeerKAT dishes were designed with an *offset Gregorian* shape, which is highly efficient, as it allows to mount four cryogenically cooled receiver systems in the turret close to the subreflector without creating obstacles on the light optical path. As can be seen from Figure 4.2, the subreflector with the receiver feeds is positioned close to the bottom of the dish. MeerKAT is currently the most sensitive decimetre-wavelength radio-interferometer in the world before the advent of SKA1-MID, and one example of its exceptional sensitivity is the $\simeq$0.5 μJy rms reached in 155 hours of exposure time at L-band (Mauch et al., 2020).

The MeerKAT correlator is of the FX type, meaning that the Fourier transform (F) to the frequency domain is performed before the cross-correlation (X). Data are recorded in full polarisation, with the four cross-correlations XX, XY, YX and YY. The correlator supports two types of channelisation: coarse and fine. The coarse mode is characterised by 4096 channels, each with a bandwidth of 209 kHz, while the fine mode offers 32768 channels, each with a bandwidth of 26 kHz.

Moreover, as one of the scientific goals of MeerKAT is the observations of radio transients, it benefits from the presence of the MeerLICHT optical telescope (Bloemen et al., 2016). This telescope has a diameter of 65 cm and a large field of view, and it is coupled to MeerKAT for simultaneous pointings during night-time observations. In this way, it is possible to collect simultaneous optical and radio data, which is important for the classification of astrophysical transients.



Figure 4.3: Five of the six antennas of the Australia Telescope Compact Array (ATCA), here arranged in a compact configuration. *Credit*: ATNF.

4.2.2 ATCA

The Australia Telescope Compact Array (ATCA) is an array of six antennas located at the Paul Wild Observatory, 25 km west of Narrabri, in the New South Wales, Australia (Frater, Brooks, and Whiteoak, 1992). The antennas have a diameter of 22 m and are aligned on a east-west (EW) track, therefore relying on the Earth's rotation for an efficient coverage of the u-v plane (see Section 4.1.1). The array has a 3 km east-west track with a 214 m northern spur. Five antennas can be moved along these tracks, with the sixth antenna fixed at a position 3 km to the west of the EW track. Therefore, the longest possible baseline is 6 km. The array cycles periodically between all the available antenna configurations, switching between compact and extended configurations that results adequate for different scientific goals (e.g. the study of large-scale emission or high-resolution observations). Five ATCA antennas are shown in Figure 4.3. The antennas have a Cassegrain design, and the receivers are located in a turret that is sustained by a structure located directly at the center of the main reflector.

The array can be used for observations in five frequency bands, from the L-band to the W-band, between frequencies of approximately 1.1 and 105 GHz. The ATCA correlator is called CABB (Compact Array Broadband Backend, Wilson et al. 2011) and it allows to observe simultaneously in two frequency bands with a large bandwidth of 2 GHz per band.

4.3 X-ray observatories

X-ray observations are essential for the study of black holes in general, and in particular for the study of stellar-mass black holes in XRBs. I present in this section the two X-ray observatories that I used in my work: the *Swift* satellite, with its X-ray Telescope, and the MAXI all sky monitor, with its Gas Slit Camera. Their X-ray data have been of key importance for following the outburst of the XRB considered in this thesis, to identify its spectral/accretion state and to coordinate the corresponding radio observations. I discuss here the technical specification of the two instruments, beginning with *Swift*.

4.3.1 *Swift*

The Neil Gehrels Swift Observatory is a NASA space telescope launched in 2004, with the goal of studying gamma-ray bursts (GRB) and other X-ray transients (Gehrels et al., 2004). It carries three instruments: the Burst Alert Telescope (BAT), the X- ray Telescope (XRT) and the Ultraviolet/Optical Telescope (UVOT). The combination of the three instruments makes *Swift* a powerful multi-wavelength observatory, capable of rapid response to any new known or unknown high-energy transient. An artistic representation of the spacecraft is shown in Figure 4.4. *Swift* often operates on a Target of Opportunity (ToO) mode, observing in reaction to the discovery of new transients, which in our case are outbursts from new or known XRBs. Remarkably, there is no proprietary data period for *Swift*, as all its data are immediately public and freely available to the scientific community.

BAT

The Burst Alert Telescope (BAT) is a telescope designed for *hard* X-rays and operates in the 15–150 keV range (Barthelmy et al., 2005). Its semiconductor detector consists of a 5200 cm^2 array of Cadmium Zinc Telluride (CZT) elements located 1 meter behind a 2.7 m^2 coded-aperture mask, resulting in a telescope point spread function (PSF) of 17 arcminutes and a field of view of 1.4 steradians. BAT is highly sensitive to GRB triggers, and it provides a much better accuracy than its homologous instrument aboard the *Fermi* satellite, the Gamma-ray Burst Monitor (GBM). BAT is also extremely useful for observing other X-ray transients, such as XRBs in outburst during bright phases in the hard spectral state.

UVOT

The UltraViolet and Optical Telescope (UVOT) is a 30 cm Ritchey-Chrétien telescope, sensitive to magnitude 22.3 in 1 ks of exposure, which can observe in the the 170-600 nm wavelength range (Roming et al., 2005). While it was designed to do rapid optical/UV follow-up of new GRBs, UVOT can also be useful for providing optical and UV flux densities of XRBs in outburst. This information turns out to be important for estimating the absorption in the direction of the target and for building the spectral-energy distribution (SED) of the observed XRBs. UVOT data were not used in the work presented in the next chapters.

XRT

The *Swift* X-ray Telescope (XRT) is a focusing *soft* X-ray telescope which uses a grazing incidence Wolter 1 telescope to focus X-rays onto a CCD (Burrows et al., 2005). The mirrors of XRT are protected by a thermal baffle that prevents temperature gradients that can cause deformations and degrade the PSF. XRT observes in the 0.2–10 keV energy range and it is characterised by a 110 cm^2 effective area, a field of view of 23.6 arcmin, a 18 arcsec PSF and a pixel size of 2.36 arcsec. It can detect sources down to a flux of $\simeq 8 \times 10^{-14}$ erg cm^{-2} s^{-1} in the 0.3–10 keV range in 10 ks of exposure time.

For observation of XRBs, XRT supports two readout modes to ensure the coverage of the whole brightness dynamic range of these highly variable objects, and it is capable to autonomously determine which readout mode to use. When the source count rate is less than 1 counts s^{-1}, XRT uses the Photon Counting mode (PC), for which two-dimensional imaging is possible and data from the detectors are collected every 2.5 s. For sources above 0.5 counts s^{-1},

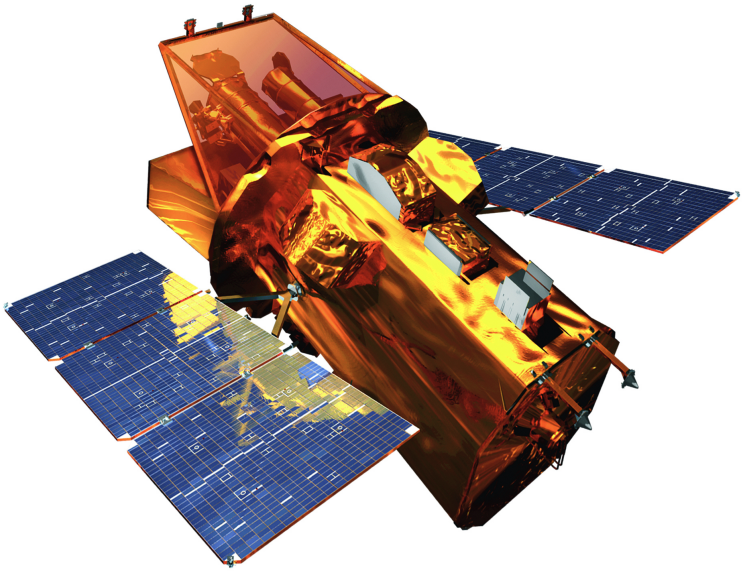

Figure 4.4: Artistic representation of the *Swift* spacecraft with its three main components: the central payload, the scientific instruments (BAT, XRT and UVOT) on both ends of the payload and the solar panel arrays on both sides. *Credit:* Sonoma State University/Aurore Simonnet.

the observation might be affected by photon pile-up. Pile-up occurs when multiple incoming photons arrive in a short time and have overlapping charge distributions on the CCD, which is not able to separate them (often because the readout time is too large compared to the source count rate, Ballet 1999). This means that the resulting charge spatial distribution is recognised as a single event, with an energy that is the sum of the energy of the incoming photons. For very bright sources, with more than 1 counts s^{-1}, XRT uses the Windowed Timing mode (WT), in which the light curve has 1.8 ms time resolution, and only one-dimensional images can be obtained. In this mode pile-up is avoided, except for extremely bright sources with count rates above 100 counts s^{-1}. The data analysis procedure for XRT is detailed in Chapter 5.

4.3.2 MAXI

The Monitor of All-sky X-ray Image (MAXI) mission is located on the Japanese Experiment Module - Exposed Facility on the International Space Station (ISS) since 2009, as it is shown in Figure 4.5. It carries two instruments: the Gas Slit Camera (GSC) and the Solid State Camera (SSC). Capable of detecting sources down to fluxes of $\simeq 10^{-10}$ erg cm^{-2} s^{-1} in the 2–30 keV energy range, the goals of the MAXI all-sky monitor are: to alert the community of new transient X-ray sources, including new XRBs in outburst, in order to trigger multi-wavelength observations of variable objects, and to monitor the long-term variability of X-ray sources (Matsuoka et al., 2009). Both cameras obtain X-ray all-sky images every 90 minutes, following the ISS orbit. The data are immediately sent through the downlink between the ISS and a ground station and this allows MAXI to rapidly report new transients to the global astronomical community with a $0.1°$–$0.2°$ accuracy.

The Gas Slit Camera (GSC) is the main X-ray camera and consists of twelve one-dimensional proportional counters containing Xe at 1.4 atmospheres with 1% CO_2, and equipped with slit & slat collimators. The GSC has a total effective area of 5350 cm^2, a field of view of $1.5°\times$

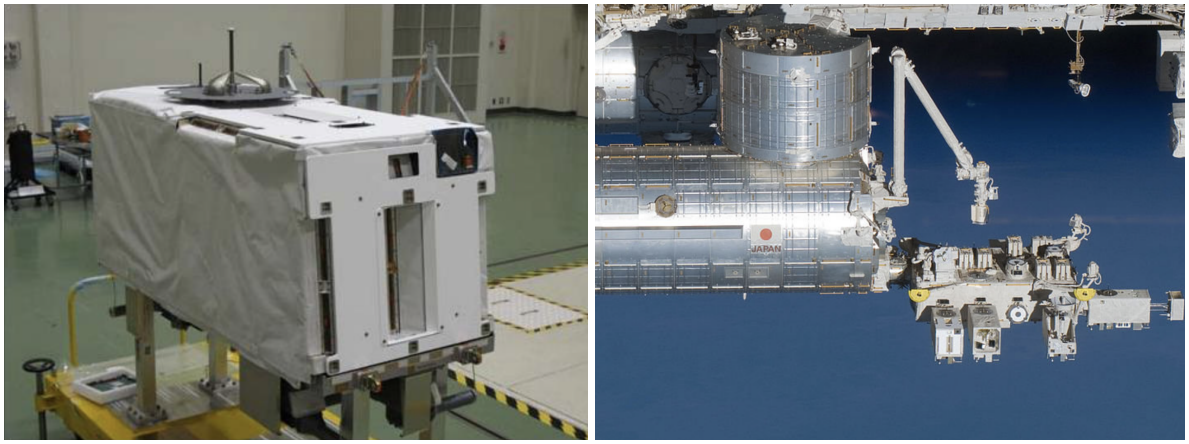

Figure 4.5: *Left*: the MAXI payload. *Right*: MAXI on the Japanese Experiment Module (JEM) "Kibo" on the International Space Station. It is the first instrument on the left on the so-called Exposed Facility of the JEM. *Credit:* JAXA.

160°and observes in the 2–30 keV energy range. The second instrument is the Solid State Camera (SSC), which consists of 32 X-ray CCDs observing in the 0.2–12 keV energy range.

4.4 Statistical techniques

In this section I discuss the basis of the statistical methods that I have used to model the motion of the jet from the new BH XRB MAXI J1348−630, which I first present in Chapter 7. Then, in Chapter 8, I discuss the fit to the jet motion realised with a Bayesian approach, with the use of Monte Carlo Markov Chains.

As the complexity of physical models kept increasing over time, Bayesian statistics has become more and more important in many fields of science, including astrophysics, as it turns out to be essential when many physical parameters of a given model have to be constrained, and when previous knowledge on a given experiment or phenomenon has to be taken into account. The application of these models to the data often requires the use of numerical techniques, and nowadays one of the most powerful and versatile of them is the Markov Chain Monte Carlo (MCMC) method, which (relatively easily) allows us to both sample from an unknown probability distribution and then to use those simulated samples to perform subsequent analyses. In the next sections, I discuss the basics principles of Bayesian statistics and I introduce the Monte Carlo Markov Chains, with the example of the Metropolis-Hastings algorithm and other MCMC algorithms, including the one used in our work. In this treatment, I mostly follow Speagle (2019) and Trotta (2017).

4.4.1 Bayesian statistics

In Bayesian statistics, the probability represents our degree of belief in a given proposition, which is based on the data and on the knowledge available to the author. When performing Bayesian inference, we assume that a particular model (which is described by the parameters θ) is true, and, given the data d, our goal is to obtain the probability distribution of the model parameters. Since it is obtained from both data and previous assumptions, this distribution is called *posterior*, and it is used to compute the expectation values and the uncertainties of such

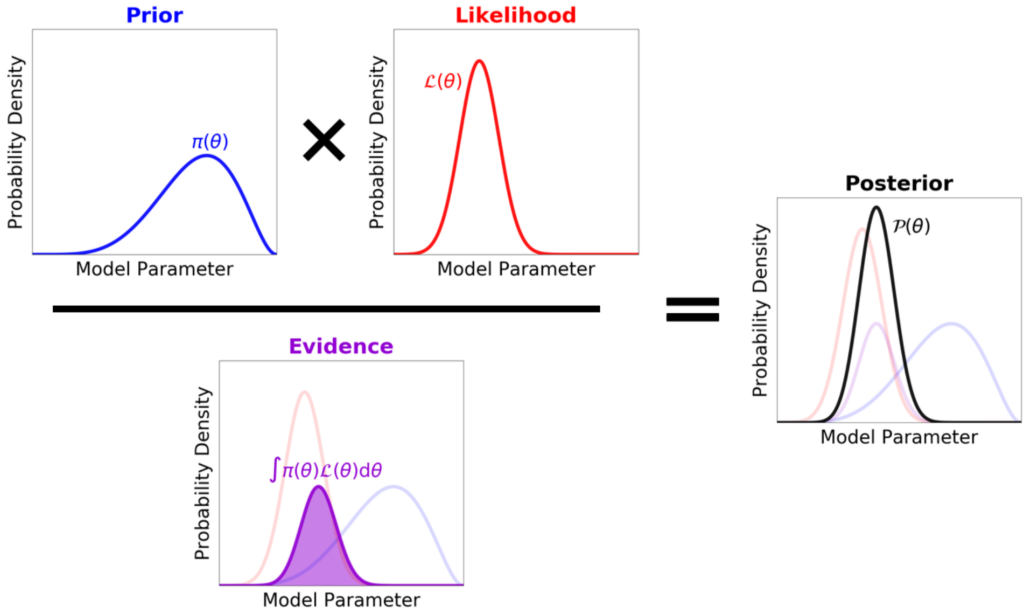

Figure 4.6: Intuitive illustration of the Bayes theorem. The posterior (here $P(\theta)$, in black) of the parameters of our model is obtained from the combination of the prior (here $\pi(\theta)$, in blue) and of the likelihood (here $\mathcal{L}(\theta)$, in red), normalized by the overall evidence (shown in purple). From Speagle (2019).

parameters. From the Bayes theorem, the posterior can be written as the probability of a certain parameter to have the value θ, given the observation of the data d

$$P(\theta|d) = \frac{P(d|\theta)P(\theta)}{P(d)} \tag{4.10}$$

using the formalism of conditional probability. Here $P(d|\theta)$ is called the *likelihood*, and represents the the probability of observing the data d given a certain set of parameters θ in our model. $P(\theta)$ is called the *prior*, and represents the probability that the parameters has the value θ *before* the data d are collected. Hence, it is determined from the prior knowledge of a given model from the literature, from fundamental physical constraints (for instance forbidding negative masses) or from previous experiments. The choice of the prior in any Bayesian analysis is critical for the overall result, as its shape might influence the shape of the posterior itself. Finally, $P(d)$ is the *evidence*, a denominator that ensures the posterior normalization

$$P(d) = \int P(d|\theta)P(\theta)d\theta \tag{4.11}$$

This can be seen as the probability of the data d as determined by integrating across all possible values of θ, weighted by the prior distribution of the model parameters. A schematic representation of the Bayes theorem is shown in Figure 4.6. As it can be seen from there, the posterior often reflects both the prior and the likelihood, with the exact combination of the two depending on the constraints introduced by the prior shape and on the quality of the data used to derive the likelihood.

Once the posterior distribution for the parameters θ of a given model is obtained from priors and data, we can then optimally estimate the true value of all the parameters of the model, as well as estimating the uncertainties on them.

4.4.2 The MCMC technique

While the Bayesian framework is conceptually simple, an analytical computation of the posterior is impossible in most cases. Hence, its estimation requires the use of numerical methods. The purpose of a MCMC algorithm is to construct a sequence of points, called *chain*, in the model parameter space. Such chain has the key property that the density of samples is proportional to the posterior, and hence it makes possible to construct a map of the posterior distribution without obtaining an explicit analytical expression of it. This allows in practice to draw samples from such posterior distribution.

We start with the introduction of Markov chains. A Markov chain is a sequence of N random variables $\{x_0, x_1, ..., x_{N-1}\}$ for which the probability of the $(t+1)$-th element in the chain only depends on the value of the t-th element. This means that the transition to a new state of the system depends only on the single previous state before the transition, and not on the whole history of the system. In our case, we assume that the elements of the chain are the points of the parameter space of our model. The generation of each sample of the chain is probabilistic, and it is characterised by a transition probability $T(\theta_t, \theta_{t+1})$, which represents the probability of passing from the point θ_t to the point θ_{t+1} in the parameter space. These chains are extremely useful in our case because they can converge to a stationary state, in which the samples are drawn from an *equilibrium distribution* $\mathcal{P}(\theta)$, regardless of t. It is possible to construct a Markov chain with a desired equilibrium distribution, and hence the idea behind MCMC algorithms is to construct a Markov chain for which the equilibrium distribution is the posterior distribution $P(\theta|d)$ that we want to sample. Therefore, once the stationary state is reached, the chain will generate new samples $\theta_t \to \theta_{t+1}$ such that their final distribution of the samples converges and is equal to $P(\theta|d)$.

Using the conservation of probability when moving between positions in the parameter space, which ensures that the whole process is reversible, we can use the so-called *detailed balance* property, and hence we can write

$$T(\theta_t, \theta_{t+1})\mathcal{P}(\theta_t) = T(\theta_{t+1}, \theta_t)\mathcal{P}(\theta_{t+1}) \tag{4.12}$$

where $\mathcal{P}(\theta_t)$ is the probability of the chain to be in the point θ_t of the parameter space. Rearranging the previous equation, such relation becomes

$$\frac{T(\theta_t, \theta_{t+1})}{T(\theta_{t+1}, \theta_t)} = \frac{\mathcal{P}(\theta_{t+1})}{\mathcal{P}(\theta_t)} = \frac{P(\theta_{t+1}|d)}{P(\theta_t|d)} \tag{4.13}$$

where the last equality means that the distribution we are trying to generate samples from is indeed the posterior. In other words, the ratio of the transition probabilities is inversely proportional to the ratio of the posterior probabilities at the two points, so that we are effectively tracing the posterior.

The Metropolis-Hastings algorithm

Many different algorithms have been developed for implementing Markov chains capable of sampling from posterior distributions, and I discuss here a classical example. The Metropolis-Hastings (MH) is the simplest MCMC algorithm (Metropolis et al., 1953) and it has been widely used in the literature. I present it here by listing the different steps required to compute the transition probabilities, to perform a move in the parameter space and to create a Markov chain with the properties outlined in the previous section. For a general move in the parameter space,

we need to propose a new position and then decide whether to accept or reject it based on a transition probability T. The steps can be summarised as follows:

1 We start from a random point θ_0, with a posterior probability $P_0 = P(\theta_0|d)$.

2 We propose a new candidate point θ_c by drawing from the *proposal distribution* $Q(\theta_0, \theta_c)$. A possible choice for Q could be a Gaussian centered on the starting point and with a fixed width σ.

3 We evaluate the posterior $P_c = P(\theta_c|d)$ at the candidate position (with Equation 4.10) and we compute the transition probability from θ_0 to θ_c with the *Metropolis criterion*

$$T(\theta_0, \theta_c) = \min\left(\frac{P_c Q(\theta_0, \theta_c)}{P_0 Q(\theta_c, \theta_o)}, 1\right) \tag{4.14}$$

which satisfies the detailed balance of equation 4.13.

5 To decide to accept/reject the step, we generate a random number U from a uniform distribution $[0, 1)$. The move is accepted if $T > U$, and it is rejected otherwise.

4 If the candidate point is accepted, we move to θ_c and we add it to the chain. Otherwise we stay at the old point, which is again added to the chain. Finally, we go back to the step 2.

At the beginning of the chain, the distribution starts at θ_0, and might be significantly far from the equilibrium one. The agreement between the two distributions increases over time, and it is considered acceptable after the so-called *burn-in* period, that can be considered as the time after which the chain "loses the memory" of where it started. Therefore, in order for the initial state to not have any impact on the final results, one needs to throw away the samples obtained in the first part of the sampling, as those first samples do not represent adequately the posterior. One of the goals for the development of MCMC algorithm is to minimize the burn-in time, in order to have the chains to converge fast to equilibrium and to improve the overall performance of the code.

The Metropolis-Hastings algorithm is at the core of the MCMC methods, and many works in the astrophysics field largely profited from the use of this first implementation of MCMC. Nowadays there are many algorithms with increased complexity, but with a faster convergence, which is preferred because of the reduction of computational cost due to the smaller number of iterations required to obtain the equivalent level of accuracy.

MCMC in practice

The choice of proposal distribution Q is of key importance for an efficient exploration of the parameter space and for the mapping of the posterior. If the scale of Q is too small compared to the scale of the posterior, the chain will spend too much time in a small region of the parameter space, resulting in an incomplete sampling. On the contrary, if the scale is too large, many steps will be rejected by the chain, which will be offered positions significantly far from the posterior peaks. It has been shown that an optimal choice of the proposal distribution results in an acceptance rate of $\sim$25%, where the acceptance rate is the ratio between the accepted moves and the total steps (Gelman, Roberts, and Gilks, 1996). It can also be shown that the optimal scale of the proposal distribution is $\simeq 2.4/\sqrt{D}$ times the scale of the posterior distribution, where D is the parameter space dimensionality. However, the posterior scale might not be

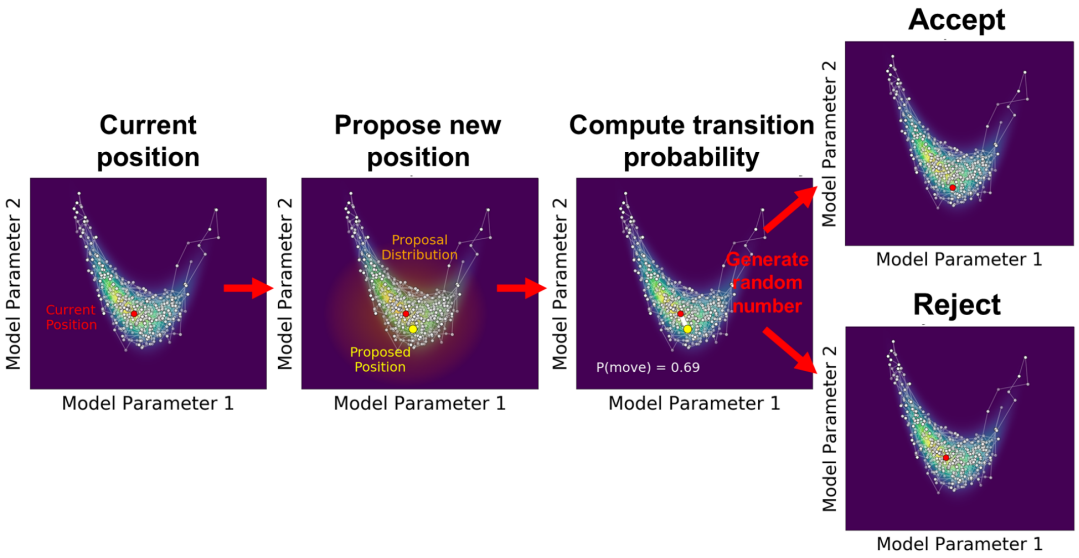

Figure 4.7: A schematic illustration of the Metropolis-Hastings algorithm in a two-dimensional parameter space, including the steps listed in Section 4.4.2. From Speagle (2019).

known *a-priori*, hence it might not be possible to fix the proposal scale before the MCMC run, and algorithms with fixed-scale proposals might not be efficient in every situation. Moreover, sampling the posterior is computationally heavy and might require a long running time with a single sampler.

To mitigate both issues, new classes of MCMC algorithms have been proposed. We consider here the so-called ensemble methods, which use many Markov chains running simultaneously in parallel to improve the performance of any individual chain. In our work on the jet motion fitting with MCMCs, we used EMCEE (Foreman-Mackey et al., 2013), which is implemented in a publicly available Python package and significantly outperforms standard MH implementations. Based on the results of Goodman and Weare (2010), this algorithm evolves a series of *walkers* in parallel rather than just one sampler at the time, and, since the proposal optimization is of key importance, it uses the position of the other points in the ensemble inside the proposal, which removes the need to fine-tune the proposal distribution to match the posterior density scale. However, a detailed discussion of the properties of the proposal implemented in EMCEE is beyond the scope of this work.

Once the samples from the posterior have been collected, it is straightforward to obtain estimates for best values of the parameters. For a chain of N samples, the posterior mean is given by

$$E[\theta] = \int P(\theta|d)\theta d\theta \simeq \frac{1}{N}\sum_{t=0}^{N-1}\theta_t \tag{4.15}$$

and this is valid also for any function of the parameters $f(\theta)$.

It is common to provide the final results of the MCMC run by presenting the one-dimensional marginal posterior for each of parameters in the chosen model $\theta^{(1)}, ..., \theta^{(j)}$. Usually, this can be obtained through a $(j-1)$-dimensional integration, which is often numerically difficult, but it turns out to be extremely simple when dealing with MCMCs. Since the samples are obtained from the full posterior, their density profile traces the shape of the full posterior. It is then sufficient to order all the chain element with respect to a single coordinate in the parameter

space, as for instance $\theta^{(1)}$, and simply ignoring the other parameters $\theta^{(2)}, ..., \theta^{(j)}$, in order to obtain the marginalized posterior $P(\theta^{(1)}|d)$.

Chapter 5

The new black hole X-ray binary MAXI J1348–630

Contents

5.1 Introducing MAXI J1348−630 . . . 78
5.2 Description of the campaign . . . 79
5.2.1 MeerKAT observations . . . 79
5.2.2 ATCA observations . . . 80
5.2.3 *Swift* observations . . . 80
5.2.4 MAXI observations . . . 82
5.3 Outburst presentation . . . 82
5.3.1 X-ray light curve . . . 84
5.3.2 Radio light curve . . . 84
5.3.3 X-ray spectral evolution . . . 88
5.3.4 Evolution of the compact jets . . . 90
5.4 The distance to MAXI J1348−630 . . . 91
5.4.1 H I absorption . . . 91
5.4.2 X-ray light echoes . . . 93
5.5 Tabulated data . . . 94
5.5.1 Radio data . . . 94
5.5.2 X-ray data . . . 98

Starting from this chapter, I present the result of the work done in the last three years in the field of multi-wavelength observations of BH XRBs. My entire PhD work revolved mainly around the observation of a single source, the new black hole X-ray binary MAXI J1348−630, which was active for more than a year, and whose observations provided us with an unprecedented wealth of results and implications both for the study of compact jets and discrete ejecta in XRBs. This is an interesting example of what can be done by monitoring the outburst of a XRB. Between

January 2019 and January 2021, I performed the radio and X-ray monitoring campaign of the discovery outburst of the black hole X-ray binary (XRB) MAXI J1348-630. The observing campaign was conducted with MeerKAT, ATCA and *Swift* (see Chapter 4), totaling more than 200 observations in radio and X-rays. Specifically, I performed the full data reduction, analysis and interpretation of all the radio and X-ray observations presented in this chapter. During the outburst, the source transitioned through all the canonical X-ray spectral states typical of XRBs and we detected the presence of compact jets, that strongly evolved during the different phases of the outburst. I detected two rare and subsequent relativistic discrete ejecta (which we refer to as RK1 and RK2 in this work, see Chapter 7) that displayed the highest proper motion ever measured for all XRBs. In this second part of my thesis, I outline and discuss the totality of my results on the jets of MAXI J1348−630, starting with a description of the outburst in Chapter 5, followed by a discussion of the disk/jet coupling in Chapter 6. In Chapters 7 and 8 I present the "spectacular" discrete ejecta launched by MAXI J1348−630 and analyse in depth their motion and I model it to extract the maximum amount of physical information.

I present in this chapter the dense and comprehensive radio and X-ray monitoring of MAXI J1348−630 during its discovery outburst. Specifically, I introduce MAXI J1348−630 in Section 5.1 while on Section 5.2 I describe the observations and the data processing. In Section 5.3 I present the results of the monitoring from the X-ray point of view and I describe the evolution of the compact jets. I then discuss in Section 5.4 the current measurements of the distance of MAXI J1348−630. The radio and X-ray data obtained from my monitoring campaign are tabulated in Section 5.5. The results presented in this chapter have been published in Carotenuto et al. (2021a) and Chauhan et al. (2021).

5.1 Introducing MAXI J1348−630

MAXI J1348−630 was discovered as a bright X-ray transient on 2019 January 26 (Yatabe et al., 2019) by the Monitor of All-sky X-ray Image (MAXI) onboard the International Space Station (Matsuoka et al., 2009) and, thanks to immediate and intense multi-wavelength follow-up observations, it was subsequently identified as a black hole candidate (Kennea and Negoro, 2019; Sanna et al., 2019; Chen et al., 2019; Denisenko et al., 2019; Nesci and Fiocchi, 2019; Russell, Baglio, and Lewis, 2019; Russell et al., 2019b). MAXI J1348−630 displayed a typical outburst that was followed by four reported subsequent hard state re-flares (Russell et al., 2019a; Negoro et al., 2019; Al Yazeedi et al., 2019; Pirbhoy et al., 2020; Carotenuto et al., 2020b; Zhang et al., 2020b; Shimomukai et al., 2020). While currently no information is available on the black hole inclination, mass, spin and companion star, we measured a source distance $D = 2.2^{+0.5}_{-0.6}$ kpc (Chauhan et al., 2021) from observations of HI absorption carried out with the Australian Square Kilometre Array Pathfinder (ASKAP) and with MeerKAT. The distance measurements of MAXI J1348−630 are discussed more in detail in Section 5.4. From the analysis of the MAXI data for the first part of the outburst, Tominaga et al. (2020) estimated a black hole mass $M_{\rm BH} \simeq 16(D/5\ {\rm kpc})\ M_{\odot}$, assuming a face-on system with a non-spinning BH (with the $M_{\rm BH}$ estimate increasing with the BH spin and inclination). Although the mass measurement is very speculative, at the known distance of MAXI J1348−630 this corresponds to $M_{\rm BH} \sim 7\ M_{\odot}$, which is fully consistent with measured mass values among the known population of Galactic BHs (e.g. Tetarenko et al. 2016).

MAXI J1348−630 has also been monitored with the Neutron Star Interior Composition Explorer (NICER) on board the ISS and the spectral-timing analysis of the fast X-ray variability has been recently conducted, with the observations of state transitions, the detection of different

types of QPOs and the identification of a dominant hard Comptonised emission in the Type-B QPOs at the hard-to-soft state transition (Zhang et al., 2020a; Belloni et al., 2020; García et al., 2021; Zhang et al., 2021).

5.2 Description of the campaign

I outline here the radio and X-ray observations of MAXI J1348−630 and I refer to Chapter 4 for the technical details on the telescopes.

5.2.1 MeerKAT observations

We observed MAXI J1348−630 with MeerKAT (see Section 4.2.1) as part of the ThunderKAT Large Survey Programme (Fender et al., 2017). ThunderKAT is the image-plane transients programme for MeerKAT, whose goal is to perform detailed observing campaigns of a many different classes of radio transients produced by different objects, including XRBs, GRBs, Cataclysmic variables (CVs) and Supernovae. In addition, ThunderKAT has commensal access to all MeerKAT data to search for potential radio transients, which would not be discovered otherwise (e.g. Driessen et al. 2020). In the specific, ThunderKAT has been allocated 500 hours of observing time over 5 years (2018-2023) for the study of X-ray binaries, including both BHs and NSs.

MAXI J1348−630 was monitored with an approximately weekly cadence from 2019 January 29 (MJD 58512) to 2020 March 03 (MJD 58910) for a total of 48 epochs. Each observation consisted of a single 15 min long scan on source, except for the first observation (MJD 58512), which was 20 mins of on-source time separated into two 10 min scans. The primary calibrator PKS 1934–638 was observed either at the beginning or at the end of each observing block, and it was used for flux, bandpass, and complex gain calibration. All observations were taken with 8 seconds of integration times, at a central frequency of 1.28 GHz and with a total bandwidth of 860 MHz, divided into 4096 equivalent 209 kHz channels.

The data were first flagged using AOFlagger (Offringa, 2010) and then averaged in frequency to reduce the number of channels (and the data size) by a factor 8. The calibration was subsequently performed using standard practices with the Common Astronomy Software Application (CASA version 4.7, McMullin et al. 2007), while imaging was carried out with the wide-band, wide-field imager DDFACET (Tasse et al., 2018), adopting a uniform weighting scheme to achieve the best possible angular resolution. To mitigate the presence of artifacts from bright sources close to the target, the images were then self-calibrated in amplitude and phase using the calibration software KILLMS (Tasse et al., 2018) and DDFACET, with a solution interval of 5 min. Between the observations of 2019 July 22 and November 01, the sky coordinates of PKS 1934–638 used by MeerKAT were slightly offset from the VLBI ones, therefore we artificially rotated the visibilities to the correct position using the `chgcentre` task, which is part of the WSCLEAN package (Offringa et al., 2014). The level of rms noise reached ranged from 30 to 60 μJy beam^{-1}, depending on the observing conditions of the telescope and variable levels of radio-frequency interference (RFI). To obtain the radio flux density S_ν, we fit point sources in the image plane with the CASA task `imfit`. Positions were extracted before self-calibration, while flux densities were extracted afterwards.

5.2.2 ATCA observations

MAXI J1348−630 was also monitored with the Australia Telescope Compact Array (ATCA) for 31 epochs in total, from January to December 2019 (project codes C1199 and CX423). The first part of the monitoring consisted of a dense coverage at the beginning of the outburst, with observations performed roughly every two days, from 2019 January 26 (MJD 58509) to 2019 February 17 (MJD 58531), and a total observing time that ranged from 8 minutes to 5 hours, depending on the expected flux density of the target. The second part of the monitoring started on 2019 March 31 (MJD 58573) and ended on 2019 December 14 (MJD 58789), with observations taken every 1–2 or 3 weeks and longer exposure times of up to 12 hours on MJD 58689. We do not consider the 5.5 and 9 GHz ATCA observation performed on MJD 58816 (2019 November 29), as we noticed significant discrepancies in the flux densities of background check sources at both frequencies, which are likely of instrumental origin. All of the observations were taken simultaneously at central frequencies of 5.5 and 9 GHz, while for some epochs (specified in Table 5.2) we added a second pair of bands, and the central frequencies were either 17.0 and 19.0 GHz, or 16.7 and 21.2 GHz. For each central frequency, the total bandwidth was 2 GHz. We also included two epochs (MJD 58515 and 58608), during which ATCA was part of the Long Baseline Array (LBA) as a phased-array element for VLBI observations (project code V447). In this configuration, the central frequency was 8.4 GHz, with a total bandwidth of 128 MHz. In this work we report results of the ATCA-only correlated data. We used either PKS 1934–638 (preferred) or PKS 0823–500 as primary calibrators, depending on the visibility of the calibrator at the time of the observation, while PKS 1352–63 was used for complex gain calibration. The data were first flagged and then calibrated using standard procedures in CASA. Imaging was carried out with the standard `tclean` algorithm in CASA with a Briggs weighting scheme. We chose a robust parameter of 0 for an optimal trade-off between angular resolution and sensitivity. The level of rms reached 6 μJy beam^{-1} for the longest duration observations. To obtain the radio flux density S_ν, we again fitted a point source in the image plane with the CASA tasks `imfit`, except for several short observations, in which the poor *uv*-coverage did not allow a proper deconvolution: in that case the flux densities were obtained by directly fitting the visibility data, using UVMULTIFIT (Martí-Vidal et al., 2014).

5.2.3 *Swift* observations

To monitor the evolution of the X-ray emission, MAXI J1348−630 was observed with the Neil Gehrels *Swift* Observatory (Gehrels et al., 2004), as part of a dedicated monitoring associated with the ThunderKAT Large Survey Program on X-ray transients, and with *Target of Opportunity* observations (PI Carotenuto) for a total of 85 epochs since its discovery (target ID: 00011107). The on-board X-ray Telescope (XRT, Burrows et al. 2005) was operated in Windowed Timing (WT) mode for the first part of the outburst (from MJD 58509 to 58720), during which MAXI J1348−630 became extremely bright, up to a count rate of $\sim$1700 counts s^{-1}. The Photon Counting (PC) mode was used for the rest of the monitoring, when the count rate was $\lesssim 1$ count s^{-1}. We used the HEASOFT package (version 6.25) and the related calibration files to reduce the publicly available raw XRT data. We ran the `xrtpipeline` task to first reprocess the data and create exposure maps for each observation. The source spectra were then manually extracted using `xselect`. For observations in WT mode, a circular region of 20 pixels (1 pixel = 2.35 arcsec) radius centered on the target position was used to extract the source spectrum when the source count rate was lower than 100 counts s^{-1}. To mitigate the well-known pile-up problem affecting observations of bright sources, for higher count rates we filtered grade 0

events and used an annulus of variable (increasing with the count rate) inner and outer radii. The radii values (listed in Table 5.3) were chosen to have $\lesssim 100$ counts s^{-1} in the extraction region and to avoid the presence of calibration residuals in the source spectra. For the annulus extraction region, the inner radius ranged between 1 and 33 pixels and the outer radius ranged between 30 and 50 pixels. To extract the source spectrum in observations carried out in PC mode, we used a circular region with a radius of 20 pixels centered on the target, except for the epochs on MJD 58816, 58821 and 58889. During these three epochs we used an annulus of fixed 30 pixels outer radius and variable inner radius (listed in Table 5.3) to ensure $\lesssim 0.5$ counts s^{-1} in the extraction region and avoid pile-up. The background spectrum for all observations were extracted using an annulus region centred on the source with a 50 pixels inner radius and 100 pixels outer radius. We created ancillary response files with `xrtmkarf` and used the up-to-date response matrix files from the High Energy Astrophysics Science Archive Research Center (HEASARC) calibration database (CALDB). When possible, we used `grppha` to group the spectra in bins of 20 counts each to enable the use of χ^2 statistics for the spectral fitting. For low-counts observations we used Cash statistics `cstat` (Cash, 1979) instead.

Spectral models

Spectral analysis was carried out in the 0.7–10 keV energy range with XSPEC (Arnaud, 1996). Our main goal with the X-ray spectral analysis was to estimate the unabsorbed flux in the 1–10 keV band. Therefore, we used three simple models to achieve acceptable fits, and we present them here. First, a power law to model the non-thermal emission from the inner accretion flow

$$f(E) = K \left(\frac{E}{1\mathrm{keV}} \right)^{-\Gamma} \tag{5.1}$$

where Γ is the photon index of the power law and K is the normalization constant, in units of photons keV^{-1} cm^{-2} s^{-1}. This component is called `powerlaw` in XSPEC. The second component models the thermal emission from a multicolor accretion disk

$$f(E) = \frac{8\pi R_{\mathrm{in}}^2 \cos\theta}{3D^2} \int_{T_{\mathrm{out}}}^{T_{\mathrm{in}}} \frac{1}{T_{\mathrm{in}}} \left(\frac{T}{T_{\mathrm{in}}} \right)^{-\frac{11}{3}} B(E,T) dT \tag{5.2}$$

where R_{in} is the internal radius of the disk, D is the source distance and θ is the disk inclination angle with respect to the line of sight (Mitsuda et al., 1984). T_{in} and T_{out} are, respectively, the temperatures of the inner and outer edge of the accretion disk, and $B(E,T)$ is the Planck formula for blackbody emission. This component is called `diskbb` in XSPEC.

To account for interstellar absorption, we used the Tuebingen-Boulder ISM absorption model (`tbabs` in XSPEC). This model computes the cross section for X-ray absorption by the interstellar medium (ISM) as the sum of the cross sections for X-ray absorption due to the gas-phase and grain-phase ISM, including the presence of molecules. Considering the ISM abundances obtained by Wilms, Allen, and McCray (2000), the absorption can be modelled as

$$S_{\mathrm{obs}}(E) = e^{-\sigma(E) N_{\mathrm{H}}} S_{\mathrm{source}}(E) \tag{5.3}$$

where S_{source} is the intrinsic, unabsorbed flux from the source and S_{obs} is the measured flux. Here $\sigma(E)$ is the photoionization cross section from Verner et al. (1996) and N_{H} is the equivalent hydrogen column density in cm^{-2}.

Table 5.1: Summary of the X-ray spectral state evolution of MAXI J1348−630 during the 2019/2020 major outburst. Dates are obtained from Zhang et al. (2020a), using spectral and timing NICER data. We note that frequent excursions to the SIMS were observed during the first part of the soft state (until MJD 58542, see Zhang et al. 2020a).

X-ray state	MJD interval
Hard state	58509 – 58517
HIMS	58517 – 58522.6
Soft state	58522.6 – 58597
IMS	58597 – 58604
Hard state	58604 – 58910

For hard state observations, we fit the spectra with a simple absorbed power law model (`tbabs`×`powerlaw`). For the soft state, we used the `diskbb` model to which we add a power law component to take into account residual high energy tails, so that the total model is `tbabs`×(`diskbb`+`powerlaw`). Since in the latter cases the power law photon index Γ could not be constrained, for soft state observations we fixed $\Gamma = 2.4$. We first fitted all the epochs while leaving the $N_{\rm H}$ free to vary, and then, assuming no variation of the hydrogen column density due to the source activity, we froze the $N_{\rm H}$ to the average value of 0.86×10^{22} cm^{-2}. We then calculated the 1–10 keV X-ray unabsorbed flux using the XSPEC convolution model `cflux`. All the results of the spectral analysis are reported in Table 5.3. In case of hard-state observations close to quiescence, for which the photon index could not be constrained, we fixed $\Gamma = 2.2$, as measured for BH LMXBs approaching quiescence (Corbel, Tomsick, and Kaaret, 2006; Plotkin, Gallo, and Jonker, 2013).

5.2.4 MAXI observations

The Monitor of All-sky X-ray Image (MAXI, Matsuoka et al. 2009) observed MAXI J1348−630 with the Gas Slit Camera (GSC) throughout the whole outburst and all the data are publicly available. We downloaded the data from the MAXI on demand website (`http://maxi.riken.jp/mxondem/`) and we primarily used them to follow the outburst evolution and to obtain the Hardness-Intensity Diagram (HID), which is shown in Figure 5.1. See Tominaga et al. (2020) for details on the MAXI data.

5.3 Outburst presentation

With our MeerKAT, ATCA, Swift, and MAXI observations, we monitored the entire 2019/2020 outburst of MAXI J1348–630. During the discovery outburst, MAXI J1348–630 was detected early during the rise and subsequently transitioned through all the typical BH XRB accretion states, displaying a complex and rich behaviour in terms of X-ray and radio emission, as can be seen from the MAXI HID in Figure 5.1.

A global view on the outburst can first be obtained from the MAXI count-rate light curve and from the *Swift*/XRT flux light curve, both shown in Figure 5.2. We describe the outburst evolution using our observations, but we rely on the Neutron Star Interior Composition Explorer (NICER) X-ray data (Zhang et al., 2020a) for the dates of the state transitions, which are obtained with high accuracy from spectral and timing analysis, and are reported in Table 5.1.

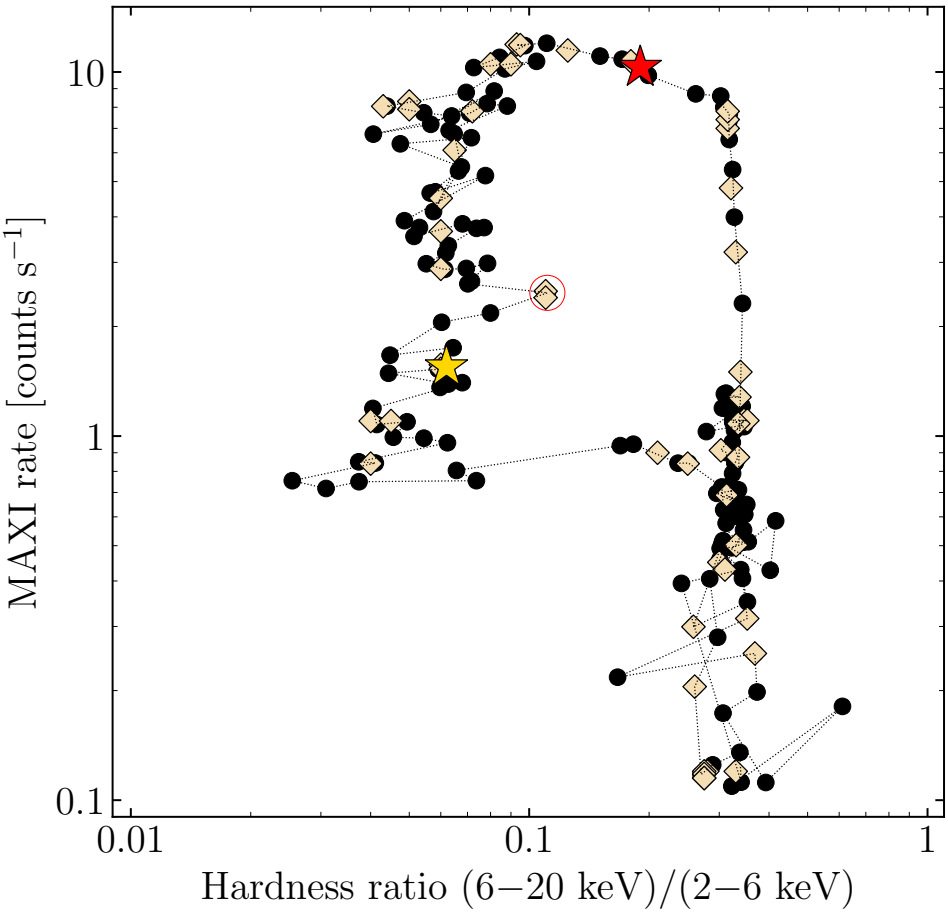

Figure 5.1: Hardness-Intensity Diagram (HID) of MAXI J1348−630 during its major outburst, where the hardness ratio (HR) was determined from MAXI data. The source performs a typical cycle in the HID during the major outburst. For clarity, we only show MAXI observations above 0.1 counts s^{-1} in the MJD interval 58505–58710, to include the brightest part of the outburst that covered an entire cycle in the HID. Times of radio observations are marked on the HID as beige diamonds. Radio observations for the second part of the outburst (MJD $>$ 58710) lie on the bottom part of the hard line (HR $\sim$ 0.4). The inferred ejection dates for RK1 and RK2 are shown, respectively, as red and yellow stars (see Chapter 3). The hardness spike on MJD 58574, believed to be associated with a short excursion to the SIMS (see Section 7.7.1), is highlighted with a red circle.

5.3.1 X-ray light curve

The outburst started with a rapid rise that was first detected by MAXI and *Swift* on MJD 58509 (2019 January 26, Yatabe et al. 2019; Kennea and Negoro 2019). During the rise, the system was in the hard state, as can be initially seen from Figure 5.1 and 5.2. In this state the X-ray spectrum can be well fitted with a single absorbed power law, with a photon index starting from $\Gamma \sim 1.4$ and becoming softer as the system became brighter. MAXI J1348−630 entered the IMS on MJD 58517 (2019 February 03), during which the flux continued increasing and the spectrum started to be dominated by the thermal accretion disk emission at ∼keV energies.

On MJD 58522 (2019 February 08) the system subsequently entered the soft state, approaching the outburst peak on MJD 58524. During the soft state the disk temperature evolution clearly tracked the light curve, reaching ∼0.8 keV during the brightest part, a low value among BH XRBs (Tominaga et al., 2020). Then the system exponentially decayed for two months, during which the spectrum stayed soft (see Figure 5.1). The system transitioned back to the IMS on MJD 58597 and the low hard state started on MJD 58604. During the first weeks of the low hard state the source exhibited an exponential decay. As the decay progressed, the spectrum initially became steeper, but, after MJD 58612, we observed a progressive spectral softening, as typically observed when BH LMXBs get closer to their quiescent state (Corbel, Tomsick, and Kaaret, 2006; Plotkin, Gallo, and Jonker, 2013). Then, MAXI J1348−630 was not detected on MJD 58627, as it was below the detection threshold of *Swift*/XRT in WT mode, during an observation characterised by an unusually high background level, but during the following weeks we observed a rise in flux (hereafter R1, the first re-flare, as marked on Figure 5.2). A smooth decay then followed, the first half of which was not densely covered by *Swift*, but was monitored with MAXI. Again, in the decay phase of R1, between MJD 58699 and 58706 (August 2019), the spectrum became softer as the system approached quiescence. MAXI J1348−630 was then detected again in X-rays on MJD 58775 (2019 October 19, R2), after the optical re-brightening reported by Al Yazeedi et al. (2019), but went quickly below our detection threshold.

The last part of the outburst is characterised by two additional short hard-state re-flares, in November-December 2019 (R3, MJD interval 58789–58831) and the fourth in February 2020 (R4), after which MAXI J1348−630 faded back to quiescence. We note that after the main outburst and R1, from MJD 58706 the majority of the observations had to be fitted with Cash statistics due to low total counts, except for epochs on MJD 58816 and MJD 58889, for which the number of counts was high enough to allow χ^2 statistics to be used. Moreover, the photon index Γ had to be frozen for the hard-state epochs on MJD 58720, 58775, 58826, 58828 and 58831, since the low number of counts did not allow the power law to be constrained. Their values are listed on Table 5.3.

5.3.2 Radio light curve

With the start of the radio monitoring immediately after the X-ray detection of MAXI J1348−630, our initial ATCA and MeerKAT observations clearly detected the radio counterpart of the source (Russell et al., 2019b), consistent with the X-ray position. The radio light curve and the evolution of the radio spectral index for the entire monitoring are reported in Table 5.2 and shown in the two lower panels of Figure 5.2, while a wide field image of the MAXI J1348−630 field observed with MeerKAT is shown in Figure 5.3.

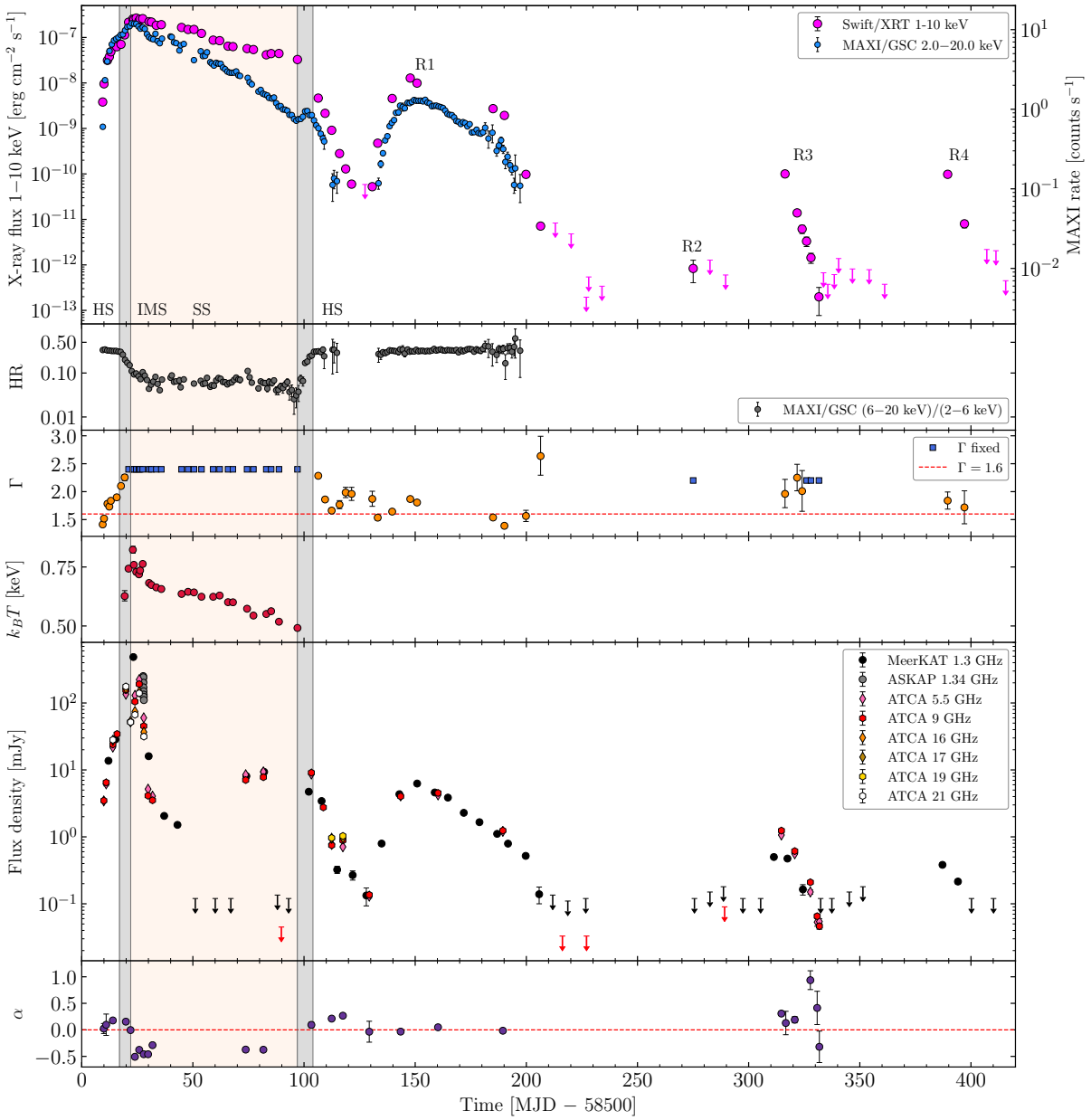

Figure 5.2: X-ray and radio light curves of MAXI J1348−630 during its 2019/2020 outburst. The unshaded regions mark the periods in which the source was in the hard state, while the light grey shaded regions indicate the IMS and the light pink regions indicate the soft state (see Section 5.3 and Table 5.1 for the timing of the spectral state transitions, which are obtained from Zhang et al. 2020a). *First (top) panel*: Unabsorbed X-ray flux light curve of MAXI J1348−630 from *Swift*/XRT observations in the 1–10 keV energy range (left *y-axis*). The four re-flares that followed the main outburst are marked on the figure with R1,2,3,4. We also show the MAXI/GSC daily count rate (right *y-axis*). For clarity, we only show the first part of the outburst, in the MJD interval 58505–58710, and select daily epochs with a count rate above 0.1 counts s^{-1}. *Second panel*: MAXI/GSC daily hardness ratio, defined as the ratio between the counts in the two adjacent *hard* and *soft* bands of 6–20 keV and 2–6 keV, respectively. *Third panel*: X-ray photon index Γ obtained from *Swift*/XRT spectra. Epochs for which the value of the photon index was fixed are shown with blue square points. *Fourth panel*: Temperature of the inner edge of the accretion disk obtained from *Swift*/XRT spectra fitted with `diskbb`. *Fifth panel*: Radio light curve of MAXI J1348−630 at the core location (excluding large scale jets). Black dots are for 1.28 GHz MeerKAT observations, while the others are for multi-frequency ATCA observations. ASKAP 1.34 GHz data taken on MJD 58527 from Chauhan et al. (2021) are also shown. *Sixth (bottom) panel*: Radio spectral index of MAXI J1348−630 obtained from ATCA simultaneous multi-frequency observations, as reported in Table 5.2.

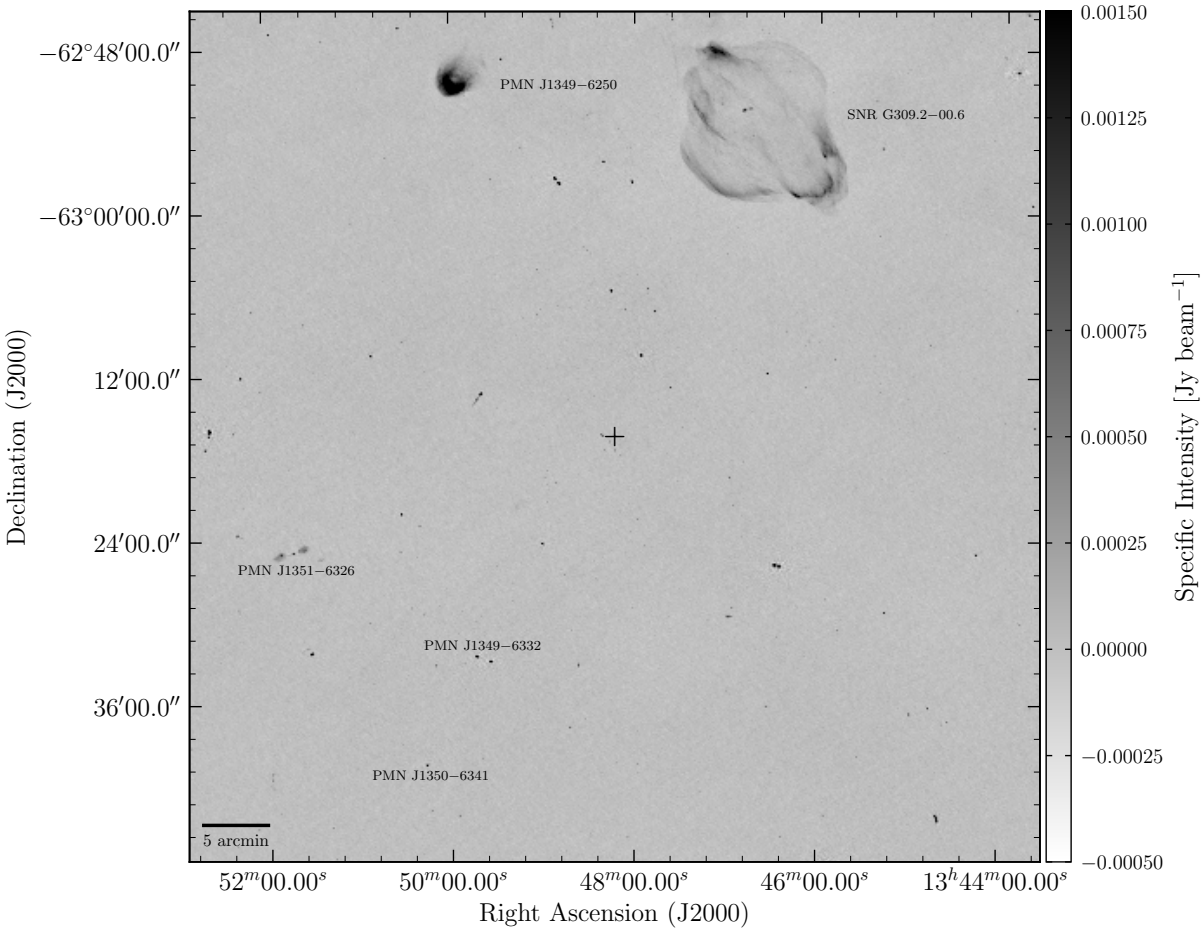

Figure 5.3: MeerKAT large scale radio image at 1.28 GHz of the MAXI J1348−630 field. The image is obtained by concatenating the individual observations of July 14, 22, 27 and August 04 2019, corresponding to 1 hour of total observing time, and in which the MAXI J1348−630 core was reasonably stable in radio brightness (see Table 5.2). North is up and East is left. The colour bar shows the radio brightness in units of Jy beam^{-1} and the black cross marks the position of MAXI J1348−630. The rms is $\sim$30 μJy beam^{-1}. The size of the image is approximately 1 deg^2, containing a field largely dominated by point sources, with the presence of several jetted radio galaxies. The two prominent sources to the North are the SNR G309.2–00.6 in the West (Gaensler, Green, and Manchester, 1998) and the HII region PMN J1349–6250 in the East.

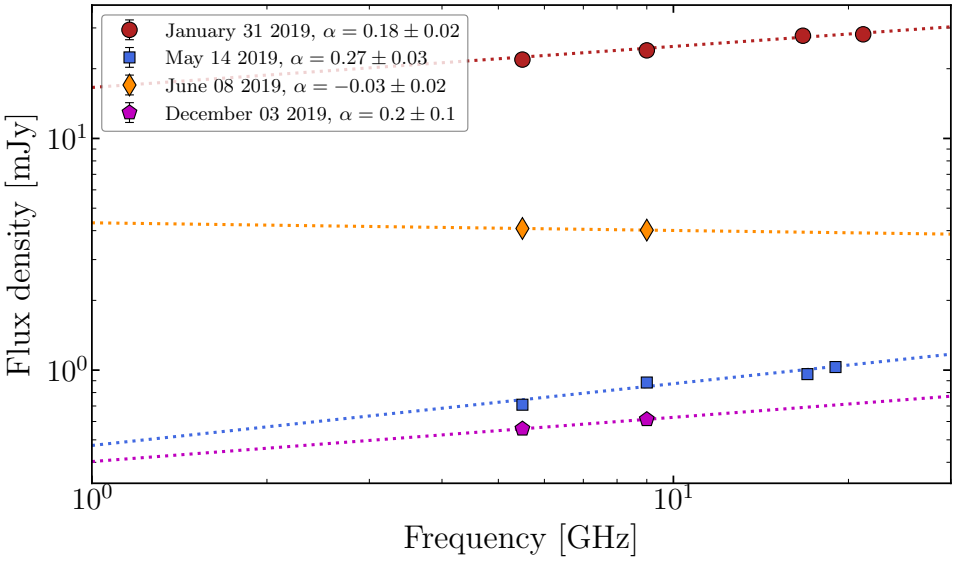

Figure 5.4: Radio spectra of MAXI J1348−630 of four epochs in the hard state, obtained with ATCA observations. Respectively in red, blue, yellow and purple we show data from MJD 58514, 58617, 58643, 58820, between January and December 2019. The fitted power law spectrum is shown as a dotted line for each plotted observation. Due to the fast evolution of radio emission, for the spectra we only use simultaneous ATCA multi-frequency observations. The flat-to-inverted spectra observed throughout the whole outburst are a signature that the radio emission is coming from the self-absorbed compact jets.

We first report our best measured position of MAXI J1348−630, obtained from the weighted average of all the ATCA hard-state compact jet detections at 9 GHz, which are optimal in terms of resolution and signal-to-noise ratio. The Right Ascension (R.A.) and Declination (Dec) of the radio counterpart of MAXI J1348−630 are:

$$\text{R.A. (J2000)} = 13^{\text{h}}48^{\text{m}}12.79^{\text{s}} \pm 0.01^{\text{s}}$$
$$\text{Dec (J2000)} = -63°16'28.6'' \pm 0.2'',$$

which is consistent with the *Swift* localization (Kennea and Negoro, 2019). The associated errors are obtained from the combination in quadrature of the statistical and systematic errors that take into account the distance between the source and the phase calibrator and the accuracy on the position of the phase calibrator itself.

Radio emission was immediately detected at the beginning of the outburst, at a level of ∼3 mJy with ATCA, as the first epoch is on the same day as the first MAXI detection (MJD 58509 – 2019 January 26). As the system became brighter in the hard state, the emission quickly rose, reaching ∼30 mJy with ATCA and MeerKAT on MJD 58515, before the transition to the IMS. In this phase the rising radio emission is consistent with the presence of powerful compact jets. This is confirmed by the positive spectral index, as the flat-to-inverted spectrum is a signature of self-absorbed synchrotron emission, typical of compact radio jets (Blandford and Königl, 1979; Falcke and Biermann, 1996; Heinz and Sunyaev, 2003b). Spectral indices are only computed using strictly simultaneous multi-frequency ATCA observations. We detected a sharp drop in the radio flux density between the ATCA observations of MJD 58519 and 58521, when the 5.5 GHz flux density decreased from ∼135 mJy to ∼52 mJy, before rising again to ∼130 mJy on MJD 58523. A strong radio flare was observed on MJD 58523, when the system reached the peak flux density of ∼486 mJy at 1.28 GHz (Carotenuto et al., 2019). To understand if the flare

peaked before or after our observation, we divided the 15 minutes long scan of MJD 58523 into three chunks of equal length, and we imaged them separately. We found a decreasing flux density ($\sim$1%), which implies that the first flare peak was located before MJD 58523.214 (see Table 5.2). A second, shorter flare ($\sim$150 mJy) was observed some days later with ATCA and ASKAP (Chauhan et al., 2021). We note that the radio flare was accompanied by a significant evolution of the spectral index towards a steep spectrum (from $\alpha \gtrsim 0$ to $\alpha < 0$). The details of the transition are discussed in Section 5.3. During the weeks following the flare, the emission displayed a steep spectrum and quickly decayed until no radio source was detected on MJD 58551, with a 3σ upper limit of 120 μJy beam^{-1}. This is not surprising, as generally no compact jet radio emission is expected for BH XRBs in the soft state (Fender et al., 1999; Corbel et al., 2004b; Fender, Belloni, and Gallo, 2004). Interestingly, optically thin radio emission was again detected between MJD 58573 and 58582, before the transition back to the IMS. The emission faded from $\sim$10 mJy to less than 1 mJy, and its origin is discussed more in detail in Section 7.7.

From MJD 58597, the system re-entered the IMS and then transitioned back to the hard state. During this period, we started to detect again optically thick ($\alpha \gtrsim 0$) radio emission, a clear signature of the re-activation of compact jets (see Figure 5.2), and the radio and X-ray light curves followed the same smooth evolution. We observed a first decay from MJD 58603 to 58628, in which the flux density decreased from $\sim$5 mJy to $\sim$0.13 mJy (at 1.28 GHz, MeerKAT) and the spectrum became more inverted, a behaviour already observed in several BH XRBs (e.g. Fender 2001; Corbel et al. 2013a; Russell et al. 2015). We then tracked the compact jet in a first re-flare, during which the jet flux reached $\sim$6 mJy at 1.28 GHz on MJD 58650, and then slowly faded for $\sim$3 months, while maintaining a flat spectrum, until non-detection on MJD 58711 (3σ upper limit of 135 μJy beam^{-1} with MeerKAT). During this period of non-detection, the monitoring was interrupted, and it was subsequently resumed in October 2019 after the optical re-brightening reported by Al Yazeedi et al. (2019). However, the radio core was not detected during the second, short re-flare. The radio core was detected with MeerKAT and ATCA during the third re-flare (November-December 2019). During the third re-flare the spectrum was consistently flat-to-inverted, when the compact jet re-activated at the $\sim$mJy level, at the same time as the hard-state X-ray re-flare (Figure 5.2), before fading below our detection threshold on MJD 58832. At the faintest level, we clearly detected MAXI J1348−630 at 50 μJy with ATCA at 5.5 and 9 GHz on MJD 58830 and 58831 (2019 December 13–14) with two 12 hours long observations. A fourth, fainter radio flare was observed with MeerKAT in February 2020 (MJD 58887 and 58894), until MAXI J1348−630 went back to quiescence. Our last MeerKAT observations yielded no detection, with a 3σ upper limit of 120 μJy beam^{-1}.

5.3.3 X-ray spectral evolution

Thanks to the dense coverage of MAXI and *Swift*/XRT, the X-ray evolution of MAXI J1348−630 was tracked over almost 6 orders of magnitude in X-ray luminosity, with L_X ranging from 10^{32} to 10^{38} erg s^{-1} in the 1–10 keV energy range, a luminosity interval typical for BH XRBs in outburst (e.g. Corral-Santana et al. 2016). The mass of the BH is not known, but if we assume a 7 $M_\odot$ black hole (see Section 5.1), this corresponds to a range from $\sim 10^{-7}$ to $\sim 10^{-1}$ in units of Eddington luminosity (The Eddington luminosity is $L_{\rm Edd} \sim 1.3 \times 10^{38}$ $(M_{\rm BH}/M_\odot)$ erg s^{-1} for a BH accreting hydrogen). During the first part of the outburst, MAXI J1348−630 performed a whole cycle in the Hardness-Intensity diagram, tracing the complete well-known Q-shape, as can be seen from Figure 5.1. The appearance in succession of a fast rise in X-ray flux, the transition between the hard, intermediate and soft state, a flare episode and an exponential decay

has been already observed in a large number of sources, including, for example, GX 339−4 (e.g Belloni et al. 2005; Tomsick et al. 2008, Tremou et al. *in prep.*), MAXI J1535−571 (Russell et al., 2019c), XTE J1752–223 (Brocksopp et al., 2013), XTE J1550−564 (Sobczak et al., 2000) and H1743−322 (McClintock et al., 2009; Miller-Jones et al., 2012). The first state transition from the hard state to the IMS happened at ∼3 $(M_{\rm BH}/10M_{\odot})$ % $L_{\rm Edd}$, while the following transition to the soft state was at ∼10 $(M_{\rm BH}/10M_{\odot})$ % $L_{\rm Edd}$. The reverse transition to the IMS instead took place at ∼1.5 $(M_{\rm BH}/10M_{\odot})$ % $L_{\rm Edd}$, while the system went back to the hard state at ∼0.4 $(M_{\rm BH}/10M_{\odot})$ % $L_{\rm Edd}$, consistent with the hysteresis observed in the majority of XRBs undergoing a canonical outburst (Maccarone, 2003; Dunn et al., 2010; Kalemci et al., 2013; Vahdat Motlagh, Kalemci, and Maccarone, 2019).

Reflaring behaviour

The following evolution is marked by four smaller re-flares in the hard state, interleaved with periods of quiescence, as shown in Figure 5.2. Re-flares have already been observed in several BH LMXBs (e.g. Chen, Shrader, and Livio 1997; Tomsick, Kalemci, and Kaaret 2004; Homan et al. 2013; Parikh et al. 2019), but these phenomena are not easily explained by the commonly accepted Disk Instability Model (e.g. Lasota 2001) and the mechanism producing them is not yet understood. This behaviour might be due to a smaller amount of available mass in the disk that was not fully replenished after the first flare. Irradiation of the outer accretion disk might also be important in this case. X-ray irradiation illuminates the disk and increases the duration of the outburst by contributing to the disk ionization (Dubus, Hameury, and Lasota, 2001). Once in the soft state, the system transitions between a viscous decay and an irradiation-controlled decay, and these two phases determine different profiles in the X-ray light curve (Tetarenko et al., 2018c). In this context, an irradiation geometry that varies in space or in time could possibly explain the re-flaring episodes observed after the main outburst (Tetarenko et al., 2018c; Tetarenko et al., 2020b). Alternatively, re-flares might also be triggered by increased irradiation from the companion star (Hameury, Lasota, and Warner, 2000). During the re-flares, the source did not exhibit again an hysteresis pattern in the HID, in a similar manner as the 2017/2018 outburst of MAXI J1535−571 (Russell et al., 2019c; Parikh et al., 2019).

Low flux spectral softening

It is interesting to note how the X-ray spectrum becomes softer as the source approaches phases of quiescence. This behaviour has been observed in the majority of BH LMXBs, with the photon index that appears to saturate to $\Gamma \sim 2.2$ in the quiescent state (Corbel, Tomsick, and Kaaret, 2006; Corbel, Koerding, and Kaaret, 2008; Plotkin, Gallo, and Jonker, 2013; Liu et al., 2019). The anti-correlation between the luminosity and Γ in the low luminosity part of the outburst is predicted in the context of Advection-Dominated Accretion Flow (ADAF) models, which are used to describe radiatively inefficient accretion flows (Esin, McClintock, and Narayan, 1997). The spectral softening is explained as a result of the decrease in efficiency at low luminosities of the inverse Compton scattering that is responsible for the hard X-ray emission. Alternatively, compact jets could start to dominate the X-ray emission at low luminosities and synchrotron cooling from the jet, due to increased radiative losses, would produce a steeper X-ray spectrum (Yuan and Cui, 2005), although this scenario has been ruled out for V404 Cyg (Plotkin et al., 2017a). Moreover, synchrotron self-Compton from thermal particles at the base of the jet has also been invoked as a possible explanation for the X-ray emission at low luminosities (Markoff, Nowak, and Wilms, 2005; Poutanen, Veledina, and Revnivtsev, 2014; Plotkin et al., 2015).

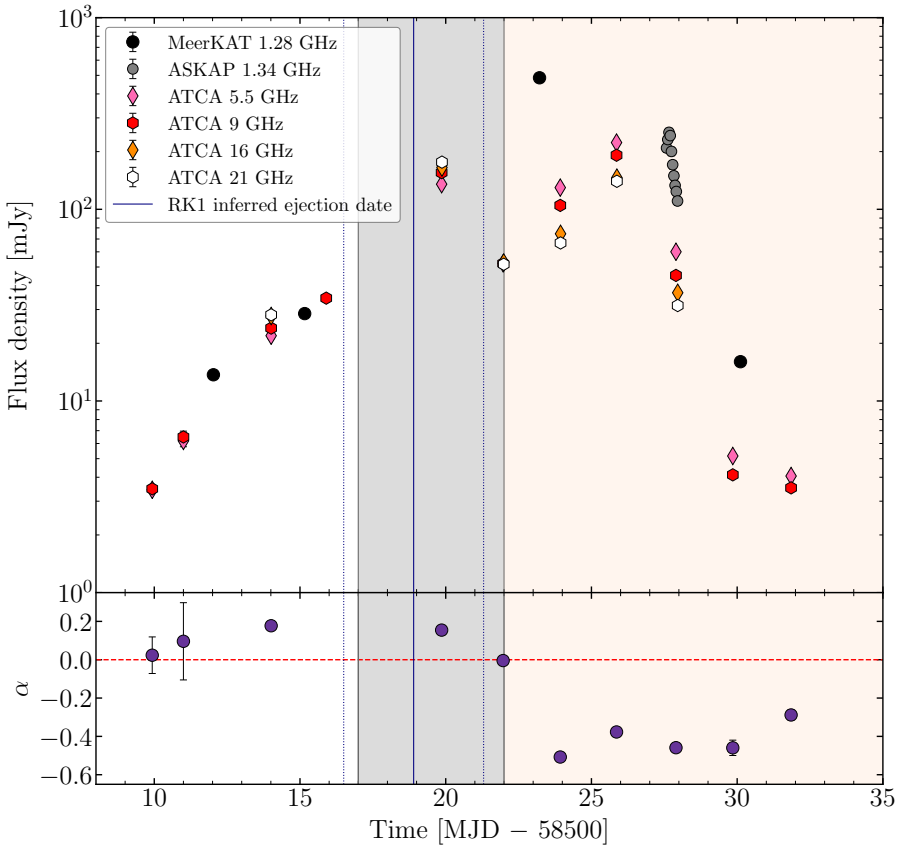

Figure 5.5: First part of the radio light curve at the core location of MAXI J1348−630, as shown in the last two panels of Figure 5.2. We choose here the MJD interval 58508–58535 to clearly follow the evolution of the light curve at different frequencies and of the spectral index. The white regions mark the periods in which the source was in a hard state, while the light grey shaded regions indicate the IMS and the light pink regions indicate the soft state. The dates of the state transitions are obtained from Zhang et al. (2020a). The blue vertical line marks the inferred ejection date of RK1: $t_{\rm ej}$ = MJD 58518.9 ± 2.4 (see Chapter 7), where the two blue dashed lines represent the upper and lower bounds of the $t_{\rm ej}$ confidence interval.

5.3.4 Evolution of the compact jets

The onset and evolution of compact jets in the 2019/2020 outburst of MAXI J1348−630 has been detected and tracked with the radio monitoring performed with MeerKAT and ATCA. According to the standard model, compact jets emit self-absorbed synchrotron radiation (Blandford and Königl, 1979). The resulting spectrum is flat or slightly inverted at radio frequencies, with a turnover frequency observed in the near infrared band (Corbel and Fender, 2002; Russell et al., 2013b). Our observations followed the rise of the compact radio jets during the initial hard state and followed it through the transition to the IMS and then to the soft state.

To better visualize the jet behaviour in this phase, we show in Figure 5.5 the radio light curve at the core location for the first 25 days of the outburst, taken from Figure 5.2. The compact jet emission peaks on MJD 58520 and then starts to decay on MJD 58521, one day before the system enters in the soft state and two days after the inferred RK1 ejection date (see Section 7.5). This whole evolution is accompanied by a smooth transition between the optically thick and the optically thin regimes of synchrotron radio emission. Compact jets are usually observed to quench at the transition from the hard to soft state (e.g. Fender et al. 1999; Corbel et al. 2000). This phenomenon is observed to start at higher frequencies (where the emission

is produced closer to the compact object) and terminate as the jet break evolves through the radio band (Russell et al., 2013a; Russell et al., 2014; Russell et al., 2020). It is not yet clear if compact jets switch off before or during the launch of discrete ejections, and how (or if) the two events are linked (Russell et al., 2020). We do not have a MeerKAT observation on MJD 58521, but, as the flat spectrum obtained with ATCA suggests, the flux density would have been at the ∼50 mJy level. The following observations show instead a quick rise in flux density and a subsequent decay until MJD 58531, when the source is steadily in the soft state. With our data, we cannot conclude on the origin of the radio emission on MJD 58521, which could be produced either from the compact jet that is quenching (with no evidence of the spectral break in the radio band), or by the first self-absorbed part of the radio flare observed to peak on MJD 58523. The latter scenario implies that the jet significantly quenched in less than two days, a shorter timescale with respect to what observed for other sources (e.g. Russell et al. 2013a; Russell et al. 2020). Therefore, we are not able to precisely order in time the ejection of RK1 and the quenching of the compact jets, and thus we cannot draw conclusions on a potential link between the two events.

Jet quenching factor

During the soft state, we detect no radio emission from the compact jets, hence we can place constraints on the jet quenching factor by using the highest flux density compatible with the compact jet in hard state and the lowest upper limit on the non-detection during the following soft state. We find a ∼3.5 orders of magnitude quenching factor, which is, so far, one of the strongest constraints on the suppression of compact jets during the soft state of a BH LMXB (Coriat et al., 2011; Russell et al., 2019c; Maccarone et al., 2020).

5.4 The distance to MAXI J1348−630

The distance to any astrophysical object is a fundamental physical parameter, as it allows us to determine physical quantities from observables. The parallax is the best model-independent method for estimating distances, but the measured parallax is extremely small (at the mas level) for the typical XRB distances of few kpc. Therefore, instruments capable of probing sub-milliarcsecond scales are required, and this can be achieved either with *Gaia* (Gaia Collaboration et al., 2018) or with radio VLBI measurements (imaging the compact jets, e.g. Atri et al. 2020). However, a high-precision trigonometric parallax measurement is not possible for most BH XRBs. Other methods valid for XRBs include studying the lines in the IR/optical spectra of the companion star (Jonker and Nelemans, 2004), or the motion of bipolar discrete ejecta (Mirabel and Rodríguez, 1994). However, these methods provide large uncertainties on the estimated distance. Moreover, if no bipolar jets are detected (as for most of XRBs) and if the companion star is too faint (due to the high extinction) then other methods must be used. We discuss in this section two model-dependent methods that were used to estimate the distance of MAXI J1348−630, and we start with neutral hydrogen absorption, for which I have contributed with our MeerKAT data (Chauhan et al., 2021).

5.4.1 H I absorption

In order to estimate the distance of a radio-emitting XRB, it is possible to use the Doppler shifted 21 cm absorption line of neutral hydrogen (H I), as intervening interstellar clouds are

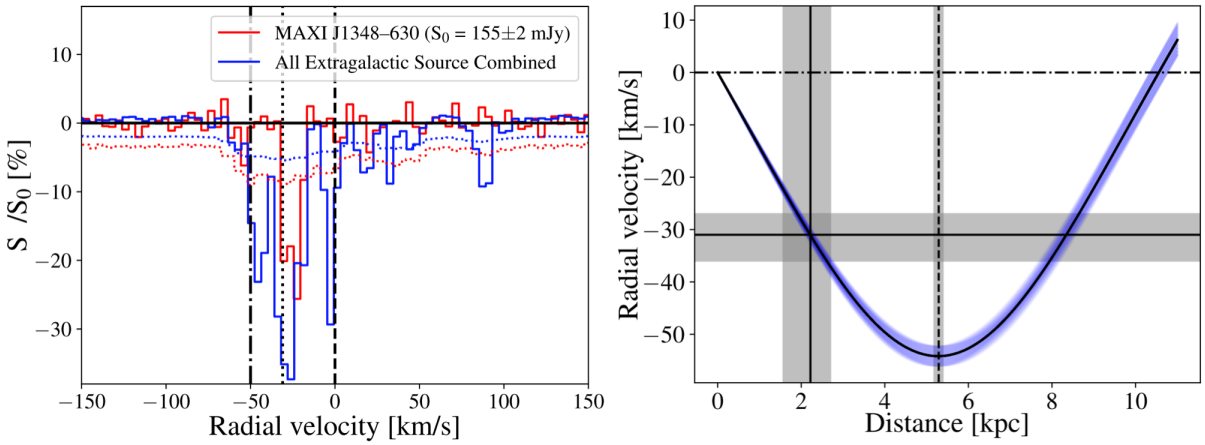

Figure 5.6: *Left:* The H I absorption complex observed with ASKAP in the direction of MAXI J1348−630. The flux S is calculated from the spectral cube and S_0 is measured from the continuum ASKAP image. The red and blue curves show the H I absorption against MAXI J1348−630 and the stack of the eight extragalactic sources, respectively. The dotted lines represent the 3σ noise levels for each channel taken from nearby source-free regions. The black dashed vertical line marks the rest frequency of the H I line. The dotted (-31 km s^{-1}) and dot-dashed vertical (-50 km s^{-1}) lines mark, respectively, the maximum negative radial velocities observed from the spectra of MAXI J1348−630, and from the spectra of the merged extragalactic sources. From Chauhan et al. (2021).
Right: The variation of the predicted velocity of the local standard of rest ($V_{\rm LSR}$) as a function of distance from the Sun (D). The black line represents the expected curve, and the blue shaded region shows the effect of incorporating the 1σ uncertainties on the Galactic rotation parameters from Reid et al. (2014). The horizontal solid line shows the maximum negative radial velocity (with respect to the LSR) measured from the H I absorption spectrum (see left panel). The solid and dashed vertical lines show the most likely distance and the tangent point distance, respectively. The grey shaded regions represent the 1σ uncertainties. The preferred distance of MAXI J1348−630 is the near kinematic distance of $2.2^{+0.5}_{-0.6}$ kpc. From Chauhan et al. (2021).

presumed to follow the rotation of the Milky Way and their absorption features allow us to constrain the kinematic distance to the source (Gathier, Pottasch, and Goss, 1986; Koribalski et al., 1995; Dhawan, Goss, and Rodríguez, 2000; Chauhan et al., 2019). When the source is located beyond the Solar circle, the kinematic distance estimates obtained from this method are accurate, but can suffer from ambiguities if the source is located within the Solar circle, since only the radial velocity can be measured, and this leads to two distance estimates (near and far) for a single velocity measurement.

In this section, we present how the H I absorption spectra from the Australian Square Kilometre Array Pathfinder (ASKAP, Hotan et al. 2014) and MeerKAT observations have been used to constrain the distance to MAXI J1348−630, as published in Chauhan et al. (2021). ASKAP observed MAXI J1348−630 on 2019 February 13 for 9.91 hr using the full array of 36 dishes, with 36 overlapping beams. The large field of view ($\simeq 30$ deg^2) of ASKAP allowed made possible to simultaneously detect the H I absorption towards both MAXI J1348−630 and a set of nearby extragalactic sources, enabling a discrimination between near and far kinematic distances. The observation were performed at a central frequency of 1.34 GHz, with a total bandwidth of 288 MHz divided into 15368 fine channels, each with an individual bandwidth of 18.519 kHz, corresponding to a velocity resolution of 3.9 km s^{-1}. The full data processing is described in Chauhan et al. (2021).

In the left panel of Figure 5.6, we show the spectrum for MAXI J1348−630, together with a stacked spectrum for all eight extragalactic sources, and the 3σ noise levels measured from

nearby region. H I absorption complexes are detected with a significance higher than 3σ, out to maximum negative velocities with respect to the local standard of rest (LSR) of -31 ± 4 km s^{-1} for MAXI J1348−630 and -50 ± 4 km s^{-1} for the extragalactic sources.

To obtain the distance to MAXI J1348−630, the Galactic rotation curve is computed for the Galactic longitude l of our source, and the variation of the radial velocity ($V_{\rm LSR}$) of the LSR as a function of distance from the Sun (D) is determined. The Galactic rotation curve is assumed to be flat, so that the Milky Way is rotating with a circular velocity (V_0) of 240 ± 8 km s^{-1} and that the Sun is located at a distance $R_0 = 8.34 \pm 0.16$ kpc from the Galactic centre (Reid et al., 2014). The obtained radial velocity curve is shown in the right panel of Figure 5.6. We can see that the LSR radial velocities are negative within a few kpc of the Sun, and comparing the curve with the H I spectrum allows us to determine the near distance, the far distance, and the tangent point distance ($R_{\rm T} = R_0 \cos l = 5.3 \pm 0.1$ kpc) for this line of sight. The uncertainties on the distances are obtained by taking into account the uncertainties on the Milky Way rotation curve, following the recipe of Wenger et al. (2018). Hence, the obtained values for the near and far distances of MAXI J1348−630 are $2.2^{+0.5}_{-0.6}$ and $8.4^{+0.6}_{-0.6}$ kpc. The next step is too discriminate between these two values. First, we note that the maximum negative absorption velocity observed for the extragalactic sources (-50 ± 4 km s^{-1}), which is due to more distant clouds, is consistent with the tangent point velocity for this line of sight (-54 ± 4 km s^{-1}). However, H I absorption at the tangent point velocity is not observed towards MAXI J1348−630, implying that our source must lie closer than $R_{\rm T}$, hence pointing to the near kinematic distance of $D = 2.2^{+0.5}_{-0.6}$ kpc.

The MeerKAT H I spectrum of MAXI J1348−630 (obtained from the coarse 4k-channels mode) is consistent with the re-binned ASKAP spectrum, highlighting the potential of the eventual capabilities of MeerKAT for XRB spectral line studies.

5.4.2 X-ray light echoes

The distance to MAXI J1348−630 was estimated also by Lamer et al. (2021), which used the detection with the X-ray telescope *SRG*/eROSITA of X-ray light echoes from giant dust-scattering rings. We briefly explain here this method and its results for MAXI J1348−630.

Dust grains in the ISM affects X-rays, both with photo-electric absorption and with scattering at small angles. The scattered radiation can form a halo around the X-ray emitting point source. Since the optical path of the scattered light is longer than the path of the direct light from the source, brightness variations of the central source appear with a delay in the *echo* of the dust scattering halo. The produced echoes can be used to obtain the geometrical distances of X-ray sources (Trümper and Schönfelder, 1973; Predehl et al., 2000). However, most X-ray sources are variable on all timescales, and hence the variability of the halo, which is the convolution of the source variability and the impulse response of the halo, is often very complex. Therefore, X-ray binaries with bright, but transitory outbursts are the ideal sources for the application of this method, since for them the light echoes will be well-defined and will simply grow in time. For dust scattering rings of known distance (possibly from other observations) the distance of the source that illuminated them can be calculated using the ring radius and the time lag of the scattered X-rays.

Lamer et al. (2021) discovered a giant dust scattering ring around MAXI J1348−630 with *SRG*/eROSITA (Merloni et al., 2012) during its first X-ray all-sky survey. During the discovery observation, in February 2020, the ring had an outer diameter of 1.3 deg, growing to 1.6 deg by the time of the second all sky survey scan in August 2020. The two images are shown in

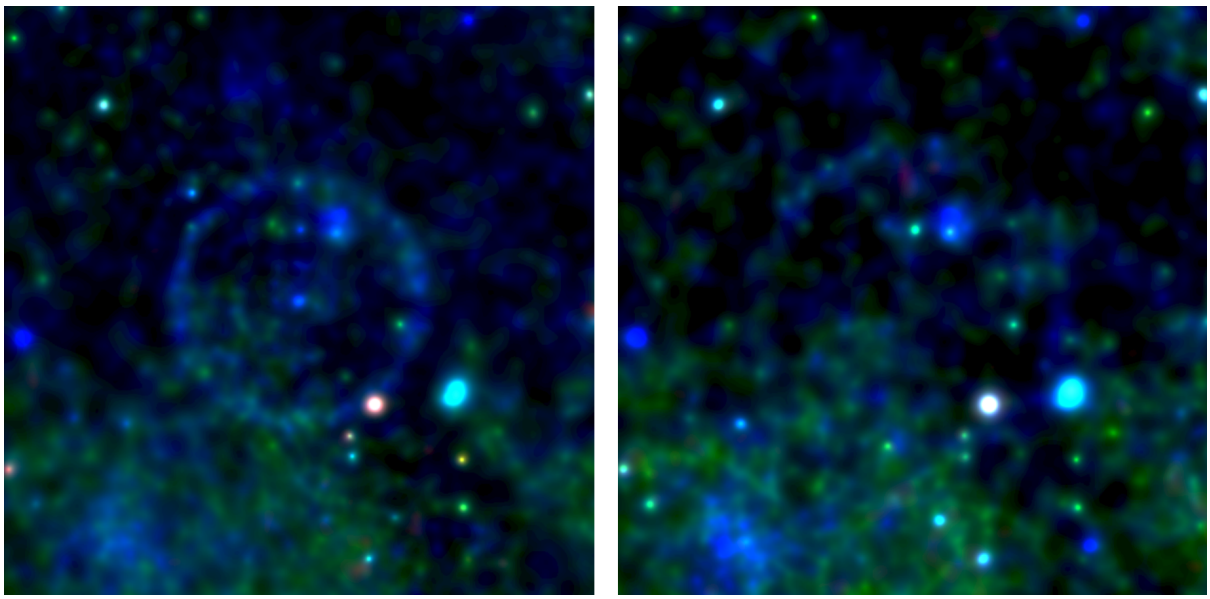

Figure 5.7: *Left*: False-colour 3° × 3° image of the eRASS1 (eROSITA All-Sky Survey, February 2020) observation, combining the energy bands 0.2–0.6 keV (red), 0.6–1.0 keV (green) and 1.0–2.3 keV (blue). *Right*: The same observation, but from eRASS2 (August 2020). From Lamer et al. (2021).

Figure 5.7. Since the ring distance of 2050 pc is known from extinction mapping performed by *Gaia*, it is possible to obtain the distance of MAXI J1348−630 from the measured time lags and the geometry of the ring. Lamer et al. (2021) find that MAXI J1348−630 is located at a distance of 3390 pc with a statistical uncertainty of 1.1% and a systematic uncertainty of 10%, coming from the *Gaia* data. With a final distance $D = 3.39 \pm 0.34$ kpc, this method provides results that are in mild tension with the distance obtained with H I absorption. Such tension could be potentially solved with a VLBI parallax measurement during a new outburst phase.

5.5 Tabulated data

5.5.1 Radio data

Table 5.2: Radio flux densities S_ν of MAXI J1348−630. Observation MJDs represent the middle of the observation, where errors represent the observation duration (time on source). The reported frequency is the central value of the used band, whose bandwidth is 856 MHz for MeerKAT and 2 GHz for ATCA. For the ATCA observations we report the array configuration as a subscript. The spectral index α of each component ($S_\nu \propto \nu^\alpha$) is computed only for simultaneous ATCA multi frequency observations. Upper limits are reported at the 3σ level

Calendar date [UT]	MJD	Telescope	Frequency [GHz]	$S_{\nu,\mathrm{core}}$ [mJy]	α_{core}
2019-01-26	58509.93 ± 0.09	$\mathrm{ATCA_{H75}}$	5.5	3.44 ± 0.11	0.02 ± 0.09
			9	3.48 ± 0.12	
2019-01-28	58511.00 ± 0.13	$\mathrm{ATCA_{H75}}$	5.5	6.19 ± 0.42	0.1 ± 0.2
			9	6.49 ± 0.47	
2019-01-29	58512.029 ± 0.007	MeerKAT	1.3	13.70 ± 0.05	
2019-01-31	58514.01 ± 0.09	$\mathrm{ATCA_{H75}}$	5.5	21.9 ± 0.8	0.18 ± 0.02

Continued on the next page

Table 5.2: Continued from the previous page. Radio flux densities S_ν of MAXI J1348−630.

Calendar date [UT]	MJD	Telescope	Frequency [GHz]	$S_{\nu,\mathrm{core}}$ [mJy]	α_{core}
			9	24.0 ± 0.5	
			16.7	27.76 ± 0.20	
			21.2	28.49 ± 0.22	
2019-02-01	58515.161 ± 0.005	MeerKAT	1.3	28.57 ± 0.12	
2019-02-01	58515.90 ± 0.21	$\mathrm{ATCA_{H75}}$	8	34.4 ± 1.4	
2019-02-05	58519.860 ± 0.003	$\mathrm{ATCA_{H75}}$	5.5	135.3 ± 0.9	0.155 ± 0.003
			9	155.4 ± 0.4	
	58519.870 ± 0.003		16.7	165.2 ± 0.4	
			21.2	176.3 ± 0.4	
2019-02-07	58521.97 ± 0.09	$\mathrm{ATCA_{H75}}$	5.5	52.27 ± 0.06	-0.004 ± 0.003
			9	52.13 ± 0.08	
	58521.99 ± 0.07		16.7	52.8 ± 0.6	
			21.2	51.68 ± 0.6	
2019-02-09	58523.219 ± 0.005	MeerKAT	1.3	485.6 ± 1.6	
2019-02-09	58523.93 ± 0.06	$\mathrm{ATCA_{H75}}$	5.5	129.8 ± 1.5	-0.508 ± 0.009
			9	105 ± 1	
	58523.94 ± 0.03		16.7	74.5 ± 0.4	
			21.2	66.7 ± 0.5	
2019-02-11	58525.861 ± 0.003	$\mathrm{ATCA_{H75}}$	5.5	223.0 ± 0.7	-0.377 ± 0.003
			9	191.5 ± 0.5	
	58525.871 ± 0.003		16.7	146.3 ± 0.3	
			21.2	140.0 ± 0.5	
2019-02-13	58527.9 ± 0.1	$\mathrm{ATCA_{H75}}$	5.5	60.0 ± 0.5	-0.46 ± 0.01
			9	45.2 ± 1.4	
	58527.96 ± 0.07		16.7	36.7 ± 0.4	
			21.2	31.5 ± 0.5	
2019-02-15	58529.85 ± 0.02	$\mathrm{ATCA_{H75}}$	5.5	6.27 ± 0.04	-0.46 ± 0.04
			9	4.54 ± 0.03	
2019-02-16	58530.114 ± 0.005	MeerKAT	1.3	16.0 ± 0.2	
2019-02-17	58531.85 ± 0.02	$\mathrm{ATCA_{H75}}$	5.5	5.17 ± 0.03	-0.29 ± 0.03
			9	3.61 ± 0.03	
2019-02-23	58537.092 ± 0.005	MeerKAT	1.3	2.06 ± 0.04	
2019-03-01	58543.076 ± 0.005	MeerKAT	1.3	1.51 ± 0.04	
2019-03-09	58551.100 ± 0.005	MeerKAT	1.3	<0.12	
2019-03-18	58560.075 ± 0.005	MeerKAT	1.3	<0.12	
2019-03-25	58567.074 ± 0.005	MeerKAT	1.3	<0.12	
2019-03-31	58573.76 ± 0.11	$\mathrm{ATCA_{6A}}$	5.5	8.48 ± 0.12	-0.37 ± 0.04
			9	7.06 ± 0.11	
2019-04-01	58574.061 ± 0.005	MeerKAT	1.3	8.09 ± 0.07	
2019-04-08	58581.72 ± 0.18	$\mathrm{ATCA_{H75}}$	5.5	9.36 ± 0.13	-0.37 ± 0.03
			9	7.78 ± 0.08	

Continued on the next page

Table 5.2: Continued from the previous page. Radio flux densities S_ν of MAXI J1348−630.

Calendar date [UT]	MJD	Telescope	Frequency [GHz]	$S_{\nu,\mathrm{core}}$ [mJy]	α_{core}
2019-04-09	58582.053 ± 0.005	MeerKAT	1.3	9.35 ± 0.09	
2019-04-15	58588.053 ± 0.005	MeerKAT	1.3	<0.14	
2019-04-16	58589.81 ± 0.11	$\mathrm{ATCA}_{750\mathrm{C}}$	5.5	<0.12	
			9	<0.045	
2019-04-20	58593.074 ± 0.005	MeerKAT	1.3	<0.12	
2019-04-29	58602.144 ± 0.005	MeerKAT	1.3	4.73 ± 0.04	
2019-04-30	58603.31 ± 0.08	$\mathrm{ATCA}_{750\mathrm{C}}$	5.5	8.68 ± 0.14	0.09 ± 0.05
			9	9.09 ± 0.18	
2019-05-04	58607.908 ± 0.005	MeerKAT	1.3	3.43 ± 0.04	
2019-05-05	58608.68 ± 0.21	$\mathrm{ATCA}_{1.5\mathrm{B}}$	8.4	2.75 ± 0.05	
2019-05-09	58612.44 ± 0.04	$\mathrm{ATCA}_{1.5\mathrm{B}}$	5.5	0.77 ± 0.02	0.21 ± 0.02
			9	0.75 ± 0.11	
			17	0.95 ± 0.02	
			19	0.96 ± 0.03	
2019-05-11	58614.909 ± 0.005	MeerKAT	1.3	0.32 ± 0.04	
2019-05-14	58617.47 ± 0.06	$\mathrm{ATCA}_{1.5\mathrm{B}}$	5.5	0.71 ± 0.02	0.27 ± 0.03
			9	0.88 ± 0.11	
			17	0.96 ± 0.04	
			19	1.03 ± 0.03	
2019-05-18	58621.888 ± 0.005	MeerKAT	1.3	0.27 ± 0.04	
2019-05-25	58628.019 ± 0.005	MeerKAT	1.3	0.13 ± 0.04	
2019-05-26	58629.340 ± 0.045	$\mathrm{ATCA}_{6\mathrm{A}}$	5.5	0.153 ± 0.011	0.0 ± 0.2
			9	0.150 ± 0.010	
2019-05-31	58634.896 ± 0.005	MeerKAT	1.3	0.79 ± 0.06	
2019-06-08	58642.878 ± 0.005	MeerKAT	1.3	3.99 ± 0.05	
2019-06-09	58643.46 ± 0.10	$\mathrm{ATCA}_{6\mathrm{A}}$	5.5	4.09 ± 0.02	−0.03 ± 0.02
			9	4.02 ± 0.03	
2019-06-16	58650.881 ± 0.005	MeerKAT	1.3	6.25 ± 0.09	
2019-06-24	58658.797 ± 0.005	MeerKAT	1.3	4.60 ± 0.04	
2019-06-26	58660.27 ± 0.10	$\mathrm{ATCA}_{6\mathrm{A}}$	5.5	4.18 ± 0.04	0.05 ± 0.03
			9	4.28 ± 0.05	
2019-06-30	58664.724 ± 0.005	MeerKAT	1.3	4.95 ± 0.05	
2019-07-07	58671.861 ± 0.005	MeerKAT	1.3	2.29 ± 0.03	
2019-07-14	58678.912 ± 0.005	MeerKAT	1.3	1.66 ± 0.03	
2019-07-22	58686.860 ± 0.005	MeerKAT	1.3	1.11 ± 0.03	
2019-07-25	58689.44 ± 0.22	$\mathrm{ATCA}_{750\mathrm{C}}$	5.5	1.19 ± 0.01	−0.02 ± 0.03
			9	1.18 ± 0.02	
2019-07-27	58691.750 ± 0.005	MeerKAT	1.3	0.70 ± 0.03	
2019-08-04	58699.713 ± 0.005	MeerKAT	1.3	0.44 ± 0.04	
2019-08-10	58705.765 ± 0.005	MeerKAT	1.3	0.14 ± 0.04	
2019-08-16	58711.867 ± 0.005	MeerKAT	1.3	<0.14	

Continued on the next page

Table 5.2: Continued from the previous page. Radio flux densities S_ν of MAXI J1348−630.

Calendar date [UT]	MJD	Telescope	Frequency [GHz]	$S_{\nu,\mathrm{core}}$ [mJy]	α_{core}
2019-08-21	58716.22 ± 0.10	$\mathrm{ATCA}_{750\mathrm{C}}$	5.5	<0.033	
			9	<0.033	
2019-08-23	58718.658 ± 0.005	MeerKAT	1.3	<0.11	
2019-08-31	58726.741 ± 0.005	MeerKAT	1.3	<0.12	
2019-09-01	58727.08 ± 0.13	$\mathrm{ATCA}_{6\mathrm{A}}$	5.5	<0.033	
			9	<0.024	
2019-10-19	58775.616 ± 0.005	MeerKAT	1.3	<0.15	
2019-10-26	58782.597 ± 0.005	MeerKAT	1.3	<0.15	
2019-11-01	58788.670 ± 0.005	MeerKAT	1.3	<0.18	
2019-11-02	58789.183 ± 0.045	$\mathrm{ATCA}_{750\mathrm{C}}$	5.5	<0.09	
			9	<0.09	
2019-11-10	58797.408 ± 0.005	MeerKAT	1.3	<0.12	
2019-11-18	58805.403 ± 0.005	MeerKAT	1.3	<0.12	
2019-11-24	58811.345 ± 0.005	MeerKAT	1.3	0.50 ± 0.03	
2019-11-27	58814.72 ± 0.09	$\mathrm{ATCA}_{1.5\mathrm{C}}$	5.5	1.07 ± 0.01	0.31 ± 0.04
			9	1.24 ± 0.02	
2019-11-30	58817.449 ± 0.005	MeerKAT	1.3	0.47 ± 0.03	
2019-12-03	58820.73 ± 0.13	$\mathrm{ATCA}_{1.5\mathrm{C}}$	5.5	0.56 ± 0.01	0.19 ± 0.06
			9	0.61 ± 0.01	
2019-12-07	58824.396 ± 0.005	MeerKAT	1.3	0.16 ± 0.03	
2019-12-10	58827.75 ± 0.16	$\mathrm{ATCA}_{1.5\mathrm{C}}$	5.5	0.15 ± 0.01	0.9 ± 0.2
			9	0.21 ± 0.01	
2019-12-13	58830.82 ± 0.24	$\mathrm{ATCA}_{1.5\mathrm{C}}$	5.5	0.053 ± 0.007	0.4 ± 0.3
			9	0.065 ± 0.005	
2019-12-14	58831.82 ± 0.24	$\mathrm{ATCA}_{1.5\mathrm{C}}$	5.5	0.054 ± 0.006	−0.3 ± 0.3
			9	0.046 ± 0.005	
2019-12-15	58832.387 ± 0.005	MeerKAT	1.3	<0.12	
2019-12-20	58837.428 ± 0.005	MeerKAT	1.3	<0.12	
2019-12-28	58845.272 ± 0.005	MeerKAT	1.3	<0.15	
2020-01-03	58851.397 ± 0.005	MeerKAT	1.3	<0.18	
2020-02-08	58887.185 ± 0.005	MeerKAT	1.3	0.38 ± 0.03	
2020-02-15	58894.147 ± 0.005	MeerKAT	1.3	0.22 ± 0.02	
2020-02-21	58900.236 ± 0.005	MeerKAT	1.3	<0.12	
2020-03-02	58910.147 ± 0.005	MeerKAT	1.3	<0.12	

5.5.2 X-ray data

Table 5.3: X-ray spectral parameters of MAXI J1348−630 obtained from *Swift*/XRT observations. The models used are discussed in Section 5.2.3 and interstellar absorption is accounted for adopting $N_{\rm H} = 0.86 \times 10^{22}$ cm^{-2} . We report the annulus inner and outer radii of the spectrum extraction region in pixels (1 pixel = 2.357 arcsec) and the source spectral state. We then show the obtained unabsorbed 1–10 keV flux in units of 10^{-10} erg cm^{-2} s^{-1}, the photon index Γ, the accretion disk inner temperature $k_{\rm B}T_{\rm in}$ in keV units (for the epochs in which the `diskbb` component was needed) and the reduced χ^2 over the degrees of freedom of the fit. Epochs for which the χ^2 is not reported were fitted using Cash statistics due to low number of counts. Throughout this table, we quote 90% confidence errors. To fit the table in the page, we removed the initial two "0" for each ObsID.

ObsID	Day [UT]	MJD[a]	Exposure time [s]	Extraction region	Spectral state	Unabsorbed flux 1–10 keV[b]	Γ	$k_{\rm B}T_{\rm in}$ [keV]	χ^2/d.o.f
885807000[c]	2019-01-26	58509.438	1221	0−20	HS	$38.13^{+0.35}_{-0.35}$	$1.41^{+0.01}_{-0.01}$		0.99/618
885960000	2019-01-27	58510.038	1453	3−30	HS	$95.57^{+0.72}_{-0.72}$	$1.52^{+0.01}_{-0.01}$		1.09/646
886266000	2019-01-28	58511.576	1838	6−30	HS	$313.9^{+1.7}_{-1.7}$	$1.783^{+0.008}_{-0.008}$		1.06/682
886496000	2019-01-29	58512.420	317	7−30	HS	$375.6^{+4.7}_{-4.6}$	$1.73^{+0.02}_{-0.02}$		1.00/487
011107001	2019-01-30	58513.108	832	10−30	HS	$484.1^{+3.9}_{-3.9}$	$1.836^{+0.012}_{-0.012}$		0.98/613
088843001	2019-02-01	58515.753	2019	12−30	HS	$625.3^{+3.4}_{-2.7}$	$1.898^{+0.008}_{-0.008}$		1.14/673
011107002	2019-02-03	58517.672	868	12−30	IMS	$707.0^{+4.6}_{-5.7}$	$2.10^{+0.01}_{-0.01}$		1.02/585
011107003	2019-02-05	58519.335	1370	17−30	IMS	$1143.0^{+9.5}_{-9.5}$	$2.25^{+0.06}_{-0.05}$	$0.63^{+0.02}_{-0.02}$	1.06/581
011107004	2019-02-07	58521.074	1750	31−50	IMS	2164^{+14}_{-14}	2.4	$0.743^{+0.009}_{-0.009}$	1.25/528
011107005	2019-02-09	58523.000	219	28−50	SS	2594^{+44}_{-44}	2.4	$0.823^{+0.014}_{-0.014}$	1.16/296
011107006	2019-02-09	58523.450	1412	33−50	SS	2444^{+16}_{-16}	2.4	$0.759^{+0.007}_{-0.007}$	1.11/525
011107007	2019-02-10	58524.526	760	33−50	SS	2670^{+23}_{-23}	2.4	$0.729^{+0.009}_{-0.009}$	1.03/461
011107008	2019-02-11	58525.774	1472	33−50	SS	2314^{+15}_{-15}	2.4	$0.719^{+0.007}_{-0.007}$	1.14/517
011107009	2019-02-12	58526.257	1120	32−50	SS	2670^{+18}_{-18}	2.4	$0.735^{+0.007}_{-0.007}$	1.13/474
011107010	2019-02-13	58527.440	1462	32−50	SS	2590^{+16}_{-16}	2.4	$0.763^{+0.007}_{-0.007}$	1.17/533
011107011	2019-02-16	58530.28	1462	32−50	SS	2217^{+14}_{-14}	2.4	$0.682^{+0.005}_{-0.005}$	1.03/469
011107012	2019-02-17	58531.362	1457	31−50	SS	2181^{+26}_{-25}	2.4	$0.674^{+0.005}_{-0.005}$	1.05/484
011107013	2019-02-19	58533.547	1023	30−50	SS	1847^{+14}_{-14}	2.4	$0.664^{+0.007}_{-0.007}$	0.99/449
011107014	2019-02-21	58535.800	1128	30−50	SS	1905^{+13}_{-13}	2.4	$0.657^{+0.006}_{-0.006}$	1.04/438
011107015	2019-03-02	58544.918	1100	26−50	SS	1655^{+11}_{-11}	2.4	$0.636^{+0.006}_{-0.006}$	1.03/435
011107016	2019-03-05	58547.835	1003	25−50	SS	1496^{+10}_{-10}	2.4	$0.645^{+0.006}_{-0.006}$	1.06/453
088843002	2019-03-08	58550.497	2081	22−50	SS	1501^{+9}_{-9}	2.4	$0.642^{+0.005}_{-0.005}$	1.05/474
011107017	2019-03-11	58553.873	935	17−30	SS	$1233^{+7.7}_{-7.7}$	2.4	$0.624^{+0.006}_{-0.006}$	1.06/424
011107019	2019-03-17	58559.134	1191	15−30	SS	$873.4^{+5.1}_{-5.1}$	2.4	$0.624^{+0.004}_{-0.004}$	1.04/406
011107020	2019-03-20	58562.049	999	15−30	SS	$849.3^{+5.6}_{-5.6}$	2.4	$0.629^{+0.006}_{-0.006}$	1.07/422
011107021	2019-03-23	58565.820	1102	13−30	SS	$643.5^{+3.7}_{-3.7}$	2.4	$0.601^{+0.005}_{-0.005}$	1.03/401
011107022	2019-03-26	58568.025	1008	13−30	SS	$629.1^{+3.8}_{-3.8}$	2.4	$0.600^{+0.005}_{-0.005}$	1.05/402

Continued on the next page

Table 5.3: Continued from the previous page. X-ray spectral parameters of MAXI J1348−630 obtained from *Swift*/XRT observations.

ObsID	Day [UT]	MJD[a]	Exposure time [s]	Extraction region	Spectral state	Unabsobed flux 1–10 keV[b]	Γ	$k_{\rm B}T_{\rm in}$ [keV]	χ^2/d.o.f
011107024	2019-04-01	58574.383	1023	12−30	SS	$569.1^{+3.6}_{-3.6}$	2.4	$0.573^{+0.005}_{-0.005}$	1.06/422
011107025	2019-04-04	58577.239	1572	13−30	SS	$542.2^{+2.6}_{-2.6}$	2.4	$0.544^{+0.003}_{-0.003}$	1.05/401
011107026	2019-04-10	58583.029	1224	11−30	SS	$415.5^{+2.4}_{-2.4}$	2.4	$0.551^{+0.004}_{-0.004}$	1.00/384
011107027	2019-04-12	58585.209	977	11−30	SS	$442.4^{+2.8}_{-2.8}$	2.4	$0.563^{+0.004}_{-0.004}$	1.17/362
011107028	2019-04-15	58588.727	1018	12−30	SS	$443.5^{+2.8}_{-2.8}$	2.4	$0.518^{+0.004}_{-0.004}$	1.17/345
011107029	2019-04-24	58597.045	1013	10−30	IMS	$326.7^{+2.1}_{-2.1}$	2.4	$0.491^{+0.004}_{-0.004}$	0.95/314
011107032	2019-05-03	58606.396	529	2−30	HS	$46.4^{+0.5}_{-0.6}$	$2.28^{+0.03}_{-0.03}$		1.11/391
011107033	2019-05-06	58609.474	875	0−20	HS	$21.5^{+0.3}_{-0.3}$	$1.86^{+0.02}_{-0.02}$		1.10/435
011107034	2019-05-09	58612.438	975	0−20	HS	$9.11^{+0.26}_{-0.26}$	$1.66^{+0.04}_{-0.04}$		1.17/256
011107035	2019-05-12	58615.972	604	0−20	HS	$2.80^{+0.13}_{-0.13}$	$1.76^{+0.07}_{-0.07}$		0.88/107
011107036	2019-05-15	58618.746	1080	0−20	HS	$1.29^{+0.07}_{-0.07}$	$1.98^{+0.09}_{-0.09}$		1.18/70
011107037	2019-05-18	58621.397	913	0−20	HS	$0.59^{+0.02}_{-0.04}$	$1.96^{+0.11}_{-0.11}$		
011107038	2019-05-21	58624.075	602	0−20	HS	$0.29^{+0.03}_{-0.03}$	$2.88^{+0.26}_{-0.25}$		
011107039	2019-05-24	58627.445	993	0−20	HS	<0.59			
011107040	2019-05-27	58630.699	986	0−20	HS	$0.52^{+0.04}_{-0.04}$	$1.87^{+014}_{-0.13}$		0.89/31
011107041	2019-05-30	58633.148	861	0−20	HS	$4.74^{+0.14}_{-0.12}$	$1.53^{+0.04}_{-0.04}$		1.07/219
011107042	2019-06-05	58639.659	998	0−20	HS	$45.5^{+0.4}_{-0.4}$	$1.64^{+0.01}_{-0.01}$		0.98/600
011107043	2019-06-13	58647.781	1070	0−20	HS	$128.2^{+1.9}_{-1.9}$	$1.87^{+0.02}_{-0.02}$		1.08/468
011107044	2019-06-16	58650.831	998	0−20	HS	$99.3^{+1.5}_{-1.5}$	$1.81^{+0.03}_{-0.03}$		1.04/415
011107045	2019-07-21	58685.017	935	0−20	HS	$27.2^{+0.3}_{-0.3}$	$1.54^{+0.02}_{-0.02}$		0.88/547
011107047[d]	2019-07-26	58690.131	918	0−20	HS	$19.3^{+0.4}_{-0.4}$	$1.39^{+0.03}_{-0.03}$		1.03/325
011107048	2019-08-04	58699.836	988	0−20	HS	$0.98^{+0.06}_{-0.05}$	$1.56^{+0.10}_{-0.10}$		1.09/55
011107049	2019-08-11	58706.413	898	0−20	HS	$0.071^{+0.012}_{-0.007}$	$2.64^{+0.35}_{-0.34}$		
011107050	2019-08-18	58713.044	928	0−20	HS	<0.083			
011107051	2019-08-25	58720.155	673	0−20	HS	<0.048			
011107052	2019-08-31	58726.999	3024	0−20	HS	<0.002			
011107054[e]	2019-09-02	58728.059	1115	0−20	HS	<0.005			
011107055	2019-09-08	58734.030	1702	0−20	HS	<0.003			
011107056	2019-10-19	58775.046	714	0−20	HS	$0.008^{+0.006}_{-0.004}$	2.2		
011107057	2019-10-26	58782.616	657	0−20	HS	<0.013			
011107058	2019-11-02	58789.649	812	0−20	HS	<0.006			
011107059	2019-11-29	58816.360	971	7−30	HS	$1.00^{+0.15}_{-0.14}$	$1.96^{+0.26}_{-0.25}$		0.86/27
011107060	2019-12-04	58821.802	1019	1−30	HS	$0.139^{+0.022}_{-0.019}$	$2.25^{+0.24}_{-0.23}$		

Continued on the next page

Table 5.3: Continued from the previous page. X-ray spectral parameters of MAXI J1348−630 obtained from *Swift*/XRT observations.

ObsID	Day [UT]	MJD[a]	Exposure time [s]	Extraction region	Spectral state	Unabsobed flux 1–10 keV[b]	Γ	$k_{\rm B}T_{\rm in}$ [keV]	χ^2/d.o.f
011107061	2019-12-07	58824.050	932	0−20	HS	$0.061^{+0.017}_{-0.013}$	$2.01^{+0.37}_{-0.36}$		
011107062	2019-12-09	58826.041	864	0−20	HS	$0.033^{+0.009}_{-0.008}$	2.2		
011107064	2019-12-11	58828.032	1623	0−20	HS	$0.014^{+0.004}_{-0.003}$	2.2		
011107065	2019-12-14	58831.616	2707	0−20	HS	$0.0020^{+0.0018}_{-0.0012}$	2.2		
011107066	2019-12-16	58833.673	944	0−20	HS	<0.007			
011107067	2019-12-18	58835.598	2947	0−20	HS	<0.004			
011107068	2019-12-21	58838.522	2166	0−20	HS	<0.006			
011107069	2019-12-23	58840.457	1447	0−20	HS	<0.014			
011107070	2019-12-29	58846.697	948	0−20	HS	<0.006			
011107071	2020-01-06	58854.210	757	0−20	HS	<0.006			
011107072	2020-01-13	58861.179	1096	0−20	HS	<0.004			
011107073	2020-02-10	58889.521	1186	4−30	HS	$0.98^{+0.10}_{-0.08}$	$1.84^{+0.15}_{-0.15}$		0.93/19
011107074[f]	2020-02-18	58897.057	1274	0−20	HS	$0.08^{+0.01}_{-0.01}$	$1.72^{+0.30}_{-0.29}$		
011107076	2020-02-28	58907.132	267	0−30[g]	HS	<0.022			
011107077	2020-03-03	58911.244	537	0−20	HS	<0.021			
011107078	2020-03-07	58915.621	1382	0−20	HS	<0.004			

[a] Starting date of the observation.
[b] In units of 10^{-10} erg cm^{-2} s^{-1}.
[c] Another observations was taken on MJD 58509 (ObsID 00885807001), but we discard it since it was erroneously performed in PC mode.
[d] We discard the observation taken one day before (ObsID 00011107046) due to a satellite pointing error.
[e] We do not consider the observation taken one day before, on MJD 58727 (ObsID 00011107053), as it was taken in WT mode, providing a less constraining upper limit.
[f] Epoch combined with ObsID 00011107075, as it was performed less than 3 hours after ObsID 00011107074.
[g] Due to the shorter exposure time, a larger circular region was needed to have enough basckground counts for the upper limit estimation.

Chapter 6

The hybrid disk/jet connection of MAXI J1348–630

Contents

6.1 Radio and X-ray observations in the hard state . . . 102
6.2 Hybrid correlation . . . 106
6.3 Radio quiet hypothesis . . . 107
6.4 X-ray loud hypothesis . . . 108
6.5 MAXI J1348-630 in quiescence . . . 110

As I have discussed in Chapter 2, black hole low mass X-ray binaries in their hard spectral state are found to display two different correlations between the radio emission from the compact jets and the X-ray emission from the inner accretion flow. Having collected a large amount of simultaneous radio and X-ray data on MAXI J1348−630 during the hard state phases, I have studied the correlation between the radio and X-ray luminosities that are produced, respectively, by the compact jets and by the inner accretion flow during the hard state. I present my findings in this Chapter, and I find that MAXI J1348−630 belongs to the population of outliers and displays a *hybrid* radio/X-ray correlation, a behavior that today is not yet understood and has been clearly observed only in another source. I discuss the behaviour of MAXI J1348−630 in light of the currently proposed scenarios and I highlight the importance of future deep monitorings of hybrid correlation sources, especially close to the transitions and in the low luminosity regime. These results have been published in Carotenuto et al. (2021b). Moreover, we also observed MAXI J1348−630 in quiescence in radio and X-rays, obtaining an important detection that will be presented at the end of the chapter. My results span almost seven orders of magnitude in X-ray luminosity, allowing us to probe the accretion-ejection coupling from the bright phases of the outburst down to very low levels of activity of a BH XRB, which are still greatly unexplored.

6.1 Radio and X-ray observations in the hard state

In this section I present radio and X-ray observations of MAXI J1348−630 to highlight its behaviour on the radio/X-ray diagram. Thanks to the deep and long term coverage of our multi-wavelength monitoring, we are able to probe the source behaviour on the radio/X-ray diagram in great detail, from the bright phases, down to the lowest level of emission in outburst, when the source is close to its quiescent state. A subset of our hard state observation is shown in Figure 6.1. So far this has been possible for only a limited number of sources, especially over a single outburst (see for instance Corbel et al. 2013b and Shaw et al. 2021). While MAXI J1348−630 is believed to be located at a distance $D = 2.2^{+0.6}_{-0.5}$ kpc (Chauhan et al., 2021), we note that Lamer et al. (2021) recently reported a distance $D = 3.39 \pm 0.34$ kpc from observations with eROSITA (see Section 5.4). In this work I assume $D = 2.2$ kpc, but to include the second distance measurement I quote all derived luminosities with a factor $(D/2.2 \text{ kpc})^2$. In Carotenuto et al. (2021a) and in Chapter 5 I have presented the full X-ray and radio monitoring of the source during its 2019/2020 outburst. The source first completed a whole cycle in the Hardness Intensity Diagram (HID), and then exhibited a sequence of hard state re-brightenings (e.g. Russell et al. 2019a; Al Yazeedi et al. 2019; Pirbhoy et al. 2020). Our radio observations detected and monitored the rise, quenching and re-activation of compact jets through the different phases of the outburst.

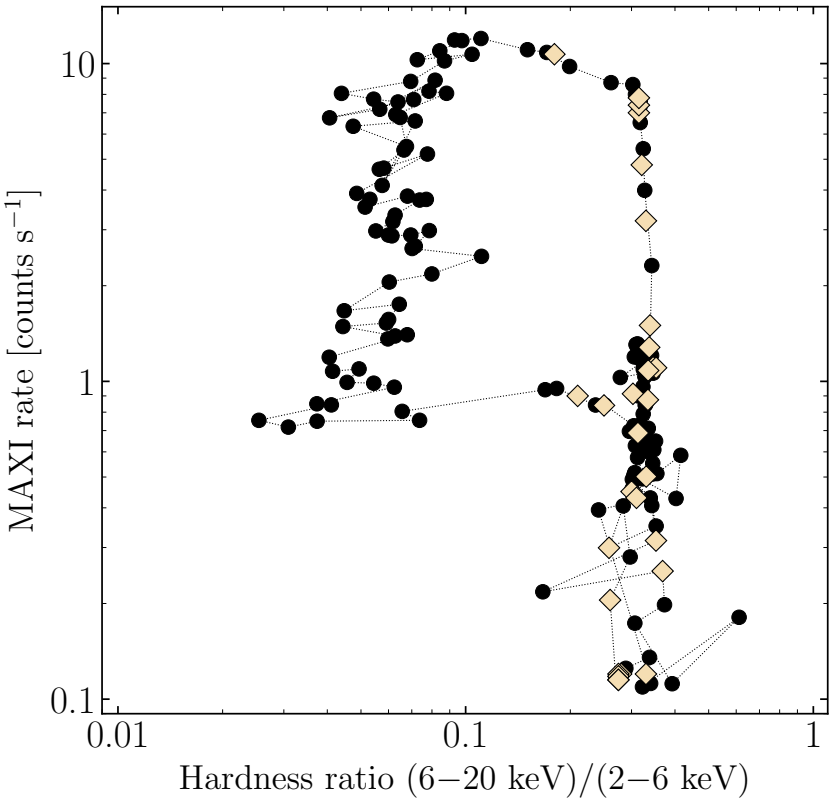

Figure 6.1: Hardness-intensity diagram (HID) of MAXI J1348−630 during its main outburst, where the hardness ratio (HR) was determined from MAXI data. For clarity, we only show MAXI observations in the MJD interval 58505–58710 with a count rate above 0.1 counts s^{-1}, thus including the brightest part of the outburst, which tracked an entire cycle in the HID. The beige diamonds mark the time of radio observations used for the radio/X-ray correlation on the HID. Radio observations taken during the second part of the outburst (MJD > 58710) lie on the bottom part of the hard-line ($0.3 \lesssim$ HR $\lesssim 0.4$).

MAXI J1348−630 has been monitored with MeerKAT at 1.28 GHz, as part of the ThunderKAT Large Survey Programme, and with the Australia Telescope Compact Array (ATCA) at 5.5 and 9 GHz. On the X-ray side, MAXI J1348−630 was regularly monitored by *Swift*/XRT and by MAXI. The full observing campaign on MAXI J1348−630 has already been presented in Chapter 5 and I refer to that for details on the radio and X-ray data processing. In this Chapter I also include two additional detections of MAXI J1348−630 during its seventh hard state re-flare (September-October 2020, Negoro et al. 2020; Carotenuto et al. 2020a), from observations performed with MeerKAT, ATCA and *Swift*/XRT and not reported in Carotenuto et al. (2021a).

To characterise the behaviour of MAXI J1348−630 in the radio/X-ray diagram, we selected epochs with quasi-simultaneous ($\Delta t \leq 24$ h) radio and X-ray observations between MJD 58509 and 58522, and after MJD 58597, during which the system was in the hard and intermediate state (see Zhang et al. 2020a, Carotenuto et al. 2021a and Chapter 5 for details on the state transitions). For each epoch we converted the measured radio flux density S_ν to the 5 GHz monochromatic luminosity

$$L_{\rm R} = 4\pi D^2 \nu S_\nu \tag{6.1}$$

assuming a distance $D = 2.2$ kpc and using either the measured spectral index α (see Table 6.1) when available, or the average spectral index $\langle\alpha\rangle = 0.14 \pm 0.01$. The unabsorbed 1–10 keV X-ray flux $S_{\rm X}$ obtained from *Swift*/XRT was converted to the integrated luminosity

$$L_{\rm X} = 4\pi D^2 S_{\rm X} \tag{6.2}$$

For simultaneity, we selected *Swift* epochs taken less than 24 hours before or after the corresponding radio observations. When this was not possible, we interpolated the X-ray flux from a exponential fit to the smoothly-evolving *Swift*/XRT light curve, adding a conservative 10% error on the interpolated X-ray fluxes and checking the consistency with the simultaneous MAXI data. This leads to a sample of 44 measurements on the radio/X-ray diagram, with a total of 39 detections of MAXI J1348−630 in radio and X-rays.

The full data set is provided in Table 6.1, and the radio/X-ray measurements of MAXI J1348−630 are shown in Figure 6.2.

Table 6.1: Radio flux densities and unabsorbed X-ray fluxes selected for the radio/X-ray correlation presented in this work, along with the radio spectral index (when available) and the telescopes used for obtaining the data (see Carotenuto et al. 2021a). Upper limits are reported at the 3σ level.

MJD	Outburst phase	X-ray flux[b] 1–10 keV	Radio flux density [mJy]	Spectral index[c] α	Telescopes
58509.9	Main outburst − rise	38.1 ± 0.3	3.4 ± 0.1	0.02 ± 0.09	ATCA/*Swift*
58511.0	–	201 ± 20	6.2 ± 0.4	0.1 ± 0.2	ATCA/*Swift*[a]
58512.0	–	346 ± 35	13.70 ± 0.05		MeerKAT/*Swift*[a]
58514.0	–	528 ± 53	21.9 ± 0.8	0.18 ± 0.02	ATCA/*Swift*[a]
58515.2	–	590 ± 59	28.6 ± 0.1		MeerKAT/*Swift*[a]
58515.9	–	625 ± 3	34.4 ± 1.4		ATCA/*Swift*
58519.9	–	1320 ± 132	135 ± 1	0.155 ± 0.003	ATCA/*Swift*[a]
58602.1	Main outburst − decay	113 ± 11	4.73 ± 0.04		MeerKAT/*Swift*[a]
58603.3	–	89 ± 9	8.7 ± 0.1	0.09 ± 0.05	ATCA/*Swift*[a]

Continued on the next page

Table 6.1: Continued from the previous page. Radio flux densities and unabsorbed X-ray fluxes selected for the radio/X-ray diagram of MAXI J1348−630.

MJD	Outburst phase	X-ray flux[b] 1–10 keV	Radio flux density [mJy]	Spectral index[c] α	Telescopes
58607.9	–	32 ± 3	3.43 ± 0.04		MeerKAT/*Swift*[a]
58608.7	–	26 ± 3	2.75 ± 0.06		ATCA/*Swift*[a]
58612.4	–	9.1 ± 0.3	0.77 ± 0.02	0.21 ± 0.02	ATCA/*Swift*
58614.9	–	4.2 ± 0.4	0.32 ± 0.04		MeerKAT/*Swift*[a]
58617.5	–	2.0 ± 0.2	0.71 ± 0.02	0.27 ± 0.03	ATCA/*Swift*[a]
58621.9	–	0.52 ± 0.05	0.27 ± 0.04		MeerKAT/*Swift*[a]
58628.0	First reflare − rise	0.047 ± 0.005	0.13 ± 0.04		MeerKAT/*Swift*[a]
58629.3	–	0.15 ± 0.02	0.15 ± 0.01	0.0 ± 0.2	ATCA/*Swift*[a]
58634.9	–	8.7 ± 0.9	0.79 ± 0.06		MeerKAT/*Swift*[a]
58642.9	–	67 ± 7	4.34 ± 0.06		MeerKAT/*Swift*[a]
58643.5	–	74 ± 7	4.09 ± 0.02	-0.03 ± 0.02	ATCA/*Swift*[a]
58650.9	–	99 ± 2	6.26 ± 0.09		MeerKAT/*Swift*
58658.8	–	103 ± 10	4.60 ± 0.05		MeerKAT/*Swift*[a]
58660.3	First reflare − decay	102 ± 10	4.18 ± 0.04	0.05 ± 0.03	ATCA/*Swift*[a]
58664.7	–	69 ± 7	3.86 ± 0.05		MeerKAT/*Swift*[a]
58671.9	–	54 ± 5	2.29 ± 0.03		MeerKAT/*Swift*[a]
58678.9	–	43 ± 4	1.66 ± 0.03		MeerKAT/*Swift*[a]
58686.9	–	24 ± 2	1.11 ± 0.03		MeerKAT/*Swift*[a]
58689.4	–	19.3 ± 0.4	1.19 ± 0.01	-0.02 ± 0.03	ATCA/*Swift*
58691.8	–	11 ± 1	0.70 ± 0.03		MeerKAT/*Swift*[a]
58699.7	–	0.98 ± 0.05	0.44 ± 0.04		MeerKAT/*Swift*
58705.8	–	0.071 ± 0.007	0.14 ± 0.04		MeerKAT/*Swift*
58726.7	–	<0.002	<0.12		MeerKAT/*Swift*[a]
58727.1	–	<0.005	<0.033		ATCA/*Swift*[a]
58775.6	Second reflare − decay	0.008 ± 0.004	<0.12		MeerKAT/*Swift*
58782.6	–	<0.01	<0.12		MeerKAT/*Swift*[a]
58789.6	–	<0.006	<0.06		ATCA/*Swift*[a]
58817.4	Third reflare − decay	0.67 ± 0.07	0.47 ± 0.03		MeerKAT/*Swift*[a]
58820.7	–	0.21 ± 0.02	0.56 ± 0.01	0.19 ± 0.06	ATCA/*Swift*[a]
58824.4	–	0.059 ± 0.006	0.16 ± 0.03		MeerKAT/*Swift*[a]
58827.8	–	0.016 ± 0.002	0.15 ± 0.01	0.9 ± 0.2	ATCA/*Swift*[a]
58831.3	–	0.002 ± 0.001	0.054 ± 0.006	-0.3 ± 0.3	ATCA/*Swift*
58894.1	Fourth reflare − decay	0.21 ± 0.02	0.22 ± 0.02		MeerKAT/*Swift*[a]
59112.7	Seventh reflare − decay	0.08 ± 0.02	0.17 ± 0.02		MeerKAT/*Swift*
59127.0	–	0.003[d]± 0.001	0.09 ± 0.01	-1.2 ± 0.3	ATCA/*Swift*[d]

[a] Interpolated X-ray flux.

[b] In units of 10^{-10} erg cm^{-2} s^{-1}.

[c] Only computed for ATCA multi-frequency observations. For the results reported in the Chapter 6, we also added values of α reported in Carotenuto et al. (2021a) for detections of compact jets at epochs for which we did not have a corresponding X-ray observation: $\alpha = 0.31 \pm 0.04$ (MJD 58814) and $\alpha = 0.4 \pm 0.3$ (MJD 58830).

[d] The corresponding X-ray flux was extrapolated (and not interpolated) from the *Swift*/XRT light curve, as the last X-ray observation of our monitoring was performed ∼36 h before the radio observation. We add a conservative 30% error to this measurement.

We note that our monitoring allowed us to probe the behaviour of MAXI J1348−630 over six orders of magnitude in the X-ray luminosity and almost four in its radio luminosity, which so far has rarely been possible for XRBs. Moreover, our measurements include three detections at $L_{\rm X} < 10^{33}(D/2.2\ {\rm kpc})^2$ erg s^{-1}, which are of key importance to probe the accretion/ejection connection at the lowest luminosities. To allow a direct comparison, measurements of GX 339−4 (Corbel et al., 2013b; Tremou et al., 2020) and H1743−322 (Coriat et al., 2011) are also shown, as the two sources are representative of the standard and outlier branches, respectively. MAXI J1348−630 immediately appeared to be incompatible with the standard track, being significantly fainter in radio than GX 339−4 below $L_{\rm X} < 10^{38}(D/2.2\ {\rm kpc})^2$ erg s^{-1}. For $L_{\rm X}$ between $\sim$5 $\times 10^{35}$ and $10^{38}(D/2.2\ {\rm kpc})^2$ erg s^{-1} the source appeared to follow a steep correlation, globally consistent with the population of outliers. We note that the track followed during the decay of the main outburst was brighter in radio with respect to the rising phase, possibly similar to the rise and decay phases of the 2010/2011 outburst of GX 339−4 (Corbel et al., 2013b). For $L_{\rm X} \lesssim 5 \times 10^{35}(D/2.2\ {\rm kpc})^2$ erg s^{-1}, MAXI J1348−630 transitioned to a flatter correlation. Unlike the main outburst, the rise and decay of the first reflare are consistent with the same track. On MJD 58614, 58621 and 58628 the radio core detected with MeerKAT was not completely separated due to the presence of discrete ejecta, hence we put a *caveat* on the radio fluxes obtained from source fitting in those three epochs (the two detections with the lowest radio emission during the decay of the main outburst and the faintest radio detection during the rise of the first reflare, see Figure 6.2. As $L_{\rm X}$ decreased, the source ultimately re-joined the standard track at $L_{\rm X} \simeq 10^{33}(D/2.2\ {\rm kpc})^2$ erg s^{-1} and was clearly detected down to $\sim 10^{32}(D/2.2\ {\rm kpc})^2$ erg s^{-1}, displaying a behaviour similar to H1743−322 (Coriat et al., 2011), but transitioning between the two tracks at vastly lower radio and X-ray luminosities.

We fit our radio and X-ray data of MAXI J1348−630 using `curve_fit` from the SciPy package to obtain a tentative estimation of the correlation slopes. Visual inspection shows that, given the evolution of MAXI J1348−630 on the diagram, a single power law does not appear to be adequate to fit the whole data set. Therefore, we adopt a double-broken power law, making the distinction between a *steep* branch followed when $L_{\rm X} \geq L_{\rm trans}$, a *flatter* correlation for $L_{\rm stand} < L_{\rm X} < L_{\rm trans}$, and assuming that the source follows the standard track with $\beta = 0.6$ for $L_{\rm X} \leq L_{\rm stand}$. We note that this fit is for illustrative purposes, and the results should only be taken as indicative, given the significant dispersion of the data obtained by merging the various phases of the outburst. The results of the fit are shown in the inset of Figure 6.2. For the high luminosity part, we obtain a slope $\beta_{\rm steep} = 0.95 \pm 0.04$ with

$$L_{\rm trans} = 6.3^{+1.5}_{-1.2} \times 10^{35}\ (D/2.2\ {\rm kpc})^2 {\rm erg\ s^{-1}}, \tag{6.3}$$

while the fit yields $\beta_{\rm flat} = 0.24 \pm 0.05$ for the flat branch. Since we fixed $\beta_{\rm stand} = 0.6$, the only parameter left is $L_{\rm stand}$, namely the transition luminosity between the flat branch and the standard track, which is not constrained by the fit, as we obtain

$$L_{\rm stand} = 3.2^{+61.3}_{-3.0} \times 10^{32}\ (D/2.2\ {\rm kpc})^2\ {\rm erg\ s^{-1}}. \tag{6.4}$$

While the other parameters of the fit depend weakly on the unconstrained value of $L_{\rm stand}$, this means that we cannot in principle rule out that the flat branch extends down to quiescence. However, we note that for H1743−322 and Swift J1753.5–0127, the two sources more similar to MAXI J1348−630, there is clear evidence that the standard track is followed in the low-flux regime (Coriat et al., 2011; Williams et al., 2020; Plotkin et al., 2017b). Moreover, we note that points with $L_{\rm X} \gtrsim 10^{37}(D/2.2\ {\rm kpc})^2$ erg s^{-1} seem to be more consistent with the steeper

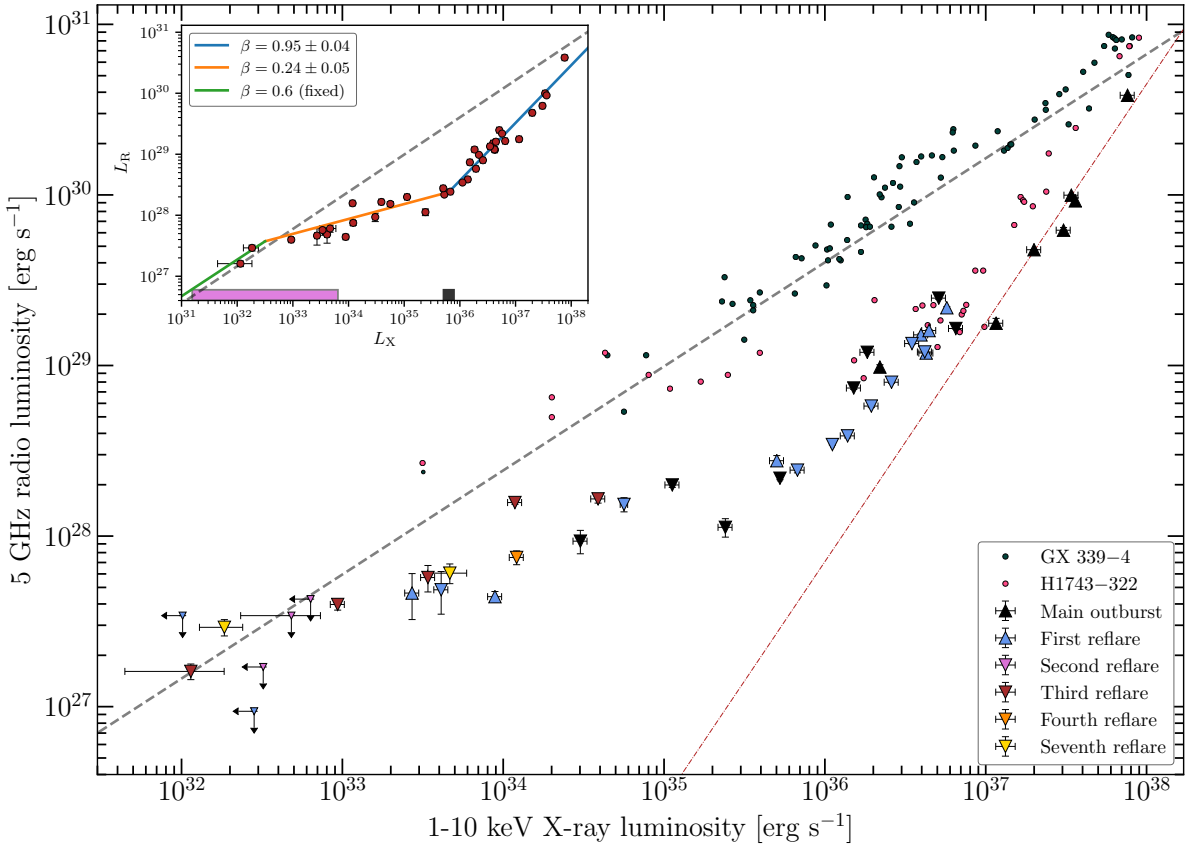

Figure 6.2: MAXI J1348−630 radio/X-ray diagram during its 2019/2020 outburst. We assume $D = 2.2$ kpc (Chauhan et al., 2021). Points from different phases of the outburst are plotted with different colors, and triangles pointing upwards or downwards differentiate between, respectively, rise and decay. The red and grey dashed lines represent, respectively, the $\beta = 1.4$ and $\beta = 0.6$ correlations (see Section 6.1), and are shown for illustrative purposes. The source transitions between tracks while going from higher to lower luminosities. For comparison, H1743−322 (Coriat et al., 2011) and GX 339−4 (Corbel et al., 2013b; Tremou et al., 2020) are shown on the diagram with smaller size points. A tentative fit to the same data is shown in the inset in the top-left corner. The magenta and grey rectangles represent the lower and upper bounds on the x-axis of, respectively, the $L_{\rm stand}$ and $L_{\rm trans}$ confidence intervals (see Section 6.1).

correlation $\beta = 1.4$, which is also shown for illustrative purpose on Figure 6.2.

6.2 Hybrid correlation

I have presented a detailed view of the radio/X-ray correlation of MAXI J1348−630 during its 2019/2020 outburst. The source clearly belongs to the growing population of *outlier* BHs. We traced the evolution of MAXI J1348−630 down to very low luminosities and observed it as it rejoined the standard correlation. Spanning six orders of magnitude in X-ray luminosity, the observations collected on MAXI J1348−630 constitute the most complete data set of an outlier obtained over a single outburst.

We find that MAXI J1348−630 is a new member of a restricted group of sources which appear to transition between the two known tracks. This particular behaviour, labeled *hybrid* (Xie and Yuan, 2016), has already been observed (usually only partially) in H1743−322 (Coriat et al., 2011; Williams et al., 2020), Swift J1753.5–0127 (Plotkin et al., 2017b), XTE J1752–223

(Ratti et al., 2012), MAXI J1659–152 (Jonker et al., 2012), GRS 1739–278 (Xie, Yan, and Wu, 2020), MAXI J1535−571 (Russell et al., 2019c; Parikh et al., 2019) and MAXI J1631–472 (Monageng et al., 2021). However, MAXI J1348−630 is, after H1743−322, only the second source in this regime to have such detailed monitoring, allowing the radio/X-ray behaviour to be so well constrained. Other sources classified as outliers have not been observed at such low luminosity (e.g. Corbel et al. 2004a; Brocksopp et al. 2005). In fact, all outliers could also belong to the hybrid class (Motta, Casella, and Fender 2018, see Bahramian et al. 2018 for a global display of the diagram). The path of MAXI J1348−630 in the radio/X-ray diagram agrees well with H1743−322 (Jonker et al., 2010; Coriat et al., 2011). We note that, while both sources display a steep correlation at high luminosities and re-join the standard track before approaching quiescence, MAXI J1348−630 overall spans a broader range in $L_{\rm R}$ and $L_{\rm X}$, and is significantly fainter in radio than H1743−322 in the flat part of the correlation. Moreover, the transition luminosity between the two correlations is harder to identify in MAXI J1348−630 than in H1743−322, for which Coriat et al. (2011) find $L_{\rm trans} \simeq 5 \times 10^{36}$ erg s^{-1} assuming a distance of 8 kpc, corresponding to $\sim 5 \times 10^{-3} L_{\rm Edd}$, and for which the standard track is reached at $\sim 5 \times 10^{-5} L_{\rm Edd}$. This is higher than what is inferred for MAXI J1348−630 in this work. If we assume a 7 $M_\odot$ black hole (Tominaga et al., 2020; Carotenuto et al., 2021a), the indicative value of $L_{\rm trans} \simeq 7 \times 10^{35} (D/2.2 \text{ kpc})^2$ erg s^{-1} corresponds to a transition happening at $\sim 7 \times 10^{-4} (D/2.2 \text{ kpc})^2 L_{\rm Edd}$, while MAXI J1348−630 would re-join the standard track at the low value of $\sim 10^{-6} (D/2.2 \text{ kpc})^2 L_{\rm Edd}$. It is important to note that our monitoring was conducted during a single outburst (including the following reflares), while the data on H1743−322 were accumulated over multiple outbursts (Coriat et al., 2011; Williams et al., 2020).

6.3 Radio quiet hypothesis

There is not yet a universal consensus on the origin of the two tracks and on what drives the change in correlation of a given source on the radio/X-ray diagram. As outlined by Coriat et al. (2011), the two groups might be characterised by different levels of radio emission, possibly arising from different jet properties. Standard track sources and outliers could be labeled as, respectively, *radio-loud* and *radio-quiet*.

Geometry

As suggested by Motta, Casella, and Fender (2018), the existence of two populations on the diagram may be the result of geometric effects, rather than intrinsic differences between sources. Low inclination sources could appear radio-louder due to geometry and Doppler boosting, and thus would lie on the standard track. While we still lack a precise estimation of the MAXI J1348−630 inclination angle θ, considerations on the discrete ejecta proper motion yield $\theta \lesssim 45°$ (see Section 7.4 and Carotenuto et al. 2021a). Hence, as a medium-low inclination source, geometric effects might not be suited to explain the fainter level of radio emission from MAXI J1348−630, similarly to what has been found for MAXI J1535−571 (Russell et al., 2019c; Parikh et al., 2019). However, misaligned jets are possible (e.g. Miller-Jones et al. 2019).

A different jet physics?

Alternatively, physical differences between compact jets from different systems might be at the basis of the observed dichotomy on the diagram. Hints of a radio spectral difference between standard sources and outliers have been found by Espinasse and Fender (2018), possibly supporting this hypothesis. Compact jets powered by MAXI J1348−630 showed an average spectral index $\langle\alpha\rangle = 0.14 \pm 0.01$, which is more in agreement with a standard-track source than with an outlier. We tested the agreement with a Kolmogorov-Smirnov test on our spectral index distribution against the Gaussian distributions from Espinasse and Fender (2018), similarly to Williams et al. (2020). The null hypothesis was our distribution being consistent either with the standard or with the outlier distribution. For the outlier case, we find a p-value of $\sim 10^{-5}$, while we obtain a p-value of 0.33 when we test our distribution against the standard one. Therefore, we are able to reject the null hypothesis in the first case, concluding that the jet spectral index distribution of MAXI J1348−630 is inconsistent with what is observed for the population of outliers. We cannot draw conclusions regarding the agreement with the distribution observed in standard sources.

If a physical difference in the jets can explain the two tracks, this could possibly imply a change in the properties or in the morphology of the jets when sources belonging to the hybrid correlation transition between the two groups, as argued in Koljonen and Russell (2019). This should produce observable effects, including, according to Espinasse and Fender (2018), a significant change in the radio spectral index distribution between the tracks. For MAXI J1348−630 we could not constrain the spectral index at low luminosities, hence we cannot confirm or rule out a potential radio spectral difference between the two tracks, but such effect is not observed in other sources (e.g. Shaposhnikov et al. 2007), questioning the validity of this scenario. Alternatively, outliers could be characterised by compact jets with higher magnetic fields with respect to standard track sources (Pe'er and Casella, 2009). While we have no measurement on the jet's magnetic field in MAXI J1348−630, an evolution of the magnetic field throughout the outburst, possibly increasing with the accretion rate and, thus, with L_X, could explain the observed hybrid correlation, as argued by Coriat et al. (2011).

6.4 X-ray loud hypothesis

An alternative approach is to invoke differences in the X-ray emission produced by the accretion flow between the two groups.

Radiative efficiency of the acccretion flow

It has been proposed that sources on the outlier track could be characterised by radiatively efficient accretion flows (e.g. Coriat et al. 2011; Huang, Wu, and Wang 2014), such as the Luminous Hot Accretion Flow (LHAF, Yuan and Zdziarski 2004) and would be brighter in X-rays than standard track sources. Those might in turn be modeled with the radiatively inefficient accretion flows, such as the Advection Dominated Accretion Flows (ADAF, e.g. Narayan and Yi 1994). Outliers could then be called *X-ray-loud* instead of *radio-quiet*. Switching between tracks, hybrid sources would change from an an inefficient ADAF in the low flux regime to an efficient LHAF at high luminosity (Coriat et al., 2011). This is also supported by the detection of hard X-ray cutoffs in the spectra of sources on the outlier track, implying an effective cooling

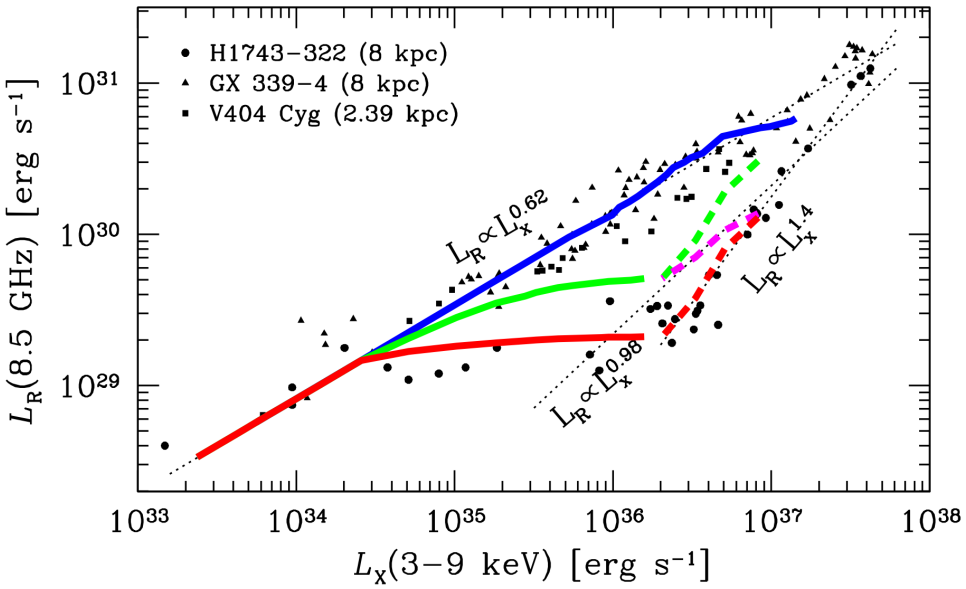

Figure 6.3: The radio/X-ray diagram of the three BH XRBs GX 339−4, V404 Cyg and H1743−322, taken from (Xie and Yuan, 2016), with the results of the application of the *accretion-jet* model (Xie and Yuan, 2012; Xie and Yuan, 2016). The three black dotted lines show the previous power law fitting results to the data. The lines with different colour show the results calculated from the accretion–jet model. The blue, green, and red solid lines represent the ADAF and type-I LHAF solutions, while the green, magenta, and red dashed lines represent the result of the two-phase (type-II LHAF) accretion model (see Xie and Yuan 2016 for details on the accretion-jet model). The blue line corresponds to a viscosity parameter $\alpha = 0.6$, while the others are obtained with $\alpha = 0.06$.

of the electrons responsible for the Comptonization of disk photons (Koljonen and Russell, 2019).

It has been shown that the radiative efficiency of the accretion flow could depend on the mass accretion rate and hence on L_X (Narayan and Yi, 1995), and a change from an ADAF to various types of LHAF is possible above a given critical luminosity

$$L_C \propto 5\theta_e^{3/2}\alpha_v^2 \dot{M}_{Edd} \tag{6.5}$$

where $\theta_e = k_b T_e / m_e c^2$ is the electron temperature in keV and α_v is the viscosity parameter of the accretion disk (Xie and Yuan, 2012). This would produce the outlier track. In the context of the *accretion-jet* model (Xie and Yuan, 2016), different values of α_v lead to different L_C, playing a key role in differentiating between standard track sources and outliers. The application of this model on the data of GX 339−4, V404 Cyg and H1743−322 is shown in Figure 6.3, where the agreement with the data appears to be excellent (Xie and Yuan, 2016).

The path of MAXI J1348−630 agrees quite well with this scenario, since it is consistent with the standard track at $L_X \lesssim 10^{33}(D/2.2\,\mathrm{kpc})^2$ erg s^{-1} and then moves to the flat part at the transition between the two tracks above $\sim 10^{33}(D/2.2\,\mathrm{kpc})^2$ erg s^{-1}, which could be a proxy for a low value of L_C, and possibly a low α_v. Future insights on the values of α_v (see for instance Tetarenko et al. 2018b) and θ_e (e.g. Koljonen and Russell 2019) would be crucial to quantify this agreement. A radiatively efficient accretion flow could also explain the behaviour of neutron star systems (NS XRBs), which are found to be generally fainter in radio than BH XRBs (e.g. Migliari and Fender 2006a; Tudor et al. 2017). At a given L_R, the observed L_X might be increased by the additional X-ray emission coming from the solid surface. However, given the

various nature of NS systems (Tudor et al., 2017; Gallo, Degenaar, and van den Eijnden, 2018), the global situation appears to be more complex and a full comparison with NS XRBs is beyond the scope of this work.

Inner accretion disk

As an alternative, Meyer-Hofmeister and Meyer (2014) suggested the presence of a weak, cool inner accretion disk, which would bring the source to the steep track by providing additional soft photons for Comptonization in the corona. The inner disk, resulting from partial re-condensation of the coronal material, would be present in the hard state at $L_{\rm X} \gtrsim 10^{-4} L_{\rm Edd}$. Despite the difficulty of detecting such disk with the current X-ray instruments, this scenario appears to reproduce well the path on the diagram followed by H1743−322 (Meyer-Hofmeister and Meyer, 2014). However, MAXI J1348−630 leaves the standard track at $\sim 10^{-6} (D/2.2 \text{ kpc})^2 L_{\rm Edd}$, and the existence of such disk is unlikely at these low accretion rates.

6.5 MAXI J1348-630 in quiescence

The low luminosity and quiescent regions of the radio/X-ray diagram are still greatly unexplored, this being due to the increasing difficulty of monitoring and detecting source at their lowest levels of emission. Observations in quiescence are, however, particularly needed to completely constrain the overall behaviour of a source on the diagram. So far, only a handful of BH LMXBs have been detected in quiescence, mostly appearing to be compatible with the standard track (e.g. Gallo et al. 2006; Miller-Jones et al. 2011a; Corbel et al. 2013b; Ribó et al. 2017; Tremou et al. 2020). Therefore, in the case of MAXI J1348−630, after covering all the phases of activity, constraining its behaviour in quiescence was critical for completing the full track of the source on the radio/X-ray diagram, which is something unprecedented for a hybrid source. MAXI J1348−630 has been in quiescence since early 2020, and hence I requested, obtained and performed a simultaneous radio and X-ray observation of the source during its quiescence phase between June and July 2021, using the *Chandra* X-ray observatory and ATCA in the radio band. I discuss in the following the results of the two quasi-simultaneous observations, that will be published in a paper to be submitted.

Chandra observation

Chandra observed MAXI J1348−630 for 30 ks on June 28 2021, with the observing time awarded as Director's Discretionary Time (DDT, PI Carotenuto). Observing in the 0.3−8 keV energy range, the NASA *Chandra X-ray observatory* is one of the two most sensitive X-ray telescopes that are currently operational (together with *XMM-Newton*, from ESA), and it is the instrument with the highest angular resolution in the X-ray band, with a PSF of ∼0.5 arcsec (Weisskopf et al., 2000). Using the back-illuminated ACIS-S3 CCD, we obtained a highly significant detection of MAXI J1348−630 in quiescence, which is shown in the right panel of Figure 6.4. 20 counts from MAXI J1348−630 were collected in the 30 ks of exposure, corresponding to an integrated flux $F_{\rm X} = (1.40 \pm 0.28) \times 10^{-14}$ erg cm^{-2} s^{-1} in the 1−10 keV energy range, converted using the Heasarc Webpimms[1] online tool, assuming a power law spectrum with $\Gamma = 2.2$ and a column density of 0.86×10^{22} cm^{-2} (Corbel, Koerding, and Kaaret, 2008; Carotenuto et al., 2021a), to which we attribute a conservative 20% uncertainty

[1] https://heasarc.gsfc.nasa.gov/cgi-bin/Tools/w3pimms/w3pimms.pl

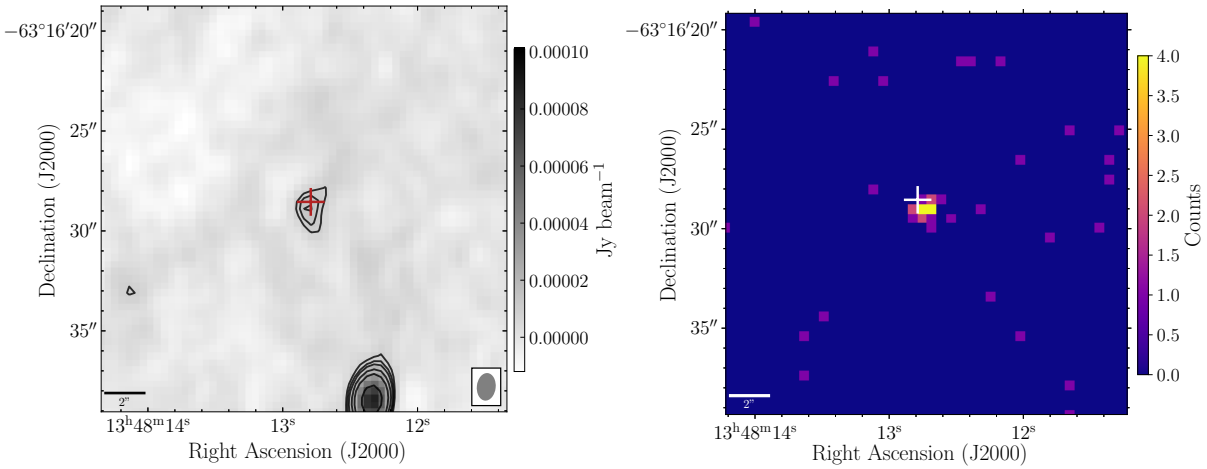

Figure 6.4: *Left*: ATCA radio detection of MAXI J1348−630 in quiescence. The location of MAXI J1348−630 is marked with a purple cross. Contours start a 3 times the rms (∼3 μJy beam^{-1}). *Right*: *Chandra* X-ray detection of MAXI J1348−630 in quiescence. The location of MAXI J1348−630 is marked with a white cross, and the units on the color bar are photon counts. Both radio and X-ray detection are at a significance level higher than 5σ.

on the flux estimate. A more detailed spectral analysis is currently in progress. This flux corresponds to a luminosity $L_{\rm X} = (8.0 \pm 1.6) \times 10^{30}$ erg s^{-1} at 2.2 kpc (Equation 6.2).

ATCA observation

A long ATCA observation was performed between 3 and 5 July 2021, less than a week after the *Chandra* observation, for a total of 24 hours on source (proposal ID C3416, PI Carotenuto). The observation was taken simultaneously in the C and X bands, at central frequencies of 5.5 and 9 GHz, respectively. For each central frequency, the total bandwidth was 2 GHz. As in the case of the monitoring of 2019/2020, PKS 1934–638 was used as a primary calibrator, while PKS 1352–63 was used for the complex gain calibration. The data were first flagged and then calibrated using standard procedures in CASA. Imaging was carried out with the standard `tclean` algorithm in CASA with a natural weighting scheme chosen in order to maximize sensitivity. To obtain the lowest possible rms, we stacked the two bands into a single image adopting the Multi-term (Multi Scale) Multi-Frequency Synthesis (MTMFS, or MS-MFS, Rau and Cornwell 2011) as a deconvolution algorithm in order to take into account the large fractional bandwidth, using two Taylor terms. In this configuration, the level of rms reached 3 μJy beam^{-1}. To obtain the radio flux density S_ν, we fitted a point source in the image plane with the CASA task `imfit`. As can be seen from the left panel of Figure 6.4, MAXI J1348−630 is detected at its known location at a significance level of 5σ and with a peak flux of 15.3 ± 2.5 μJy, that corresponds to a monochromatic radio luminosity at 5 GHz of $L_{\rm R} = (4.3 \pm 0.9) \times 10^{26}$ erg s^{-1}, from Equation 6.1, conservatively assuming a flat radio spectrum.

MAXI J1348−630 on the standard track in quiescence

With the quasi-simultaneous radio and X-ray detection in quiescence, we can add a critical point on the radio/X-ray diagram shown in Figure 6.2. The updated radio/X-ray diagram is shown in Figure 6.5, and we find immediately that MAXI J1348−630 aligns very well with the standard track defined by GX 339−4, V404 Cyg and MAXI J1820+070. The clear confirmation that

MAXI J1348−630 lies on the standard track in quiescence is the main result of this work (to be submitted). The firm detection in radio and X-rays allowed us to obtain this major result, and led us to confirm, for the first time, that hybrid sources follow the standard track when heading towards quiescence.

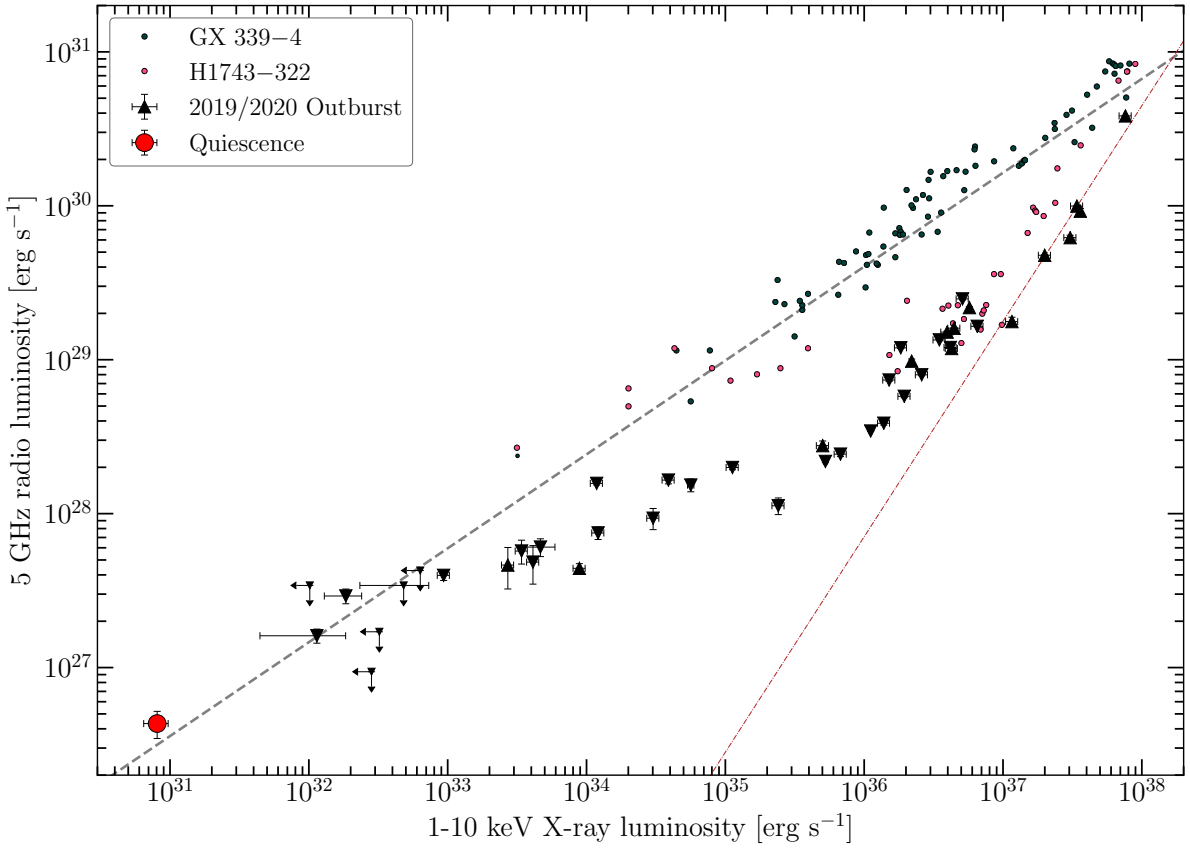

Figure 6.5: Same as Figure 6.2, but with the addition of the detection in quiescence of MAXI J1348−630, highlighted in red, while the other measurements during the outburst are shown in black. MAXI J1348−630 is unambiguously confirmed to follow the standard track at low luminosities and in quiescence.

Moreover, MAXI J1348−630 becomes the first BH LMXB to be characterised on the radio/X-ray diagram for over seven orders of magnitude in X-ray luminosity and almost four orders of magnitude in radio luminosity during a single outburst.

The quiescence X-ray luminosity of MAXI J1348−630 corresponds to an Eddington fraction $\sim 10^{-8.3} L_{\rm Edd}$ for a $10 M_{\odot}$ BH. Currently, the BH XRB with the lowest known X-ray luminosity in quiescence is GS 2000+25, detected at $\sim 10^{30}$ erg s^{-1}, namely $\sim 10^{-9} L_{\rm Edd}$ (Rodriguez et al., 2020). MAXI J1348−630 appears to have higher quiescence luminosities than some sources detected in quiescence and placed on the radio/X-ray diagram, namely GS 2000+25 (Rodriguez et al., 2020), A0620–00 (Gallo et al., 2006), MWC 656 (Ribó et al., 2017), XTE J1118+480 (Gallo et al., 2014) and possibly Swift J1357.2–0933 (Plotkin et al., 2016). The location of these sources on the diagram is shown in Figure 6.6. Interestingly, while the orbital period of MAXI J1348−630 is currently unknown, the system is characterised by a high peak luminosity ($\sim 10^{38}$ erg s^{-1}), and thus it is expected to have a larger orbital period when compared to the known BH XRBs population (Wu et al., 2010). This, according to Menou et al. (1999), implies a larger quiescence luminosity, assuming that the properties of the accretion flow are consistent

with an ADAF. However, it seems that the X-ray quiescence luminosity of MAXI J1348−630 is lower than the median among several sources observed by Reynolds et al. (2014), and it appears to be significantly lower than what is observed in GX 339−4 (Corbel et al., 2013b; Tremou et al., 2020) and V404 Cyg (Plotkin et al., 2017a).

A detection in quiescence on the standard track also supports the findings of Plotkin et al. (2017a) for V404 Cyg, excluding the possibility that a synchrotron-emitting jet dominates the X-ray emission in quiescence, which would produce a steepening of the observed correlation at low luminosities that is not observed.

Since these results are particularly recent, additional work is needed in order to fully exploit the scientific potential of this detection in quiescence, including its implication for the overall behaviour of MAXI J1348−630 on the radio/X-ray diagram and, in general, for the physics of BH LMXBs. Nevertheless, the results will be published in a forthcoming paper, and the full data set of MAXI J1348−630 on the diagram will be particularly important for testing different models for the disk/jet coupling and for improving our understanding on the behaviour of hybrid sources and on the difference between the two populations of black holes.

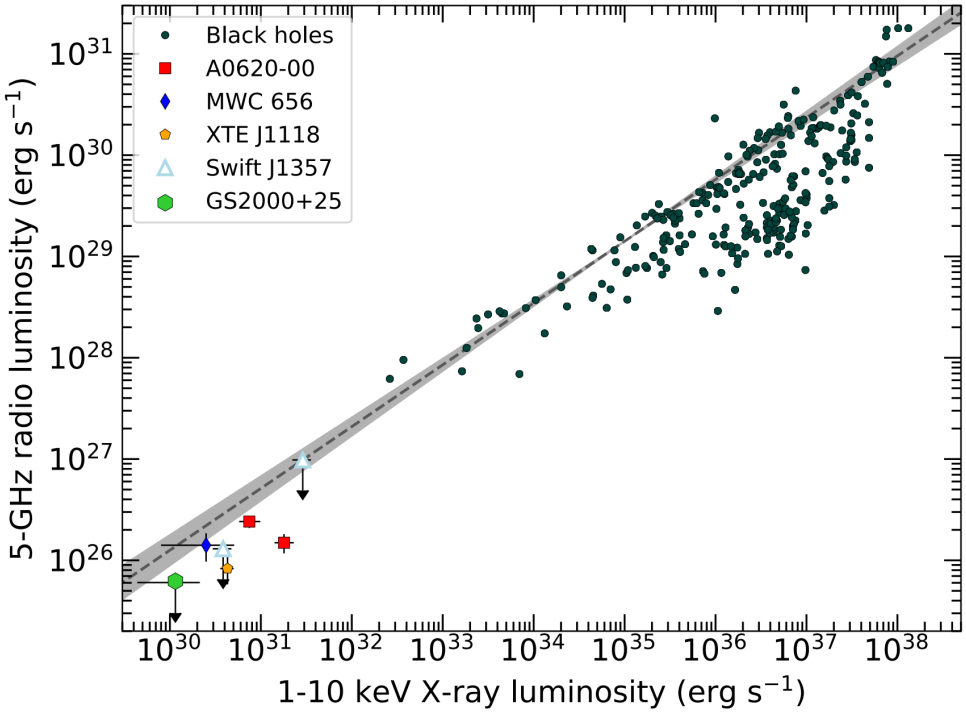

Figure 6.6: Radio/X-ray diagram with the known BH LMXBs detected in quiescence, either in radio and X-rays, or only in X-rays, from Rodriguez et al. (2020). Black circles mark the known population of black holes in the hard state (e.g. Coriat et al. 2011; Corbel et al. 2013a and references in Bahramian et al. 2018). The dashed line, from Gallo et al. (2014), marks the standard track, with the 1σ confidence interval represented as the grey shaded region. Sources in quiescence are marked with different colors. The diagram shows the location (or the costraints on it) on the diagram for GS 2000+25 (Rodriguez et al., 2020), A0620–00 (Gallo et al., 2006), MWC 656 (Ribó et al., 2017), XTE J1118+480 (Gallo et al., 2014) and Swift J1357.2–0933 (with the two points corresponding to the extremes of the confidence interval on the source distance Plotkin et al. 2016).

Chapter 7

The discrete ejecta of MAXI J1348–630

Contents

7.1 Observations of the first discrete ejecta . . . 116
7.1.1 Light curve evolution . . . 117
7.2 Observations of the second discrete ejecta . . . 119
7.2.1 Light curve evolution . . . 119
7.3 Ejecta motion . . . 121
7.3.1 Astrometry correction . . . 121
7.3.2 Motion of the first discrete ejecta . . . 125
7.3.3 Motion of the second discrete ejecta . . . 126
7.4 Constraints from the jet motion . . . 128
7.4.1 Jet opening angle . . . 129
7.5 Ejection of the first component . . . 130
7.5.1 Link with X-ray observations . . . 130
7.5.2 Multiple radio flares . . . 130
7.5.3 Flare energetics . . . 131
7.6 Late time behaviour of the first discrete ejecta . . . 133
7.6.1 Cavity scenario . . . 133
7.6.2 Alternative hypotheses . . . 134
7.7 Considerations on the second discrete ejecta . . . 135
7.7.1 Ejection . . . 135
7.7.2 Late time behaviour . . . 136
7.8 Radio flux densities of the first ejecta . . . 137

MAXI J1348−630 displayed spectacular discrete ejecta. Two single-sided jet components were launched ∼2 months apart and displayed the highest proper motion ever measured for an accreting BH ($\gtrsim 100$ mas day^{-1}). After traveling with constant speed, the first component underwent a strong deceleration, which was covered with unprecedented detail and suggested

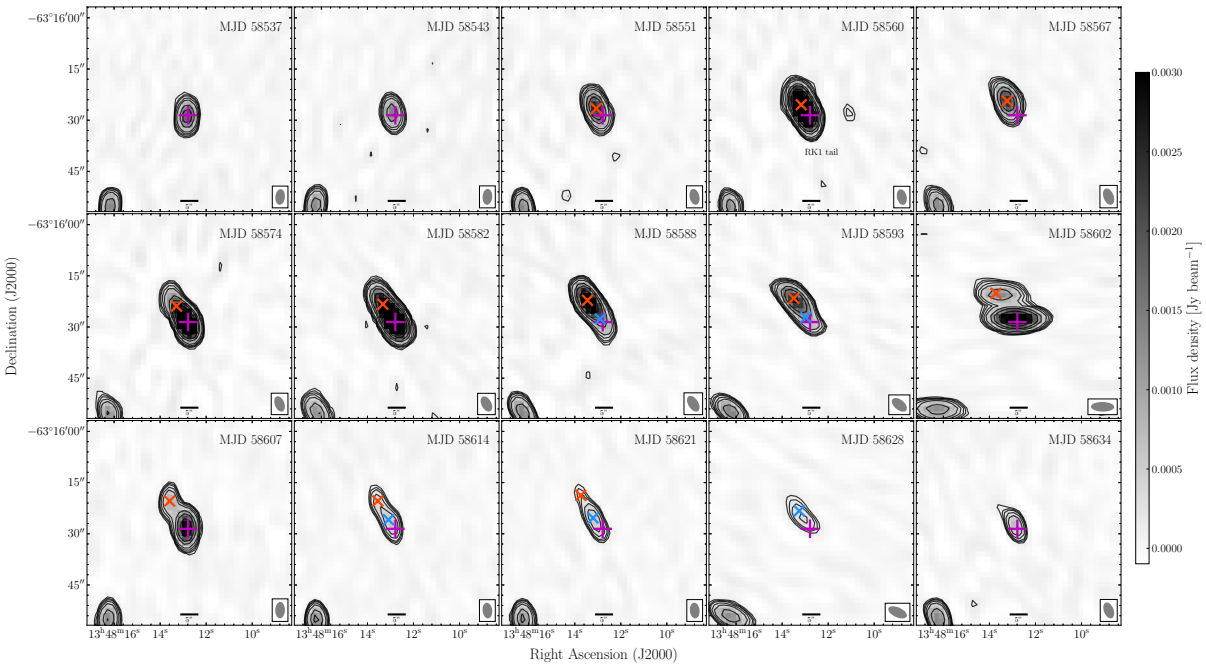

Figure 7.1: A sample of the 1.28 GHz MeerKAT monitoring of MAXI J1348−630, including 15 images that cover a period between MJD 58537 (2019 February 23) and MJD 58634 (2019 May 31). Contours start at three times the rms, with the rms ranging between ∼35 and ∼60 μJy beam^{-1}. The MAXI J1348−630 position is marked with a magenta cross, while red and blue crosses are used, respectively, for the fitted positions of RK1 and RK2. We show the first part of the evolution of RK1, as it moved away from the core at a position angle of $33.2° \pm 1.4°$ East of North, and we also show the detections of RK2, which was never completely resolved with MeerKAT. The re-activated compact jets are present in the panels starting from MJD 58602. We show on MJD 58560 a resolved radio source that we fitted with two components: a jet *head* and a jet receding *tail* (see Section 7.1). The radio emission at the core position detected on MJD 58574 and 58582 is discussed in Section 7.7. The stable, background, point source (possibly consistent with the IR source 2MASS J13481645–6316501) in the bottom left corner is used to correct the astrometry for all the MeerKAT observations.

that MAXI J1348−630 could be located inside a low-density cavity in the interstellar medium. In this chapter with present the MeerKAT and ATCA observations of these two jets, and I discuss their ejection, motion, and late-time behaviour. Moreover, I discuss a large number of observational constraints that we can place on some of their physical parameters. The results presented in this chapter have been published in Carotenuto et al. (2021a).

7.1 Observations of the first discrete ejecta

We first detected radio emission slightly displaced from the core position (∼2.5 arcsec) on the MeerKAT observation of MJD 58551 (2019 March 09), while MAXI J1348−630 was in the soft state. The source displayed a flux density of ∼3 mJy and appeared to be moving in the North-East direction. We followed the motion of this component for the rest of the outburst, and hereafter we refer to it as RK1. It is likely that the emission of RK1 was initially confused with the fading core emission before MJD 58551. With the proper motion and ejection date obtained for RK1 (discussed in Section 7.3.2), we deduce that RK1 would have reached an angular distance from the core of ∼2 arcsec (∼25–40% of the MeerKAT synthesized beam) on MJD 58538. However, we do not detect such displacement on MJD 58538 and 58545, during

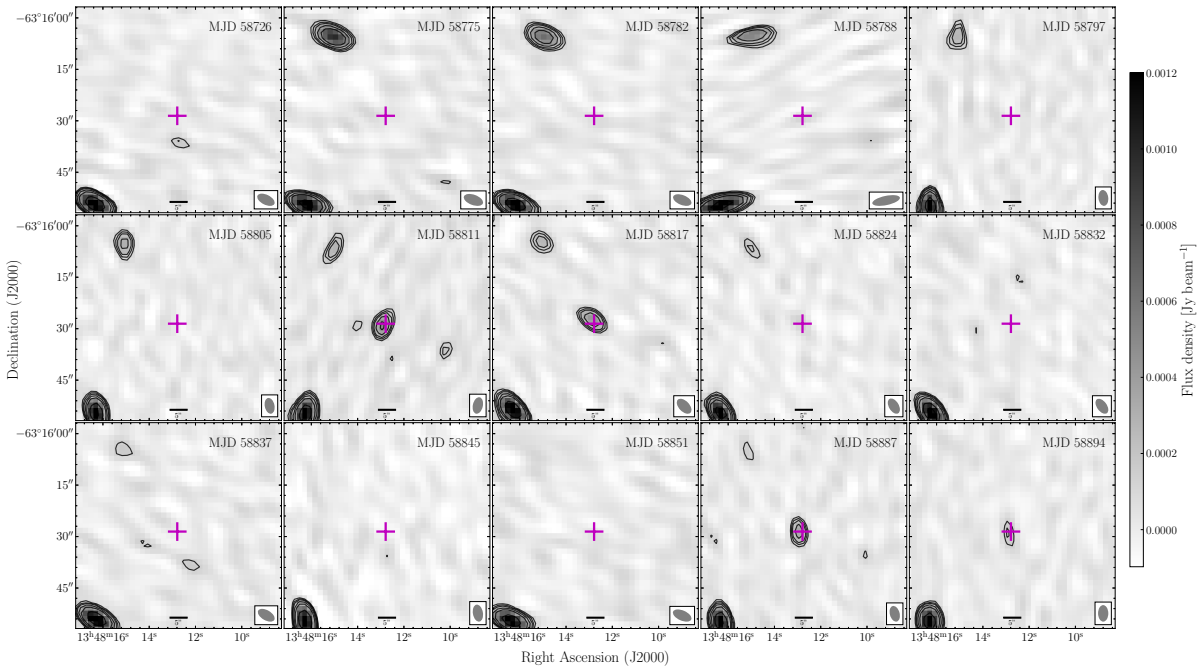

Figure 7.2: Same as Figure 7.1, but including 15 MeerKAT images that cover a period between MJD 58726 (2019 August 31) and MJD 58894 (2020 February 15). We show the late-time evolution of RK1, as it re-brightened ∼8 months after the ejection at a distance of ∼27 arcsec from the core position, undergoing a strong deceleration (see Figure 7.7). Compact jets re-activated and decayed during the third and fourth re-flares.

which we still observe decaying emission at the core position. This could be due to RK1 being still too close to the core for its emission to be resolved, similarly to Russell et al. (2019c), or being too faint with respect to the fading core, as the emission appeared to be rising during its first detection (see Figure 7.3). MeerKAT radio images from the first part of the outburst are shown in Figure 7.1 and illustrate the motion of RK1 during the first phase, while the detections of RK1 at large scale with MeerKAT are shown in Figure 7.2. The radio light curve is shown in Figure 7.3 and radio data are reported in Table 7.5 and 7.2. We observed RK1 moving away from MAXI J1348−630 with a linear trajectory, at a position angle of $33.2° \pm 1.4°$ East of North.

7.1.1 Light curve evolution

The first part of the RK1 light curve is characterized by some flux variability between MJD 58551 and MJD 58588, as can be seen in Figure 7.3. On the MeerKAT observation of MJD 58560 (2019 March 18), the source appeared to be resolved along the jet axis, as it is shown on Figure 7.1 (fourth panel on the top row). We simultaneously fitted the extended emission with two point sources, interpreting the component located further from the core position as the jet *head*, and obtaining a second component consistent with the core position (at a distance of 0.5 ± 0.5 arcsec from the core). In the study of the motion of RK1, which is discussed in Section 7.3.2, we use the coordinates of the jet *head*. For the second component, the emission is unlikely to be produced by the core. On MJD 58560 MAXI J1348−630 was in the soft state, and we do not detect any quick excursion to the SIMS around that time. While we cannot exclude a short radio flare from the core, signature of an additional ejection on very short timescales (e.g.

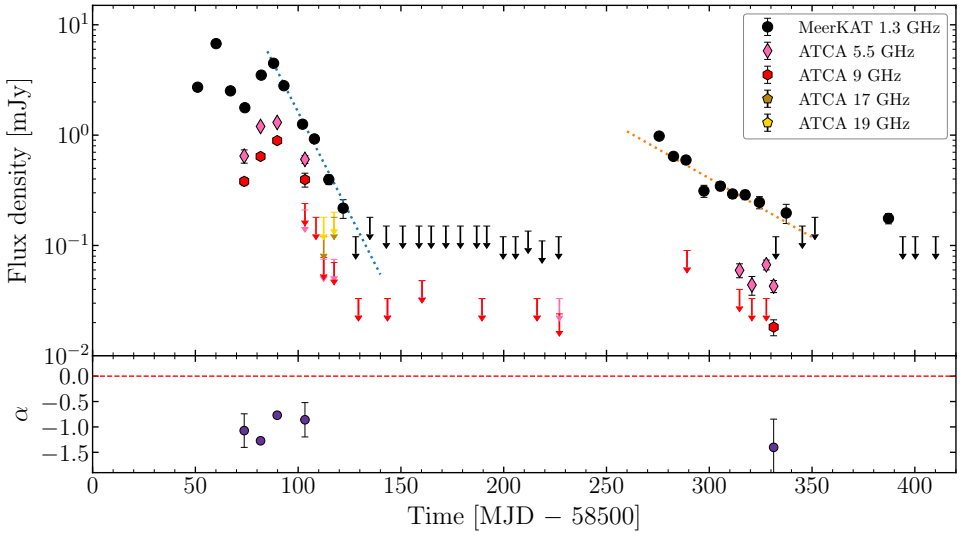

Figure 7.3: Radio monitoring of RK1. *Top panel*: Radio light curve of RK1 obtained with MeerKAT and ATCA observations. Exponential fits to the decay phases (only MeerKAT) are represented with dashed lines. *Second panel*: Radio spectral index of RK1 obtained from ATCA simultaneous multi-frequency observations, as reported in Table 7.5.

Tetarenko et al. 2017), we expect that such flare would have been accompanied by a change in X-ray spectral state, and that such ejection would have been detected in the following epochs. Therefore, our adopted scenario is that the second component is a receding *tail* associated with RK1. Discrete knot tails have been already observed in X-rays for XTE J1550−564 (Migliori et al., 2017), where electrons could be accelerated by a reverse shock and undergo a fast adiabatic cooling. This rapid cooling could explain why the tail is only detected in this epoch.

This phase is followed by a smooth exponential decay that lasted ∼6 weeks, from ∼4.4 mJy on MJD 58588 until non-detection on MJD 58628, with a 3σ upper limit of 120 μJy beam^{-1} with MeerKAT. The decay can be well-fitted with an exponential function, which yields a characteristic timescale of 11.8 ± 0.2 days (e-folding time). At this point the ejected jet knot appeared to have travelled ∼10 arcsec on the plane of the sky in less than 3 months, displaying an extremely high proper motion, which can be seen in Figure 7.1 and that we discuss in Section 7.3.2. On MJD 58628, the jet knot decayed below our detection threshold and remained undetected until MJD 58775 (2019 October 19), when additional MeerKAT observations were performed in response to the core optical detection during the second re-flare (R2, Al Yazeedi et al. 2019). On MJD 58775 we detected emission from RK1, this time at an angular distance of ∼27 arcsec from MAXI J1348−630 and at a flux level of ∼1 mJy. The re-brightening of RK1 was then followed by a 9 week-long smooth decay, with the exception of the non detection of RK1 on MJD 58832. MeerKAT images of the detection at large scale of RK1 are shown in Figure 7.2. RK1 was also detected with ATCA during the re-flare phase, but only in four epochs, when the length of the observations was large enough to achieve the required ∼10 μJy sensitivity, and mostly at 5.5 GHz. For the last ATCA detection of RK1, we stacked the two observations taken on December 13 and 14 2019 (MJD 58830 and 58831). While the two epochs were considered separately for the core, as it was quickly decaying in this phase, we do not have hints of variation of RK1 between the two epochs, and therefore the combination of the two observations led to an rms noise of ∼6 μJy and a detection of RK1 both at 5.5 and 9 GHz, as reported in Table 7.5. During the re-brightening, RK1 was moving extremely slowly,

or not moving at all, as its angular separation from MAXI J1348−630 ranged between ∼26.4 and ∼28 arcsec (see Figure 7.2, discussed in Section 7.3.2). Following the reports of as the re-brightening in February 2020 (Pirbhoy et al., 2020; Shimomukai et al., 2020), we obtained our last detection of RK1 with MeerKAT at ∼170 μJy on MJD 58887, roughly 11 months after the first detection.

The radio spectrum of RK1 was steep for all of the five double-frequency ATCA detections, with a spectral index that ranged from -0.7 to -1.4. This explains why RK1 was mostly detected with MeerKAT, despite the lower rms achieved in the several ∼10 hours observations performed with ATCA during the monitoring. In addition, in case of a diffuse knot, we expect ATCA to resolve out some of the emission due to the higher frequencies and to the smaller number of short baselines compared to MeerKAT. The second decay, without including the last detection on MJD 58887, can also be well-fitted by an exponential function, yielding a much longer characteristic timescale of 41 ± 4 days, with respect to the first decay.

Given the light curve evolution, the radio spectrum and the proper motion, RK1 is qualitatively consistent with a typical discrete ejection from an X-ray binary, consisting in synchrotron-emitting plasma bubbles that first expand adiabatically (e.g. van der Laan 1966) and then re-brighten due to later interactions with the interstellar medium at large scales (e.g. Corbel et al. 2002; Migliori et al. 2017).

7.2 Observations of the second discrete ejecta

A second radio knot launched by MAXI J1348−630 was detected approximately one month after the first detection of RK1, when on MJD 58589 (2019 April 16) the radio emission detected with ATCA at 5.5 GHz and 9 GHz was incompatible with the location of the core (see Figure 7.4). We detected it three more times with MeerKAT in May 2019, as it traveled further from MAXI J1348−630 at a position angle of 33° ± 11° East of North, which is fully consistent with the measured sky direction of RK1. We can therefore exclude a significant projected precession of the jet axis of the system, (which instead was observed for V404 Cygni, Miller-Jones et al. 2019) between February and April 2019. Hereafter we refer to the second detected radio knot as RK2. The MeerKAT images in which RK2 is detected are shown in Figure 7.1.

7.2.1 Light curve evolution

The light curve of RK2 is shown in Figure 7.5, the radio data are listed on Table 7.1 and its motion is displayed in Figures 7.7 and 7.8. Lower resolution MeerKAT observations on April 15 and 20 2019 (MJD 58588 and 58593) showed a point source slightly offset from the core position in the direction of the RK2 motion. While the lower resolution MeerKAT data alone for these two epochs would not have allowed us to firmly conclude on a possible displacement (offsets of less than 20% of the synthesised beam, see Figure 7.1, third and fourth panels on the central row), the detection of RK2 with ATCA (see Figure 7.4) in between the two MeerKAT observations allows us to associate also the MeerKAT radio emission to RK2. From the ATCA detection, we measured $\alpha = -0.6 \pm 0.1$. This index is consistent with optically thin synchrotron emission from a second transient jet launched by MAXI J1348−630 during its 2019/2020 outburst, in the same direction as the previous radio knot. Again we detect no counter-jet in the opposite direction. Due to the steep spectrum and radio emission fainter than RK1, RK2 was mostly detected with MeerKAT, and its evolution was tracked for roughly 1 month. The detections

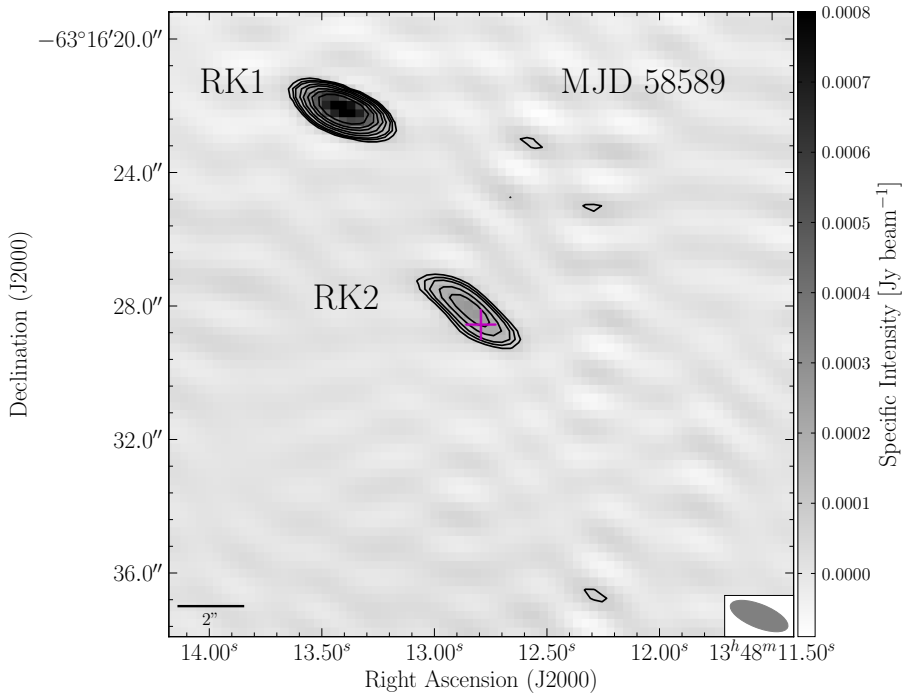

Figure 7.4: ATCA 9 GHz image of the 2019 April 16 observation (MJD 58589), showing the motion of the discrete ejecta RK1 and RK2 as the two jets moved away from the core at position angles of, respectively, $33.2° \pm 1.4°$ and $33° \pm 11°$ East of North. Contours start a 3 times the rms ($\sim$20 μJy beam^{-1}). The MAXI J1348−630 position is marked with a magenta cross. RK1 detected an angular separation of $\sim$7.7 arcsec from the core, while RK2 at this stage is at the beginning of its motion, at an angular distance of $\sim$0.7 arcsec from the core.

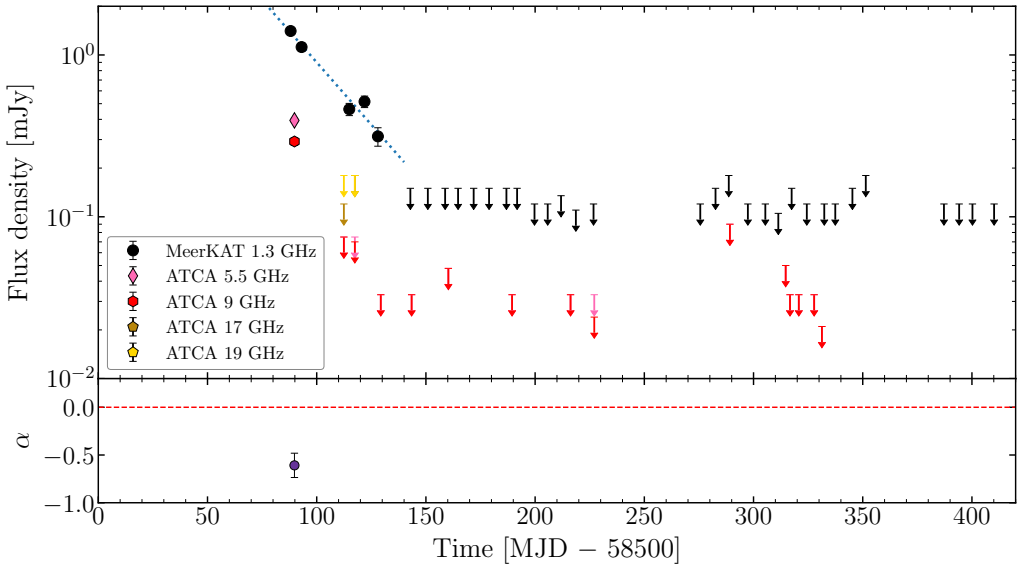

Figure 7.5: *Top panel*: Radio light curve of RK2 obtained with MeerKAT and ATCA observations. An exponential fit to the decay (only MeerKAT) is represented with a dashed line. *Bottom panel*: Radio spectral index of RK2 obtained from ATCA simultaneous multi-frequency observations, as reported in Table 7.1.

are characterised by lower positional accuracy and lower signal-to-noise ratio with respect to RK1, since, for the last three MeerKAT detections, RK2 was never completely resolved from the re-activated compact jet in the second hard state of MAXI J1348−630. With the first radio detection, on MJD 58588, RK2 shows a moderate flux density of ∼1.4 mJy at 1.3 GHz, while on the following weeks the emission faded to ∼400 μJy at 1.3 GHz with a 28 ± 2 days decay timescale. After the last detection on MJD 58628, RK2 faded below our detection limits for the rest of the whole outburst.

Table 7.1: Radio flux densities S_ν of the second radio knot RK2. Observation MJDs represent the middle of the observation, where errors represent the observation duration (time on source). For the ATCA observations we report the array configuration as a subscript. The spectral index α of each component ($S_\nu \propto \nu^\alpha$) is computed only for simultaneous ATCA multi frequency observations. For brevity, we only report the 6 detections of RK2.

Calendar date [UT]	MJD	Telescope	Central frequency [GHz]	$S_{\nu,\mathrm{RK2}}$ [mJy]	α_{RK2}
2019-04-15	58588.053 ± 0.005	MeerKAT	1.3	1.41 ± 0.06	
2019-04-16	58589.81 ± 0.11	$\mathrm{ATCA}_{750\mathrm{C}}$	5.5	0.39 ± 0.01	-0.6 ± 0.1
			9	0.29 ± 0.02	
2019-04-20	58593.074 ± 0.005	MeerKAT	1.3	1.12 ± 0.07	
2019-05-11	58614.909 ± 0.005	MeerKAT	1.3	0.46 ± 0.04	
2019-05-18	58621.888 ± 0.005	MeerKAT	1.3	0.52 ± 0.04	
2019-05-25	58628.019 ± 0.005	MeerKAT	1.3	0.31 ± 0.04	

7.3 Ejecta motion

The proper motion of RK1 is shown in Figure 7.7 and the data are reported in Table 7.2, for which we used data from MeerKAT and from ATCA at 5.5 GHz that have a higher signal-to-noise ratio with respect to the 9 GHz ones. The offset is computed as the great circle distance between the radio knot and the MAXI J1348−630 position, either the fitted one in case of core detection on the same epoch, or the core position reported in Section 5.3.2 in case of core non-detection. In the first case we are not affected by global systematics in the position error estimation.

7.3.1 Astrometry correction

In order to precisely reconstruct the trajectory of the jet and to study in detail its motion, it is crucial to have an accurate astrometry for all the observations. Throughout the monitoring, we noticed some positional offset in the MeerKAT epochs at the arcsec level. Such offset, probably due to some residual phase error after calibration, was global and it could be identified in a significant number (at least seven) stable background point sources. We show in Figure 7.6 the coordinate evolution in time of the background source closest to MAXI J1348−630 (less than one arcmin). Such short angular distance is important, because it means that the same source is also seen in the smaller ATCA field at higher frequencies. Therefore, for each MeerKAT epoch we computed its offset in both Right Ascension and Declination from a reference position

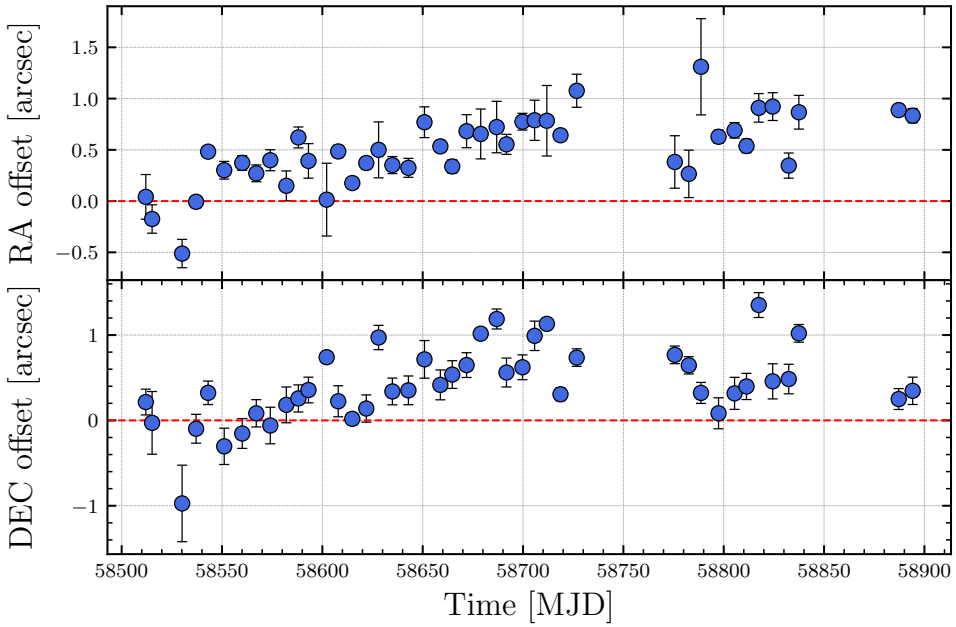

Figure 7.6: Positional offset of a stable background point source observed with MeerKAT with respect to the higher resolution coordinates obtained with ATCA. Such global offset was used to correct the coordinates obtained for the core and the jets of MAXI J1348−630.

determined from higher resolution ATCA observations at 9 GHz (which were part of the monitoring and are presented in Section 5.3.2). Subsequently, we subtracted this global offset to the position of the core and of the jets of MAXI J1348−630, to obtain a zero-order (but highly significant) improvement of the astrometric accuracy. For ATCA, such correction was not necessary, as no global offsets were observed throughout the monitoring campaign. A similar correction was implemented by Russell et al. (2019c) in the study of motion of the jet from MAXI J1535−571.

Table 7.2: Measured positions of RK1 and its angular separation from MAXI J1348−630. The positions are corrected using a bright background point source close to the target. The errors reported for the coordinates are only the statistical ones from source fitting. The angular separation is computed as the great circle distance between the radio knot and the MAXI J1348−630 position, either the one obtained from the fit in case of core detection in the same epoch, either the reference one reported in Section 5.3.2, in case of core non-detection. This allows to ignore global systematics in the error associated to the angular separation for the epochs in which both the RK1 and the core are detected.

Calendar date [UT]	MJD	Right Ascension	Declination	Angular separation [arcsec]
2019-03-09	58551.100	$13^{h}48^{m}13.03^{s} \pm 0.09''$	$-63°16'26.26'' \pm 0.20''$	2.80 ± 0.46
2019-03-18	58560.075	$13^{h}48^{m}13.11^{s} \pm 0.02''$	$-63°16'25.31'' \pm 0.04''$	3.89 ± 0.44
2019-03-25	58567.074	$13^{h}48^{m}13.19^{s} \pm 0.04''$	$-63°16'24.45'' \pm 0.08''$	4.92 ± 0.44
2019-03-31	58573.759	$13^{h}48^{m}13.29^{s} \pm 0.19''$	$-63°16'23.57'' \pm 0.23''$	6.00 ± 0.20
2019-04-01	58574.061	$13^{h}48^{m}13.23^{s} \pm 0.42''$	$-63°16'23.83'' \pm 0.52''$	5.58 ± 0.49
2019-04-08	58581.715	$13^{h}48^{m}13.363^{s} \pm 0.005''$	$-63°16'22.77'' \pm 0.01''$	6.78 ± 0.02

Continued on the next page

Table 7.2: Continued from the previous page. Measured positions of RK1 and its angular separation from MAXI J1348−630.

Calendar date [UT]	MJD	Right Ascension	Declination	Angular separation [arcsec]
2019-04-09	58582.053	$13^h48^m13.31^s \pm 0.41''$	$-63°16'23.51'' \pm 0.13''$	6.15 ± 0.48
2019-04-15	58588.053	$13^h48^m13.36^s \pm 0.04''$	$-63°16'22.43'' \pm 0.05''$	7.23 ± 0.44
2019-04-16	58589.806	$13^h48^m13.40^s \pm 0.02''$	$-63°16'22.13'' \pm 0.01''$	7.64 ± 0.25
2019-04-20	58593.074	$13^h48^m13.44^s \pm 0.08''$	$-63°16'21.97'' \pm 0.07''$	7.90 ± 0.44
2019-04-29	58602.144	$13^h48^m13.72^s \pm 0.75''$	$-63°16'20.88'' \pm 0.15''$	9.39 ± 0.25
2019-04-30	58603.306	$13^h48^m13.58^s \pm 0.21''$	$-63°16'21.05'' \pm 0.04''$	9.14 ± 0.18
2019-05-04	58607.908	$13^h48^m13.52^s \pm 0.08''$	$-63°16'20.64'' \pm 0.28''$	9.20 ± 0.25
2019-05-11	58614.909	$13^h48^m13.53^s \pm 0.15''$	$-63°16'20.40'' \pm 0.37''$	9.69 ± 0.31
2019-05-18	58621.888	$13^h48^m13.69^s \pm 0.31''$	$-63°16'18.88'' \pm 0.81''$	11.61 ± 0.68
2019-10-19	58775.616	$13^h48^m14.99^s \pm 0.28''$	$-63°16'06.31'' \pm 0.15''$	26.74 ± 0.46
2019-10-26	58782.597	$13^h48^m14.94^s \pm 0.25''$	$-63°16'06.28'' \pm 0.15''$	26.58 ± 0.46
2019-11-01	58788.670	$13^h48^m14.84^s \pm 0.58''$	$-63°16'05.68'' \pm 0.14''$	26.73 ± 0.48
2019-11-10	58797.408	$13^h48^m14.99^s \pm 0.28''$	$-63°16'05.47'' \pm 0.67''$	27.45 ± 0.71
2019-11-18	58805.403	$13^h48^m14.99^s \pm 0.13''$	$-63°16'05.50'' \pm 0.36''$	27.41 ± 0.53
2019-11-24	58811.345	$13^h48^m14.97^s \pm 0.18''$	$-63°16'06.92'' \pm 0.39''$	26.63 ± 0.41
2019-11-27	58814.722	$13^h48^m14.82^s \pm 0.78''$	$-63°16'06.05'' \pm 0.05''$	26.36 ± 0.26
2019-11-30	58817.449	$13^h48^m14.90^s \pm 0.25''$	$-63°16'06.27'' \pm 0.27''$	27.19 ± 0.31
2019-12-03	58820.734	$13^h48^m15.16^s \pm 0.79''$	$-63°16'06.74'' \pm 0.41''$	27.03 ± 0.43
2019-12-07	58824.396	$13^h48^m14.85^s \pm 0.50''$	$-63°16'07.20'' \pm 0.65''$	26.40 ± 1.36
2019-12-10	58827.754	$13^h48^m14.93^s \pm 0.17''$	$-63°16'05.48'' \pm 0.15''$	27.33 ± 0.24
2019-12-14[a]	58831.316	$13^h48^m15.05^s \pm 0.16''$	$-63°16'05.88'' \pm 0.28''$	27.44 ± 0.33
2019-12-20	58837.428	$13^h48^m14.93^s \pm 1.19''$	$-63°16'05.28'' \pm 0.53''$	27.38 ± 0.69
2020-02-08	58887.185	$13^h48^m15.03^s \pm 0.23''$	$-63°16'05.23'' \pm 0.59''$	27.94 ± 0.56

[a] Combination of the MJD 58830 and 58831 ATCA epochs to obtain a higher significance detection of RK1 at both 5.5 and 9 GHz.

The motion of RK1 can be divided in two parts: a first phase in which the jet appeared to travel ballistically with a high, constant proper motion and a second part in which the jet underwent a strong deceleration, after the re-brightening on MJD 58775. We discuss the possible reasons for the deceleration in Section 7.6.

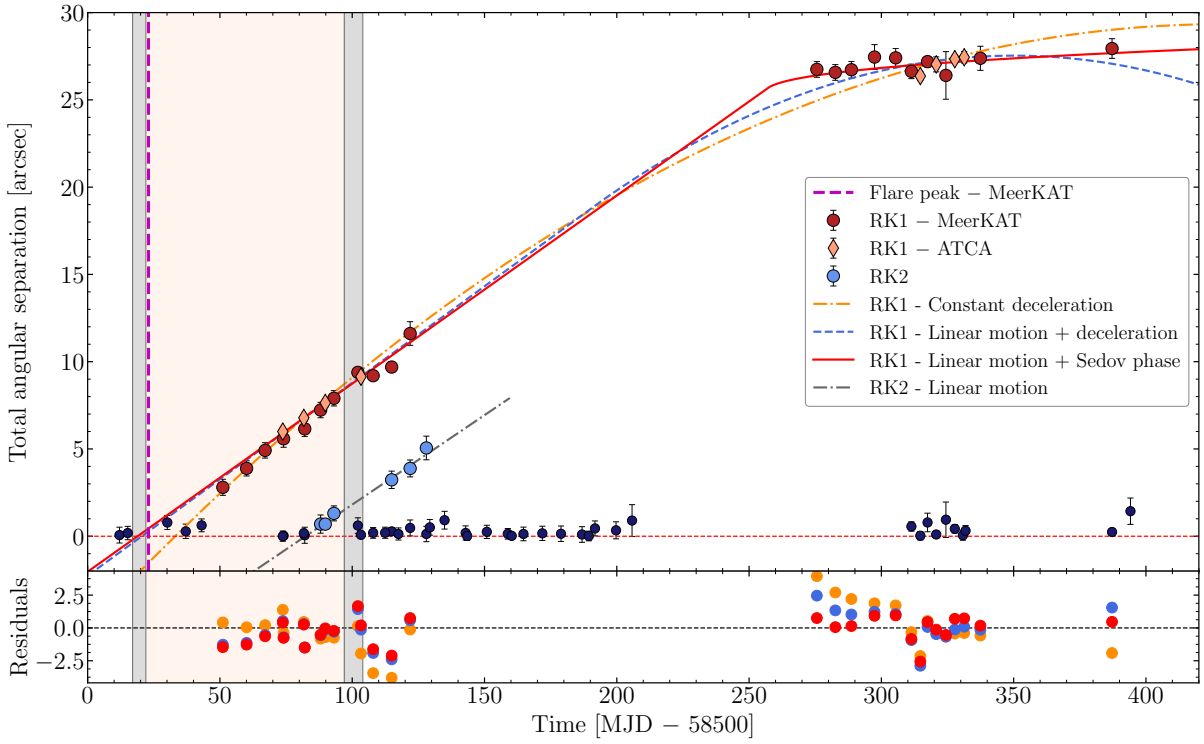

Figure 7.7: Angular separation in arcsec between RK1 and MAXI J1348−630. We use here MeerKAT 1.28 GHz and ATCA 5 GHz observations, shown respectively as red and orange points. Detections of the core are shown as dark blue points. The un-shaded, grey and pink regions mark periods in which MAXI J1348−630 was, respectively, in the hard, intermediate and soft state. The data are listed in Table 7.2. The astrometry has been corrected using a stable background point source. The red horizontal line represents the zero separation from the core, while the time of the major flare observed with MeerKAT (MJD 58523) is represented with a magenta vertical line. As discussed in Section 7.3.2, we fitted the RK1 motion with a constant deceleration model and with two models consisting of a combination of a linear motion with either a simple deceleration, or with a Sedov phase (Wang, Dai, and Lu, 2003). Residuals ([data – model]/uncertainties) are reported for each model in the bottom panel with corresponding colors and show the better agreement of the linear+Sedov model with the data. Our best estimate for the RK1 ejection date is $t_{\rm ej}$ = MJD 58518.9 ± 2.4. We also show the angular separation of the second discrete ejection RK2, which is discussed in Section 7.3.3. A simple linear motion was used to fit the data of RK2, and our best estimate for the RK2 ejection date is $t_{\rm ej}$ = MJD 58582.3 ± 2.5. All fit results are shown in Table 7.3.

7.3.2 Motion of the first discrete ejecta

We start with a simple linear motion model:

$$\alpha(t) = \mu(t - t_{\text{ej, lin}}) \tag{7.1}$$

where $\alpha(t)$ is the total angular separation from MAXI J1348−630, μ is the proper motion of the jet and t_{ej} is the time on which the plasmon is launched. This simple model is clearly not adequate for fitting the whole data set. If we assume instead a constant deceleration throughout out its evolution, we can use the following model:

$$\alpha(t) = \frac{1}{2}\dot{\mu}(t - t_{\text{ej, decel}})^2 + \mu(t - t_{\text{ej, decel}}) \tag{7.2}$$

A preliminary fit of the data with a simple constant deceleration shows that the model does not seem to describe well the later part of the jet motion, with a reduced $\chi^2 = 3.09$ $(80.3/26)$. The fit yielded an extremely high launching proper motion of $\mu = 148 \pm 4$ mas day^{-1} and a deceleration of $\dot{\mu} = -0.38 \pm 0.03$ mas day^{-2}, while the inferred ejection date is $t_{\text{ej, decel}} =$ MJD 58533.1 $\pm$ 1.3, $\sim$10 days after the radio flare. A better (statistical and physical) result can be obtained by combining the two motions mentioned above in Equation 7.1 and 7.2, assuming a jet that starts with constant speed and then decelerates after a *change* time t_{c}, after eventually having swept up enough mass on its path. By fitting the data with the combined model, we obtain a lower reduced $\chi^2 = 1.69$ $(42.3/25)$. For the linear part we obtain a constant proper motion of $\mu = 111 \pm 4$ mas day^{-1}. Then the motion changes at an inferred $t_{\text{c}} =$ MJD 58689 $\pm$ 17, to continue with a constant deceleration of $\dot{\mu} = -0.68 \pm 0.08$ mas day^{-2}. We note that the model predicts that the jet completely stops at MJD 58850. The fit yields an ejection at earlier times, $t_{\text{ej, lin+decel}} =$ MJD 58520.4 $\pm$ 2.3.

We then follow the approach of Miller-Jones et al. (2011b) by applying the external shock dynamic model from Wang, Dai, and Lu (2003), in analogy with models developed for GRB afterglows (Rees and Meszaros, 1992; Mészáros and Rees, 1997). In the context of such model, the relativistic motion of the ejecta should produce a shock wave that propagates into the ISM and that decelerates as material is swept up along the plasmon trajectory. As a result, the late time behaviour of the adiabatically expanding jet obeys the known Sedov solution $\alpha(t) \propto t^{\frac{2}{5}}$ that in our case reads

$$\alpha(t) = \alpha_0 + k(t - t_0)^{\frac{2}{5}} \tag{7.3}$$

where t_0 is the time at which the jet is at an angular separation α_0 from the core position. In this model, the motion is first linear, with a proper motion μ, until a *change* time t_{c}, after which it follows Equation 7.3. This fit yields a better reduced $\chi^2 = 1.17$ $(29.3/25)$, and we can also see from Figure 7.7 that this model is more adequate to describe the jet motion. For the first, ballistic part we still obtain a high proper motion $\mu = 108 \pm 4$ mas day^{-1}. The jet motion later approaches the Sedov phase on $t_{\text{c}} =$ MJD 58757 $\pm$ 11, with a $t_0 =$ MJD 58755 $\pm$ 12, two days earlier than t_{c}. Our best estimate for the jet ejection date is $t_{\text{ej, lin+Sedov}} =$ MJD 58518.9 $\pm$ 2.4, a result very similar to the one obtained with the linear+deceleration model. We find $\alpha_0 = 25.2 \pm 3.8$ arcsec and a normalization parameter $k = 0.3^{+3.7}_{-0.3}$ arcsec day$^{-0.4}$, which is not well constrained. Given that from our fit k could also be 0, we have to consider the possibility that the jet simply stopped at $\alpha(t) = \alpha_0$ before MJD 58750. Therefore, we tried to fit the data with a combination of a linear motion (Equation 7.1) and a constant position. The result is a reduced $\chi^2 = 1.39$, which is slightly worse than the one obtained from the linear+Sedov model,

implying that the scenario of a moving jet is still favored with respect to that of an arrested jet. All the fits for the different models are shown in Figure 7.7 and the parameters obtained are listed in Table 7.3.

Table 7.3: Parameters obtained from the fitting of the motion of RK1 and RK2, discussed in Sections 7.3.2 and 7.3.3. We show the proper motion μ, the acceleration $\dot{\mu}$, and, for the composite models, the time t_c at which the deceleration starts. For composite models, the parameter μ refers only to the initial, linear part of the motion. For all the models we present the best estimate for the ejection date t_{ej} and the reduced χ^2.

Ejecta	Model	μ [mas day^{-1}]	$\dot{\mu}$ [mas day^{-2}]	t_c [MJD]	t_{ej} [MJD]	Reduced χ^2
RK1	Constant deceleration	148 ± 4	-0.38 ± 0.03		58533.1 ± 1.3	3.09 (80.3/26)
RK1	Linear+Deceleration	111 ± 4	-0.68 ± 0.08	58689 ± 17	58520.4 ± 2.3	1.69 (42.3/25)
RK1	Linear+Sedov	108 ± 4		58757 ± 11	58518.9 ± 2.4	1.17 (29.3/25)
RK2	Linear motion	103 ± 12			58582.3 ± 2.5	0.21 (0.84/4)

While our data seem to favour the scenario of a linear motion followed by a Sedov phase, we can also consider the information provided by the X-ray and radio monitoring to discriminate between diferent models, with an approach very similar to the one adopted for the single radio knot of MAXI J1535−571 (Russell et al. 2019c). In Section 5.3 we report that the system transitions from the hard state to the IMS on MJD 58517, and then enters in the soft state on MJD 58522.6 (see Table 5.1). Moreover, we observe with MeerKAT the peak of the strong radio flare on MJD 58523. It is generally accepted that radio flares in XRBs are produced by the adiabatic expansion of ejected plasma blobs, hence these components should be launched before strong radio flares are observed (e.g. Fender, Belloni, and Gallo 2004; Miller-Jones et al. 2012; Fender and Bright 2019). On that basis, we can discard the scenario of constant deceleration, since its inferred ejection date $t_{ej,\,decel} = \text{MJD } 58533.1 \pm 1.3$ is $\sim$10 days after the bright radio flare, when the radio emission from the core had been constantly fading, until reaching non detection on MJD 58551. However, we note that, although unlikely, we cannot in principle rule out a totally unrelated radio flare. On the other hand, the two other models both start with a linear motion and yield very similar results regarding the inferred ejection date, with the t_{ej} ranging between MJD 58518 and 58520 (see Table 7.3), which are more plausible as they lie before the MeerKAT radio flare, when the system was still in the IMS. We note that, since these ejection dates are obtained from composite models, our estimates for t_{ej} are based for the most part on the first half of the data (RK1 detections before MJD 58640).

Assuming that our best estimate for the proper motion is the one obtained by the linear+Sedov model, our measurement of $\mu = 108 \pm 4$ mas day^{-1} during the ballistic part of the motion corresponds to a superluminal, apparent transverse speed of $1.37 \pm 0.05\ c$, assuming a distance of 2.2 kpc, while it is still superluminal ($\sim c$) for the closest acceptable distance (1.6 kpc). We can then conclude that RK1 is almost certainly the approaching component and that it is intrinsically relativistic for the first part of its motion. MAXI J1348−630 is, therefore, a new source displaying discrete ejecta with apparent superluminal motion.

7.3.3 Motion of the second discrete ejecta

To fit the motion of RK2 we adopt a simple linear, ballistic motion from Equation 7.1. Fitting the data with such model yields a reduced χ^2 of 0.21 (0.84/4), with the low value likely to be

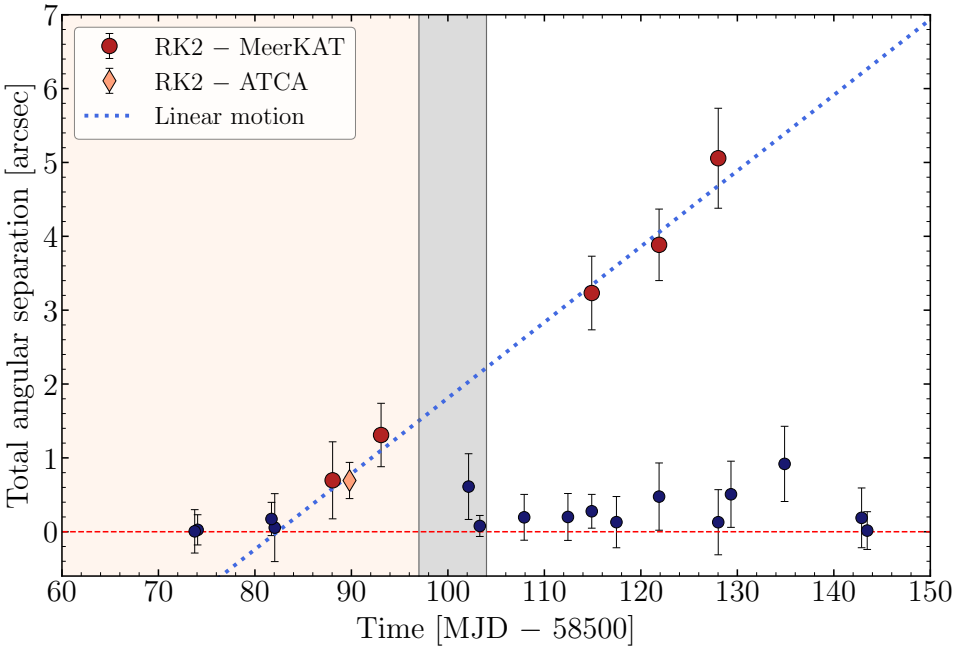

Figure 7.8: Angular separation in arcsec between RK2 and MAXI J1348−630, obtained from Figure 7.7. We use here MeerKAT 1.28 GHz and ATCA 5 GHz observations, shown respectively as red and orange points. Detections of the core are shown as dark blue points. The un-shaded, grey and pink regions mark periods in which MAXI J1348−630 was, respectively, in the hard, intermediate and soft state. The data are listed in Table 7.4. The astrometry has been corrected using a stable background point source. A simple linear motion was used to fit the data of RK2, and our best estimate for the RK2 ejection date is $t_{\rm ej}$ = MJD 58582.3 ± 2.5. All fit results are shown in Table 7.3.

coming from overestimated uncertainties on the data points. The parameters obtained from the fits are listed in Table 7.3. We obtain again a very high proper motion of $\mu = 103 \pm 12$ mas day^{-1}, similar to RK1. The ejection date, $t_{\rm ej,\,linear}$ = MJD 58582.3 ± 2.5, points towards an unusual ejection in the middle of the soft state; this is discussed in Section 7.7. For RK2, the proper motion derived from the linear fit corresponds to an apparent transverse speed of $1.30 \pm 0.15\ c$ at 2.2 kpc, and the jet appears to be superluminal for all but the closest distance (transverse speed $\sim$0.95 c at 1.6 kpc). Hence, RK2 is likely to be the approaching component of a second, intrinsically relativistic, discrete ejection.

Table 7.4: Measured positions of RK2 and its angular separation from MAXI J1348−630. The positions are corrected using a bright background point source close to the target. The errors reported for the coordinates are only the statistical ones from source fitting. The angular separation is computed as the great circle distance between the radio knot and the MAXI J1348−630 position, either the one obtained from the fit in case of core detection in the same epoch, either the reference one reported in Section 5.3.2, in case of core non-detection. This allows to ignore global systematics in the error associated to the angular separation for the epochs in which both the RK2 and the core are detected.

Calendar date [UT]	MJD	Right Ascension	Declination	Angular separation [arcsec]
2019-04-15	58588.053	$13^{\rm h}48^{\rm m}12.81^{\rm s} \pm 0.11''$	$-63°16'27.87'' \pm 0.16''$	0.70 ± 0.52
2019-04-16	58589.806	$13^{\rm h}48^{\rm m}12.86^{\rm s} \pm 0.07''$	$-63°16'28.01'' \pm 0.04''$	0.69 ± 0.24

Continued on the next page

Table 7.4: Continued from the previous page. Measured positions of RK2 and its angular separation from MAXI J1348−630.

Calendar date [UT]	MJD	Right Ascension	Declination	Angular separation [arcsec]
2019-04-20	58593.074	$13^{h}48^{m}12.92^{s} \pm 0.21''$	$-63°16'27.57'' \pm 0.18''$	1.31 ± 0.43
2019-05-11	58614.909	$13^{h}48^{m}13.07^{s} \pm 0.12''$	$-63°16'25.90'' \pm 0.31''$	3.23 ± 0.50
2019-05-18	58621.888	$13^{h}48^{m}13.15^{s} \pm 0.12''$	$-63°16'25.52'' \pm 0.32''$	4.15 ± 0.23
2019-05-25	58628.019	$13^{h}48^{m}13.18^{s} \pm 0.49''$	$-63°16'24.25'' \pm 0.59''$	4.96 ± 0.52

7.4 Constraints from the jet motion

We detected and tracked the motion of the two discrete ejecta RK1 and RK2 for more than 300 days. Discrete ejections have only been detected so far in a limited subset of the known BH XRBs population (e.g. Mirabel and Rodríguez 1994; Hjellming and Rupen 1995; Corbel et al. 2002; Yang et al. 2010; Rushton et al. 2017; Russell et al. 2019c; Bright et al. 2020). The two ejecta both displayed initial proper motions larger than 100 mas day^{-1}, which are the highest ever measured for BH XRBs ejections, and, more in general, for objects outside the Solar System. This can be likely ascribed to the relative proximity (2.2 kpc) of MAXI J1348−630 in comparison to other XRBs.

We can put constraints on the true speed β of the knots and their inclination angle θ to the line of sight at the time of ejection, under the assumption of intrinsically symmetric jets. For unpaired components we can only solve for $\beta \cos\theta$ in the following equation, once the distance is known (e.g. Rees 1966; Mirabel and Rodríguez 1994)

$$\mu_{\rm app} = \frac{\beta \sin\theta}{1 - \beta\cos\theta}\frac{c}{D} \qquad \mu_{\rm rec} = \frac{\beta \sin\theta}{1 + \beta\cos\theta}\frac{c}{D} \tag{7.4}$$

where μ is the proper motion for the approaching or receding component and D is the source distance. The results for RK1 and RK2 are shown in Figure 7.9, where we plot the existing solutions for the best distance estimate and for its upper and lower bounds. For RK1, Equation 7.4 has solutions only for the jet being the approaching component at all possible distances, in agreement with its apparent superluminal motion. We obtain $\beta_1 \cos\theta_1 \geq 0.51$, which implies that $\beta_1 \geq 0.70$ and that $\theta_1 \leq 44°$ (accepting only solutions for which β decreases as θ increases). A low inclination angle is consistent with RK1 appearing brighter due to Doppler boosting, and at the same time it is consistent with the non detection of the receding paired component, as strongly Doppler de-boosted. Moreover, if we assume a jet axis perpendicular to the accretion disk (even if this does not appear to be universal among BH XRBs, e.g. Maccarone 2002; Miller-Jones et al. 2019; Poutanen et al. 2021), our constraints point to a relatively face-on configuration of the system, which can in turn suggest a significant Doppler boosting of the compact jet itself.

Regarding RK2, we can see from Figure 7.9 that the detected knot is almost certainly the approaching component of the second ejection. Similarly to RK1, we obtain $\beta_2 \cos\theta_2 \geq 0.48$, leading to $\beta_2 \geq 0.69$ and $\theta_2 \leq 46°$. However, Equation 7.4 has also a small number of

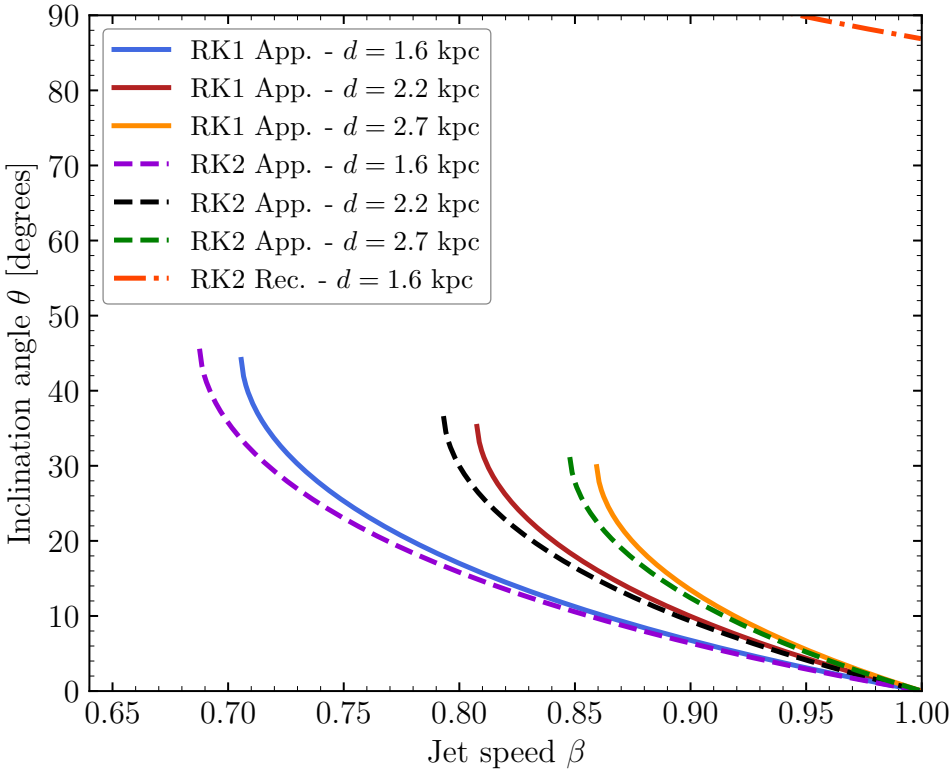

Figure 7.9: Constraints on the jet speed and inclination angle to the line of sight for RK1 (continuous lines) and RK2 (dashed lines). The constraints are derived from Equation 7.4, by using the initial measured proper motions and the whole range of possible distances ($2.2^{+0.5}_{-0.6}$ kpc, Chauhan et al. 2021). RK1 has only solutions as the approaching component. RK2, while being almost certainly another approaching jet, does have a small subset of solutions as a receding component for the closest possible distance (top right corner of the bottom panel, dot-dashed line), but we deem them unlikely, as discussed in the text.

solutions with RK2 being the receding component, only at the closest possible distance of 1.6 kpc, implying an extremely fast jet with β close to 1 and an inclination angle close to 90°. This scenario is highly unlikely for two main reasons. First, with such an intrinsically fast jet we would expect to detect also the approaching component, which would be highly Doppler boosted and should be even brighter than the receding component. Second, the results would suggest an almost edge-on disk configuration, which we can discard on the basis of the fact that we do not detect any modulation of the X-ray light curve that would eventually be due to the occultation by the companion star. Moreover, these constraints would be totally inconsistent with the ones obtained for RK1. Hence, we can safely affirm that also RK2 is the approaching component, which is possibly traveling with the same trajectory of RK1, given that we do not find any evidence for a varying jet speed or inclination angle between the two ejections.

7.4.1 Jet opening angle

RK1 remained unresolved in the direction perpendicular to its motion for the entire monitoring. Hence, we can put constraints on the jet opening angle and on the speed of its transverse expansion. Our best constraints can be obtained with the last detection of RK1 with ATCA, on MJD 58831. Using the ∼2.5 arcsec ATCA beam at 9 GHz and an angular separation from the core of 27 arcsec, we conclude that the RK1 opening angle is ≤6°(half-opening angle ≤3°)

and the transverse expansion speed must be $\leq$0.05 c. These values are consistent with what is derived for other BH LMXBs (e.g. Miller-Jones, Fender, and Nakar 2006; Russell et al. 2019c). In particular, our values are consistent in terms of transverse expansion speed with the multiple ejections (except the two fastest components) observed and modeled in V404 Cyg (Tetarenko et al., 2017), although we find a smaller jet opening angle for RK1. Our results are in agreement with the small jet expansion speeds calculated in Fender and Bright (2019). Similar computations are not informative for RK2, given that the second knot was detected at a maximum separation of only $\sim$5 arcsec from the core position.

7.5 Ejection of the first component

I discuss in this section the ejection date of RK1 and I put it in relation with the other radio and X-ray observational results. Such discussion is particularly important because, as I mentioned in Chapter 3, the sequence of the changes in the properties of the accretion flow and on the jet during these powerful ejections is currently poorly understood, and having a comprehensive view of the source evolution during this phase is fundamental to improve our understanding on these phenomena.

7.5.1 Link with X-ray observations

The strong radio flare observed on MJD 58523 is likely to be associated with the ejection of RK1, but the mechanism capable of launching and accelerating these relativistic plasma knots is still not understood. The current picture links the launch of the jets with the transition from the HS to the SS, i.e. during the IMS, where usually ejections take place prior to strong radio flares (e.g. Corbel et al. 2004a; Fender, Belloni, and Gallo 2004; Fender 2006; Miller-Jones et al. 2012) and are marked by changes in the X-ray timing and spectral properties (Belloni et al., 2005). RK1 fits very well in this picture, as the inferred ejection date $t_{\rm ej,\ lin+Sedov}$ = MJD 58518.9 $\pm$ 2.4 (see Section 7.3.2) is only 4 days before the strong radio flare observed with MeerKAT, and when MAXI J1348$-$630 was in the IMS. The presence of Type-B QPOs (tentatively linked to discrete ejections, e.g. Soleri, Belloni, and Casella 2008; Fender, Homan, and Belloni 2009; Miller-Jones et al. 2012; Homan et al. 2020) has been detected with NICER close to the first hard-to-soft state transition during the main outburst of MAXI J1348$-$630 (Belloni et al., 2020; Zhang et al., 2020a). In particular, Type-B QPOs started to be detected on MJD 58522.6 (Zhang et al., 2020a). This is $\gtrsim$ 3 days after our inferred ejection date, similar to what was already observed for H1743$-$322 (Miller-Jones et al., 2012) and MAXI J1535$-$571 (Russell et al., 2019c). However, a detailed discussion of the NICER timing results in relation to the inferred ejection dates will be discussed in a forthcoming work.

7.5.2 Multiple radio flares

The $\sim$5 arcsec MeerKAT resolution does not allow us to resolve the two components soon after the ejection, while the ATCA observations were short (providing a non optimal *uv*-coverage). As the synchrotron-emitting component is launched and expands, it is predicted to have an optically thick rising phase due to an increasing surface area, followed by an optically thin decay produced by adiabatic expansion losses (van der Laan, 1966). Flares produced by discrete ejecta are observed to rise on very different timescales (from minutes or hours to days, e.g. Brocksopp et al. 2007; Tetarenko et al. 2017; Bright et al. 2020), depending on the size

and energy of the ejected component. It is possible that the flare had a fast rise, and thus we missed the optically thick phase with our coverage. Another possibility is that the flare was entirely optically thin, as already observed for some sources (e.g. Fender et al. 1997). The ATCA observation taken on MJD 58524 and the decreasing flux observed on MJD 58523 (see Section 5.3.4) seem to confirm that we are observing the optically thin decay of the transient jet (see Figure 5.5).

The following ATCA observations clearly show a second, longer, optically thin flare taking place after the first one, and the emission detected between MJD 58526 and 58532 is possibly resulting from the superposition of the decaying first flare with the rise of the second flare. This is also confirmed by the 1.34 GHz ASKAP observation of MJD 58527, showing a low frequency emission rising, peaking ($\sim$250 mJy) and decaying within the same epoch (Chauhan et al., 2021). In this context, it is not clear what could be producing the second flare. We might be observing the signature of a second ejection, as multiple ejections have been already associated to multiple radio flares on short timescales (e.g. Tetarenko et al. 2017; Miller-Jones et al. 2019). This would also be consistent with the fact that lower frequencies (ASKAP) appear to peak after the higher ones (ATCA), as predicted for ejected plasmons (van der Laan, 1966). However, we caution that we might not have sampled the flare adequately, and we cannot infer precisely the location in time of the high frequency peaks. Moreover, we do not detect any additional discrete component leaving the system. A possibility is that the emission linked to RK1, observed at later times, could arise from the collision of two ejecta launched in coincidence with the two radio flares. As an alternative, pairs of flares close in time could be produced by the approaching and receding components of a single ejection event, as for instance reported in Tetarenko et al. (2017) for V404 Cyg. However, in V404 Cyg the timescales for the detection of both flares were of the orders of minutes to hours, while in our case there are at least three days between the two flare peaks, hence it seems unlikely that they are produced by a single ejection event.

Our data do not allow us to draw more precise conclusions regarding the origin of the second flare. Obtaining a more accurate estimation of the RK1 ejection date would be useful to get a better understanding of the observations, and a denser coverage, or higher-resolution VLBI observations, could have helped us to discriminate between different scenarios. Nevertheless, this highlights the importance of radio monitorings during flares and state transitions.

7.5.3 Flare energetics

We constrain the minimum energy and the corresponding magnetic field required to produce the synchrotron luminosity of the first, strong radio flare (e.g. Longair 2011; Fender 2006). If we make the standard assumption of equipartition between electrons and magnetic fields in the jet plasma, we can compute the minimum energy as following:

$$E_{\rm min} \simeq 8 \times 10^6 \eta^{\frac{4}{7}} \left(\frac{V}{\rm cm^3}\right)^{\frac{3}{7}} \left(\frac{\nu}{\rm GHz}\right)^{\frac{2}{7}} \left(\frac{L_\nu}{\rm erg\ s^{-1} Hz^{-1}}\right)^{\frac{4}{7}} \rm erg \tag{7.5}$$

where η is a parameter linked to the ratio of energy in protons to that in electrons. Here we assume that synchrotron emission from protons is negligible, so that $\eta = 1$. Since the knot cannot expand faster than light, we can estimate an upper limit on the volume of the emission region V at launch: $V = (4/3)\pi(c\Delta t)^3$. However, we mention that Fender and Bright (2019) suggest that these ejections expand at only at small fractions (0.01–0.1) of c. The conservative

rise time Δt of the RK1 ejection can be obtained by the interval between the last optically thick ATCA detection of the MAXI J1348−630 core on MJD 58521.9 and the high ∼0.5 Jy peak observed with MeerKAT on MJD 58523.2, for which optically thin emission is detected with ATCA on the same day, likely produced by the adiabatic expansion of the plasma knot. We then convert the peak flux of the flare observed with MeerKAT at 1.3 GHz to the monochromatic radio luminosity $L_\nu = 4\pi D^2 S_\nu$, where S_ν is the measured flux density. Neglecting for the moment any Doppler effects, we obtain a minimum energy $E_{\rm min} \sim 10^{42}$ erg, a minimum average power $P_{\rm min} \sim 10^{37}$ erg s^{-1} (∼10% of the simultaneous X-ray luminosity) and a corresponding equipartition magnetic field $B_{\rm eq} \sim 10$ mGauss. The Lorentz factor of electrons radiating around 1.3 GHz is ∼5000. Those numbers are consistent with what has been found for other discrete ejections (Fender et al., 1999; Curran et al., 2014; Russell et al., 2019c; Bright et al., 2020), but the magnetic field is two orders of magnitude higher than what was obtained for MAXI J1820+070 (Espinasse et al., 2020).

Given the constraints on the ejecta speed and inclination angle provided in Section 7.4 (see Figure 7.9), it is possible to estimate the effect of Doppler boosting on the inferred jet energetics. Assuming the bulk jet Lorentz factor $\Gamma_{\rm j}$ to be in the range between ∼1.4 (from the constraint $\beta_1 \gtrsim 0.7$) and 5, with a corresponding inclination angle $1^\circ \lesssim \theta \lesssim 44^\circ$ from Equation 7.4, we obtain the Doppler factor of an approaching component

$$\delta_{\rm app} = \frac{1}{\Gamma_{\rm j}^{-1}(1 - \beta\cos\theta)} \tag{7.6}$$

to be in the range between ∼1.4 and ∼9.8. The minimum energy in the ejecta rest frame can be computed as

$$E_{\rm min,\,RF} \simeq \Gamma_{\rm j} E_{\rm min} \delta^{(4\alpha-5)/7} \tag{7.7}$$

(including the jet kinetic energy, Fender 2006), where $E_{\rm min}$ comes from Equation 7.5 and α is the radio spectral index of the ejecta. We take $\alpha = -0.5$ (measured value on MJD 58523, see Table 5.2) and we obtain a $E_{\rm min,\,RF}$ in the range $4\text{–}8 \times 10^{41}$ erg. We can also derive the minimum intrinsic power and magnetic field as, respectively

$$P_{\rm min,\,RF} \simeq \Gamma_{\rm j} P_{\rm min} \delta^{(4\alpha-12)/7} \tag{7.8}$$

and

$$B_{\rm eq,\,RF} = B_{\rm eq} \delta^{(2\alpha-13)/7}, \tag{7.9}$$

obtaining $P_{\rm min,\,RF}$ to range between ∼0.3 and ∼5 $\times 10^{36}$ erg s^{-1} and $B_{\rm eq,\,RF}$ to range between ∼0.1 and ∼6 mGauss. In the rest frame of the ejecta, the minimum energy, power and equipartion magnetic field are lower than the ones derived ignoring Doppler effects. We then conclude that the inclusion of Doppler boosting reduces the energetics constraints obtained with the equipartition assumption for the acceptable combinations of $\Gamma_{\rm j}$ and θ.

Considering the major flare, an independent estimation of the ejecta expansion speed and on the minimum energy can be obtained by assuming that the flare was due to synchrotron self-absorption, that it was initially optically thick and that at the peak the optical depth was $\tau \simeq 1$, as outlined in Fender and Bright (2019). From Equations 27 and 28 of Fender and Bright (2019), and ignoring Doppler effects, we obtain an expansion speed of $\beta_{\rm exp} \simeq 0.015$ and a minimum energy of $E_{\rm min} \sim 10^{39}$ erg (less constraining than the previous estimation). This expansion speed leads to a size of the emitting region that is much smaller than what was previously estimated and is consistent with what discussed in Section 7.4.1 and with previous

results for other sources (Miller-Jones, Fender, and Nakar, 2006; Tetarenko et al., 2017; Russell et al., 2019c; Fender and Bright, 2019). The minimum energy limit is less constraining, but both the values inferred for $E_{\rm min}$ in MAXI J1348−630 in this Section are likely to be largely conservative, as it appears that a dominant fraction of the ejecta energy is not radiated, but is instead transferred as kinetic energy to the surrounding environment (Bright et al., 2020). If we include again Doppler boosting in our estimation, we can obtain in the rest frame of the ejecta the minimum energy

$$E_{\rm min,\,RF} \simeq \Gamma_{\rm j} E_{\rm min} \delta^{-97/34} \tag{7.10}$$

and an ejecta expansion speed

$$\beta_{\rm RF,\,exp} = \beta_{\rm exp} \delta^{-49/34} \tag{7.11}$$

as outlined in Fender and Bright (2019). Assuming the same range as above for $\Gamma_{\rm j}$ and θ, we obtain $E_{\rm min,\,RF}$ in the range between 0.09–6 $\times$ 10^{38} erg and an expansion speed $\beta_{\rm RF,\,exp}$ to range between $\sim$6$\times10^{-4}$ and $\sim$0.01. Also in this case, taking into account Doppler corrections leads to a lower minimum energy for the synchrotron flare, and yields an even smaller jet expansion speed, in agreement with Fender and Bright (2019). For RK2, similar estimations are not possible, given that we do not have a good constraint on the rise time of the radio flare at the moment of its ejection.

7.6 Late time behaviour of the first discrete ejecta

The motion of RK1 was monitored for $\sim$300 days and, after a first phase in which it traveled at constant speed, it appeared to re-brighten while being strongly decelerated in the second phase of its motion. Decelerating discrete ejecta have been observed in a number of other sources, namely XTE J1550−564 (Corbel et al., 2002), H1743−322 (Corbel et al., 2005), XTE J1752–223 (Yang et al., 2010; Miller-Jones et al., 2011b), MAXI J1535−571 (Russell et al., 2019c) and MAXI J1820+070 (Bright et al., 2020; Espinasse et al., 2020). For some of them the discrete knots were detected both in radio and X-rays, with the *Chandra* observatory. The current picture is that the plasma blob decelerates via interactions with the ISM, causing constant *in-situ* particle acceleration (up to TeV energies) and producing broadband, optically thin synchrotron radiation (Corbel et al., 2002; Migliori et al., 2017; Espinasse et al., 2020).

After a first part of ballistic, high-speed motion, the deceleration of RK1 was rather abrupt, which is something not observed in the majority of discrete ejecta from BH XRBs (e.g. Mirabel and Rodríguez 1994; Fender et al. 1999; Miller-Jones et al. 2012).

7.6.1 Cavity scenario

This scenario is consistent with a jet travelling first at constant speed in a low-density region of the ISM, which constitutes a large scale cavity around the system, before hitting the higher-density wall of the cavity itself, as already proposed in Hao and Zhang (2009). Radio emission at late times would be produced by the external shock between the plasma blob and the ISM cavity wall, in analogy with GRB afterglows (Wang, Dai, and Lu, 2003). Those cavities have been suggested to exist at $\sim$pc scales at least for XTE J1550−564 and H1743−322 (Hao and Zhang, 2009; Steiner and McClintock, 2012; Steiner, McClintock, and Reid, 2012; Migliori et al., 2017). We obtained the best modeling for the RK1 motion by a combination of a linear motion and a Sedov phase (see Section 7.3.2), achieved at late times due to the jet sweeping

up ISM material on its path, in a similar way as Miller-Jones et al. (2011b), which derived it from Wang, Dai, and Lu (2003). We therefore suggest that MAXI J1348−630 is located in a similar cavity, possibly carved by previous jet activity, or resulting from the action of accretion disk winds. However, so far such winds have not been detected for MAXI J1348−630. If we take our estimate of $\alpha_0 \sim 25$ arcsec, the upper limit on the inclination angle of the discrete ejection of $\theta_1 \sim 44°$and the lowest acceptable distance of 1.6 kpc, we obtain that RK1 traveled at least ∼0.3 pc before reaching the angular distance α_0, which is consistent with what has been observed for other discrete ejections (Corbel et al., 2002; Gallo et al., 2004) and could be taken as a rough lower limit on the size of the cavity (at least in the NE direction, as an asymmetric cavity has been reported for XTE J1550−564, Hao and Zhang 2009; Steiner and McClintock 2012). As argued by Hao and Zhang (2009), the presence of an under-dense cavity could be a common characteristic of BH XRBs environments (Heinz, 2002), and its existence could be strictly required for the jet to travel such a long distance (Hao and Zhang, 2009).

This scenario is also supported by the flux evolution of RK1, which is shown in Figure 7.3 and consists for the most part of two optically thin decay phases. The first decay, between MJD 58588 and 58621, has an e-folding time of ∼12 days (see Section 7.1.1), during which the quickly decaying radio emission is likely produced by the ejecta radiating while in free adiabatic expansion (e.g. van der Laan 1966). The second decay (MJD 58782–58837) is significantly slower than the first, with an e-folding time of ∼41 days, and for which the radio emission is likely produced by particles re-accelerated in external shocks between the jet and the ISM, possibly at the cavity wall. This is similar to what was observed in XTE J1550−564 (Corbel et al., 2002; Tomsick et al., 2003; Migliori et al., 2017) and H1743−322 (Corbel et al., 2005). Decelerating ejecta have also been observed in the 2017/2018 outburst of MAXI J1535−571 (Russell et al., 2019c), and in the 2018 outburst of MAXI J1820+070 by Bright et al. (2020), which reported a ∼6 days quick first decay, immediately followed by two slower ∼50 and ∼20 days decay phases. However, while jet-ISM interaction may take place, MAXI J1820+070 is unlikely to be located in a low density cavity (Bright et al., 2020), and this could explain the lack of late-time re-brightenings of the discrete ejecta.

7.6.2 Alternative hypotheses

There are other possible scenarios for the late time behaviour of RK1. The knot was unresolved in all observations during the second part of the motion, and, as it becomes fainter, we notice some scatter in its position between MJD 58810 and 58840 (see Figure 7.7). This may be due either to a partial jet fragmentation, or to the presence of residual emission from cooling particles, or also to the presence of a receding jet tail, if the radio emission is connected to reverse shocks (Migliori et al., 2017). Internal shocks between unseen shells of plasma have also been invoked to explain the re-brightening of discrete ejections (Fomalont, Geldzahler, and Bradshaw, 2001; Fender, Belloni, and Gallo, 2004; Motta and Fender, 2019).

Given the observation of possibly two radio flares at the hard-to-soft state transition, we could speculate that another possible explanation for the late re-brightening of RK1 is that the radio emission observed after MJD 58775 was produced by the collision of two separate, approaching discrete ejections, launched previously at different times on the same trajectory. We assume that the first component was RK1, inferred to be launched on MJD 58518.9 and tracked until MJD 58621, and the second one was ejected on the second radio flare reported to peak on MJD 58527 (see Figure 5.5). The second component cannot be RK2, as this would have required an acceleration of the discrete ejecta. Using Equation 7.4 and assuming constant

speed, we obtain that, for the second component to catch up with RK1 on MJD 58775 at an angular distance from the core of ∼26 arcsec, we should have a difference in speed between the two jets of $\Delta\beta = \beta_2 - \beta_1$ between 10^{-2} and 10^{-3}, considering the whole range of acceptable values of inclination angles θ inferred for RK1 (see discussion in Section 7.4 and Figure 7.9). While in in principle such values of $\Delta\beta$ could be possible, the difference in speed between the two components appears to be rather small, especially if we compare it with what obtained for multiple ejections in other sources (e.g. Tetarenko et al. 2017). Therefore, some *fine-tuning* seems to be required for this scenario to match the observational constraints. However, we mention that we could have missed the exact time of the re-brightening of RK1, and a different (earlier) re-appearance of RK1 could alleviate the requirement on $\Delta\beta$.

7.7 Considerations on the second discrete ejecta

7.7.1 Ejection

Considering RK2, we obtained the ejection date $t_{\rm ej} =$ MJD 58582.6 ± 2.3, implying an ejection during an interval in which the system appeared to be in the soft state, a behaviour that has never been clearly observed before in BH XRBs. We discuss here that the ejection rather happened during a short excursion from the soft state to the IMS. While the sequence of events leading to a discrete ejection from a BH XRB has not been understood yet, these events are classically linked to the hard-to-soft state transitions (e.g. Fender, Belloni, and Gallo 2004; Corbel et al. 2004b; Fender 2006). Optically-thin radio emission from the core position was detected with MeerKAT and ATCA between MJD 58573 and 58582, reaching almost 10 mJy at 1.3 GHz on MJD 58582, the same day as our inferred ejection date. The emission then faded below our detection threshold on the following epoch. While the observed flux density is one order of magnitude lower than the one measured at the beginning of the outburst (on MJD 58523), it may still indicate the presence of a radio flare in coincidence with our inferred ejection date. Considering the information provided by the X-ray monitoring, a possible additional hint can be found in the MAXI hardness-ratio evolution: while the system was in the soft state and the X-ray emission was completely dominated by the accretion disk (see Section 5.3.1), we detected a fast spike in the hardness, with the source getting harder on MJD 58574 (see Figures 5.1 and 5.2). This may suggest a very quick return of the source to a particularly short-lived IMS, a spectral state that is strongly connected to discrete ejections (e.g. Corbel et al. 2004b; Fender, Belloni, and Gallo 2004). While the spike in hardness happens at least ∼5 days prior to our inferred $t_{\rm ej}$, the sudden change in spectral state of the source is likely associated to the ejection of RK2.

This behaviour is not new among the known population of BH XRBs. Sources have already been observed to rapidly oscillate between the soft and the hard state (e.g. Rao, Yadav, and Paul 2000; Homan et al. 2001; Fender, Homan, and Belloni 2009) and multiple radio flares and discrete ejections have already been observed as as the source moved back and forth across the top branch of the HID (e.g. Brocksopp et al. 2001; Tetarenko et al. 2017). An example is the 1999 outburst of XTE J1859+226, during which several short excursions to the hard-intermediate state (or the so-called Steep Power Law state, given the spectral hardness and the presence of high-frequency QPOs), were clearly correlated with radio flares, signature of multiple ejections (Brocksopp et al., 2002; Fender, Homan, and Belloni, 2009). In our case, however, the quick return to the IMS did not happen on the top branch of the HID, but at later

times, when the source was in the middle of the soft state, descending the left branch on the diagram (see Figure 5.1).

7.7.2 Late time behaviour

For the second discrete ejections RK2, we are only able to constrain the first part of its motion, as RK2 quickly faded below our detection limits, roughly 1 month after its inferred ejection date. However, as RK2 was ejected in the same direction of RK1 and with a very similar initial proper motion, we would expect a similar behaviour between the two discrete components. With an e-folding time of $\sim$28 days, the decay of RK2 (between MJD 58588 and 58628, see Figure 7.5) is slower than the first decay of RK1, although the emission is more likely to be produced by the adiabatically expanding ejecta rather than particle re-acceleration in external shocks with the ISM, as RK2 was only detected during the early phase of its motion. If that is the case, this implies that RK2 has a smaller fractional expansion speed in comparison to RK1.

In the context of a cavity surrounding MAXI J1348$-$630, if RK2 had the same energetic content of RK1, it should have hit the wall at the same angular distance as RK1 did before. It is thus possible that the detection of radio emission $\sim$27 arcsec from the core on MJD 58887, which we attributed to RK1, is in fact due to RK2 reaching the same ISM density bump, hence undergoing deceleration and subsequent re-brightening. If we assume that RK2 kept the same initial proper motion of $\sim$100 mas day^{-1}, it would have taken roughly 270 days for it to get $\sim$27 arcsec far from the core, which is broadly consistent with the last point attributed to RK1. It becomes even more consistent if we include deceleration in this scenario. However, the flux of RK1 on its last detection is roughly consistent with the overall decay in its re-brightening, and RK2 was never detected at late times at the $\sim$mJy levels the re-brightening of RK1. Hence it is possible that RK2 had less material to interact with, after RK1 swept up most of the material first.

7.8 Radio flux densities of the first ejecta

Table 7.5: Radio flux densities S_ν of the first radio knot RK1. Observation MJDs represent the middle of the observation, where errors represent the observation duration (time on source). The reported frequency is the central value of the used band, whose bandwidth is 856 MHz for MeerKAT and 2 GHz for ATCA. For the ATCA observations we report the array configuration as a subscript. The spectral index α of each component ($S_\nu \propto \nu^\alpha$) is computed only for simultaneous ATCA multi frequency observations. Upper limits are reported at the 3σ level.

Calendar date [UT]	MJD	Telescope	Frequency [GHz]	$S_{\nu,\mathrm{RK1}}$ [mJy]	α_{RK1}
2019-03-09	58551.100 ± 0.005	MeerKAT	1.3	2.72 ± 0.04	
2019-03-18	58560.075 ± 0.005	MeerKAT	1.3	6.75 ± 0.06	
2019-03-25	58567.074 ± 0.005	MeerKAT	1.3	2.52 ± 0.04	
2019-03-31	58573.76 ± 0.11	$\mathrm{ATCA_{6A}}$	5.5	0.65 ± 0.09	-1.1 ± 0.3
			9	0.38 ± 0.03	
2019-04-01	58574.061 ± 0.005	MeerKAT	1.3	1.78 ± 0.07	
2019-04-08	58581.72 ± 0.18	$\mathrm{ATCA_{H75}}$	5.5	1.12 ± 0.01	-1.27 ± 0.03
			9	0.64 ± 0.05	
2019-04-09	58582.053 ± 0.005	MeerKAT	1.3	3.50 ± 0.09	
2019-04-15	58588.053 ± 0.005	MeerKAT	1.3	4.48 ± 0.06	
2019-04-16	58589.81 ± 0.11	$\mathrm{ATCA_{750C}}$	5.5	1.30 ± 0.01	-0.77 ± 0.05
			9	0.89 ± 0.02	
2019-04-20	58593.074 ± 0.005	MeerKAT	1.3	2.80 ± 0.07	
2019-04-29	58602.144 ± 0.005	MeerKAT	1.3	1.32 ± 0.05	
2019-04-30	58603.31 ± 0.08	$\mathrm{ATCA_{750C}}$	5.5	0.60 ± 0.05	-0.9 ± 0.3
			9	0.40 ± 0.06	
2019-05-04	58607.908 ± 0.005	MeerKAT	1.3	0.92 ± 0.04	
2019-05-05	58608.68 ± 0.21	$\mathrm{ATCA_{1.5B}}$	8.4	<0.18	
2019-05-09	58612.44 ± 0.04	$\mathrm{ATCA_{1.5B}}$	5.5	<0.08	
			9	<0.08	
			17	<0.12	
			19	<0.18	
2019-05-11	58614.909 ± 0.005	MeerKAT	1.3	0.40 ± 0.04	
2019-05-14	58617.47 ± 0.06	$\mathrm{ATCA_{1.5B}}$	5.5	<0.08	
			9	<0.08	
			17	<0.18	
			19	<0.18	
2019-05-18	58621.888 ± 0.005	MeerKAT	1.3	0.22 ± 0.04	
2019-05-25	58628.019 ± 0.005	MeerKAT	1.3	<0.12	
2019-05-26	58629.340 ± 0.045	$\mathrm{ATCA_{6A}}$	5.5	<0.03	
			9	<0.03	
2019-05-31	58634.896 ± 0.005	MeerKAT	1.3	<0.12	
2019-06-08	58642.878 ± 0.005	MeerKAT	1.3	<0.15	
2019-06-09	58643.46 ± 0.10	$\mathrm{ATCA_{6A}}$	5.5	<0.03	
			9	<0.03	
2019-06-16	58650.881 ± 0.005	MeerKAT	1.3	<0.15	

Continued on the next page

Table 7.5: Continued from the previous page. Radio flux densities S_ν of the first radio knot RK1.

Calendar date [UT]	MJD	Telescope	Frequency [GHz]	$S_{\nu,\mathrm{RK1}}$ [mJy]	α_{RK1}
2019-06-24	58658.797 ± 0.005	MeerKAT	1.3	<0.15	
2019-06-26	58660.27 ± 0.10	$\mathrm{ATCA_{6A}}$	5.5	<0.05	
			9	<0.05	
2019-06-30	58664.724 ± 0.005	MeerKAT	1.3	<0.15	
2019-07-07	58671.861 ± 0.005	MeerKAT	1.3	<0.15	
2019-07-14	58678.912 ± 0.005	MeerKAT	1.3	<0.15	
2019-07-22	58686.860 ± 0.005	MeerKAT	1.3	<0.15	
2019-07-25	58689.44 ± 0.22	$\mathrm{ATCA_{750C}}$	5.5	<0.03	
			9	<0.03	
2019-07-27	58691.750 ± 0.005	MeerKAT	1.3	<0.15	
2019-08-04	58699.713 ± 0.005	MeerKAT	1.3	<0.12	
2019-08-10	58705.765 ± 0.005	MeerKAT	1.3	<0.12	
2019-08-16	58711.867 ± 0.005	MeerKAT	1.3	<0.14	
2019-08-21	58716.22 ± 0.10	$\mathrm{ATCA_{750C}}$	5.5	<0.03	
			9	<0.03	
2019-08-23	58718.658 ± 0.005	MeerKAT	1.3	<0.12	
2019-08-31	58726.741 ± 0.005	MeerKAT	1.3	<0.12	
2019-09-01	58727.08 ± 0.13	$\mathrm{ATCA_{6A}}$	5.5	<0.03	
			9	<0.024	
2019-10-19	58775.616 ± 0.005	MeerKAT	1.3	0.98 ± 0.04	
2019-10-26	58782.597 ± 0.005	MeerKAT	1.3	0.64 ± 0.03	
2019-11-01	58788.670 ± 0.005	MeerKAT	1.3	0.60 ± 0.04	
2019-11-02	58789.183 ± 0.045	$\mathrm{ATCA_{750C}}$	5.5	<0.09	
			9	<0.09	
2019-11-10	58797.408 ± 0.005	MeerKAT	1.3	0.31 ± 0.04	
2019-11-18	58805.403 ± 0.005	MeerKAT	1.3	0.35 ± 0.03	
2019-11-24	58811.345 ± 0.005	MeerKAT	1.3	0.29 ± 0.03	
2019-11-27	58814.72 ± 0.09	$\mathrm{ATCA_{1.5C}}$	5.5	0.060 ± 0.009	
			9	<0.04	
2019-11-30	58817.449 ± 0.005	MeerKAT	1.3	0.29 ± 0.03	
2019-12-03	58820.73 ± 0.13	$\mathrm{ATCA_{1.5C}}$	5.5	0.44 ± 0.09	
			9	<0.03	
2019-12-07	58824.396 ± 0.005	MeerKAT	1.3	0.25 ± 0.03	
2019-12-10	58827.75 ± 0.16	$\mathrm{ATCA_{1.5C}}$	5.5	0.067 ± 0.007	
			9	<0.02	
2019-12-14[a]	58831.31 ± 0.73	$\mathrm{ATCA_{1.5C}}$	5.5	0.043[a]± 0.005	−1.4 ± 0.6
			9	0.018[a]± 0.003	
2019-12-15	58832.387 ± 0.005	MeerKAT	1.3	<0.12	
2019-12-20	58837.428 ± 0.005	MeerKAT	1.3	0.20 ± 0.04	
2019-12-28	58845.272 ± 0.005	MeerKAT	1.3	<0.15	
2020-01-03	58851.397 ± 0.005	MeerKAT	1.3	<0.18	
2020-02-08	58887.185 ± 0.005	MeerKAT	1.3	0.18 ± 0.2	

Continued on the next page

Table 7.5: Continued from the previous page. Radio flux densities S_ν of the first radio knot RK1.

Calendar date [UT]	MJD	Telescope	Frequency [GHz]	$S_{\nu,\mathrm{RK1}}$ [mJy]	α_{RK1}
2020-02-15	58894.147 ± 0.005	MeerKAT	1.3	<0.12	
2020-02-21	58900.236 ± 0.005	MeerKAT	1.3	<0.12	
2020-03-02	58910.147 ± 0.005	MeerKAT	1.3	<0.12	

[a] Combination of the MJD 58830 and 58831 ATCA epochs to obtain a higher significance detection of RK1 at both 5.5 and 9 GHz.

Chapter 8

Modeling the kinematics of the decelerating jets from MAXI J1348–630

Contents

8.1 The external shock model . . . 142
8.2 Bayesian analysis . . . 144
8.2.1 Data and setup . . . 145
8.2.2 The uniform density case . . . 146
8.2.3 Motion in a low-density ISM cavity . . . 146
8.3 Discussion on the jet properties . . . 151
8.3.1 Initial Lorentz factor . . . 151
8.3.2 Inclination angle . . . 152
8.3.3 Ejection time . . . 152
8.3.4 A large kinetic energy . . . 153
8.3.5 Jet power . . . 154
8.3.6 Jet mass . . . 155
8.3.7 Jet composition . . . 157
8.4 The environment of MAXI J1348−630 . . . 159
8.4.1 Alternative explanations . . . 160
8.4.2 Predictions for the receding component . . . 160
8.5 Conclusions . . . 161

This final chapter of my thesis is dedicated to a detailed study of the motion of the ejecta from BH LMXBs, showing how this approach can lead us to infer many important properties of the jet itself and on its environment. As I discussed in the previous chapter, MAXI J1348−630 displayed two single-sided discrete ejecta that were launched ∼2 months apart and were followed with our observations as they moved away from the system with the highest proper motion ever measured for an accreting BH ($\gtrsim 100$ mas day^{-1}). After travelling with constant speed, the first

jet component was detected at large scales (∼26 arcsec from the core, corresponding to a distance of at least 0.3 pc) several months after the ejection, when it underwent a strong deceleration, covered in radio in great detail (Carotenuto et al., 2021a). The motion of these ejecta has already been presented in Chapter 7 and studied with the application of phenomenological models, which allowed us to qualitatively describe the jet evolution and to obtain a reliable estimate of the ejection date for both components. In this chapter we focus on the first discrete ejecta (labelled RK1 in Carotenuto et al. 2021a) and we go one step further in the study of the motion of this jet by applying to our data a full dynamical model based on external shocks (Wang, Dai, and Lu, 2003), in order to infer physical parameters of the jet and of the environment of MAXI J1348−630. In Section 8.1 I present the external shock model that I applied in this work, while in Section 8.2 I present the data, the adopted fitting procedure and the results of the application of such model to our data. I then extensively discuss our findings in relation to the current understanding of jets from microquasars in Sections 8.3 and 8.4, and I summarize our conclusions in Section 8.5. These results have recently been published in Carotenuto, Tetarenko, and Corbel (2022).

8.1 The external shock model

The jet dynamical model that we adopt in this work was originally developed by Wang, Dai, and Lu (2003), and later expanded and applied to the discrete ejecta of XTE J1550−564 and H1743−322 (Hao and Zhang, 2009; Steiner and McClintock, 2012; Steiner, McClintock, and Reid, 2012). While in principle the model was designed for gamma-ray bursts afterglows, it can describe the evolution of mildly relativistic jets from XRBs, and we present it again for clarity. In particular, we consider the most recent implementation of Steiner and McClintock (2012).

We consider a pair of symmetric ejecta launched at the same time in opposite directions at an inclination angle θ with respect to the line of sight, with an initial Lorentz factor Γ_0 and kinetic energy E_0. The jets take the shape of confined, conical beams and expand with a constant half-opening angle ϕ inside an ambient medium with constant density n. As the jets expand, they sweep up surrounding material and transfer their kinetic energy to the internal energy of the entrained material through external shocks, heating the ISM and consequently undergoing deceleration. Radiation losses at the shock front are assumed to be negligible and hence the jet expansion can be considered adiabatic throughout the whole evolution. Considering one of the two ejected components, it is therefore possible to write the energy conservation equation, following Huang, Dai, and Lu (1999) and Wang, Dai, and Lu (2003)

$$E_0 = (\Gamma - 1)M_0c^2 + \sigma(\Gamma_{\rm sh}^2 - 1)m_{\rm sw}c^2 \tag{8.1}$$

where the first term on the right-hand side is the kinetic energy of the ejecta and the second term is the internal energy of the shock. Here Γ is instantaneous jet bulk Lorentz factor, M_0 is the jet mass and $\Gamma_{\rm sh}$ is the Lorentz factor at the shock front, while σ is a numerical factor equal to $6/17$ for ultra-relativistic shocks and ∼0.73 for non-relativistic shocks (Blandford and McKee, 1976). A numerical scaling can be adopted to interpolate between the two regimes (Huang, Dai, and Lu, 1999; Wang, Dai, and Lu, 2003; Steiner and McClintock, 2012)

$$\sigma = 0.73 - 0.38\beta \tag{8.2}$$

where $\beta = (1 - \Gamma^{-2})^{1/2}$. Moreover, $m_{\rm sw}$ is the mass of the swept-up material, and it can be written as

$$m_{\rm sw} = \frac{\phi^2 \pi m_{\rm p} n R}{3} \tag{8.3}$$

where R is the distance from the core. A forward shock develops at the contact discontinuity between the jet and the ISM. Such shock continuously heats the encountered ISM and randomly accelerates particles. By using the jump conditions for an arbitrary shock, it is possible to express the shock Lorentz factor as a function of the jet bulk Lorentz factor (Blandford and McKee, 1976; Steiner and McClintock, 2012)

$$\Gamma_{\rm sh}^2 = \frac{(\Gamma + 1)(\hat{\gamma}(\Gamma - 1) + 1)^2}{\hat{\gamma}(2 - \hat{\gamma})(\Gamma - 1) + 2} \tag{8.4}$$

where $\hat{\gamma}$ is the adiabatic index that varies between $4/3$ (ultra-relativistic shocks) and $5/3$ (non-relativistic shocks). Following Steiner and McClintock (2012), we interpolate between the two limits with

$$\hat{\gamma} = \frac{4\Gamma + 1}{3\Gamma}. \tag{8.5}$$

Due to the possible evidence of BH LMXBs being harbored in low-density ISM cavities (Hao and Zhang, 2009), including MAXI J1348−630 (see Section 7.6.1 and Carotenuto et al. 2021a), we include such cavity in the model, modifying the expression for the swept-up mass. Following the example of Steiner and McClintock (2012), we let the jet first expand in an under-dense environment parametrized with a radius $R_{\rm c}$ and a density jump δ at the cavity wall, so that, for a standard ISM density $n_{\rm ism}$ outside, we have a density $n = n_{\rm ism}/\delta$ inside. The entrained mass then becomes

$$m_{\rm sw} = \frac{\phi^2 \pi m_{\rm p} n_{\rm ism}}{3\delta} \times \begin{cases} R^3, & R \leq R_{\rm c}, \\ R_{\rm c}^3 + \delta[R^3 - R_{\rm c}^3], & R > R_{\rm c}, \end{cases} \tag{8.6}$$

This scenario is consistent with a jet that travels first at constant and high speed in a low-density environment, which constitutes a large scale ISM cavity around the system, before hitting the border of the cavity, decelerating and producing radio emission from the subsequent external shocks between the jet material and the higher-density ISM encountered, as proposed by Hao and Zhang (2009).

The relativistic kinematic equation for the approaching component is (Rees, 1966; Mirabel and Rodríguez, 1994)

$$\frac{dR}{dt} = \frac{\beta c}{1 - \beta \cos\theta} \tag{8.7}$$

and the measurable projected angular distance is

$$\alpha(t) = \frac{R(t) \sin\theta}{D} \tag{8.8}$$

where D is the source distance.

It is possible to obtain the proper motion of the jet on the plane of the sky for every set of the nine parameters that compose the model: the jet initial kinetic energy E_0 and Lorentz factor Γ_0, the jet axis inclination angle θ and half-opening angle ϕ, the source distance D, the cavity radius $R_{\rm c}$, the density jump δ, the external ISM density $n_{\rm ism}$ and the ejection time $t_{\rm ej}$.

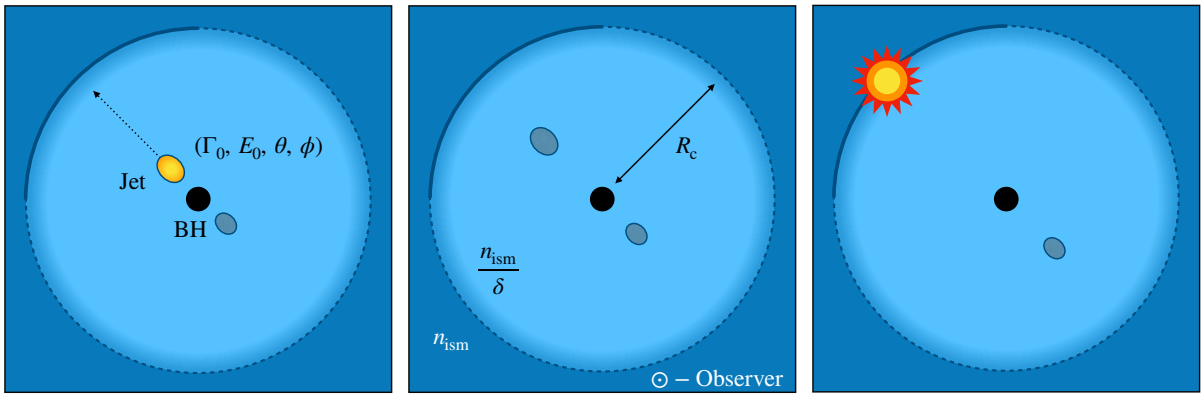

Figure 8.1: Schematic representation of the observed jet behaviour and proposed scenario for MAXI J1348−630, along with the parameters of the model adopted in this work. The line of sight is perpendicular to the plane of the drawing. The dashed line at the cavity border represents the fact that the cavity spherical geometry is an assumption of this scheme, and not of the model itself. The jet is characterized by the four parameters $\Gamma_0, E_0, \theta, \phi$ (initial bulk Lorentz factor, kinetic energy, inclination angle and half-opening angle of the jet, respectively, see Section 8.1) and displays a first phase of constant speed motion in an environment with density $n_{\rm ism}/\delta$. After a period of non-detection, the jet reaches the cavity wall at a distance $R_{\rm c}$ from the BH and transitions to a Sedov evolutionary phase. The unseen counter-jet moving in the south-west direction is also shown.

However, a degeneracy exists in this model between the three parameters E_0, ϕ and $n_{\rm ism}$, as they appear as a single term in Equation 8.1, so that only the combination $E_0/n_{\rm ism}\phi^2$ can be effectively constrained. In order to be able to have an estimate of the initial energy, we fix the external density to the canonical value $n_{\rm ism} = 1$ cm^{-3} and we choose the reasonable value for the half-opening angle of $\phi = 1°$ (Kaaret et al., 2003; Miller-Jones, Fender, and Nakar, 2006), which is also consistent with the observational constraints from Carotenuto et al. (2021a).

To obtain a jet trajectory for every set of parameters, we integrate Equation 8.7 starting at a time $t_{\rm ej}$ from a distance $R_0 = 10^8$ cm (the results depend very weakly on the choice of R_0), by numerically solving at every time step Equation 8.1 for the instantaneous jet Lorentz factor, and then we convert the distance traveled by the jet to the angular separation α (Equation 8.8), in order to compare the obtained angular separation curve with our data (see Table 7.2).

Since for MAXI J1348−630 only single-sided jets were detected, for the model application in this work we only use the angular distance information and not the flux ratios between the approaching and receding components, as for instance done for XTE J1550−564 and H1743−322 (e.g. Wang, Dai, and Lu 2003; Hao and Zhang 2009; Steiner and McClintock 2012), because the upper limits from the receding component do not allow us to obtain additional significant constraints on the physical parameters of the jet or of the cavity. In particular, this is the first time in which the external shock model is applied to a single-sided BH XRB jet. A schematic representation of the proposed scenario is shown in Figure 8.1.

8.2 Bayesian analysis

I present here the application of the external shock model outlined in the previous section, discussing the data we used, the fit of the model to the data with a Bayesian approach and using

MCMCs, and the obtained results for three different runs.

8.2.1 Data and setup

For the modeling of the jet motion, we focus on the observations of the first discrete ejecta from MAXI J1348−630, that have been presented in Carotenuto et al. (2021a) and in chapter 7 (where the jet is labelled RK1). We use the MeerKAT and ATCA detections of the first component to fit the entire jet motion, therefore we consider the position of the jet in every epoch in which it was detected, and its angular separation with respect to the core position of MAXI J1348−630, which is at R.A $= 13^{\rm h}48^{\rm m}12.79^{\rm s} \pm 0.01^{\rm s}$ and Dec $= -63°16'28.6'' \pm 0.2''$ (J2000, Carotenuto et al. 2021a).

The proper motion of the jet is shown in Figures 7.7 and 8.3, and the data are reported in Table 7.2, for which data from MeerKAT and from ATCA at 5.5 GHz were used. The jet angular separation is computed as the great circle distance between the ejecta and the MAXI J1348−630 position, either the fitted one in case of core detection on the same epoch, or the core position in case of core non-detection. In the first case, we are not affected by global systematics in the position error estimation. After a first part of ballistic, high-speed motion that started roughly between MJD 58518 and 58523, the deceleration of RK1 around MJD 58775 was rather abrupt, a phenomenon not observed in the majority of discrete ejecta from BH LMXBs (e.g Mirabel and Rodríguez 1994; Miller-Jones et al. 2012; Rushton et al. 2017; Miller-Jones et al. 2019.

We fit our data with the external shock model presented in Section 8.1 with a Bayesian approach, applying a Monte Carlo Markov Chain (MCMC) code implemented with the EMCEE package (Foreman-Mackey et al., 2013). For every point of the parameter space, Equation 8.7 was integrated using `odeint` from the SciPy package (Virtanen et al., 2020).

We include the maximum amount of available information in the choice of our priors, which are physically motivated from our knowledge of MAXI J1348−630 and BH XRBs in general. Flat priors are assumed in case we do not have a preferred expectation value for a specific parameter. The prior distributions used for all of our parameters are listed in Table 8.1. We adopted a flat prior for Γ_0 and a log-flat prior for E_0, with a large range of allowed values. For θ, we used a normal distribution (truncated outside the interval $0° - 90°$) centered on 30°and with a sigma of 20°, taking into account the observational constraints from Carotenuto et al. (2021a) and the fact that θ is unlikely to be small (i.e. the system is unlikely to be almost face-on). We then adopted a flat prior between 0 and 2 pc for $R_{\rm c}$ and a log-flat prior for δ, with boundaries at 1 and 10^4, including the whole range of inferred values for other BH LMXBs (e.g. Heinz 2002; Hao and Zhang 2009; Steiner and McClintock 2012). A truncated normal is chosen for D, and it is centered on 2.2 kpc with a sigma of 0.6 kpc (Chauhan et al., 2021), while the prior on $t_{\rm ej}$ is flat and truncated at MJD 58523.5, since the jet cannot be ejected after having produced the strong radio flare observed with MeerKAT at that time (∼0.5 Jy, Carotenuto et al. 2021a).

Every MCMC run was conducted using 110 walkers. For each run, we consider that convergence is reached when the positions of the walkers in the parameter space are no longer significantly evolving. Once the chains have converged, the best fit result for each parameter is taken as the median of the one-dimensional posterior distribution obtained from the converged chains, while the 1σ uncertainties are reported as the difference between the median and the 15th percentile of the posterior (lower error bar), and the difference between the 85th percentile and the median (upper error bar). The best fit results for our runs are shown in Table 8.2. For choosing between the different scenarios, we compute for each MCMC run the Bayesian

Table 8.1: Parameters of the external shock model applied in this work and the chosen priors with their distribution and allowed values.

Parameter	Description	Prior distribution	Prior interval
Γ_0	Initial bulk Lorentz factor at launch	Uniform	1–100
$\log_{10} E_0$	Initial kinetic energy at launch (erg)	Uniform	35–55
θ	Inclination angle (°)	Truncated normal ($\mu = 30$, $\sigma = 20$)	0–90
R_c	Cavity radius (pc)	Uniform	0–2
δ	Density jump at cavity wall	Uniform in $\log \delta$	1–10^4
D	Distance (kpc)	Truncated normal ($\mu = 2.2$, $\sigma = 0.6$)	1–8
t_{ej}	Ejection date (MJD – 58500)	Uniform	0–23.5

Information Criterion (BIC, Schwarz 1978) and we select the run with the lowest value. The BIC is defined as

$$\mathrm{BIC} = k \ln N - 2 \ln L(\hat{\theta}) \tag{8.9}$$

where k is the number of free parameters of each model, N is the number of data points and $L(\hat{\theta})$ is the likelihood function of the model evaluated with the set of parameters $\hat{\theta}$ that maximize it. The likelihood is assumed to be gaussian for all the parameters considered in this model.

8.2.2 The uniform density case

We first consider an approach that does not require the presence of a low-density ISM cavity, in order to show that this configuration appears inadequate to fit the data. In this scenario, the jet moves and then decelerates in a uniform medium and, hence, we fix $R_c = 0$ pc and $\delta = 1$. The MCMC run provides a converged solution, and the fit results are presented in Table 8.2 and are shown in Figure 8.2. In this case, the model cannot adequately reproduce the final part of the jet motion, and we obtain a BIC value of 120.4. While the results for most of the parameters are acceptable, the jet appears to require a huge amount of energy (10^{48}–10^{49} erg) in order to travel ∼0.5 pc and sweep matter in a standard ISM density, therefore we deem this scenario to be unlikely. Moreover, with a uniform density we would expect the jets to continuously interact with the ISM and thus to be constantly detected for their whole motion, with a uniform decrease in radio flux density (unless the jets are highly relativistic), similarly to what was observed in MAXI J1820+070 (Bright et al., 2020), instead of having a phase of non-detection followed by a re-brightening and deceleration, as in the case of MAXI J1348−630.

8.2.3 Motion in a low-density ISM cavity

Introducing a cavity and letting R_c and δ free to vary in the range of their priors results in a significantly improved fit. The best fit results are reported in Table 8.2 and are shown in Figure 8.3, along with the proper motion of the jet. Uncertainties on the plot are represented as the trajectories corresponding to the final positions of the walkers in the parameter space. In Figure 8.4 we present the corner plot showing the one-dimensional posterior distribution for all the parameters and the 2-parameters correlations.

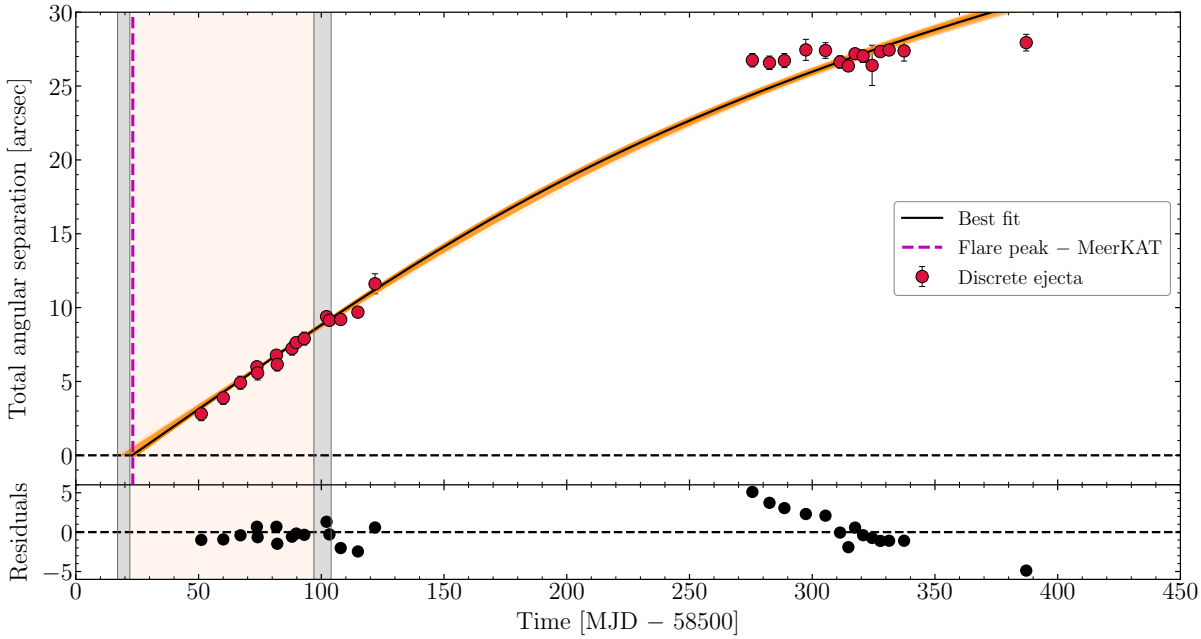

Figure 8.2: Angular separation in arcsec between the discrete ejecta and the position of MAXI J1348−630. We combine here MeerKAT 1.28 GHz and ATCA 5 GHz observations, shown as red points and taken from Carotenuto et al. (2021a). The un-shaded, grey and pink regions mark periods in which MAXI J1348−630 was, respectively, in the hard, intermediate and soft state (Zhang et al., 2020a). The black horizontal line represents the zero separation from the core, while the time of the major flare observed with MeerKAT (MJD 58523) is represented with a magenta vertical line. The black continuous line represents the best fit obtained with the external shock model developed by Wang, Dai, and Lu (2003), assuming a motion in an ISM with uniform density. The orange shaded area represents the total uncertainty on the fit and it is obtained by plotting the jet trajectories corresponding to the final positions of the MCMC walkers in the model parameter space. Residuals ([data − model]/uncertainties) are reported in the bottom panel. As the model without the inclusion of a cavity fails to reproduce accurately the jet deceleration phase, we deem this scenario unlikely.

The model appears to fit really well our data, and the good agreement with observations can be seen from the residuals in Figure 8.3. We obtain a BIC value of 49.5, which is significantly lower than the previous case, providing us with a strong evidence in favour to the cavity scenario compared to a uniform density ISM.

The motion that we obtain is similar the "linear+Sedov" phenomenological model used in Carotenuto et al. (2021a), although in this case a physical model is used to explain the whole motion. According to this model, the jet is launched at $t_{\rm ej} = 21.5^{+1.8}_{-3.0}$ (MJD -58500) with a bulk Lorentz factor $\Gamma_0 = 1.85^{+0.15}_{-0.12}$, corresponding to a mildly-relativistic speed, with an impressive amount of energy $E_0 = 4.6^{+20.0}_{-3.4} \times 10^{46}$ erg, and with a small inclination angle $\theta = 29.3^{\circ}{}^{+2.7^{\circ}}_{-3.2^{\circ}}$. We infer that MAXI J1348−630 lives in a cavity with a radius $R_{\rm c} = 0.61^{+0.11}_{-0.09}$ pc and a large density jump $\delta = 980^{+514}_{-359}$. In this context, our jet might have traveled undisturbed for the first phase, between MJD 58521 and 58750, adiabatically expanding and radiating in an environment with a low density of $n_{\rm ism}/\delta = 0.0010^{+0.0005}_{-0.0003}$ cm^{-3}, and then it decelerated and re-brightened after hitting the wall of the cavity, transitioning from a relativistic phase to a Sedov expanding phase around MJD 58750, with a sharp drop of Γ from $\sim$1.8 to $\sim$1. At the cavity wall, the jump in the ISM density caused the production of external shocks between the jet and the surrounding material, resulting in *in-situ* particle acceleration responsible for the radio emission. This emission has been observed with *Chandra* to extend up to the X-rays

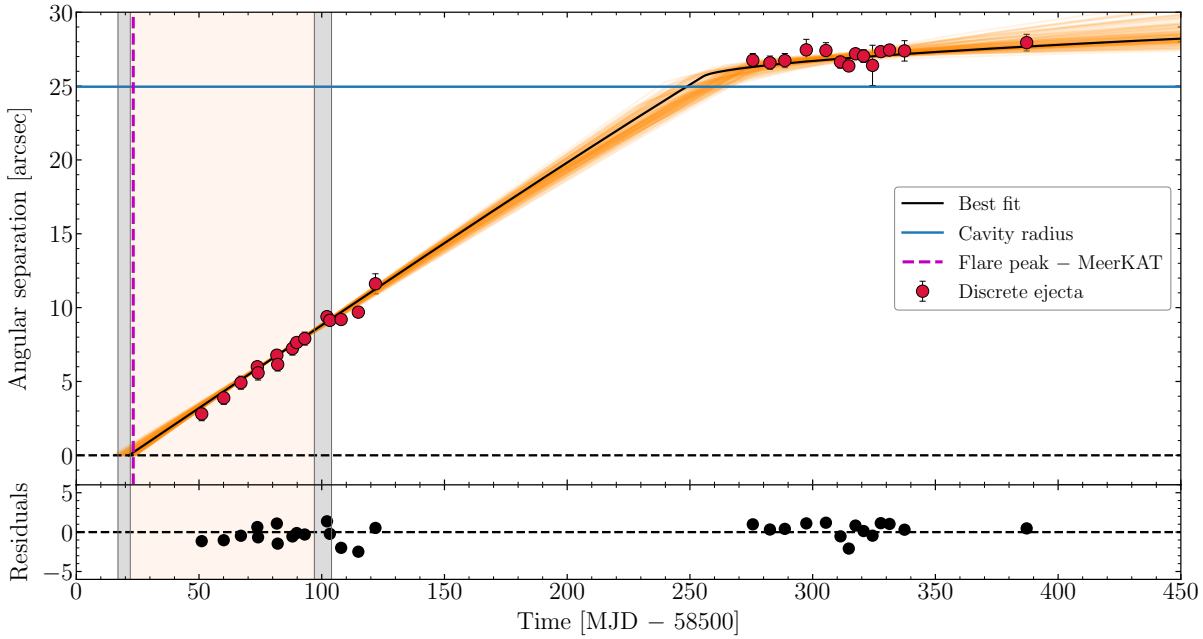

Figure 8.3: Same as Figure 8.2, but here the black continuous line represents the best fit obtained with the external shock model developed by Wang, Dai, and Lu (2003) with the inclusion of a cavity, and the horizontal blue line shows the inferred radius of such low-density ISM cavity, in which MAXI J1348−630 is embedded. The model appears to fit reasonably well our data, suggesting a jet deceleration due to the interaction with the wall of an ISM cavity.

for some decelerating jets (e.g. Corbel et al. 2002; Corbel et al. 2005; Espinasse et al. 2020). However, in the case of MAXI J1348−630 it has not been possible to observe the jets with *Chandra*. This was due to the simultaneous brightness of the core of the system during the several reflares that followed the main outburst (see Chapter 5 and Carotenuto et al. 2021a), since a bright X-ray core is expected to completely out-shine and engulf the resolved (but faint) X-ray emission from the ejecta.

Table 8.2: Parameters of the external shock model applied in this work and fit results with and without the inclusion of a low-density ISM cavity. The values quoted are the median parameter and the 1σ confidence intervals derived from the MCMC run. We also report the BIC for the two cases.

Parameter	Uniform density	ISM cavity
Γ_0	$1.85^{+0.25}_{-0.16}$	$1.85^{+0.15}_{-0.12}$
$\log_{10} E_0$	$48.65^{+0.51}_{-0.47}$	$46.66^{+0.73}_{-0.60}$
θ (°)	$28.31^{+4.77}_{-3.40}$	$29.27^{+2.71}_{-3.23}$
R_c (pc)	0 (fixed)	$0.61^{+0.11}_{-0.09}$
δ	1 (fixed)	980^{+514}_{-359}
D (kpc)	$2.38^{+0.52}_{-0.35}$	$2.46^{+0.31}_{-0.27}$
t_{ej} (MJD − 58500)	$22.92^{+1.35}_{-2.51}$	$21.45^{+1.83}_{-3.02}$
BIC	120.4	49.5

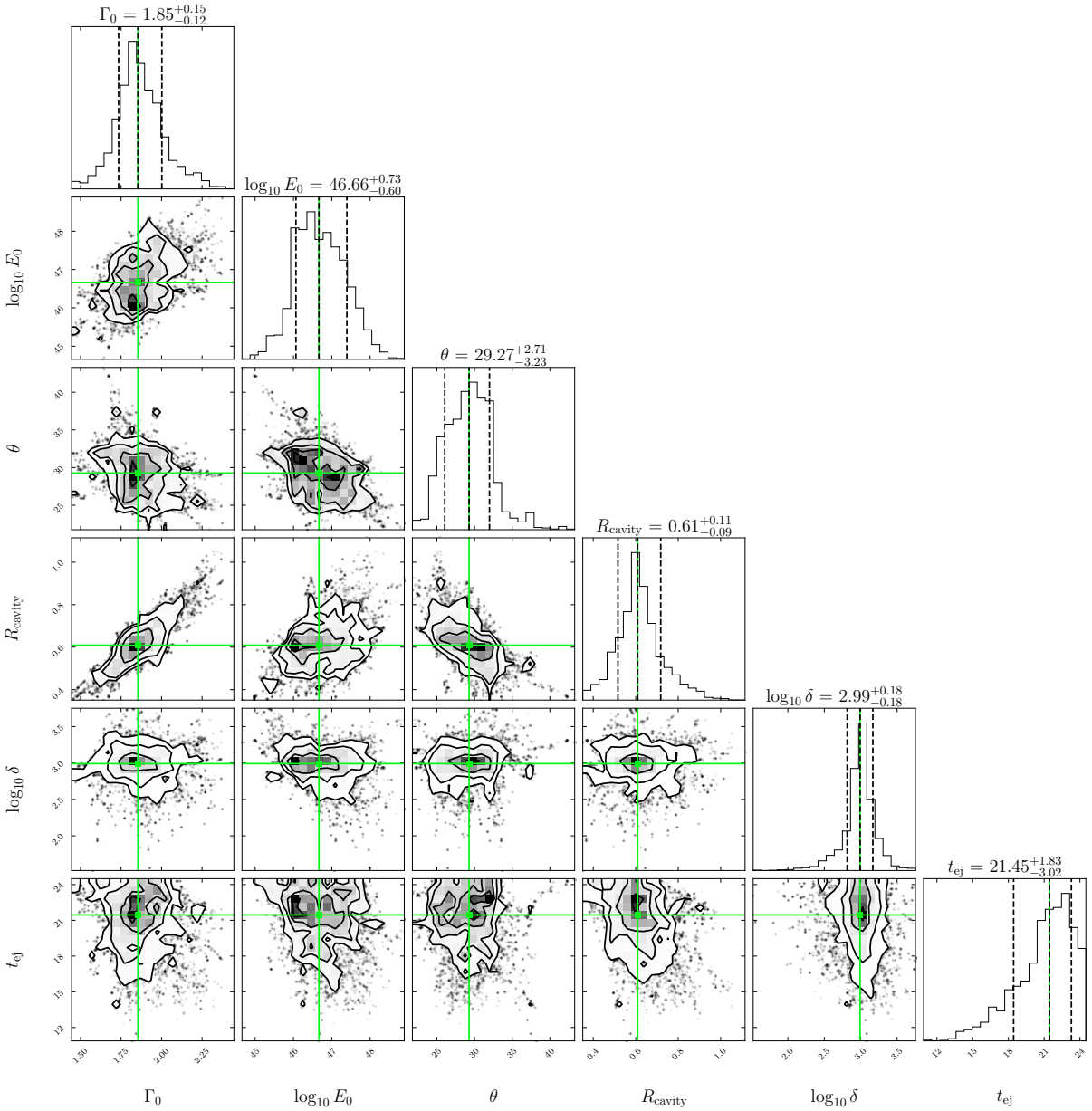

Figure 8.4: Corner plots showing the results of the external shock model fit with MCMC. The panels on the diagonal show histograms of the one dimensional posterior distributions for the model parameters, including the jet initial Lorentz factor, initial energy, inclination angle and ejection time, as well as the radius and density jump of the low-density ISM cavity. The median value and the equivalent 1σ uncertainty are marked with vertical dashed black lines. The other panels show the 2-parameter correlations, with the best-fit values of the model parameters indicated by green lines/squares. The plot was made with the CORNER plotting package (Foreman-Mackey, 2016).

Impact of the dust-scattering halo distance

We note that Lamer et al. (2021) recently reported a distance $D = 3.39 \pm 0.34$ kpc from observations of X-ray light echoes from a degree-scale dust scattering ring with eROSITA. While in this work we center our prior on $D = 2.2$ kpc, we performed a MCMC run centering the distance prior on 3.39 kpc, with a sigma value of 0.4 kpc and with the same setup described in Section 8.2.1 and 8.2.3. We obtain a good fit with a slightly higher BIC value of 63.3. The fit results are shown in Figure 8.5. As expected, a larger distance results in larger estimate for the jet parameters with respect to Section 8.2.3, of factors between 20% and 50%, with the exception of E_0, which has to be $\sim$3.5 times larger than what presented in the previous section in order to sustain a jet with the same proper motion at a distance $\sim$50% larger. While this distance might be plausible, the choice of the distance prior does not significantly affect the results and the main conclusions of this work.

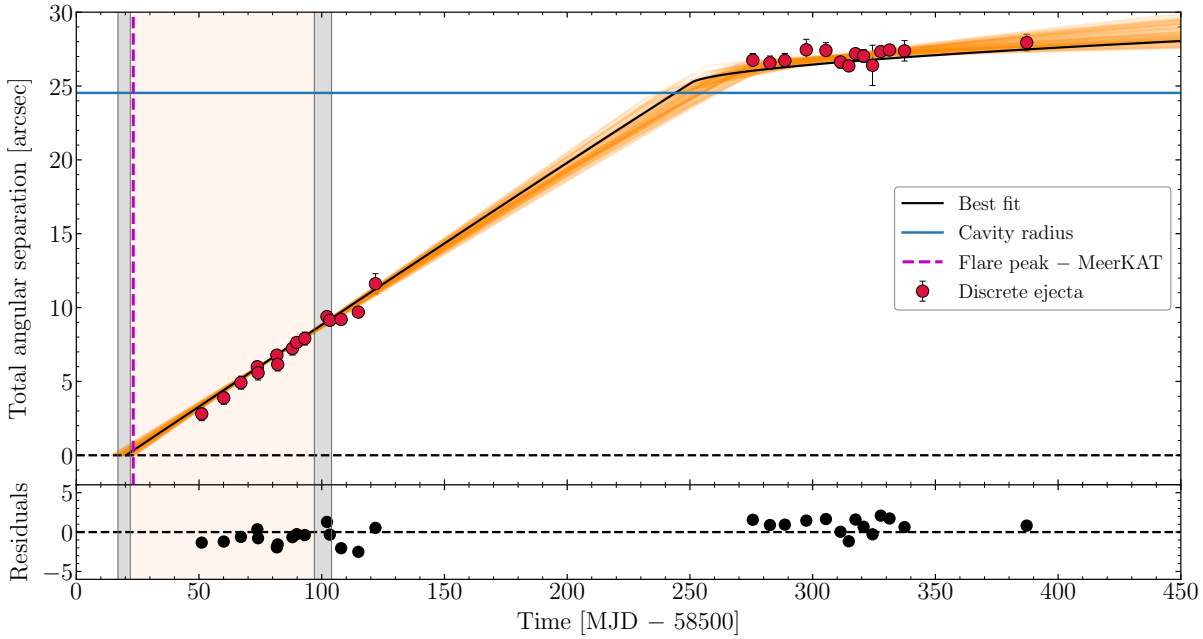

Figure 8.5: Same as Figure 8.3, but assuming a prior on the source distance centered on 3.39 kpc (Lamer et al., 2021). The model appears to fit reasonably well our data, and the results are very similar to what reported in Section 8.2.3, implying that the the choice of the prior on the source distance does not significantly affect the conclusions of this work.

8.3 Discussion on the jet properties

We successfully modelled the motion of the large-scale jet from MAXI J1348−630 with a full dynamical model based on external shocks, adopting a Bayesian approach. The model appears to describe extremely well the evolution of the jet in the different phases of its motion, and the fit we performed allows us to constrain with good or sufficient accuracy the physical parameters of the jet and of its environment. We discuss the obtained values for all the model parameters individually in the following sections, and stress that these results were achieved thanks to the dense and deep radio coverage of the jet deceleration phase.

8.3.1 Initial Lorentz factor

We obtain a precise estimate of the initial Lorentz factor of the jet: $\Gamma_0 = 1.85^{+0.15}_{-0.12}$, which implies a mildly relativistic ejecta, despite the high initial proper motion observed. By sampling from the best-fit posterior distribution of Γ_0, we can then infer the corresponding initial intrinsic jet speed

$$\beta_0 = \sqrt{1 - \frac{1}{\Gamma_0^2}} = 0.84^{+0.02}_{-0.03} \tag{8.10}$$

which is consistent with the observational constraints presented in Carotenuto et al. (2021a).

It is difficult to constrain the Lorentz factor of jets from BH LMXBs by the observations of their proper motions, especially if the ejecta are significantly relativistic (Fender, 2003), given that in those cases the source will be close to the maximum allowed distance (Fender et al., 1999)

$$D_{\rm max} = \frac{c}{\sqrt{\mu_{\rm app}\mu_{\rm rec}}} \tag{8.11}$$

which can be obtained from simultaneous observations of the approaching and receding components. Therefore, for most of the sources only lower limits on Γ can be placed (e.g. Fender 2003; Miller-Jones, Fender, and Nakar 2006; Bright et al. 2020). Jets from MAXI J1348−630 are, hence, likely to be less relativistic that the majority of bipolar ejecta from BH XRBs, and the inferred value of Γ_0 is broadly consistent with what observed for the less relativistic jets reported in Miller-Jones, Fender, and Nakar (2006). This is also supported by a rough estimation of $D_{\rm max}$, which can be obtained by solving for D the proper motion equation (Rees, 1966; Mirabel et al., 1992)

$$\mu_{\rm app} = \frac{\beta \sin\theta}{1 - \beta\cos\theta}\frac{c}{D} \tag{8.12}$$

assuming a maximum intrinsic speed $\beta = 1$ and the inferred values for θ and $\mu_{\rm app} \simeq 109$ mas day^{-1}. We obtain $D_{\rm max} \simeq 4$ kpc, which is significantly larger than the measured distance of MAXI J1348−630 (see Section 5.4).

By applying the same external shock model, it was not possible to precisely constrain Γ_0 for the two-sided ejecta of XTE J1550−564 (Steiner and McClintock, 2012) and H1743−322 (Steiner, McClintock, and Reid, 2012), but only to place lower limits on it. On the other hand, in our case we have a uniform and dense coverage of the first phase of the jet motion, which allows us to uniquely determine the jet intrinsic speed, given the reasonable results obtained for θ and D (see Section 8.3.2).

8.3.2 Inclination angle

We obtain a medium-low inclination angle of the jet axis $\theta = 29.3^{\circ}{}^{+2.7^{\circ}}_{-3.2^{\circ}}$, which suggests a relatively face-on system and it is consistent with the results presented in Chapter 7 and in Carotenuto et al. (2021a). However, we note that the posterior distribution obtained for θ clearly traces its prior (see Figure 8.4 and Table 8.1), implying that this parameter is not completely constrained from the fit. The prior choice took into account the observational constraints from Carotenuto et al. (2021a). Nevertheless, the model reproduces the jet motion very well with such inclination angle, which is likely to be fairly close to the true value.

Interestingly, the inclination angle of the accretion disk was inferred to be $i = 28^{\circ} \pm 3^{\circ}$ from X-ray spectroscopy with *NuSTAR*, using relativistic reflection models (Anczarski et al., 2020). A measurement of the orientation of the orbital plane of the system would be extremely valuable to test the potential alignment between the disk and the jet axis. Since the jet axis is presumed to be aligned with the BH's spin axis, such measurement would be also important to test the alignment between the spin axis and the orbital plane. As already mentioned by Steiner and McClintock (2012), a good alignment between the two provides support for the BH spin estimation via the X-ray continuum-fitting methods (Zhang, Cui, and Chen, 1997). However, misaligned jets have been observed (e.g. Miller-Jones et al. 2019; Poutanen et al. 2021), so such alignment is likely not to be universal among BH LMXBs.

Doppler factor

With the values obtained for Γ_0 and θ, we can compute the Doppler factor for the two ejecta. The Doppler factor for the approaching component at launch is

$$\delta_{\rm app} = \frac{1}{\Gamma_0(1 - \beta_0 \cos\theta)} \simeq 2, \tag{8.13}$$

and such value remains stable for the first part of the jet motion, as inside the cavity $\Gamma \simeq \Gamma_0$. This implies that the received radio flux is boosted by a factor $\delta_{\rm app}^{3-\alpha} \simeq 16$, considering a discrete ejecta with a radio spectral index $\alpha \simeq -1$ (Carotenuto et al., 2021a), greatly easing the detection the approaching ejecta, which peaked at a flux density of $\sim$6.7 mJy at 1.3 GHz (Carotenuto et al., 2021a). For the un-detected receding component, the Doppler factor is

$$\delta_{\rm rec} = \frac{1}{\Gamma_0(1 + \beta_0 \cos\theta)} \simeq 0.3, \tag{8.14}$$

implying that the received flux is reduced by a factor $1/\delta_{\rm rec}^{3-\alpha} \simeq 125$, which explains why the receding component was never detected in any of our radio observations.

8.3.3 Ejection time

The ejection date is one of the key parameters in the external shock model. From the fit, we infer the ejection date $t_{\rm ej} = 21.5^{+1.8}_{-3.0}$ (MJD -58500), which is roughly two days before the peak of the $\sim$0.5 Jy radio flare observed with MeerKAT and, since this value is obtained with a full dynamical model, it is likely to be more reliable than the ejection date presented in Carotenuto et al. (2021a). The estimation of the time of ejection is fundamental to reconstruct the precise evolution of the system during state transitions and to understand the contribution of the various physical components of the system (e.g. compact jets, corona, inner accretion flow)

in the production and acceleration of the discrete ejecta. The jet ejection is inferred to happen while MAXI J1348−630 was in the HIMS, roughly one day before the first detection of Type-B QPOs with NICER on MJD 58522.6 (Zhang et al., 2020a; Zhang et al., 2021). Similarly to the conclusions of Carotenuto et al. (2021a), in our case Type-B QPOs appeared to be produced after the jet ejection, as already observed for H1743−322 and MAXI J1535−571 (Miller-Jones et al., 2012; Russell et al., 2019c), and were not simultaneous with the jet launch, as instead found for MAXI J1820+070 (Bright et al., 2020; Homan et al., 2020), hence the potential causal link between the two phenomena remains unclear. To investigate such sequence of events more in depth, the NICER timing results on MAXI J1348−630 will be put in relation to the inferred ejection date in a future work.

8.3.4 A large kinetic energy

The ejecta is inferred to have an extremely large kinetic energy at the time of ejection: as one of the key outputs of the model, we obtain $E_0 = 4.6^{+20.0}_{-3.4} \times 10^{46}$ erg. The result is particularly interesting because such energy estimation is several orders of magnitude larger than what was estimated for MAXI J1348−630 ($\sim 10^{42}$ erg; Carotenuto et al. 2021a) and from what is generally inferred for ejecta from XRBs (see for instance Fender et al. 1999; Tetarenko et al. 2017; Rushton et al. 2017; Russell et al. 2019c; Miller-Jones et al. 2019; Espinasse et al. 2020), which is obtained by considering the minimum energy required to produce the observed radio synchrotron radiation, assuming equipartition between particles and magnetic fields (e.g. Longair 2011). Our estimation is instead consistent with the kinetic energy obtained for the first jets discovered in GRS 1915+105 (Mirabel and Rodríguez, 1994), and in XTE J1550−564 (by applying the same external shock model; Steiner and McClintock 2012), and it is slightly higher than what obtained for H1743−322 (Steiner, McClintock, and Reid, 2012), whose jets decelerate much earlier compared to MAXI J1348−630. These findings support the recent claim that the total energy of these jets is not well-traced by the observed electromagnetic emission, and this leads to a significant underestimation of the energetic content of these objects (e.g. Bright et al. 2020). As a result, it is likely that jets only radiate away a small fraction of their total energy, which is instead almost completely transferred to the environment, as in the case of MAXI J1820+070 (Bright et al., 2020). This implies that the overall feedback of the jet on the surrounding environment is possibly way larger than previously thought, and, at the same time, it justifies our assumption in the model of negligible radiative losses and consequent adiabatic expansion of the jet.

There is, however, a *caveat* on such energy estimation due to the degeneracy between E_0, $n_{\rm ism}$ and ϕ, since the model can only constrain the value $E_0/n_{\rm ism}\phi^2$, and, hence with our assumptions we essentially obtain

$$E_0 = 4.6^{+20.0}_{-3.4} \times 10^{46} \left(\frac{n_{\rm ism}}{1\ {\rm cm}^{-3}}\right) \left(\frac{\phi}{1^\circ}\right)^2 {\rm erg}. \tag{8.15}$$

In Section 8.1 we discussed and motivated our choice of assuming the reasonable values of $n_{\rm ism} = 1$ cm^{-3} and $\phi = 1^\circ$. The energy could be overestimated in case the opening angle is much smaller than the 1° assumed. However, if we imagine our opening angle to be $\sim 10\%$ of that value, E_0 would be $\sim 1\%$ of what reported above, but it would still be roughly two orders of magnitude larger than the radiated energy. Moreover, while for the majority of XRB jets we have un-constraining upper limits (larger than 1°) on their opening angle (Miller-Jones, Fender, and Nakar, 2006), such ejecta have been in some cases resolved with VLBI or in X-rays

(e.g. Miller-Jones et al. 2004; Rushton et al. 2017; Espinasse et al. 2020), yielding half-opening angles larger than 1°, hence it appears to be unlikely that jets in MAXI J1348−630 could have significant smaller apertures. In addition, it is difficult to imagine how such jets could be confined in such low-density environments surrounding microquasars (Heinz, 2002; Hao and Zhang, 2009; Miller-Jones, Fender, and Nakar, 2006). Another possibility is that the density of the external ISM, *outside* the cavity, is smaller than what we assumed for $n_{\rm ism}$, meaning that MAXI J1348−630 could be located in a region with a particular hot phase of the ISM. However, this is unlikely given that our source lies in the galactic plane, where we expect higher ISM densities (e.g. Cox 2005). Therefore, our estimate of E_0 appears to be reliable, and the evidence for a highly energetic jet appears to be robust.

8.3.5 Jet power

The energy E_0 discussed in Section 8.3.4 must be provided by the system in a time Δt, and hence we can consider now the average power required to accelerate the jets in MAXI J1348−630, which is $P_{\rm jet} = 2E_0/\Delta t$ (for a bipolar ejection). The exact value of Δt is unknown, but it is possible to obtain a zero-order estimate by considering the interval between our inferred $t_{\rm ej}$ at which the jet was launched and the peaking time of the radio flare produced by the jet on MJD 58523.22 observed with MeerKAT (Carotenuto et al., 2021a). We obtain an observed ejection timescale of ∼1.8 days, which, given the relativistic motion of the jet, has to be corrected to the source rest frame through $\Delta t_{\rm obs} = \delta_{\rm app}^{-1}\Delta t_{\rm RF}$. We obtain a rest-frame rising timescale of ∼3.6 days, which leads to a total mechanical power of the jets

$$P_{\rm jet} \simeq 3 \times 10^{41} \left(\frac{n_{\rm ism}}{1\ {\rm cm}^{-3}}\right) \left(\frac{\phi}{1^o}\right)^2 \left(\frac{\Delta t_{\rm RF}}{3.6\ {\rm d}}\right)^{-1} {\rm erg\ s}^{-1}. \tag{8.16}$$

As can be expected by the large value of E_0 and the short ejection timescale, such power is extremely high, and it has to be compared with the simultaneously available accretion power. This can be roughly estimated from the simultaneous bolometric X-ray luminosity, since $L_{\rm X} = \eta \dot{M} c^2$, where η is the radiative efficiency of the accretion flow. $L_{\rm X}$ can be obtained from the 1–10 keV X-ray flux observed with *Swift* on MJD 58521 (Carotenuto et al., 2021a), where the bolometric luminosity is estimated using the conversion factor from Migliari and Fender (2006b). This estimation yields an X-ray luminosity $\sim 7.9 \times 10^{38}$ erg s^{-1}. Such value is ∼61% of the Eddington luminosity, which is standard limit for stable accretion ($\simeq 1.3 \times 10^{39}$ erg s^{-1} for a $10 M_\odot$ BH accreting hydrogen). With the standard assumption $\eta = 0.1$, we obtain an accretion power of $\sim 7.9 \times 10^{39}$ erg s^{-1}. Therefore, our inferred value of $P_{\rm jet}$ is be ∼40 times higher than the available accretion power, implying a discrepancy between the available accretion power and the power required by the jets. Such value of $P_{\rm jet}/\dot{M}c^2$ (which can define as $\eta_{\rm jet}$) appears to be too large even if we include the BH spin as an additional energy reservoir, that can be extracted from the compact object through the Blandford-Znajek mechanism (Blandford and Znajek, 1977). Simulations show that $\eta_{\rm jet}$ can attain the maximum value of ∼1.4 for jets produced by rapidly spinning BHs (Tchekhovskoy, Narayan, and McKinney, 2011), well below our estimate.

However, both the quantities that we are comparing, $P_{\rm jet}$ and $\dot{M}c^2$, are affected by uncertainties in their estimation, and the tension between the two can possibly be mitigated in several ways. Since $P_{\rm jet}$ depends on the assumed values of $n_{\rm ism}$ and ϕ, it is possible that such quantities are in fact smaller than the ones we assumed (see Section 8.3.4). Hence, we can place upper limits on the two parameters that cannot be constrained from the model alone. Starting from

$P_{\rm jet} \leq 1.4\dot{M}c^2$, if we assume that $n_{\rm ism} = 1$ cm^{-3}, then we have that $\phi \leq 0.2°$. On the other hand, by assuming $\phi \leq 1°$, we can infer that $n_{\rm ism} \leq 0.04$ cm^{-3}. However, while in principle these values are possible, both the upper limits appear to be unlikely: an unusually narrow jet seems difficult to understand from the arguments discussed in Section 8.3.4, while a low value of the ISM density outside a cavity appears not plausible as well, given the location of MAXI J1348−630 in the galactic plane. Moreover, a lower value of $n_{\rm ism}$ would imply an even smaller value $n_{\rm ism}/\delta$ of the density inside the cavity, which is hard to justify.

Another reason for such discrepancy could lie in an incorrect estimation of the ejection timescale, as a larger Δt would decrease our inferred value of $P_{\rm jet}$. While the uncertainty on the flare rising timescale is of the order of days, and thus that value is unlikely to be heavily underestimated (Typical values for the radio flare rising timescales are of the order of hours to days, e.g. Russell et al. 2019c; Bright et al. 2020; Homan et al. 2020), it is possible that such timescale is not a good proxy for the timescale in which the system effectively accelerates the ejecta.

Finally, the accretion power could be higher than what we have estimated. The accretion efficiency η might be lower than 0.1 (even if that is unlikely, given that the accretion flow should be radiatively efficient in the intermediate and soft state, e.g. Done, Gierliński, and Kubota 2007), or the X-ray luminosity might have been underestimated. While our *Swift* measurement of the X-ray luminosity is not exactly simultaneous as our inferred ejection date, we speculate that in this case the main source of uncertainty lies in the conversion from the luminosity in the 1-10 keV energy range to the bolometric X-ray luminosity $L_{\rm X}$. A larger $L_{\rm X}$, possibly above the Eddington limit for a limited period of time, might be a plausible explanation for such a large discrepancy. Short super-Eddington phases linked to major ejections have likely taken place in other systems, as for instance GRS 1915+105 (Mirabel and Rodríguez, 1994), XTE J1550−564 (Steiner and McClintock, 2012) and possibly also MAXI J1820+070 (Bright et al., 2020). Persisting super-Eddington luminosities are usually observed in ultraluminous X-ray sources (ULXs), a part of which is composed of neutron stars accreting above the Eddington limit (e.g. Kaaret, Feng, and Roberts 2017).

We speculate that a combination of the options outlined above could explain the discrepancy between our inferred jet power and the available accretion power. We remark that obtaining a reliable estimate of the jet power is of prime importance for understanding of jet production and acceleration mechanisms.

8.3.6 Jet mass

From Equation 8.1, we are able to constrain the mass of the ejecta M_0 by sampling from the posterior distributions of E_0 and Γ_0 obtained with the MCMC fit. The resulting posterior distribution for M_0 is shown in Figure 8.6. We infer a jet mass

$$M_0 = 6.1^{+24.1}_{-4.5} \times 10^{25} \left(\frac{n_{\rm ism}}{1\ {\rm cm}^{-3}}\right) \left(\frac{\phi}{1^o}\right)^2 {\rm g}, \tag{8.17}$$

corresponding to $\sim 3.1 \times 10^{-8} M_\odot$. While this estimation is consistent with the first jets discovered in GRS 1915+105 (Mirabel and Rodríguez, 1994), obtained assuming one proton per electron, it is larger than the estimated masses for other ejecta observed in the same source (Mirabel et al., 1998; Fender et al., 1999), and in other sources (e.g. Steiner and McClintock 2012; Espinasse et al. 2020). It appears that, as many other physical parameters, the mass content of the jets can greatly vary among the population of XRBs, and significant variations

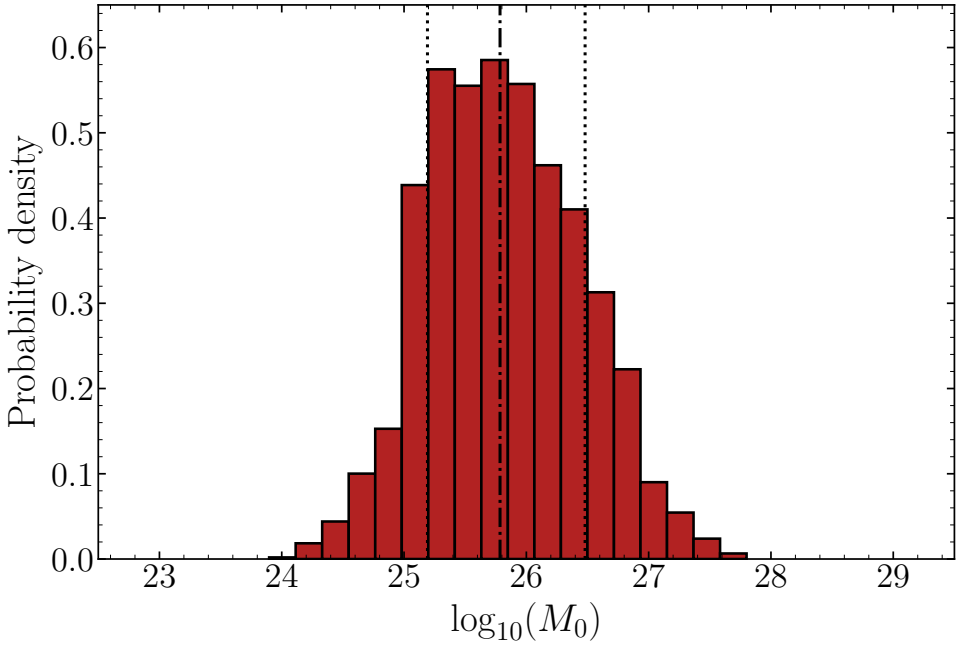

Figure 8.6: Posterior distribution for the ejecta mass M_0 in grams, obtained using the chain samples produced for E_0 and Γ_0. The median value and the equivalent 1σ uncertainty are marked, respectively, with vertical dot-dashed and dotted black lines. Assuming $n_{\rm ism} = 1$ cm^{-3} and $\phi = 1°$, we infer a jet mass $M_0 = 6.1^{+24.1}_{-4.5} \times 10^{25}$ g.

are observed even between multiple ejecta from the same source on short timescales (Tetarenko et al., 2017). However, the mass estimations for discrete ejecta are very uncertain, and often depend on parameters that are poorly constrained, such as the jet composition (specifically the proton content) and the Lorentz factor. In our case, we have also to consider the additional dependence on the two parameters $n_{\rm ism}$ and ϕ, but for which plausible values were assumed (see Section 8.3.4). Therefore, more observations are needed to increase the statistics and reduce the uncertainties on these physical quantities.

By considering the ejection timescale Δt introduced in Section 8.3.5, we can estimate the mass outflow rate to be $\simeq 3.9 \times 10^{20}$ g s^{-1} (for a bipolar ejection), implying a huge transfer of mass from the system to the jet during the ejection. Not surprisingly, such outflow rate is higher than what was obtained for other sources (e.g. SS 433 and GRS 1915+105, Kotani et al. 1996; Fender et al. 1999), and higher than the accretion rate of a system radiating at a significant fraction of the Eddington luminosity. This possibly implies that during the formation and launch of discrete ejecta, the majority of the inflowing mass is directly channeled into the jets and it is not advected into the event horizon (Fender and Pooley, 1998; Fender et al., 1999). Transitory mass outflow rates above the Eddington limit on the accretion rate are also consistent with simulations of accretion disks of stellar mass BHs (Okuda et al., 2005). Such mass outflow rate is also higher than the mass loss rate commonly attributed to disk winds, that can be as large as roughly ten times the mass accretion rate (Ponti et al., 2012). However, disk winds have not been detected for MAXI J1348−630 to our knowledge, hence a direct comparison of the two mass outflow rates is not possible.

8.3.7 Jet composition

The composition of discrete ejecta is generally unknown. Evidences for a baryonic content have been found in the jets from SS 433 (possibly from the ISM matter entrained by the jets), with the detection of Doppler-shifted iron line emission (Kotani et al., 1996; Migliari, Fender, and Méndez, 2002), but the rest of known ejecta displays featureless synchrotron spectra and might be composed of proton-electron or electron-positron plasma (Fender, 2006).

Hints on the composition of the ejecta from MAXI J1348−630 can be obtained by estimating the number of protons and electrons required to match the observational constraints from the jet radiation and motion. To begin, the number of relativistic electrons $N_{\rm e}$ in the jet can be obtained through widely-applied minimum energy calculations (Longair, 2011). We consider a synchrotron source with volume V and with monochromatic luminosity L_ν at frequency ν, characterised by a power law spectrum $L_\nu \propto \nu^{-\alpha}$ (we note that here we use a different notation compared to the rest of the thesis for the radio spectral index α). We assume a standard electron distribution modelled as a power law with index $p = 2\alpha+1$, where the electron energy spectrum per unit volume is

$$N(E)dE = kE^{-p}dE \tag{8.18}$$

The synchrotron radio luminosity L_ν depends on the energy spectrum of relativistic electrons and on the magnetic field B as

$$L_\nu = A(\alpha)VkB^{1+\alpha}\nu^{-\alpha} \tag{8.19}$$

for which the constant $A(\alpha)$ can be expressed as

$$A(\alpha) = \frac{\sqrt{3}e^3}{4\pi\epsilon_0 m_{\rm e} c}\left[\frac{3}{2}\frac{e}{\pi m_{\rm e}^3 c^4}\right]^{\frac{p-1}{2}} a(p) \tag{8.20}$$

where ϵ_0 is the permittivity of free space, and for which

$$a(p) = \frac{\sqrt{\pi}}{2}\frac{\Gamma\left(\frac{p}{4}+\frac{19}{12}\right)\Gamma\left(\frac{p}{4}-\frac{1}{12}\right)\Gamma\left(\frac{p}{4}+\frac{5}{4}\right)}{(p+1)\Gamma\left(\frac{p}{4}+\frac{7}{4}\right)} \tag{8.21}$$

where $\Gamma(x)$ is the Gamma function.

We can obtain $L_\nu = 4\pi D^2 S_\nu$ as the monochromatic luminosity of the synchrotron flare, with a flux density $S_\nu \simeq 486$ mJy observed at a frequency $\nu = 1.28$ GHz with MeerKAT on MJD 58523 (see Section 5.3.2 and Carotenuto et al. 2021a). To obtain the total number of relativistic electrons, we integrate Equation 8.18 between the minimum and maximum electron energies

$$N_e = V\int_{E_{\rm min}}^{E_{\rm max}} N(E)dE = V\int_{E_{\rm min}}^{E_{\rm max}} kE^{-p}dE = \frac{\nu^{\left(\frac{p-1}{2}\right)}}{p-1}\left(\frac{1}{C}\right)^{\frac{1-p}{2}}\left[\frac{L_\nu}{A(\alpha)B}\right]\left[\nu_{\rm min}^{\frac{1-p}{2}} - \nu_{\rm max}^{\frac{1-p}{2}}\right] \tag{8.22}$$

for which we express $E_{\rm min}$ and $E_{\rm max}$ as a function of the minimum and maximum frequencies at which the electrons radiate

$$E_{\rm min} = \left(\frac{\nu_{\rm min}}{CB}\right)^{\frac{1}{2}}, \quad E_{\rm max} = \left(\frac{\nu_{\rm max}}{CB}\right)^{\frac{1}{2}} \tag{8.23}$$

where

$$C = 0.29 \cdot \frac{3}{2} \frac{e}{2\pi m_{\rm e}} \frac{1}{(m_{\rm e}c^2)^2} \tag{8.24}$$

We assume that the electrons radiate between a minimum frequency $\nu_{\rm min} = 10^9$ Hz (lower limit of the MeerKAT observing band) and a maximum frequency $\nu_{\rm max} = 10^{15}$ Hz. The real value of both frequencies is unknown, but the results depend very weakly on $\nu_{\rm max}$, since the emission is dominated by the low-energy electrons.

At equipartition conditions, the magnetic field B corresponding to the minimisation of the total energy, that appears in Equation 8.22, can be written as

$$B = \left[\frac{3\mu_0}{2} \frac{G(\alpha)\eta L_\nu}{V} \right]^{\frac{2}{7}} \tag{8.25}$$

where μ_0 is the permeability of free space, η is assumed to be 1 (see Section 3.2.2), and where

$$G(\alpha) = \frac{1}{a(p)} \frac{1}{(p-2)} \left[\nu_{\rm min}^{-(\frac{p-2}{2})} - \nu_{\rm max}^{-(\frac{p-2}{2})} \right] \nu^{\frac{p-1}{2}} C^{-(\frac{p-2}{2})} \frac{4\pi\epsilon_0 m_{\rm e} c}{\sqrt{3}e^3} \left[\frac{3}{2} \frac{e}{\pi m_{\rm e}^3 c^4} \right]^{\frac{1-p}{2}} \tag{8.26}$$

The volume V of the jet at launch (when it produced the synchrotron flare) is a key parameter for the calculation of $N_{\rm e}$, and we estimate it by considering the ejection timescale Δt, discussed in Section 8.3.5, and a reasonable jet expansion speed of $0.05c$, which is consistent with results from Fender and Bright (2019) and with observational constraints from Carotenuto et al. (2021a). We take into account Doppler boosting due to the relativistic speed of the jet in the first phase of its motion, and we convert our measured quantities to the jet rest frame by correcting the observed frequency with $\nu_{\rm obs} = \delta_{\rm app} \nu_{\rm rest\ frame}$, the observed ejection timescale $\Delta t_{\rm obs} = \delta_{\rm app}^{-1} \Delta t_{\rm rest\ frame}$ and observed flux $S_{\nu,{\rm obs}} = \delta_{\rm app}^{3-\alpha} S_{\nu,{\rm rest\ frame}}$, assuming $\alpha = -0.5$ from Carotenuto et al. (2021a). An upper limit on the size of the emitting region can also be obtained by considering the unresolved radio point source and the MeerKAT beam on MJD 58523, but this would lead to an overestimation of the actual volume V due the $\sim$5 arcsec MeerKAT L-band resolution.

From equation 8.22, we obtain $N_{\rm e} \simeq 3 \times 10^{43}$, which is smaller compared to other discrete ejecta (e.g. Fender et al. 1999; Espinasse et al. 2020). If we consider that each electron is accompanied by a cold proton, we obtain a total jet mass $N_{\rm e}(m_{\rm e} + m_{\rm p}) \simeq 5 \times 10^{19}$ g, which is much smaller than our inferred total jet rest mass, discussed in Section 8.3.6. Therefore, there seems to be evidence for the jet to be made up of non-radiating particles. Such jet could be possibly dominated by "cold" protons which would carry most of the kinetic energy. In principle, the number of protons could simply be estimated as

$$N_{\rm p} = \frac{M_0}{m_{\rm p}} \simeq 4 \times 10^{49} \left(\frac{n_{\rm ism}}{1\ {\rm cm}^{-3}} \right) \left(\frac{\phi}{1^o} \right)^2 \tag{8.27}$$

which greatly exceeds the number of synchrotron-emitting relativistic electrons, even taking into account the uncertainty due to the dependence on $n_{\rm ism}$ and ϕ (see Section 8.3.4). We could speculate that the jet might include a population of non-relativistic (and hence non-radiating) electrons coupled to the cold protons for charge balance. However, such estimation is purely qualitative, and this is due to the large uncertainty present on many parameters involved in this calculation, and to our likely over-simplification of the problem.

The discrepancy between $N_{\rm e}$ and M_0 could be alleviated in several ways: with a more precise

estimation of the jet volume at launch (which could be underestimated), or if the jet plasma is far from equipartition, with a stronger magnetic field. Moreover, electrons in the jet could radiate even below $\nu_{\rm min}$, with more protons associated, although there is not yet observational evidence of ejecta radiating at lower radio frequencies, as argued in Fender et al. (1999). Lastly, E_0, and consequently M_0, might be overestimated, in particular if the ejecta has a significantly smaller opening angle ϕ than what assumed in this work, although we deem this as unlikely, as discussed in Section 8.3.4.

8.4 The environment of MAXI J1348−630

The external shock model applied in this work considers the source to be embedded in a low density cavity present in the ISM. After a first phase of constant speed motion, the jet hits the cavity border and decelerates as a result of the interaction with a much denser environment. From the fit, we infer the low-density ISM cavity to have a radius $R_{\rm c} = 0.61^{+0.11}_{-0.09}$ pc, which is consistent with the constraints from Carotenuto et al. (2021a). We also infer a density jump $\delta = 980^{+514}_{-359}$. As mentioned in Section 8.2.3, this implies a density $n_{\rm ism}/\delta = 0.0010^{+0.0005}_{-0.0003}$ cm^{-3} inside the empty bubble, assuming a standard external ISM external density $n_{\rm ism} = 1$ cm^{-3}. Interestingly, the value of δ is roughly one order of magnitude larger than the ones inferred for other BH XRBs possibly located inside a cavity, such as XTE J1550−564 and H1743−322 (Wang, Dai, and Lu, 2003; Hao and Zhang, 2009; Steiner and McClintock, 2012; Migliori et al., 2017). However, our density estimate is consistent with what was inferred for the environments of GRS 1915+105 and GRO J1655–40, obtained assuming that the discrete ejecta are travelling in a constant density medium up to distances of at least ∼0.04 pc (Heinz, 2002). The size of the cavity $R_{\rm c}$ is consistent with what obtained for XTE J1550−564 and H1743−322 (e.g. Hao and Zhang 2009). XTE J1752–223 might also be located in an under-dense cavity, although such bubble would have a smaller size compared to other sources (Yang et al., 2010; Miller-Jones et al., 2011b).

As argued in Carotenuto et al. (2021a), MAXI J1348−630 is fully consistent with the scenario of microquasars embedded in low density environments proposed by Hao and Zhang (2009). It is currently unclear how such cavities might be produced. BH XRBs might be located in small regions occupied by the hot ISM phase, or, more likely, the low-density region could result from the system's activity (Heinz, 2002; Hao and Zhang, 2009). The stability of these cavity would depend on the pressure balance with the external ISM, and their evolution is likely to take place on timescales much longer than the common recurrence outburst times for XRBs, which is estimated to span from years to centuries (Remillard and McClintock, 2006; Corral-Santana et al., 2016). Even if we imagine the cavity to be completely empty, it would take roughly $\sim 5 \times 10^4$ years (much longer than the typical XRB evolving timescale) for the external gas expanding at the sound speed to refill a ∼0.6 pc cavity, assuming an external ISM with density $n_{\rm ism} = 1$ cm^{-3} and temperature ∼8000 K (Ferrière, 2001).

An empty bubble might be created by the supernova that produced the BH in MAXI J1348−630 in case of low kick-out velocity, although we deem this first option as unlikely due to the fact that the system has to be significantly young for the ISM cavity not be yet refilled by the surrounding material. However, in that case we would expect to clearly detect the radio supernova remnant, for which there is no evidence (Carotenuto et al., 2021a), suggesting that MAXI J1348−630 might be an old system. Several other possibilities involve previous outbursts and the feedback of jets or winds on the ISM surrounding the system.

The cavity might have been carved out by jet activity in previous outbursts. There are examples of jets from XRBs developing at large scales and creating hot spots at the terminal shock surface, where kinetic energy is continuously transferred from the system to the ISM (Seward et al., 1980; Mirabel et al., 1992; Heinz et al., 2007; Marti et al., 2017; Coriat et al., 2019). A pc-scale cavity is also believed to be produced by the jets of Cyg X-1 (Gallo et al., 2005). In this case, and in absence of fast jet precession, we would expect rather a tunnel or a narrow under-dense region instead of a cavity, which would justify the jet collimation but it would require frequent ejections from the system in order to be sustained over time, as argued in Hao and Zhang (2009). A wide, symmetrical cavity might be created by more steady and uncollimated outflows, such as winds, which could be produced by the companion star (e.g. Sell et al. 2015), by the more massive progenitor of the compact object (e.g. Gaensler et al. 2005), or by the accretion disk itself during phases of outburst (e.g. Miller et al. 2006; Fuchs, Koch Miramond, and Ábrahám 2006; Muñoz-Darias et al. 2019). While the companion stars of BH LMXBs might not be massive enough to produce strong winds, the accretion disks represent more plausible candidates, possibly displaying high mass outflow rates (e.g. Muñoz-Darias et al. 2016). Due to their non-relativistic speeds, winds have necessarily to be produced during previous outbursts in order to push away the ISM and produce the cavity, since the mildly-relativistic ejecta from MAXI J1348−630 is way faster than the winds and it is ejected close to the beginning of the outburst. However, it is not clear at this stage if the winds have enough power to carve out cavities at at pc-scale (Hao and Zhang, 2009).

8.4.1 Alternative explanations

A scenario alternative to the cavity might involve a denser ISM region, such as a molecular cloud, encountered by the jet on its path, which could be responsible for the sudden deceleration of the ejecta. However, this is unlikely because it would imply that the jet is travelling in an environment with a standard ISM density $n_{\rm ism} = 1$ cm^{-3}, before hitting a higher density region. From our results, such scenario would require an initial energy of the jet to be a factor $\sim$1000 larger than the estimated E_0 (see Sections 8.2.3 and 8.3.4) to match the observations. This is due to the fact that the swept-up mass would be much higher than what expected in the cavity scenario, unless the jet is strongly collimated, with a half-opening angle $\phi \ll 1°$.

It is important to mention that a physical obstacle, such as the border of a cavity, is not strictly required for a relativistic object to produce a proper motion curve similar to the one of MAXI J1348−630, shown in Figure 8.3. In fact, the object might have a high initial Lorentz factor and could be continuously decelerating in a uniform medium with constant density, as for instance could be the case in MAXI J1820+070 (Bright et al., 2020; Espinasse et al., 2020). The observed sudden deceleration would be simply the signature that the jet's Lorentz factor reached values $\Gamma \lesssim 2$, starting from values much higher than the ones obtained for our run of the model in a uniform density environment (Section 8.2.2). In this context, Doppler boosting might explain the light curve of the highly relativistic jet, including the late-time re-brightening. Such interpretation is discussed in Fender & Rhodes (*in prep.*).

8.4.2 Predictions for the receding component

The receding component paired to the discrete ejection considered in this work has never been detected in radio (Carotenuto et al., 2021a), and Doppler de-boosting is likely responsible for this, as discussed in Section 8.3.2. Assuming a perfectly bipolar ejection, and the same physical

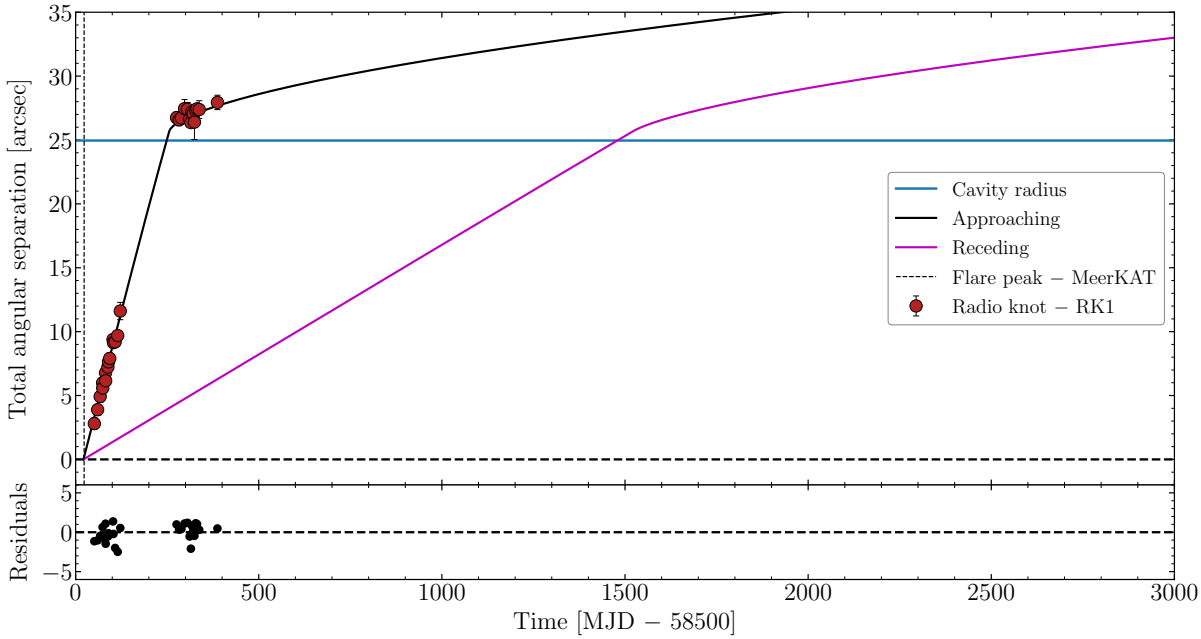

Figure 8.7: Predicted proper motion of the unseen receding component of the discrete ejecta from MAXI J1348−630. We show in black the obtained best fit for the approaching ejecta (same as Figure 8.3) and in pink the trajectory of the receding component, obtained with Equations 8.7 and 8.8 and the same physical parameters of the approaching component. If the cavity is symmetrical, we expect to observe the collision between the receding jet and cavity wall around MJD 60000 (February 2023).

parameters obtained for the approaching component, we expect the receding component to display a proper motion

$$\mu_{\rm rec} = \frac{\beta \sin\theta}{1 + \beta \cos\theta} \frac{c}{D} \simeq 16.7 \text{ mas day}^{-1} \tag{8.28}$$

Hence, from the ejection time, it would take approximately 1500 days (∼4.1 years) for the receding ejecta to reach the cavity border at 25 arcsec from the core position, assuming a symmetrical cavity (which appears to not be the case for XTE J1550−564; Hao and Zhang 2009; Steiner and McClintock 2012). This means that in our reference frame the receding jet has not reached yet the cavity border. It might be possible to detect emission from the receding component once the border is reached, since the ejecta will transition to a non-relativistic motion, synchrotron emission from re-accelerated particles will be produced and Doppler boosting will cease to be effective. The predicted trajectory of the receding jet is shown in Figure 8.7, from which it can be seen that the cavity wall (if we assume it to be symmetrical) will be reached around MJD 56000. To test this prediction, sensitive and high-resolution radio observations will be performed close to the expected jet/wall collision.

8.5 Conclusions

In this chapter, I have presented the application of the external shock model developed by Wang, Dai, and Lu (2003) to the decelerating discrete ejecta detected during the 2019/2020 outburst of MAXI J1348−630. We fitted the jet angular distance data with a Bayesian approach and we

found that the model provides an excellent description of the jet motion, from the first phase of high, constant speed to the last deceleration phase. From the fit, we are able to obtain important insights on the physical parameters of the jet and of the system's environment. We infer a mildly-relativistic jet with an initial Lorentz factor $\Gamma_0 = 1.85^{+0.15}_{-0.12}$ and with a low inclination angle with respect to the line of sight $\theta = 29.3^{\circ}{}^{+2.7^{\circ}}_{-3.2^{\circ}}$, implying that Doppler boosting is likely responsible for the non-detection of the receding jet component. The initial energy of the jet ($E_0 = 4.6^{+20.0}_{-3.4} \times 10^{46}$ erg) is very large and it provides support to the recent claim that ejecta from BH LMXBs do not radiate away most of their energy, which is instead largely transferred to the surrounding environment. Due to the large amount of energy contained in the jet and the short launching timescale, its ejection presumably required a power larger than what is available from accretion only, and we discuss in this work several options that might cause this discrepancy, including the possible underestimation of the accretion power and/or of the launching timescale, or the overestimation of two key parameters, $n_{\rm ism}$ and ϕ, that cannot be constrained from the model alone. Additional observations of discrete ejecta from BH LMXBs, with detailed estimations of the jet energy and ejection time, will also be needed to improve our estimations of the true jet power.

We are able to place constraints on the jet mass and on its ejection date, and we infer that the matter content of such jet might be dominated by cold protons, which largely exceed the number of relativistic electrons responsible for the jet synchrotron emission. The jet travels inside a low-density cavity which is inferred to have a radius $R_{\rm c} = 0.61^{+0.11}_{-0.09}$ pc and a density jump $\delta = 980^{+514}_{-359}$ with respect to the external standard ISM density $n_{\rm ism} = 1$ cm^{-3}, before encountering the cavity border and strongly decelerating, with possible *in-situ* particle acceleration. This is the first time that such external shock model, which is simple but rich of physical information, is applied to a one-sided jet component. In this context, the coverage of the jet deceleration, which is not common among jets from XRBs, is fundamental, as it allows us to properly constrain the jet trajectory and, as a consequence, to constrain the model parameters. More observations of decelerating ejecta from BH LMXBs are needed in order to confirm our results and to increase the size of our sample, which will lead us to a significant improvement of the current understanding of the jet production, acceleration and feedback on the surrounding environment. In order to cover the whole jet motion, dense, uniform and sensitive radio monitoring campaigns are required, and the new generation of radio-interferometers, such as MeerKAT (which already detected a significant number of discrete ejecta), its upcoming upgraded version, SKA-MID (Braun et al., 2015) and the ngVLA (Selina et al., 2018) will be ideal to achieve this goal.

Conclusions and perspectives

The goal of this thesis is to provide new insights into the properties of compact jets and discrete ejecta from black hole low mass X-ray binaries through intensive monitoring campaigns. Every source shows peculiar properties linked to the compact jet formation, evolution and connection with the accretion flow, and the launch and motion of discrete ejecta. In this thesis, rather than aiming at population studies, our approach was to target a single object and to perform a dense multi-wavelength monitoring campaign, as we believe that progress in this field can be achieved by improving the data quality and the detail with which every source is observed. The physics of jets from black hole X-ray binaries is incredibly complex, and a single thesis is certainly not enough to answer the many open questions that we discussed in the first chapters of this manuscript. I will summarize here the main results of this thesis, briefly discussing their implications, and then I will present some perspectives for the future continuation of my work.

In this thesis I have presented the X-ray and radio monitoring of MAXI J1348−630 during its 2019/2020 discovery outburst. MAXI J1348−630 is a new black hole candidate in a low mass X-ray binary system that fits very well in the general picture adopted for X-ray binaries. With our MAXI and *Swift* X-ray monitoring, we have been able to follow the whole outburst, in which the source displayed a rather typical X-ray evolution in the first part, completing a whole cycle in the Hardness-Intensity Diagram, and then exhibited a complex sequence of hard-state-only re-brightenings in the second part.

Discrete ejecta

Two subsequent, single-sided, approaching discrete ejecta have been tracked as they moved away from the core in the same direction, with the highest proper motion ($\gtrsim 100$ mas day^{-1}) observed so far among X-ray binaries. We were able to place similar constraints for the two ejecta on the intrinsic speed $\beta \geq 0.7$ and the inclination angle of the jet axis $\theta \leq 45°$. Since the first component was followed for 11 months, we were able to constrain its half-opening angle to $\leq 3°$. We precisely characterised its motion, composed of a first part of ballistic motion followed by a strong deceleration happening after the ejecta traveled at least 0.3 pc. This deceleration is in agreement with the scenario of microquasars embedded in low density, parsec-scale cavities in the interstellar medium. From a first, simple phenomenological modeling of the motion of the two ejecta, we can infer that the ejection of the first component happened before a strong radio flare, while the system was in the intermediate state. Moreover, the constraints on the minimum energy and power required to produce the observed radio flare are in agreement with the values generally measured for discrete ejecta.

Since the trajectory of the first ejecta was covered with high accuracy, this allowed us to model the jet motion and to constrain some important physical parameters. In fact, we successfully modelled the jet motion with a dynamical external shock model, with a Bayesian approach and using Monte Carlo Markov Chains. This allowed us to constrain the jet initial Lorentz factor $\Gamma_0 = 1.85^{+0.15}_{-0.12}$, inclination angle $\theta = 29.27°^{+2.71°}_{-3.23°}$ and ejection date $t_{\rm ej} = 21.45^{+1.88}_{-3.19}$ (MJD – 58500). Under simple assumptions on the jet opening angle and on the

external ISM density, we find that the jet has a large initial kinetic energy $E_0 = 4.6^{+20.0}_{-3.4} \times 10^{46}$ erg, far greater than what commonly measured for black hole X-ray binaries from the jet's synchrotron emission. This implies that discrete ejecta only radiate away a small fraction of their total energy, which is instead transferred to the environment via their kinetic energy alone. The jet power estimate is larger than the simultaneous available accretion power, and we presented several options to mitigate this discrepancy. We infer that MAXI J1348−630 is likely embedded in a cavity in the interstellar medium with internal density $n = 0.0010^{+0.0005}_{-0.0003}$ cm^{-3} and radius $R_{\rm c} = 0.61^{+0.11}_{-0.09}$ pc, which could have been produced by the system's previous activity, as proposed for other black hole low mass X-ray binaries.

Overall, our work provides important results on discrete ejecta from black hole low mass X-ray binaries. Thanks to our monitoring strategy, we have been able to cover the jet's entire "life", and this allowed us to constrain the jet physical properties, especially its initial kinetic energy, which is something that has rarely been possible for this type of jets. Our results confirm that the total energy of these jets is larger than previously thought, and it is not well-traced by the observed electromagnetic emission. This might have important implications for the proposed jet production mechanisms, and the estimation of the true energy content of these jets is currently an important open question. The ejection time is also particularly important, since it allows us to connect the jet launch to the status of the accretion disk and hence to obtain information on how the jet is produced. The wealth of physical information obtained for the jets of MAXI J1348−630 was not accessible for the majority of the discrete ejecta observed so far, and it is important to remark that the observations of the jet deceleration were essential to constrain the physical parameters of the jet and of the environment surrounding MAXI J1348−630.

The second ejecta from MAXI J1348−630 was likely launched during a short excursion of system from the soft to the intermediate state, a behaviour observed in a few X-ray binaries, but that today is still greatly unexplored. The link between the discrete ejecta and the spectral and timing properties of the X-ray emission is a core topic of the current research efforts, and future high-cadence multi-wavelength monitorings of black hole X-ray binaries at state transitions (and in the soft state) will be needed to characterise the causal sequence of events leading to the launch of discrete ejecta.

Compact jets and disk/jet coupling

Thanks to our radio observations conducted with MeerKAT and ATCA, we monitored the rise, quenching, and re-activation of the compact jets in different phases of the outburst, specifically constraining the jet quenching factor to 3.5 orders of magnitude in the soft state.

Our radio and X-ray monitoring campaign also allowed us to study the correlation between the radio and X-ray luminosities in the hard state that are produced, respectively, by the compact jets and by the inner accretion flow. Our results span almost 6 orders of magnitude in X-ray luminosity within a single outburst (very rare for a single source), allowing us to probe the accretion-ejection coupling from the bright phases of the outburst down to very low levels of activity of a black hole X-ray binary, which are still greatly unexplored. We find that MAXI J1348−630 belongs to the growing population of outliers at the highest observed luminosities. Interestingly, MAXI J1348−630 deviates from the outlier track at $L_{\rm X} \lesssim 7 \times 10^{35} (D/2.2\,{\rm kpc})^2$ erg s^{-1} and ultimately rejoins the standard track at $L_{\rm X} \simeq 10^{33} (D/2.2\,{\rm kpc})^2$ erg s^{-1}, displaying a hybrid radio/X-ray correlation, partially observed in only a handful of sources. However, for MAXI J1348−630 these transitions happen at luminosities much lower than what observed for similar sources (at least an order of magnitude). We discussed the behaviour of MAXI J1348−630 in light of the currently proposed scenarios, finding that our data are not consistent

with some proposed explanations for the observed dichotomy. In addition, our dedicated, sensitive and simultaneous *Chandra* and ATCA observations allowed us to obtain a detection in radio and X-rays of MAXI J1348−630 in quiescence, at $\sim 10^{-8.3} L_{\rm Edd}$, which has been rarely done for BH LMXBs and it is unprecedented for hybrid-correlation sources.

Our observations led us to discover a new hybrid-correlation source, and we remark that at this time MAXI J1348−630 is the only source of this group that has been observed over the entire range of luminosities within a single outburst and down to quiescence. Moreover, MAXI J1348−630 has the lowest transition luminosity from the outlier to the standard track among the known hybrid sources. Thanks to the observations in the low luminosity regime, and to the detection in quiescence, we confirm that, after H1743−322, hybrid sources re-join the standard track in the low flux regime. While several proposed explanations have been discussed in the previous chapters, the physical mechanism responsible for this change in the disk/jet coupling is still unknown and it is a key open question in the study of the connection between the disk and the jets in black hole X-ray binaries. The hybrid behaviour might result from a change in the properties of the accretion flow at different luminosities, or from a change in the jet's emission at different accretion rates. This data set will be of high importance for future studies of the jet/disk connection in BH LMXBs, and it will allow to place constraints on the jet emission mechanisms and to break degeneracies between different models.

To conclude, this work has shown how multi-wavelength (radio and X-ray) observations and detailed physical modeling can be used to probe the evolution of jets produced by accreting black holes, from the connection of the compact jets with the accretion disk, to the launch, motion and impact of superluminal ejecta. The key information on the jets that we obtained in this thesis will ultimately help to understand how these types of powerful jets are produced and launched from accreting compact objects, potentially across all physical scales.

Perspectives

The work presented in this thesis can be possibly extended in multiple directions. As mentioned above, covering the full trajectory of these jets allows us to model their motion with great accuracy and it is essential to measure their physical properties. In particular, observing the jet deceleration phase can yield a reliable estimate of the jet total energy. Therefore, more observations of decelerating jets are needed to improve their understanding. In this context, the MeerKAT interferometer turns out to be ideal for this purpose, as it is really "changing the game" in this field with its exceptional sensitivity and imaging capabilities at low (GHz) frequencies. In just two years, MeerKAT/ThunderKAT observations detected and traced the motion of the discrete ejecta from four new sources: MAXI J1535−571 (Russell et al., 2019c), MAXI J1820+070 (Bright et al., 2020), MAXI J1348−630 (this work) and the new MAXI J1848–015 (in progress, Tremou et al. 2021). In addition, a great contribution can be given by the new generation of radio-interferometers, such as MeerKAT+, the Square Kilometre Array (Braun et al., 2015) and the ngVLA (Selina et al., 2018). These extremely sensitive future arrays will allow us to monitor black hole X-ray binaries down to their low-luminosity regimes and quiescent states, possibly also greatly increasing the sample of the detected discrete ejecta. The monitoring strategies will be also aided by future all-sky monitoring instruments, such as the upcoming French-Chinese mission *SVOM* (Space-based multi-band astronomical Variable Objects Monitor, Cordier et al. 2015), that, while designed for gamma-ray bursts, will also be able discover new black hole transients in outburst and trigger follow-up multi-wavelength observing campaigns.

The external shock model used in this thesis can be improved in several ways (as for instance introducing a potentially variable jet opening angle, or by considering a stratified ISM). Such model will then be applied (testing the cavity scenario) to additional sources for which we have evidence of decelerating ejecta, such as MAXI J1820+070, MAXI J1535−571 and MAXI J1848–015. The latter is particularly interesting as it is the first example of resolved relativistic jets interacting with the ISM of a globular cluster (Tremou et al. *in prep.*).

Regarding the jet energy, the application of the external shock model will be important, as the total jet energy was previously estimated only from the initial radio flares, with large uncertainties. By comparing energy estimations from the decelerating phase and from the initial flare for the same jet, we can begin to calibrate this relationship, being thus able to infer the true energy budget for the majority of discrete ejecta from BH LMXBs observed so far, but for which the deceleration phase was not monitored. This also allow us to estimate the fraction of energy transferred to the environment and not radiated away by the jet, quantifying an important contribution of the black hole feedback to the surrounding environment.

Studying the interstellar medium surrounding black hole X-ray binaries is also of primary importance in order to improve our understanding of the jet/ISM interaction. New observational methods for identifying jet/ISM interaction sites are needed for constraining the ISM parameters and taking advantage of the diagnostic potential of these regions (e.g. Tetarenko et al. 2018a). For instance, searching for molecular line emission near black hole X-ray binaries with ALMA can be a powerful method to identify jet/ISM interaction regions, and accurately probe the ISM conditions at these sites.

Regarding the disk/jet coupling, there is yet no consensus on what produces the observed tracks, and it is not clear at the moment if all outliers belong to the hybrid correlation. It will be crucial for future monitorings of hybrid correlation sources to obtain a deep and dense coverage of the outburst, especially close to the transition luminosities, in the low-flux regime and in quiescence. Constraining the radio/X-ray correlation at low luminosities will allow us to discriminate between the existing models and to improve our understanding of the disk/jet connection among X-ray binaries. A first example of such approach is being currently performed with observations triggered by our active joint *Swift*/VLA proposal, targeting the new BH LMXB MAXI J1803–298 (Espinasse et al., 2021).

If pursued, I believe that all these possible extension of the work presented in this thesis can allow us to make the next step in our understanding of the phenomenology and physics of accretion and ejection in black hole X-ray binaries.

Bibliography

[1] B. P. Abbott et al. “Observation of Gravitational Waves from a Binary Black Hole Merger”. In: *Phys. Rev. Lett.* 116.6, 061102 (Feb. 2016), p. 061102. DOI: 10.1103/PhysRevLett.116.061102. arXiv: 1602.03837 [gr-qc].

[2] Marek A. Abramowicz et al. “Thermal Equilibria of Accretion Disks”. In: *ApJ* 438 (Jan. 1995), p. L37. DOI: 10.1086/187709. arXiv: astro-ph/9409018 [astro-ph].

[3] Aisha Al Yazeedi et al. “Rebrightening of MAXI J1348-630”. In: *The Astronomer’s Telegram* 13188 (Oct. 2019), p. 1.

[4] J. Anczarski et al. “X-ray Analysis of MAXI J1348-630 with NuSTAR”. In: *American Astronomical Society Meeting Abstracts #235*. Vol. 235. American Astronomical Society Meeting Abstracts. Jan. 2020, p. 369.02.

[5] Lorella Angelini and Nicholas E. White. “An XMM-Newton Observation of 4U 1755-33 in Quiescence: Evidence of a Fossil X-Ray Jet”. In: *ApJ* 586.1 (Mar. 2003), pp. L71–L75. DOI: 10.1086/374682. arXiv: astro-ph/0302315 [astro-ph].

[6] K. A. Arnaud. “XSPEC: The First Ten Years”. In: *Astronomical Data Analysis Software and Systems V*. Ed. by George H. Jacoby and Jeannette Barnes. Vol. 101. Astronomical Society of the Pacific Conference Series. Jan. 1996, p. 17.

[7] P. Atri et al. “A radio parallax to the black hole X-ray binary MAXI J1820+070”. In: *MNRAS* 493.1 (Mar. 2020), pp. L81–L86. DOI: 10.1093/mnrasl/slaa010. arXiv: 1912.04525 [astro-ph.HE].

[8] W. Baade and R. Minkowski. “Identification of the Radio Sources in Cassiopeia, Cygnus A, and Puppis A.” In: *ApJ* 119 (Jan. 1954), p. 206. DOI: 10.1086/145812.

[9] Arash Bahramian et al. May 2018. DOI: 10.5281/zenodo.1252036.

[10] Steven A. Balbus and John F. Hawley. “Instability, turbulence, and enhanced transport in accretion disks”. In: *Reviews of Modern Physics* 70.1 (Jan. 1998), pp. 1–53. DOI: 10.1103/RevModPhys.70.1.

[11] J. Ballet. “Pile-up on X-ray CCD instruments”. In: *A&AS* 135 (Mar. 1999), pp. 371–381. DOI: 10.1051/aas:1999179.

[12] Cosimo Bambi. "Astrophysical Black Holes: A Compact Pedagogical Review". In: *Annalen der Physik* 530.6 (June 2018), p. 1700430. DOI: 10.1002/andp.201700430. arXiv: 1711.10256 [gr-qc].

[13] James M. Bardeen and Jacobus A. Petterson. "The Lense-Thirring Effect and Accretion Disks around Kerr Black Holes". In: *ApJ* 195 (Jan. 1975), p. L65. DOI: 10.1086/181711.

[14] James M. Bardeen, William H. Press, and Saul A. Teukolsky. "Rotating Black Holes: Locally Nonrotating Frames, Energy Extraction, and Scalar Synchrotron Radiation". In: *ApJ* 178 (Dec. 1972), pp. 347–370. DOI: 10.1086/151796.

[15] Scott D. Barthelmy et al. "The Burst Alert Telescope (BAT) on the SWIFT Midex Mission". In: *Space Sci. Rev.* 120.3-4 (Oct. 2005), pp. 143–164. DOI: 10.1007/s11214-005-5096-3. arXiv: astro-ph/0507410 [astro-ph].

[16] Mitchell C. Begelman, Marta Volonteri, and Martin J. Rees. "Formation of supermassive black holes by direct collapse in pre-galactic haloes". In: *MNRAS* 370.1 (July 2006), pp. 289–298. DOI: 10.1111/j.1365-2966.2006.10467.x. arXiv: astro-ph/0602363 [astro-ph].

[17] T. Belloni et al. "The evolution of the timing properties of the black-hole transient GX 339-4 during its 2002/2003 outburst". In: *A&A* 440.1 (Sept. 2005), pp. 207–222. DOI: 10.1051/0004-6361:20042457. arXiv: astro-ph/0504577 [astro-ph].

[18] T. M. Belloni. "States and Transitions in Black Hole Binaries". In: *Lecture Notes in Physics*. Vol. 794. Berlin Springer Verlag, 2010, p. 53. DOI: 10.1007/978-3-540-76937-8_3.

[19] Tomaso M. Belloni and Sara E. Motta. "Transient Black Hole Binaries". In: *Astrophysics of Black Holes: From Fundamental Aspects to Latest Developments*. Vol. 440. Springer, 2016, p. 61. DOI: 10.1007/978-3-662-52859-4_2.

[20] Tomaso M. Belloni and Sara E. Motta. "Transient Black Hole Binaries". In: *Astrophysics of Black Holes: From Fundamental Aspects to Latest Developments*. Vol. 440. Springer-Verlag, 2016, p. 61. DOI: 10.1007/978-3-662-52859-4_2.

[21] Tomaso M. Belloni et al. "Time lags of the type-B quasi-periodic oscillation in MAXI J1348-630". In: *MNRAS* 496.4 (Aug. 2020), pp. 4366–4371. DOI: 10.1093/mnras/staa1843. arXiv: 2006.12872 [astro-ph.HE].

[22] Tomaso M Belloni et al. "Time lags of the type-B quasi-periodic oscillation in MAXI J1348-630". In: *MNRAS* 496.4 (June 2020), pp. 4366–4371. ISSN: 0035-8711. DOI: 10.1093/mnras/staa1843. eprint: https://academic.oup.com/mnras/article-pdf/496/4/4366/33498821/staa1843.pdf. URL: https://doi.org/10.1093/mnras/staa1843.

[23] R. D. Blandford and A. Königl. "Relativistic jets as compact radio sources." In: *ApJ* 232 (Aug. 1979), pp. 34–48. DOI: 10.1086/157262.

[24] R. D. Blandford and C. F. McKee. "Fluid dynamics of relativistic blast waves". In: *Physics of Fluids* 19 (Aug. 1976), pp. 1130–1138. DOI: 10.1063/1.861619.

[25] R. D. Blandford, C. F. McKee, and M. J. Rees. "Super-luminal expansion in extragalactic radio sources". In: *Nature* 267.5608 (May 1977), pp. 211–216. DOI: 10.1038/267211a0.

[26] R. D. Blandford and D. G. Payne. "Hydromagnetic flows from accretion disks and the production of radio jets." In: *MNRAS* 199 (June 1982), pp. 883–903. DOI: 10.1093/mnras/199.4.883.

[27] R. D. Blandford and R. L. Znajek. "Electromagnetic extraction of energy from Kerr black holes." In: *MNRAS* 179 (May 1977), pp. 433–456. DOI: 10.1093/mnras/179.3.433.

[28] Roger D. Blandford and Mitchell C. Begelman. "On the fate of gas accreting at a low rate on to a black hole". In: *MNRAS* 303.1 (Feb. 1999), pp. L1–L5. DOI: 10.1046/j.1365-8711.1999.02358.x. arXiv: astro-ph/9809083 [astro-ph].

[29] Steven Bloemen et al. "MeerLICHT and BlackGEM: custom-built telescopes to detect faint optical transients". In: *Ground-based and Airborne Telescopes VI*. Ed. by Helen J. Hall, Roberto Gilmozzi, and Heather K. Marshall. Vol. 9906. Society of Photo-Optical Instrumentation Engineers (SPIE) Conference Series. July 2016, p. 990664. DOI: 10.1117/12.2232522.

[30] R. Braun et al. "Advancing Astrophysics with the Square Kilometre Array". In: *Advancing Astrophysics with the Square Kilometre Array (AASKA14)*. Apr. 2015, p. 174.

[31] D. S. Briggs. "High Fidelity Interferometric Imaging: Robust Weighting and NNLS Deconvolution". In: *American Astronomical Society Meeting Abstracts*. Vol. 187. American Astronomical Society Meeting Abstracts. Dec. 1995, p. 112.02.

[32] J. Bright et al. "An extremely powerful long-lived superluminal ejection from the black hole MAXI J1820+070". In: *Nature Astronomy* 4 (July 2020), pp. 1–7. DOI: 10.1038/s41550-020-1023-5.

[33] Joe Bright. "Radio studies of relativistic outflows from black hole transients". PhD thesis, University of Oxford. PhD thesis. 2020. URL: https://ora.ox.ac.uk/objects/uuid:62886f2f-6a34-41e0-88f8-395b4a00255a.

[34] C. Brocksopp et al. "A highly polarized radio jet during the 1998 outburst of the black hole transient XTE J1748-288". In: *MNRAS* 378.3 (July 2007), pp. 1111–1117. DOI: 10.1111/j.1365-2966.2007.11846.x. arXiv: 0705.1125 [astro-ph].

[35] C. Brocksopp et al. "Initial low/hard state, multiple jet ejections and X-ray/radio correlations during the outburst of XTE J1859+226". In: *MNRAS* 331.3 (Apr. 2002), pp. 765–775. DOI: 10.1046/j.1365-8711.2002.05230.x. arXiv: astro-ph/0112137 [astro-ph].

[36] C. Brocksopp et al. "The 1997 hard state outburst of the x-ray transient gs 1354-64 / bw cir". In: *Astrophys. Space Sci.* 276 (2001), pp. 117–120. DOI: 10.1023/A:1011698018918. arXiv: astro-ph/0011145.

[37] C. Brocksopp et al. "The 2003 radio outburst of a new X-ray transient: XTE J1720-318". In: *MNRAS* 356.1 (Jan. 2005), pp. 125–130. DOI: 10.1111/j.1365-2966.2004.08427.x. arXiv: astro-ph/0410353 [astro-ph].

[38] C. Brocksopp et al. "XTE J1752-223 in outburst: a persistent radio jet, dramatic flaring, multiple ejections and linear polarization". In: *MNRAS* 432.2 (June 2013), pp. 931–943. DOI: 10.1093/mnras/stt493. arXiv: 1303.6702 [astro-ph.HE].

[39] Crystal L. Brogan, Todd R. Hunter, and Ed B. Fomalont. "Advanced Gain Calibration Techniques in Radio Interferometry". In: *arXiv e-prints*, arXiv:1805.05266 (May 2018), arXiv:1805.05266. arXiv: 1805.05266 [astro-ph.IM].

[40] G. E. Brown and H. A. Bethe. "A Scenario for a Large Number of Low-Mass Black Holes in the Galaxy". In: *ApJ* 423 (Mar. 1994), p. 659. DOI: 10.1086/173844.

[41] G. R. Burbidge. "On Synchrotron Radiation from Messier 87." In: *ApJ* 124 (Sept. 1956), p. 416. DOI: 10.1086/146237.

[42] David N. Burrows et al. "The Swift X-Ray Telescope". In: *Space Sci. Rev.* 120.3-4 (Oct. 2005), pp. 165–195. DOI: 10.1007/s11214-005-5097-2. arXiv: astro-ph/0508071 [astro-ph].

[43] D. E. Calvelo et al. "Millimetre observations of a sub-arcsecond jet from Circinus X-1". In: *MNRAS* 419.1 (Jan. 2012), pp. L54–L58. DOI: 10.1111/j.1745-3933.2011.01175.x. arXiv: 1110.3997 [astro-ph.HE].

[44] F. Camilo et al. "Revival of the Magnetar PSR J1622-4950: Observations with MeerKAT, Parkes, XMM-Newton, Swift, Chandra, and NuSTAR". In: *ApJ* 856.2, 180 (Apr. 2018), p. 180. DOI: 10.3847/1538-4357/aab35a. arXiv: 1804.01933 [astro-ph.HE].

[45] Floriane Cangemi. "Approche multi-diagnostique des émissions de haute énergie des microquasars à trous noirs". Theses. Université de Paris / Université Paris Diderot (Paris 7), Oct. 2020. URL: https://tel.archives-ouvertes.fr/tel-03114988.

[46] J. K. Cannizzo, P. Ghosh, and J. C. Wheeler. "Convective accretion disks and the onset of dwarf nova outbursts." In: *ApJ* 260 (Sept. 1982), pp. L83–L86. DOI: 10.1086/183875.

[47] F. Carotenuto, A. J. Tetarenko, and S. Corbel. "Modelling the kinematics of the decelerating jets from the black hole X-ray binary MAXI J1348-630". In: *MNRAS* 511.4 (Apr. 2022), pp. 4826–4841. DOI: 10.1093/mnras/stac329. arXiv: 2202.01514 [astro-ph.HE].

[48] F. Carotenuto et al. "The black hole transient MAXI J1348-630: evolution of the compact and transient jets during its 2019/2020 outburst". In: *MNRAS* 504.1 (June 2021), pp. 444–468. DOI: 10.1093/mnras/stab864. arXiv: 2103.12190 [astro-ph.HE].

[49] F. Carotenuto et al. "The hybrid radio/X-ray correlation of the black hole transient MAXI J1348-630". In: *arXiv e-prints*, arXiv:2105.06006 (Oct. 2021), arXiv:2105.06006. arXiv: 2105.06006 [astro-ph.HE].

[50] Francesco Carotenuto et al. "MeerKAT and ATCA detection of MAXI J1348-630". In: *The Astronomer's Telegram* 14029 (Sept. 2020), p. 1.

[51] Francesco Carotenuto et al. "MeerKAT and Swift/XRT detection of MAXI J1348-630". In: *The Astronomer's Telegram* 13467 (Feb. 2020), p. 1.

[52] Francesco Carotenuto et al. "MeerKAT follow-up observations of MAXI J1348-630 reveal bright radio flare at state transition". In: *The Astronomer's Telegram* 12497 (Feb. 2019), p. 1.

[53] P. Casella et al. "Fast infrared variability from a relativistic jet in GX 339-4". In: *MNRAS* 404.1 (May 2010), pp. L21–L25. DOI: 10.1111/j.1745-3933.2010.00826.x. arXiv: 1002.1233 [astro-ph.HE].

[54] W. Cash. "Parameter estimation in astronomy through application of the likelihood ratio." In: *ApJ* 228 (Mar. 1979), pp. 939–947. DOI: 10.1086/156922.

[55] S. Chandrasekhar. "The Stability of Non-Dissipative Couette Flow in Hydromagnetics". In: *Proceedings of the National Academy of Science* 46.2 (Feb. 1960), pp. 253–257. DOI: 10.1073/pnas.46.2.253.

[56] K. Chatterjee et al. "Accelerating AGN jets to parsec scales using general relativistic MHD simulations". In: *MNRAS* 490.2 (Dec. 2019), pp. 2200–2218. DOI: 10.1093/mnras/stz2626. arXiv: 1904.03243 [astro-ph.HE].

[57] S. Chaty, G. Dubus, and A. Raichoor. "Near-infrared jet emission in the microquasar XTE J1550-564". In: *A&A* 529, A3 (May 2011), A3. DOI: 10.1051/0004-6361/201015589. arXiv: 1102.5054 [astro-ph.HE].

[58] S. Chaty et al. "A search for possible interactions between ejections from GRS 1915+105 and the surrounding interstellar medium". In: *A&A* 366 (Feb. 2001), pp. 1035–1046. DOI: 10.1051/0004-6361:20000266. arXiv: astro-ph/0011297 [astro-ph].

[59] J. Chauhan et al. "An H I absorption distance to the black hole candidate X-ray binary MAXI J1535-571". In: *MNRAS* 488.1 (Sept. 2019), pp. L129–L133. DOI: 10.1093/mnrasl/slz113. arXiv: 1905.08497 [astro-ph.HE].

[60] J. Chauhan et al. "Measuring the distance to the black hole candidate X-ray binary MAXI J1348-630 using H I absorption". In: *MNRAS* 501.1 (Feb. 2021), pp. L60–L64. DOI: 10.1093/mnrasl/slaa195. arXiv: 2009.14419 [astro-ph.HE].

[61] Wan Chen, C. R. Shrader, and Mario Livio. "The Properties of X-Ray and Optical Light Curves of X-Ray Novae". In: *ApJ* 491.1 (Dec. 1997), pp. 312–338. DOI: 10.1086/304921. arXiv: astro-ph/9707138 [astro-ph].

[62] Y. P. Chen et al. "Insight-HXMT observations of MAXI J1348-630". In: *The Astronomer's Telegram* 12470 (Feb. 2019), p. 1.

[63] James J. Condon and Scott M. Ransom. *Essential Radio Astronomy*. 2016.

[64] S. Corbel and R. P. Fender. "Near-Infrared Synchrotron Emission from the Compact Jet of GX 339-4". In: *ApJ* 573.1 (July 2002), pp. L35–L39. DOI: 10.1086/341870. arXiv: astro-ph/0205402 [astro-ph].

[65] S. Corbel, E. Koerding, and P. Kaaret. "Revisiting the radio/X-ray flux correlation in the black hole V404 Cyg: from outburst to quiescence". In: *MNRAS* 389.4 (Oct. 2008), pp. 1697–1702. DOI: 10.1111/j.1365-2966.2008.13542.x. arXiv: 0806.3079 [astro-ph].

[66] S. Corbel, J. A. Tomsick, and P. Kaaret. "On the Origin of Black Hole X-Ray Emission in Quiescence: Chandra Observations of XTE J1550-564 and H1743-322". In: *ApJ* 636.2 (Jan. 2006), pp. 971–978. DOI: 10.1086/498230. arXiv: astro-ph/0509870 [astro-ph].

[67] S. Corbel et al. "Formation of the compact jets in the black hole GX 339-4." In: *MNRAS* 431 (2013), pp. L107–L111. DOI: 10.1093/mnrasl/slt018. arXiv: 1303.2551 [astro-ph.HE].

[68] S. Corbel et al. "Coupling of the X-ray and radio emission in the black hole candidate and compact jet source GX 339-4". In: *A&A* 359 (July 2000), pp. 251–268. arXiv: astro-ph/0003460 [astro-ph].

[69] S. Corbel et al. "Discovery of X-Ray Jets in the Microquasar H1743-322". In: *ApJ* 632.1 (Oct. 2005), pp. 504–513. DOI: 10.1086/432499. arXiv: astro-ph/0505526 [astro-ph].

[70] S. Corbel et al. "Large-Scale, Decelerating, Relativistic X-ray Jets from the Microquasar XTE J1550-564". In: *Science* 298.5591 (Oct. 2002), pp. 196–199. DOI: 10.1126/science.1075857. arXiv: astro-ph/0210224 [astro-ph].

[71] S. Corbel et al. "On the Origin of Radio Emission in the X-Ray States of XTE J1650-500 during the 2001-2002 Outburst". In: *ApJ* 617.2 (Dec. 2004), pp. 1272–1283. DOI: 10.1086/425650. arXiv: astro-ph/0409154 [astro-ph].

[72] S. Corbel et al. "On the Origin of Radio Emission in the X-Ray States of XTE J1650-500 during the 2001-2002 Outburst". In: *ApJ* 617.2 (Dec. 2004), pp. 1272–1283. DOI: 10.1086/425650. arXiv: astro-ph/0409154 [astro-ph].

[73] S. Corbel et al. "Radio/X-ray correlation in the low/hard state of GX 339-4". In: *A&A* 400 (Mar. 2003), pp. 1007–1012. DOI: 10.1051/0004-6361:20030090. arXiv: astro-ph/0301436 [astro-ph].

[74] S. Corbel et al. "The 'universal' radio/X-ray flux correlation: the case study of the black hole GX 339-4". In: *MNRAS* 428.3 (Jan. 2013), pp. 2500–2515. DOI: 10.1093/mnras/sts215. arXiv: 1211.1600 [astro-ph.HE].

[75] B. Cordier et al. "The SVOM gamma-ray burst mission". In: *arXiv e-prints*, arXiv:1512.03323 (Dec. 2015), arXiv:1512.03323. arXiv: 1512.03323 [astro-ph.IM].

[76] M. Coriat, R. P. Fender, and G. Dubus. "Revisiting a fundamental test of the disc instability model for X-ray binaries". In: *MNRAS* 424.3 (Aug. 2012), pp. 1991–2001. DOI: 10.1111/j.1365-2966.2012.21339.x. arXiv: 1205.5038 [astro-ph.HE].

[77] M. Coriat et al. "Radiatively efficient accreting black holes in the hard state: the case study of H1743-322". In: *MNRAS* 414.1 (June 2011), pp. 677–690. DOI: 10.1111/j.1365-2966.2011.18433.x. arXiv: 1101.5159 [astro-ph.HE].

[78] M. Coriat et al. "The infrared/X-ray correlation of GX 339-4: probing hard X-ray emission in accreting black holes". In: *MNRAS* 400.1 (Nov. 2009), pp. 123–133. DOI: 10.1111/j.1365-2966.2009.15461.x. arXiv: 0909.3283 [astro-ph.HE].

[79] M. Coriat et al. "The twisted jets of Circinus X-1". In: *MNRAS* 484.2 (Apr. 2019), pp. 1672–1686. DOI: 10.1093/mnras/stz099. arXiv: 1901.02631 [astro-ph.HE].

[80] Mickaël Coriat. "Jets relativistes des trous noirs accrétants". Thèse de doctorat dirigée par Corbel, Stéphane Astronomie et astrophysique Paris 7 2010. PhD thesis. 2010, 1 vol. (XVII–231 p.) URL: http://www.theses.fr/2010PA077257.

[81] J. M. Corral-Santana et al. "BlackCAT: A catalogue of stellar-mass black holes in X-ray transients". In: *A&A* 587, A61 (Mar. 2016), A61. DOI: 10.1051/0004-6361/201527130. arXiv: 1510.08869 [astro-ph.HE].

[82] Donald P. Cox. "The Three-Phase Interstellar Medium Revisited". In: *ARA&A* 43.1 (Sept. 2005), pp. 337–385. DOI: 10.1146/annurev.astro.43.072103.150615.

[83] P. A. Curran et al. "The evolving polarized jet of black hole candidate Swift J1745-26". In: *MNRAS* 437.4 (Feb. 2014), pp. 3265–3273. DOI: 10.1093/mnras/stt2125. arXiv: 1309.4926 [astro-ph.HE].

[84] H. D. Curtis. "Descriptions of 762 Nebulae and Clusters Photographed with the Crossley Reflector". In: *Publications of Lick Observatory* 13 (Jan. 1918), pp. 9–42.

[85] T. Dauser et al. "Irradiation of an accretion disc by a jet: general properties and implications for spin measurements of black holes". In: *MNRAS* 430.3 (Apr. 2013), pp. 1694–1708. DOI: 10.1093/mnras/sts710. arXiv: 1301.4922 [astro-ph.HE].

[86] Patrick Deegan, Céline Combet, and Graham A. Wynn. "The outburst duration and duty cycle of GRS1915+105". In: *MNRAS* 400.3 (Dec. 2009), pp. 1337–1346. DOI: 10.1111/j.1365-2966.2009.15573.x. arXiv: 0908.2566 [astro-ph.SR].

[87] D. Denisenko et al. "Optical counterpart of MAXI J1348-630". In: *The Astronomer's Telegram* 12430 (Jan. 2019), p. 1.

[88] V. Dhawan, W. M. Goss, and L. F. Rodríguez. "Small-Scale Structure in Galactic H I Absorption toward GRS 1915+105". In: *ApJ* 540.2 (Sept. 2000), pp. 863–868. DOI: 10.1086/309371.

[89] M. Díaz Trigo and L. Boirin. "Accretion disc atmospheres and winds in low-mass X-ray binaries". In: *Astronomische Nachrichten* 337.4-5 (May 2016), p. 368. DOI: 10.1002/asna.201612315. arXiv: 1510.03576 [astro-ph.HE].

[90] M. Díaz Trigo et al. "The evolving jet spectrum of the neutron star X-ray binary Aql X-1 in transitional states during its 2016 outburst". In: *A&A* 616, A23 (Aug. 2018), A23. DOI: 10.1051/0004-6361/201832693. arXiv: 1804.08322 [astro-ph.HE].

[91] T. Dinçer et al. "Complete Multiwavelength Evolution of Galactic Black Hole Transients during Outburst Decay. II. Compact Jets and X-Ray Variability Properties". In: *ApJ* 795.1, 74 (Nov. 2014), p. 74. DOI: 10.1088/0004-637X/795/1/74. arXiv: 1409.3239 [astro-ph.HE].

[92] Chris Done, Marek Gierliński, and Aya Kubota. "Modelling the behaviour of accretion flows in X-ray binaries. Everything you always wanted to know about accretion but were afraid to ask". In: *A&ARv* 15.1 (Dec. 2007), pp. 1–66. DOI: 10.1007/s00159-007-0006-1. arXiv: 0708.0148 [astro-ph].

[93] L. N. Driessen et al. "MKT J170456.2-482100: the first transient discovered by MeerKAT". In: *MNRAS* 491.1 (Jan. 2020), pp. 560–575. DOI: 10.1093/mnras/stz3027. arXiv: 1911.07713 [astro-ph.SR].

[94] G. Dubus, J. M. Hameury, and J. P. Lasota. "The disc instability model for X-ray transients: Evidence for truncation and irradiation". In: *A&A* 373 (July 2001), pp. 251–271. DOI: 10.1051/0004-6361:20010632. arXiv: astro-ph/0102237 [astro-ph].

[95] R. J. H. Dunn et al. "A global spectral study of black hole X-ray binaries". In: *MNRAS* 403.1 (Mar. 2010), pp. 61–82. DOI: 10.1111/j.1365-2966.2010.16114.x. arXiv: 0912.0142 [astro-ph.HE].

[96] A. Duquennoy and M. Mayor. "Multiplicity among solar-type stars in the solar neighbourhood. II - Distribution of the orbital elements in an unbiased sample." In: *A&A* 500 (Aug. 1991), pp. 337–376.

[97] S. S. Eikenberry et al. "Twenty Years of Timing SS 433". In: *ApJ* 561.2 (Nov. 2001), pp. 1027–1033. DOI: 10.1086/323380. arXiv: astro-ph/0107296 [astro-ph].

[98] Ann A. Esin, Jeffrey E. McClintock, and Ramesh Narayan. "Advection-Dominated Accretion and the Spectral States of Black Hole X-Ray Binaries: Application to Nova Muscae 1991". In: *ApJ* 489.2 (Nov. 1997), pp. 865–889. DOI: 10.1086/304829. arXiv: astro-ph/9705237 [astro-ph].

[99] M. Espinasse and R. Fender. "Spectral differences between the jets in 'radio-loud' and 'radio-quiet' hard-state black hole binaries". In: *MNRAS* 473.3 (Jan. 2018), pp. 4122–4129. DOI: 10.1093/mnras/stx2467. arXiv: 1709.07388 [astro-ph.HE].

[100] Mathilde Espinasse et al. "MeerKAT radio detection of MAXI J1803-298". In: *The Astronomer's Telegram* 14607 (May 2021), p. 1.

[101] Mathilde Espinasse et al. "Relativistic X-Ray Jets from the Black Hole X-Ray Binary MAXI J1820+070". In: *ApJ* 895.2, L31 (June 2020), p. L31. DOI: 10.3847/2041-8213/ab88b6. arXiv: 2004.06416 [astro-ph.HE].

[102] Event Horizon Telescope Collaboration et al. "First M87 Event Horizon Telescope Results. I. The Shadow of the Supermassive Black Hole". In: *ApJ* 875.1, L1 (Apr. 2019), p. L1. DOI: 10.3847/2041-8213/ab0ec7. arXiv: 1906.11238 [astro-ph.GA].

[103] H. Falcke and P. L. Biermann. "Galactic jet sources and the AGN connection." In: *A&A* 308 (Apr. 1996), pp. 321–329. arXiv: astro-ph/9506138 [astro-ph].

[104] H. Falcke, E. Körding, and S. Markoff. "A scheme to unify low-power accreting black holes. Jet-dominated accretion flows and the radio/X-ray correlation". In: *A&A* 414 (Feb. 2004), pp. 895–903. DOI: 10.1051/0004-6361:20031683. arXiv: astro-ph/0305335 [astro-ph].

[105] R. Fender et al. "ThunderKAT: The MeerKAT Large Survey Project for Image-Plane Radio Transients". In: *arXiv e-prints*, arXiv:1711.04132 (Nov. 2017), arXiv:1711.04132. arXiv: 1711.04132 [astro-ph.HE].

[106] R. P. Fender. "Powerful jets from black hole X-ray binaries in low/hard X-ray states". In: *MNRAS* 322.1 (Mar. 2001), pp. 31–42. DOI: 10.1046/j.1365-8711.2001.04080.x. arXiv: astro-ph/0008447 [astro-ph].

[107] R. P. Fender. "Uses and limitations of relativistic jet proper motions: lessons from Galactic microquasars". In: *MNRAS* 340.4 (Apr. 2003), pp. 1353–1358. DOI: 10.1046/j.1365-8711.2003.06386.x. arXiv: astro-ph/0301225 [astro-ph].

[108] R. P. Fender, T. M. Belloni, and E. Gallo. "Towards a unified model for black hole X-ray binary jets". In: *MNRAS* 355.4 (Dec. 2004), pp. 1105–1118. DOI: 10.1111/j.1365-2966.2004.08384.x. arXiv: astro-ph/0409360 [astro-ph].

[109] R. P. Fender, J. Homan, and T. M. Belloni. "Jets from black hole X-ray binaries: testing, refining and extending empirical models for the coupling to X-rays". In: *MNRAS* 396.3 (July 2009), pp. 1370–1382. DOI: 10.1111/j.1365-2966.2009.14841.x. arXiv: 0903.5166 [astro-ph.HE].

[110] R. P. Fender, T. J. Maccarone, and Z. van Kesteren. "Energization of interstellar media and cosmic ray production by jets from X-ray binaries". In: *MNRAS* 360.3 (July 2005), pp. 1085–1090. DOI: 10.1111/j.1365-2966.2005.09098.x. arXiv: astro-ph/0504205 [astro-ph].

[111] R. P. Fender and G. G. Pooley. "Infrared synchrotron oscillations in GRS 1915+105". In: *MNRAS* 300.2 (Oct. 1998), pp. 573–576. DOI: 10.1046/j.1365-8711.1998.01921.x. arXiv: astro-ph/9806073 [astro-ph].

[112] R. P. Fender et al. "A transient relativistic radio jet from Cygnus X-1". In: *MNRAS* 369.2 (June 2006), pp. 603–607. DOI: 10.1111/j.1365-2966.2006.10193.x. arXiv: astro-ph/0602307 [astro-ph].

[113] R. P. Fender et al. "Cygnus X-3 in outburst: quenched radio emission, radiation losses and variable local opacity". In: *MNRAS* 288.4 (July 1997), pp. 849–858. DOI: 10.1093/mnras/288.4.849. arXiv: astro-ph/9612125 [astro-ph].

[114] R. P. Fender et al. "MERLIN observations of relativistic ejections from GRS 1915+105". In: *Monthly Notices of the Royal Astronomical Society* 304.4 (Apr. 1999), pp. 865–876. ISSN: 0035-8711. DOI: 10.1046/j.1365-8711.1999.02364.x. eprint: https://academic.oup.com/mnras/article-pdf/304/4/865/3567073/304-4-865.pdf. URL: https://doi.org/10.1046/j.1365-8711.1999.02364.x.

[115] Rob Fender. "Jets from X-ray binaries". In: *Compact stellar X-ray sources*. Vol. 39. 2006, pp. 381–419.

[116] Rob Fender and Joe Bright. "Synchrotron self-absorption and the minimum energy of optically thick radio flares from stellar mass black holes". In: *MNRAS* 489.4 (Nov. 2019), pp. 4836–4846. DOI: 10.1093/mnras/stz2000. arXiv: 1907.07463 [astro-ph.HE].

[117] Rob Fender and Teo Muñoz-Darias. "The Balance of Power: Accretion and Feedback in Stellar Mass Black Holes". In: *Lecture Notes in Physics, Berlin Springer Verlag*. Ed. by Francesco Haardt et al. Vol. 905. 2016, p. 65. DOI: 10.1007/978-3-319-19416-5_3.

[118] J. Ferreira et al. "A unified accretion-ejection paradigm for black hole X-ray binaries. I. The dynamical constituents". In: *A&A* 447.3 (Mar. 2006), pp. 813–825. DOI: 10.1051/0004-6361:20052689. arXiv: astro-ph/0511123 [astro-ph].

[119] Katia M. Ferrière. "The interstellar environment of our galaxy". In: *Reviews of Modern Physics* 73.4 (Oct. 2001), pp. 1031–1066. DOI: 10.1103/RevModPhys.73.1031. arXiv: astro-ph/0106359 [astro-ph].

[120] E. B. Fomalont, B. J. Geldzahler, and C. F. Bradshaw. "Scorpius X-1: Energy Transfer from the Core to the Radio Lobes". In: *ApJ* 553.1 (May 2001), pp. L27–L30. DOI: 10.1086/320490. arXiv: astro-ph/0104325 [astro-ph].

[121] Daniel Foreman-Mackey. "corner.py: Scatterplot matrices in Python". In: *The Journal of Open Source Software* 1 (June 2016), p. 24. DOI: 10.21105/joss.00024.

[122] Daniel Foreman-Mackey et al. "emcee: The MCMC Hammer". In: *PASP* 125.925 (Mar. 2013), p. 306. DOI: 10.1086/670067. arXiv: 1202.3665 [astro-ph.IM].

[123] Juhan Frank, Andrew King, and Derek J. Raine. *Accretion Power in Astrophysics: Third Edition*. 2002.

[124] Robert H. Frater, John W. Brooks, and John B. Whiteoak. "The Australia Telescope - Overview". In: *Journal of Electrical and Electronics Engineering Australia* 12.2 (June 1992), pp. 103–112.

[125] Y. Fuchs, L. Koch Miramond, and P. Ábrahám. "SS 433: a phenomenon imitating a Wolf-Rayet star". In: *A&A* 445.3 (Jan. 2006), pp. 1041–1052. DOI: 10.1051/0004-6361:20042160. arXiv: astro-ph/0512190 [astro-ph].

[126] B. M. Gaensler, A. J. Green, and R. N. Manchester. "G309.2-00.6 and jets in supernova remnants". In: *MNRAS* 299.3 (Sept. 1998), pp. 812–824. DOI: 10.1046/j.1365-8711.1998.01814.x. arXiv: astro-ph/9805163 [astro-ph].

[127] B. M. Gaensler et al. "A Stellar Wind Bubble Coincident with the Anomalous X-Ray Pulsar 1E 1048.1-5937: Are Magnetars Formed from Massive Progenitors?" In: *ApJ* 620.2 (Feb. 2005), pp. L95–L98. DOI: 10.1086/428725. arXiv: astro-ph/0501563 [astro-ph].

[128] Gaia Collaboration et al. "Gaia Data Release 2. Summary of the contents and survey properties". In: *A&A* 616, A1 (Aug. 2018), A1. DOI: 10.1051/0004-6361/201833051. arXiv: 1804.09365 [astro-ph.GA].

[129] E. Gallo, R. P. Fender, and G. G. Pooley. "A universal radio-X-ray correlation in low/hard state black hole binaries". In: *MNRAS* 344.1 (Sept. 2003), pp. 60–72. DOI: 10.1046/j.1365-8711.2003.06791.x. arXiv: astro-ph/0305231 [astro-ph].

[130] E. Gallo et al. "A radio-emitting outflow in the quiescent state of A0620-00: implications for modelling low-luminosity black hole binaries". In: *MNRAS* 370.3 (Aug. 2006), pp. 1351–1360. DOI: 10.1111/j.1365-2966.2006.10560.x. arXiv: astro-ph/0605376 [astro-ph].

[131] E. Gallo et al. "A transient large-scale relativistic radio jet from GX 339-4". In: *MNRAS* 347.3 (Jan. 2004), pp. L52–L56. DOI: 10.1111/j.1365-2966.2004.07435.x. arXiv: astro-ph/0311452 [astro-ph].

[132] E. Gallo et al. "The radio/X-ray domain of black hole X-ray binaries at the lowest radio luminosities". In: *MNRAS* 445.1 (Nov. 2014), pp. 290–300. DOI: 10.1093/mnras/stu1599. arXiv: 1408.3130 [astro-ph.HE].

[133] Elena Gallo, Nathalie Degenaar, and Jakob van den Eijnden. "Hard state neutron star and black hole X-ray binaries in the radio:X-ray luminosity plane". In: *MNRAS* 478.1 (July 2018), pp. L132–L136. DOI: 10.1093/mnrasl/sly083. arXiv: 1805.01905 [astro-ph.HE].

[134] Elena Gallo et al. "A dark jet dominates the power output of the stellar black hole Cygnus X-1". In: *Nature* 436.7052 (Aug. 2005), pp. 819–821. DOI: 10.1038/nature03879. arXiv: astro-ph/0508228 [astro-ph].

[135] Elena Gallo et al. "ALMA observations of A0620-00: fresh clues on the nature of quiescent black hole X-ray binary jets". In: *MNRAS* 488.1 (Sept. 2019), pp. 191–197. DOI: 10.1093/mnras/stz1634. arXiv: 1906.04299 [astro-ph.HE].

[136] P. Gandhi et al. "An elevation of 0.1 light-seconds for the optical jet base in an accreting Galactic black hole system". In: *Nature Astronomy* 1 (Oct. 2017), pp. 859–864. DOI: 10.1038/s41550-017-0273-3. arXiv: 1710.09838 [astro-ph.HE].

[137] Federico García et al. "A two-component Comptonization model for the type-B QPO in MAXI J1348-630". In: *MNRAS* 501.3 (Mar. 2021), pp. 3173–3182. DOI: 10.1093/mnras/staa3944. arXiv: 2012.10354 [astro-ph.HE].

[138] J. García et al. "X-Ray Reflected Spectra from Accretion Disk Models. III. A Complete Grid of Ionized Reflection Calculations". In: *ApJ* 768.2, 146 (May 2013), p. 146. DOI: 10.1088/0004-637X/768/2/146. arXiv: 1303.2112 [astro-ph.HE].

[139] R. Gathier, S. R. Pottasch, and W. M. Goss. "Distances to planetary nebulae. II. HI absorption observations." In: *A&A* 157 (Mar. 1986), pp. 191–203.

[140] N. Gehrels et al. "The Swift Gamma-Ray Burst Mission". In: *ApJ* 611.2 (Aug. 2004), pp. 1005–1020. DOI: 10.1086/422091. arXiv: astro-ph/0405233 [astro-ph].

[141] A. Gelman, G. O. Roberts, and W. R. Gilks. "Efficient Metropolis jumping rules". In: *Bayesian Statistics*. Ed. by J. M. Bernardo et al. Oxford University Press, Oxford, 1996, pp. 599–608.

[142] G. Ghisellini, F. Tavecchio, and M. Chiaberge. "Structured jets in TeV BL Lac objects and radiogalaxies. Implications for the observed properties". In: *A&A* 432.2 (Mar. 2005), pp. 401–410. DOI: 10.1051/0004-6361:20041404. arXiv: astro-ph/0406093 [astro-ph].

[143] Riccardo Giacconi et al. "Evidence for x Rays From Sources Outside the Solar System". In: *Phys. Rev. Lett.* 9.11 (Dec. 1962), pp. 439–443. DOI: 10.1103/PhysRevLett.9.439.

[144] D. R. Gies and C. T. Bolton. "The Optical Spectrum of HDE 226868=Cygnus X-1. II. Spectrophotometry and Mass Estimates". In: *ApJ* 304 (May 1986), p. 371. DOI: 10.1086/164171.

[145] José L. Gómez et al. "Faraday Rotation and Polarization Gradients in the Jet of 3C 120: Interaction with the External Medium and a Helical Magnetic Field?" In: *ApJ* 681.2 (July 2008), p. L69. DOI: 10.1086/590388. arXiv: 0805.4797 [astro-ph].

[146] Jonathan Goodman and Jonathan Weare. "Ensemble samplers with affine invariance". In: *Communications in Applied Mathematics and Computational Science* 5.1 (Jan. 2010), pp. 65–80. DOI: 10.2140/camcos.2010.5.65.

[147] P. C. Gregory and P. P. Kronberg. "Discovery of Giant Radio Outburst from Cygnus X-3". In: *Nature* 239.5373 (Oct. 1972), pp. 440–443. DOI: 10.1038/239440a0.

[148] F. Haardt and L. Maraschi. "A Two-Phase Model for the X-Ray Emission from Seyfert Galaxies". In: *ApJ* 380 (Oct. 1991), p. L51. DOI: 10.1086/186171.

[149] Francesco Haardt and Laura Maraschi. "X-Ray Spectra from Two-Phase Accretion Disks". In: *ApJ* 413 (Aug. 1993), p. 507. DOI: 10.1086/173020.

[150] Jean-Marie Hameury, Jean-Pierre Lasota, and Brian Warner. "The zoo of dwarf novae: illumination, evaporation and disc radius variation". In: *A&A* 353 (Jan. 2000), pp. 244–252. arXiv: astro-ph/9911124 [astro-ph].

[151] D. C. Hannikainen et al. "MOST radio monitoring of GX 339-4". In: *A&A* 337 (Sept. 1998), pp. 460–464. arXiv: astro-ph/9805332 [astro-ph].

[152] J. F. Hao and S. N. Zhang. "Large-scale Cavities Surrounding Microquasars Inferred from Evolution of Their Relativistic Jets". In: *ApJ* 702.2 (Sept. 2009), pp. 1648–1661. DOI: 10.1088/0004-637X/702/2/1648. arXiv: 0907.3849 [astro-ph.HE].

[153] L. M. Heil, P. Uttley, and M. Klein-Wolt. "Inclination-dependent spectral and timing properties in transient black hole X-ray binaries". In: *MNRAS* 448.4 (Apr. 2015), pp. 3348–3353. DOI: 10.1093/mnras/stv240. arXiv: 1405.2026 [astro-ph.HE].

[154] S. Heinz. "Composition, Collimation, Contamination: The Jet of Cygnus X-1". In: *ApJ* 636.1 (Jan. 2006), pp. 316–322. DOI: 10.1086/497954. arXiv: astro-ph/0509777 [astro-ph].

[155] S. Heinz. "Radio lobe dynamics and the environment of microquasars". In: *A&A* 388 (June 2002), pp. L40–L43. DOI: 10.1051/0004-6361:20020402. arXiv: astro-ph/0203295 [astro-ph].

[156] S. Heinz and R. A. Sunyaev. "The non-linear dependence of flux on black hole mass and accretion rate in core-dominated jets". In: *MNRAS* 343.3 (Aug. 2003), pp. L59–L64. DOI: 10.1046/j.1365-8711.2003.06918.x. arXiv: astro-ph/0305252 [astro-ph].

[157] S. Heinz and R. A. Sunyaev. "The non-linear dependence of flux on black hole mass and accretion rate in core-dominated jets". In: *MNRAS* 343.3 (Aug. 2003), pp. L59–L64. DOI: 10.1046/j.1365-8711.2003.06918.x. arXiv: astro-ph/0305252 [astro-ph].

[158] S. Heinz et al. "Blazing Trails: Microquasars as Head-Tail Sources and the Seeding of Magnetized Plasma into the ISM". In: *ApJ* 686.2 (Oct. 2008), pp. 1145–1154. DOI: 10.1086/591435. arXiv: 0808.1927 [astro-ph].

[159] S. Heinz et al. "Evidence of a Parsec-Scale X-Ray Jet from the Accreting Neutron Star Circinus X-1". In: *ApJ* 663.2 (July 2007), pp. L93–L96. DOI: 10.1086/519950. arXiv: 0706.3881 [astro-ph].

[160] R. M. Hjellming and K. J. Johnston. "An analysis of the proper motions of SS 433 radio jets." In: *ApJ* 246 (June 1981), pp. L141–L145. DOI: 10.1086/183571.

[161] R. M. Hjellming and K. J. Johnston. "Radio Emission from Conical Jets Associated with X-Ray Binaries". In: *ApJ* 328 (May 1988), p. 600. DOI: 10.1086/166318.

[162] R. M. Hjellming and M. P. Rupen. "Episodic ejection of relativistic jets by the X-ray transient GRO J1655 - 40". In: *Nature* 375.6531 (June 1995), pp. 464–468. DOI: 10.1038/375464a0.

[163] R. M. Hjellming and C. M. Wade. "Radio Emission from X-Ray Sources". In: *ApJ* 168 (Aug. 1971), p. L21. DOI: 10.1086/180777.

[164] R. M. Hjellming and C. M. Wade. "The Radio Sources Associated with Scorpius X-1". In: *ApJ* 164 (Feb. 1971), p. L1. DOI: 10.1086/180680.

[165] J. A. Högbom. "Aperture Synthesis with a Non-Regular Distribution of Interferometer Baselines". In: *A&AS* 15 (June 1974), p. 417.

[166] Jeroen Homan and Tomaso Belloni. "The Evolution of Black Hole States". In: *Ap&SS* 300.1-3 (Nov. 2005), pp. 107–117. DOI: 10.1007/s10509-005-1197-4. arXiv: astro-ph/0412597 [astro-ph].

[167] Jeroen Homan et al. "A Rapid Change in X-Ray Variability and a Jet Ejection in the Black Hole Transient MAXI J1820+070". In: *ApJ* 891.2, L29 (Mar. 2020), p. L29. DOI: 10.3847/2041-8213/ab7932. arXiv: 2003.01012 [astro-ph.HE].

[168] Jeroen Homan et al. "Correlated X-Ray Spectral and Timing Behavior of the Black Hole Candidate XTE J1550-564: A New Interpretation of Black Hole States". In: *ApJS* 132.2 (Feb. 2001), pp. 377–402. DOI: 10.1086/318954. arXiv: astro-ph/0001163 [astro-ph].

[169] Jeroen Homan et al. "The X-Ray Properties of the Black Hole Transient MAXI J1659-152 in Quiescence". In: *ApJ* 775.1, 9 (Sept. 2013), p. 9. DOI: 10.1088/0004-637X/775/1/9. arXiv: 1308.2580 [astro-ph.HE].

[170] A. W. Hotan et al. "The Australian Square Kilometre Array Pathfinder: System Architecture and Specifications of the Boolardy Engineering Test Array". In: *Publ. Astron. Soc. Australia* 31, e041 (Nov. 2014), e041. DOI: 10.1017/pasa.2014.36. arXiv: 1409.1325 [astro-ph.IM].

[171] Chang-Yin Huang, Qingwen Wu, and Ding-Xiong Wang. "Modelling the 'outliers' track of the radio-X-ray correlation in X-ray binaries based on a disc-corona model". In: *MNRAS* 440.2 (Apr. 2014), pp. 965–970. ISSN: 0035-8711. DOI: 10.1093/mnras/stu364. eprint: https://academic.oup.com/mnras/article-pdf/440/2/965/18501366/stu364.pdf. URL: https://doi.org/10.1093/mnras/stu364.

[172] Y. F. Huang, Z. G. Dai, and T. Lu. "A generic dynamical model of gamma-ray burst remnants". In: *MNRAS* 309.2 (Oct. 1999), pp. 513–516. ISSN: 0035-8711. DOI: 10.1046/j.1365-8711.1999.02887.x. eprint: https://academic.oup.com/mnras/article-pdf/309/2/513/3441313/309-2-513.pdf. URL: https://doi.org/10.1046/j.1365-8711.1999.02887.x.

[173] S. Ichimaru. "Bimodal behavior of accretion disks: theory and application to Cygnus X-1 transitions." In: *ApJ* 214 (June 1977), pp. 840–855. DOI: 10.1086/155314.

[174] Adam R. Ingram and Sara E. Motta. "A review of quasi-periodic oscillations from black hole X-ray binaries: Observation and theory". In: *New Astron. Rev.* 85, 101524 (Sept. 2019), p. 101524. DOI: 10.1016/j.newar.2020.101524.

[175] Amir Jafari. "Magnetic Fields in Accretion Disks: A Review". In: *arXiv e-prints*, arXiv:1904.09677 (Apr. 2019), arXiv:1904.09677. arXiv: 1904.09677 [astro-ph.HE].

[176] O. Jamil, R. P. Fender, and C. R. Kaiser. "iShocks: X-ray binary jets with an internal shocks model". In: *MNRAS* 401.1 (Jan. 2010), pp. 394–404. DOI: 10.1111/j.1365-2966.2009.15652.x. arXiv: 0909.1309 [astro-ph.HE].

[177] J. Jonas and MeerKAT Team. "The MeerKAT Radio Telescope". In: *MeerKAT Science: On the Pathway to the SKA*. Jan. 2016, p. 1.

[178] P. G. Jonker and G. Nelemans. "The distances to Galactic low-mass X-ray binaries: consequences for black hole luminosities and kicks". In: *MNRAS* 354.2 (Oct. 2004), pp. 355–366. DOI: 10.1111/j.1365-2966.2004.08193.x. arXiv: astro-ph/0407168 [astro-ph].

[179] P. G. Jonker et al. "Following the 2008 outburst decay of the black hole candidate H 1743-322in X-ray and radio". In: *MNRAS* 401.2 (Jan. 2010), pp. 1255–1263. DOI: 10.1111/j.1365-2966.2009.15717.x. arXiv: 0909.2632 [astro-ph.HE].

[180] P. G. Jonker et al. "The black hole candidate MAXI J1659-152 in and towards quiescence in X-ray and radio". In: *MNRAS* 423.4 (July 2012), pp. 3308–3315. DOI: 10.1111/j.1365-2966.2012.21116.x. arXiv: 1204.4832 [astro-ph.HE].

[181] P. Kaaret et al. "Evolution of the X-Ray Jets from 4U 1755-33". In: *ApJ* 641.1 (Apr. 2006), pp. 410–417. DOI: 10.1086/500399. arXiv: astro-ph/0512240 [astro-ph].

[182] P. Kaaret et al. "X-Ray Emission from the Jets of XTE J1550-564". In: *The Astrophysical Journal* 582.2 (Jan. 2003), pp. 945–953. DOI: 10.1086/344540. URL: https://doi.org/10.1086/344540.

[183] Philip Kaaret, Hua Feng, and Timothy P. Roberts. "Ultraluminous X-Ray Sources". In: *Annual Review of Astronomy and Astrophysics* 55.1 (2017), pp. 303–341. DOI: 10.1146/annurev-astro-091916-055259. eprint: https://doi.org/10.1146/annurev-astro-091916-055259. URL: https://doi.org/10.1146/annurev-astro-091916-055259.

[184] C. R. Kaiser. "The flat synchrotron spectra of partially self-absorbed jets revisited". In: *MNRAS* 367.3 (Apr. 2006), pp. 1083–1094. DOI: 10.1111/j.1365-2966.2006.10030.x. arXiv: astro-ph/0601103 [astro-ph].

[185] C. R. Kaiser, R. Sunyaev, and H. C. Spruit. "Internal shock model for microquasars". In: *A&A* 356 (Apr. 2000), pp. 975–988. arXiv: astro-ph/0001501 [astro-ph].

[186] Christian R. Kaiser et al. "Revision of the Properties of the GRS 1915+105 Jets: Clues from the Large-Scale Structure". In: *ApJ* 612.1 (Sept. 2004), pp. 332–341. DOI: 10.1086/422466. arXiv: astro-ph/0405206 [astro-ph].

[187] E. Kalemci et al. "Complete Multiwavelength Evolution of Galactic Black Hole Transients during Outburst Decay. I. Conditions for "Compact" Jet Formation". In: *ApJ* 779.2, 95 (Dec. 2013), p. 95. DOI: 10.1088/0004-637X/779/2/95. arXiv: 1310.5482 [astro-ph.HE].

[188] Vassiliki Kalogera and Gordon Baym. "The Maximum Mass of a Neutron Star". In: *ApJ* 470 (Oct. 1996), p. L61. DOI: 10.1086/310296. arXiv: astro-ph/9608059 [astro-ph].

[189] J. A. Kennea and H. Negoro. "MAXI J1348-630: Swift XRT localization, possible periodicity". In: *The Astronomer's Telegram* 12434 (Jan. 2019), p. 1.

[190] Karri I. I. Koljonen and David M. Russell. "The Radio/X-Ray Correlation in X-Ray Binaries—Insights from a Hard X-Ray Perspective". In: *ApJ* 871.1, 26 (Jan. 2019), p. 26. DOI: 10.3847/1538-4357/aaf38f. arXiv: 1811.08650 [astro-ph.HE].

[191] B. Koribalski et al. "HI Line Measurements of Eight Southern Pulsars". In: *ApJ* 441 (Mar. 1995), p. 756. DOI: 10.1086/175397.

[192] Taro Kotani et al. "Iron-Line Diagnostics of the Jets of SS 433". In: *PASJ* 48 (Aug. 1996), pp. 619–629. DOI: 10.1093/pasj/48.4.619.

[193] G. Lamer et al. "A giant X-ray dust scattering ring discovered with SRG/eROSITA around the black hole transient MAXI J1348-630". In: *A&A* 647, A7 (Mar. 2021), A7. DOI: 10.1051/0004-6361/202039757.

[194] Jean-Pierre Lasota. "The disc instability model of dwarf novae and low-mass X-ray binary transients". In: *New Astron. Rev.* 45.7 (June 2001), pp. 449–508. DOI: 10.1016/S1387-6473(01)00112-9. arXiv: astro-ph/0102072 [astro-ph].

[195] H. N. Latter and J. C. B. Papaloizou. "Hysteresis and thermal limit cycles in MRI simulations of accretion discs". In: *MNRAS* 426.2 (Oct. 2012), pp. 1107–1120. DOI: 10.1111/j.1365-2966.2012.21748.x. arXiv: 1207.4727 [astro-ph.HE].

[196] Walter H. G. Lewin, Jan van Paradijs, and Edward Peter Jacobus van den Heuvel. *X-ray Binaries*. 1997.

[197] Hao Liu et al. "Evolution of the hard X-ray photon index in black-hole X-ray binaries: hints for accretion physics". In: *MNRAS* 487.4 (Aug. 2019), pp. 5335–5345. DOI: 10.1093/mnras/stz1622.

[198] Alan Loh. "Évènements Explosifs dans le Ciel Transitoire". Theses. Université Paris Diderot (Paris 7), Sept. 2016. URL: https://tel.archives-ouvertes.fr/tel-01499666.

[199] M.S. Longair. *High Energy Astrophysics*. Cambridge University Press, 2011. ISBN: 9781139494540.

[200] T. J. Maccarone. "Do X-ray binary spectral state transition luminosities vary?" In: *A&A* 409 (Oct. 2003), pp. 697–706. DOI: 10.1051/0004-6361:20031146. arXiv: astro-ph/0308036 [astro-ph].

[201] Thomas J. Maccarone. "On the misalignment of jets in microquasars". In: *MNRAS* 336.4 (Nov. 2002), pp. 1371–1376. DOI: 10.1046/j.1365-8711.2002.05876.x. arXiv: astro-ph/0209105 [astro-ph].

[202] Thomas J. Maccarone et al. "The stringent upper limit on jet power in the persistent soft-state source 4U 1957+11". In: *MNRAS* 498.1 (July 2020), pp. L40–L45. DOI: 10.1093/mnrasl/slaa120. arXiv: 2007.00834 [astro-ph.HE].

[203] J. Malzac. "Internal shocks at the origin of the flat spectral energy distribution of compact jets." In: *MNRAS* 429 (Feb. 2013), pp. L20–L24. DOI: 10.1093/mnrasl/sls017. arXiv: 1210.4308 [astro-ph.HE].

[204] Julien Malzac et al. "A jet model for the fast IR variability of the black hole X-ray binary GX 339-4". In: *MNRAS* 480.2 (Oct. 2018), pp. 2054–2071. DOI: 10.1093/mnras/sty2006. arXiv: 1807.09835 [astro-ph.HE].

[205] G. Marcel et al. "A unified accretion-ejection paradigm for black hole X-ray binaries. II. Observational signatures of jet-emitting disks". In: *A&A* 615, A57 (July 2018), A57. DOI: 10.1051/0004-6361/201732069. arXiv: 1803.04335 [astro-ph.HE].

[206] G. Marcel et al. "A unified accretion-ejection paradigm for black hole X-ray binaries. III. Spectral signatures of hybrid disk configurations". In: *A&A* 617, A46 (Sept. 2018), A46. DOI: 10.1051/0004-6361/201833124. arXiv: 1805.12407 [astro-ph.HE].

[207] G. Marcel et al. "A unified accretion-ejection paradigm for black hole X-ray binaries. IV. Replication of the 2010-2011 activity cycle of GX 339-4". In: *A&A* 626, A115 (June 2019), A115. DOI: 10.1051/0004-6361/201935060. arXiv: 1905.05057 [astro-ph.HE].

[208] Bruce Margon. "Observations of SS 433". In: *ARA&A* 22 (Jan. 1984), pp. 507–536. DOI: 10.1146/annurev.aa.22.090184.002451.

[209] S. Markoff, H. Falcke, and R. Fender. "A jet model for the broadband spectrum of XTE J1118+480. Synchrotron emission from radio to X-rays in the Low/Hard spectral state". In: *A&A* 372 (June 2001), pp. L25–L28. DOI: 10.1051/0004-6361:20010420. arXiv: astro-ph/0010560 [astro-ph].

[210] S. Markoff et al. "Exploring the role of jets in the radio/X-ray correlations of GX 339-4". In: *A&A* 397 (Jan. 2003), pp. 645–658. DOI: 10.1051/0004-6361:20021497. arXiv: astro-ph/0210439 [astro-ph].

[211] Sera Markoff and Michael A. Nowak. "Constraining X-Ray Binary Jet Models via Reflection". In: *ApJ* 609.2 (July 2004), pp. 972–976. DOI: 10.1086/421099. arXiv: astro-ph/0403468 [astro-ph].

[212] Sera Markoff, Michael A. Nowak, and Jörn Wilms. "Going with the Flow: Can the Base of Jets Subsume the Role of Compact Accretion Disk Coronae?" In: *ApJ* 635.2

(Dec. 2005), pp. 1203–1216. DOI: 10.1086/497628. arXiv: astro-ph/0509028 [astro-ph].

[213] Alan P. Marscher et al. "Observational evidence for the accretion-disk origin for a radio jet in an active galaxy". In: *Nature* 417.6889 (June 2002), pp. 625–627. DOI: 10.1038/nature00772.

[214] J. Martí et al. "Radio images of the microquasar GRS 1758-258". In: *A&A* 386 (May 2002), pp. 571–575. DOI: 10.1051/0004-6361:20020273.

[215] Josep Marti et al. "A galactic microquasar mimicking winged radio galaxies". In: *Nature Communications* 8 (Dec. 2017). DOI: 10.1038/s41467-017-01976-5.

[216] I. Martí-Vidal et al. "UVMULTIFIT: A versatile tool for fitting astronomical radio interferometric data". In: *A&A* 563, A136 (Mar. 2014), A136. DOI: 10.1051/0004-6361/201322633. arXiv: 1401.4984 [astro-ph.IM].

[217] Masaru Matsuoka et al. "The MAXI Mission on the ISS: Science and Instruments for Monitoring All-Sky X-Ray Images". In: *PASJ* 61 (Oct. 2009), p. 999. DOI: 10.1093/pasj/61.5.999. arXiv: 0906.0631 [astro-ph.IM].

[218] T. Mauch et al. "The 1.28 GHz MeerKAT DEEP2 Image". In: *ApJ* 888.2, 61 (Jan. 2020), p. 61. DOI: 10.3847/1538-4357/ab5d2d. arXiv: 1912.06212 [astro-ph.GA].

[219] Jeffrey E. McClintock and Ronald A. Remillard. "Black hole binaries". In: *Compact stellar X-ray sources*. Vol. 39. 2006, pp. 157–213.

[220] Jeffrey E. McClintock et al. "The 2003 Outburst of the X-Ray Transient H1743-322: Comparisons with the Black Hole Microquasar XTE J1550-564". In: *ApJ* 698.2 (June 2009), pp. 1398–1421. DOI: 10.1088/0004-637X/698/2/1398. arXiv: 0705.1034 [astro-ph].

[221] Jonathan C. McKinney. "General relativistic magnetohydrodynamic simulations of the jet formation and large-scale propagation from black hole accretion systems". In: *MNRAS* 368.4 (June 2006), pp. 1561–1582. DOI: 10.1111/j.1365-2966.2006.10256.x. arXiv: astro-ph/0603045 [astro-ph].

[222] J. P. McMullin et al. "CASA Architecture and Applications". In: *Astronomical Data Analysis Software and Systems XVI*. Ed. by R. A. Shaw, F. Hill, and D. J. Bell. Vol. 376. Astronomical Society of the Pacific Conference Series. Oct. 2007, p. 127.

[223] Kristen Menou et al. "Black Hole and Neutron Star Transients in Quiescence". In: *ApJ* 520.1 (July 1999), pp. 276–291. DOI: 10.1086/307443. arXiv: astro-ph/9810323 [astro-ph].

[224] A. Merloni et al. "eROSITA Science Book: Mapping the Structure of the Energetic Universe". In: *arXiv e-prints*, arXiv:1209.3114 (Sept. 2012), arXiv:1209.3114. arXiv: 1209.3114 [astro-ph.HE].

[225] Andrea Merloni, Sebastian Heinz, and Tiziana di Matteo. "A Fundamental Plane of black hole activity". In: *MNRAS* 345.4 (Nov. 2003), pp. 1057–1076. DOI: 10.1046/j.1365-2966.2003.07017.x. arXiv: astro-ph/0305261 [astro-ph].

[226] P. Mészáros. "Gamma-ray bursts". In: *Reports on Progress in Physics* 69.8 (Aug. 2006), pp. 2259–2321. DOI: 10.1088/0034-4885/69/8/R01. arXiv: astro-ph/0605208 [astro-ph].

[227] P. Mészáros and M. J. Rees. "Optical and Long-Wavelength Afterglow from Gamma-Ray Bursts". In: *ApJ* 476.1 (Feb. 1997), pp. 232–237. DOI: 10.1086/303625. arXiv: astro-ph/9606043 [astro-ph].

[228] Nicholas Metropolis et al. "Equation of State Calculations by Fast Computing Machines". In: *J. Chem. Phys.* 21.6 (June 1953), pp. 1087–1092. DOI: 10.1063/1.1699114.

[229] F. Meyer and E. Meyer-Hofmeister. "On the elusive cause of cataclysmic variable outbursts." In: *A&A* 104 (Jan. 1981), pp. L10–L12.

[230] E. Meyer-Hofmeister and F. Meyer. "The relation between radio and X-ray luminosity of black hole binaries: affected by inner cool disks?" In: *A&A* 562, A142 (Feb. 2014), A142. DOI: 10.1051/0004-6361/201322423. arXiv: 1401.7525 [astro-ph.HE].

[231] S. Migliari and R. P. Fender. "Jets in neutron star X-ray binaries: a comparison with black holes". In: *MNRAS* 366.1 (Feb. 2006), pp. 79–91. DOI: 10.1111/j.1365-2966.2005.09777.x. arXiv: astro-ph/0510698 [astro-ph].

[232] S. Migliari and R. P. Fender. "Jets in neutron star X-ray binaries: a comparison with black holes". In: *MNRAS* 366.1 (Feb. 2006), pp. 79–91. DOI: 10.1111/j.1365-2966.2005.09777.x. arXiv: astro-ph/0510698 [astro-ph].

[233] Simone Migliari, Rob Fender, and Mariano Méndez. "Iron Emission Lines from Extended X-ray Jets in SS 433: Reheating of Atomic Nuclei". In: *Science* 297.5587 (Sept. 2002), pp. 1673–1676. DOI: 10.1126/science.1073660. arXiv: astro-ph/0209131 [astro-ph].

[234] Giulia Migliori et al. "Evolving morphology of the large-scale relativistic jets from XTE J1550-564". In: *MNRAS* 472.1 (Nov. 2017), pp. 141–165. DOI: 10.1093/mnras/stx1864. arXiv: 1707.06876 [astro-ph.HE].

[235] J. M. Miller et al. "Simultaneous Chandra and RXTE Spectroscopy of the Microquasar H1743-322: Clues to Disk Wind and Jet Formation from a Variable Ionized Outflow".

In: *ApJ* 646.1 (July 2006), pp. 394–406. DOI: 10.1086/504673. arXiv: astro-ph/0406272 [astro-ph].

[236] J. C. A. Miller-Jones, R. P. Fender, and E. Nakar. "Opening angles, Lorentz factors and confinement of X-ray binary jets". In: *MNRAS* 367.4 (Apr. 2006), pp. 1432–1440. DOI: 10.1111/j.1365-2966.2006.10092.x. arXiv: astro-ph/0601482 [astro-ph].

[237] J. C. A. Miller-Jones et al. "A Deep Radio Survey of Hard State and Quiescent Black Hole X-Ray Binaries". In: *ApJ* 739.1, L18 (Sept. 2011), p. L18. DOI: 10.1088/2041-8205/739/1/L18. arXiv: 1106.0097 [astro-ph.HE].

[238] J. C. A. Miller-Jones et al. "An accurate position for the black hole candidate XTE J1752-223: re-interpretation of the VLBI data". In: *MNRAS* 415.1 (July 2011), pp. 306–312. DOI: 10.1111/j.1365-2966.2011.18704.x. arXiv: 1103.2826 [astro-ph.HE].

[239] J. C. A. Miller-Jones et al. "Disc-jet coupling in the 2009 outburst of the black hole candidate H1743-322". In: *MNRAS* 421.1 (Mar. 2012), pp. 468–485. DOI: 10.1111/j.1365-2966.2011.20326.x. arXiv: 1201.1678 [astro-ph.HE].

[240] J. C. A. Miller-Jones et al. "Evidence for deceleration in the radio jets of GRS1915+105?" In: *MNRAS* 375.3 (Mar. 2007), pp. 1087–1098. DOI: 10.1111/j.1365-2966.2007.11381.x. arXiv: astro-ph/0612211 [astro-ph].

[241] James Miller-Jones et al. "Searching for the Signatures of Jet-ISM Interactions in X-ray Binaries". In: *A Population Explosion: The Nature & Evolution of X-ray Binaries in Diverse Environments*. Ed. by Reba M. Bandyopadhyay et al. Vol. 1010. American Institute of Physics Conference Series. May 2008, pp. 50–56. DOI: 10.1063/1.2945089. arXiv: 0802.3446 [astro-ph].

[242] James C. A. Miller-Jones et al. "A rapidly changing jet orientation in the stellar-mass black-hole system V404 Cygni". In: *Nature* 569.7756 (Apr. 2019), pp. 374–377. DOI: 10.1038/s41586-019-1152-0. arXiv: 1906.05400 [astro-ph.HE].

[243] James C. A. Miller-Jones et al. "Cygnus X-1 contains a 21-solar mass black hole—Implications for massive star winds". In: *Science* 371.6533 (Mar. 2021), pp. 1046–1049. DOI: 10.1126/science.abb3363. arXiv: 2102.09091 [astro-ph.HE].

[244] James C. A. Miller-Jones et al. "Time-sequenced Multi-Radio Frequency Observations of Cygnus X-3 in Flare". In: *ApJ* 600.1 (Jan. 2004), pp. 368–389. DOI: 10.1086/379706. arXiv: astro-ph/0311277 [astro-ph].

[245] Amy J. Mioduszewski et al. "A One-sided Highly Relativistic Jet from Cygnus X-3". In: *ApJ* 553.2 (June 2001), pp. 766–775. DOI: 10.1086/320965. arXiv: astro-ph/0102018 [astro-ph].

[246] I. F. Mirabel and L. F. Rodríguez. "A superluminal source in the Galaxy". In: *Nature* 371.6492 (Sept. 1994), pp. 46–48. DOI: 10.1038/371046a0.

[247] I. F. Mirabel and L. F. Rodríguez. "Sources of Relativistic Jets in the Galaxy". In: *ARA&A* 37 (Jan. 1999), pp. 409–443. DOI: 10.1146/annurev.astro.37.1.409. arXiv: astro-ph/9902062 [astro-ph].

[248] I. F. Mirabel et al. "A double-sided radio jet from the compact Galactic Centre annihilator 1E1740.7-2942". In: *Nature* 358.6383 (July 1992), pp. 215–217. DOI: 10.1038/358215a0.

[249] I. F. Mirabel et al. "Accretion instabilities and jet formation in GRS 1915+105". In: *A&A* 330 (Feb. 1998), pp. L9–L12. arXiv: astro-ph/9711097 [astro-ph].

[250] I. F. Mirabel et al. "Jet-induced star formation by a microquasar". In: *Extragalactic Jets from Every Angle*. Ed. by F. Massaro et al. Vol. 313. IAU Symposium. Mar. 2015, pp. 370–373. DOI: 10.1017/S1743921315002501. arXiv: 1410.8493 [astro-ph.HE].

[251] I. F. Mirabel et al. "The Superluminal Source GRS 1915+105: A High Mass X-Ray Binary?" In: *ApJ* 477.1 (Mar. 1997), pp. L45–L48. DOI: 10.1086/310509.

[252] Charles W. Misner, Kip S. Thorne, and John A. Wheeler. *Gravitation*. 1973.

[253] D. Misra et al. "The origin of pulsating ultra-luminous X-ray sources: Low- and intermediate-mass X-ray binaries containing neutron star accretors". In: *A&A* 642, A174 (Oct. 2020), A174. DOI: 10.1051/0004-6361/202038070. arXiv: 2004.01205 [astro-ph.HE].

[254] K. Mitsuda et al. "Energy spectra of low-mass binary X-ray sources observed from Tenma." In: *PASJ* 36 (Jan. 1984), pp. 741–759.

[255] I. M. Monageng et al. "Radio flaring and dual radio loud/quiet behaviour in the new candidate black hole X-ray binary MAXI J1631-472". In: *MNRAS* 501.4 (Mar. 2021), pp. 5776–5781. DOI: 10.1093/mnras/stab043. arXiv: 2101.01569 [astro-ph.HE].

[256] Monika Mościbrodzka and Heino Falcke. "Coupled jet-disk model for Sagittarius A*: explaining the flat-spectrum radio core with GRMHD simulations of jets". In: *A&A* 559, L3 (Nov. 2013), p. L3. DOI: 10.1051/0004-6361/201322692. arXiv: 1310.4951 [astro-ph.HE].

[257] S. E. Motta, P. Casella, and R. P. Fender. "Radio-loudness in black hole transients: evidence for an inclination effect". In: *MNRAS* 478.4 (Aug. 2018), pp. 5159–5173. DOI: 10.1093/mnras/sty1440. arXiv: 1806.00015 [astro-ph.HE].

[258] S. E. Motta and R. P. Fender. "A connection between accretion states and the formation of ultrarelativistic outflows in a neutron star X-ray binary". In: *MNRAS* 483.3 (Mar. 2019), pp. 3686–3699. DOI: 10.1093/mnras/sty3331. arXiv: 1812.04867 [astro-ph.HE].

[259] S. E. Motta et al. "Geometrical constraints on the origin of timing signals from black holes". In: *MNRAS* 447.2 (Feb. 2015), pp. 2059–2072. DOI: 10.1093/mnras/stu2579. arXiv: 1404.7293 [astro-ph.HE].

[260] T. Muñoz-Darias et al. "Hard-state Accretion Disk Winds from Black Holes: The Revealing Case of MAXI J1820+070". In: *ApJ* 879.1, L4 (July 2019), p. L4. DOI: 10.3847/2041-8213/ab2768. arXiv: 1906.04835 [astro-ph.HE].

[261] T. Muñoz-Darias et al. "Inclination and relativistic effects in the outburst evolution of black hole transients". In: *MNRAS* 432.2 (June 2013), pp. 1330–1337. DOI: 10.1093/mnras/stt546. arXiv: 1304.2072 [astro-ph.HE].

[262] T. Muñoz-Darias et al. "Regulation of black-hole accretion by a disk wind during a violent outburst of V404 Cygni". In: *Nature* 534.7605 (June 2016), pp. 75–78. DOI: 10.1038/nature17446. arXiv: 1605.02358 [astro-ph.HE].

[263] Ramesh Narayan and Insu Yi. "Advection-dominated Accretion: A Self-similar Solution". In: *ApJ* 428 (June 1994), p. L13. DOI: 10.1086/187381. arXiv: astro-ph/9403052 [astro-ph].

[264] Ramesh Narayan and Insu Yi. "Advection-dominated Accretion: Underfed Black Holes and Neutron Stars". In: *ApJ* 452 (Oct. 1995), p. 710. DOI: 10.1086/176343. arXiv: astro-ph/9411059 [astro-ph].

[265] H. Negoro et al. "MAXI/GSC detection of successive mini-outbursts from the black hole candidate MAXI J1348-630". In: *The Astronomer's Telegram* 13994 (Sept. 2020), p. 1.

[266] H. Negoro et al. "MAXI/GSC detection of X-ray rebrightening of MAXI J1348-630". In: *The Astronomer's Telegram* 12838 (June 2019), p. 1.

[267] I. Negueruela. "Stellar Wind Accretion in High-Mass X-Ray Binaries". In: *High Energy Phenomena in Massive Stars*. Ed. by J. Martí, P. L. Luque-Escamilla, and J. A. Combi. Vol. 422. Astronomical Society of the Pacific Conference Series. May 2010, p. 57. arXiv: 0907.2883 [astro-ph.HE].

[268] Roberto Nesci and Mariateresa Fiocchi. "Optical colors of MAXIJ1348-630". In: *The Astronomer's Telegram* 12448 (Jan. 2019), p. 1.

[269] A. R. Offringa. *AOFlagger: RFI Software*. Oct. 2010. ascl: 1010.017.

[270] A. R. Offringa et al. "WSCLEAN: an implementation of a fast, generic wide-field imager for radio astronomy". In: *MNRAS* 444.1 (Oct. 2014), pp. 606–619. DOI: 10.1093/mnras/stu1368. arXiv: 1407.1943 [astro-ph.IM].

[271] G. I. Ogilvie and G. Dubus. "Precessing warped accretion discs in X-ray binaries". In: *MNRAS* 320.4 (Feb. 2001), pp. 485–503. DOI: 10.1046/j.1365-8711.2001.04011.x. arXiv: astro-ph/0009264 [astro-ph].

[272] T. Okuda et al. "Black hole accretion discs and jets at super-Eddington luminosity". In: *MNRAS* 357.1 (Feb. 2005), pp. 295–303. DOI: 10.1111/j.1365-2966.2005.08647.x. arXiv: astro-ph/0411743 [astro-ph].

[273] Jerome A. Orosz et al. "Dynamical Evidence for a Black Hole in the Microquasar XTE J1550-564". In: *ApJ* 568.2 (Apr. 2002), pp. 845–861. DOI: 10.1086/338984. arXiv: astro-ph/0112101 [astro-ph].

[274] Jerome A. Orosz et al. "The Mass of the Black Hole in Cygnus X-1". In: *ApJ* 742.2, 84 (Dec. 2011), p. 84. DOI: 10.1088/0004-637X/742/2/84. arXiv: 1106.3689 [astro-ph.HE].

[275] A. G. Pacholczyk. *Radio astrophysics. Nonthermal processes in galactic and extragalactic sources*. 1970.

[276] Don N. Page and Kip S. Thorne. "Disk-Accretion onto a Black Hole. Time-Averaged Structure of Accretion Disk". In: *ApJ* 191 (July 1974), pp. 499–506. DOI: 10.1086/152990.

[277] A. S. Parikh et al. "Rapidly Evolving Disk-Jet Coupling during Re-brightenings in the Black Hole Transient MAXI J1535-571". In: *ApJ* 878.2, L28 (June 2019), p. L28. DOI: 10.3847/2041-8213/ab2636. arXiv: 1906.01000 [astro-ph.HE].

[278] Timothy J. Pearson and J. Anton Zensus. "Superluminal radio sources: introduction." In: *Superluminal Radio Sources*. Ed. by J. Anton Zensus and Timothy J. Pearson. Jan. 1987, pp. 1–11.

[279] M. Péault et al. "Modelling the compact jet in MAXI J1836-194 with disc-driven shocks". In: *MNRAS* 482.2 (Jan. 2019), pp. 2447–2458. DOI: 10.1093/mnras/sty2796. arXiv: 1810.06435 [astro-ph.HE].

[280] Asaf Pe'er and Piergiorgio Casella. "A Model for Emission from Jets in X-Ray Binaries: Consequences of a Single Acceleration Episode". In: *ApJ* 699.2 (July 2009), pp. 1919–1937. DOI: 10.1088/0004-637X/699/2/1919. arXiv: 0902.2892 [astro-ph.HE].

[281] Saarah F. Pirbhoy et al. "XB-NEWS detection of a new outburst of MAXI J1348-630". In: *The Astronomer's Telegram* 13451 (Feb. 2020), p. 1.

[282] R. M. Plotkin et al. "Radio Variability from a Quiescent Stellar-mass Black Hole Jet". In: *ApJ* 874.1, 13 (Mar. 2019), p. 13. DOI: 10.3847/1538-4357/ab01cc. arXiv: 1901.07776 [astro-ph.HE].

[283] R. M. Plotkin et al. "The 2015 Decay of the Black Hole X-Ray Binary V404 Cygni: Robust Disk-jet Coupling and a Sharp Transition into Quiescence". In: *ApJ* 834.2, 104 (Jan. 2017), p. 104. DOI: 10.3847/1538-4357/834/2/104. arXiv: 1611.02810 [astro-ph.HE].

[284] R. M. Plotkin et al. "Up and Down the Black Hole Radio/X-Ray Correlation: The 2017 Mini-outbursts from Swift J1753.5-0127". In: *ApJ* 848.2, 92 (Oct. 2017), p. 92. DOI: 10.3847/1538-4357/aa8d6d. arXiv: 1709.05242 [astro-ph.HE].

[285] Richard. M. Plotkin, Elena Gallo, and Peter G. Jonker. "The X-Ray Spectral Evolution of Galactic Black Hole X-Ray Binaries toward Quiescence". In: *ApJ* 773.1, 59 (Aug. 2013), p. 59. DOI: 10.1088/0004-637X/773/1/59. arXiv: 1306.1570 [astro-ph.HE].

[286] Richard M. Plotkin et al. "A clean sightline to quiescence: multiwavelength observations of the high Galactic latitude black hole X-ray binary Swift J1357.2-0933". In: *MNRAS* 456.3 (Mar. 2016), pp. 2707–2716. DOI: 10.1093/mnras/stv2861. arXiv: 1512.01941 [astro-ph.HE].

[287] Richard M. Plotkin et al. "Constraints on relativistic jets in quiescent black hole X-ray binaries from broad-band spectral modelling". In: *MNRAS* 446.4 (Feb. 2015), pp. 4098–4111. DOI: 10.1093/mnras/stu2385. arXiv: 1411.2973 [astro-ph.HE].

[288] Richard M. Plotkin et al. "Using the Fundamental Plane of black hole activity to distinguish X-ray processes from weakly accreting black holes". In: *MNRAS* 419.1 (Jan. 2012), pp. 267–286. DOI: 10.1111/j.1365-2966.2011.19689.x. arXiv: 1105.3211 [astro-ph.HE].

[289] G. Ponti et al. "Ubiquitous equatorial accretion disc winds in black hole soft states". In: *MNRAS* 422.1 (May 2012), pp. L11–L15. DOI: 10.1111/j.1745-3933.2012.01224.x. arXiv: 1201.4172 [astro-ph.HE].

[290] Juri Poutanen, Alexandra Veledina, and Mikhail G. Revnivtsev. "Colours of black holes: infrared flares from the hot accretion disc in XTE J1550-564". In: *MNRAS* 445.4 (Dec. 2014), pp. 3987–3998. DOI: 10.1093/mnras/stu1989. arXiv: 1409.6504 [astro-ph.HE].

[291] Juri Poutanen et al. "Extreme black hole spin–orbit misalignment in X-ray binary MAXI J1820+070". In: *arXiv e-prints*, arXiv:2109.07511 (Sept. 2021), arXiv:2109.07511. arXiv: 2109.07511 [astro-ph.HE].

[292] P. Predehl et al. "Chandra measurement of the geometrical distance to Cyg X-3 using its X-ray scattering halo". In: *A&A* 357 (May 2000), pp. L25–L28.

[293] J. E. Pringle. "Accretion discs in astrophysics". In: *ARA&A* 19 (Jan. 1981), pp. 137–162. DOI: 10.1146/annurev.aa.19.090181.001033.

[294] Dimitrios Psaltis. "Probes and Tests of Strong-Field Gravity with Observations in the Electromagnetic Spectrum". In: *Living Reviews in Relativity* 11.1, 9 (Nov. 2008), p. 9. DOI: 10.12942/lrr-2008-9. arXiv: 0806.1531 [astro-ph].

[295] A. R. Rao, J. S. Yadav, and B. Paul. "Rapid State Transitions in the Galactic Black Hole Candidate Source GRS 1915+105". In: *ApJ* 544.1 (Nov. 2000), pp. 443–452. DOI: 10.1086/317168. arXiv: astro-ph/0007250 [astro-ph].

[296] E. M. Ratti et al. "The black hole candidate XTE J1752-223 towards and in quiescence: optical and simultaneous X-ray-radio observations". In: *MNRAS* 423.3 (July 2012), pp. 2656–2667. DOI: 10.1111/j.1365-2966.2012.21071.x. arXiv: 1204.2735 [astro-ph.HE].

[297] U. Rau and T. J. Cornwell. "A multi-scale multi-frequency deconvolution algorithm for synthesis imaging in radio interferometry". In: *A&A* 532, A71 (Aug. 2011), A71. DOI: 10.1051/0004-6361/201117104. arXiv: 1106.2745 [astro-ph.IM].

[298] M. J. Rees. "Appearance of Relativistically Expanding Radio Sources". In: *Nature* 211.5048 (July 1966), pp. 468–470. DOI: 10.1038/211468a0.

[299] M. J. Rees and P. Meszaros. "Relativistic fireballs - Energy conversion and time-scales." In: *MNRAS* 258 (Sept. 1992), p. 41. DOI: 10.1093/mnras/258.1.41P.

[300] M. J. Reid et al. "Trigonometric Parallaxes of High Mass Star Forming Regions: The Structure and Kinematics of the Milky Way". In: *ApJ* 783.2, 130 (Mar. 2014), p. 130. DOI: 10.1088/0004-637X/783/2/130. arXiv: 1401.5377 [astro-ph.GA].

[301] Pablo Reig. "Be/X-ray binaries". In: *Ap&SS* 332.1 (Mar. 2011), pp. 1–29. DOI: 10.1007/s10509-010-0575-8. arXiv: 1101.5036 [astro-ph.HE].

[302] Anthony Remijan et al. *ALMA Cycle 7 Technical Handbook*. Additional contributors to this edition: Tim Bastian, Crystal Brogan, John Carpenter, Chinshin Chang, Geoff Crew, Daniel Espada, Paul Fisher, Misato Fukagawa, Melissa Hoffman, Todd Hunter, Ruediger Kneissl, Andy Lipnicky, Ryan Loomis, Sergio Martin, Lynn Matthews, Luke Maud, Rie Miura, Yusuke Miyamoto, Hiroshi Nagai, Kouichiro Nakanishi, Masumi Shimojo, Richard Simon, Jeremy Thorley, MCarmen Toribio, Catarina Ubach, Catherine Vlahakis, Martin Zwaan. June 2019. DOI: 10.5281/zenodo.4511522. URL: https://doi.org/10.5281/zenodo.4511522.

[303] Ronald A. Remillard and Jeffrey E. McClintock. "X-Ray Properties of Black-Hole Binaries". In: *ARA&A* 44.1 (Sept. 2006), pp. 49–92. DOI: 10.1146/annurev.astro.44.051905.092532. arXiv: astro-ph/0606352 [astro-ph].

[304] Mark T. Reynolds et al. "The quiescent X-ray spectrum of accreting black holes". In: *MNRAS* 441.4 (July 2014), pp. 3656–3665. DOI: 10.1093/mnras/stu832. arXiv: 1405.0474 [astro-ph.HE].

[305] M. Ribó, V. Dhawan, and I. F. Mirabel. "The asymmetric compact jet of GRS 1915+105". In: *European VLBI Network on New Developments in VLBI Science and Technology*. Jan. 2004, pp. 111–112. arXiv: astro-ph/0412657 [astro-ph].

[306] M. Ribó et al. "The First Simultaneous X-Ray/Radio Detection of the First Be/BH System MWC 656". In: *ApJ* 835.2, L33 (Feb. 2017), p. L33. DOI: 10.3847/2041-8213/835/2/L33. arXiv: 1701.07265 [astro-ph.HE].

[307] J. Rodriguez, S. Corbel, and J. A. Tomsick. "Spectral Evolution of the Microquasar XTE J1550-564 over Its Entire 2000 Outburst". In: *The Astrophysical Journal* 595.2 (Oct. 2003), pp. 1032–1038. DOI: 10.1086/377478. URL: https://doi.org/10.1086%2F377478.

[308] Jennifer Rodriguez et al. "GS 2000+25: The Least Luminous Black Hole X-Ray Binary". In: *ApJ* 889.1, 58 (Jan. 2020), p. 58. DOI: 10.3847/1538-4357/ab5db5. arXiv: 1912.01029 [astro-ph.HE].

[309] Jérôme Rodriguez et al. "Spectral State Dependence of the 0.4-2 MeV Polarized Emission in Cygnus X-1 Seen with INTEGRAL/IBIS, and Links with the AMI Radio Data". In: *ApJ* 807.1, 17 (July 2015), p. 17. DOI: 10.1088/0004-637X/807/1/17. arXiv: 1505.02786 [astro-ph.HE].

[310] Gustavo E. Romero et al. "Relativistic Jets in Active Galactic Nuclei and Microquasars". In: *Space Sci. Rev.* 207.1-4 (July 2017), pp. 5–61. DOI: 10.1007/s11214-016-0328-2. arXiv: 1611.09507 [astro-ph.HE].

[311] Peter W. A. Roming et al. "The Swift Ultra-Violet/Optical Telescope". In: *Space Sci. Rev.* 120.3-4 (Oct. 2005), pp. 95–142. DOI: 10.1007/s11214-005-5095-4. arXiv: astro-ph/0507413 [astro-ph].

[312] A. P. Rushton et al. "Resolved, expanding jets in the Galactic black hole candidate XTE J1908+094". In: *MNRAS* 468.3 (July 2017), pp. 2788–2802. DOI: 10.1093/mnras/stx526. arXiv: 1703.02110 [astro-ph.HE].

[313] D. M. Russell et al. "An Evolving Compact Jet in the Black Hole X-Ray Binary MAXI J1836-194". In: *ApJ* 768.2, L35 (May 2013), p. L35. DOI: 10.1088/2041-8205/768/2/L35. arXiv: 1304.3510 [astro-ph.HE].

[314] D. M. Russell et al. "Jet spectral breaks in black hole X-ray binaries". In: *MNRAS* 429.1 (Feb. 2013), pp. 815–832. DOI: 10.1093/mnras/sts377. arXiv: 1211.1655 [astro-ph.HE].

[315] David M. Russell, Cristina Maria Baglio, and Fraser Lewis. "Optical brightening of MAXI J1348-630". In: *The Astronomer's Telegram* 12439 (Jan. 2019), p. 1.

[316] David M. Russell et al. "Optical re-brightening of MAXI J1348-630". In: *The Astronomer's Telegram* 12829 (June 2019), p. 1.

[317] T. Russell et al. "ATCA detects the radio brightening of the X-ray transient MAXI J1348-630". In: *The Astronomer's Telegram* 12456 (Jan. 2019), p. 1.

[318] T. D. Russell et al. "Disk-Jet Coupling in the 2017/2018 Outburst of the Galactic Black Hole Candidate X-Ray Binary MAXI J1535-571". In: *ApJ* 883.2, 198 (Oct. 2019), p. 198. DOI: 10.3847/1538-4357/ab3d36. arXiv: 1906.00998 [astro-ph.HE].

[319] T. D. Russell et al. "Radio monitoring of the hard state jets in the 2011 outburst of MAXI J1836-194". In: *MNRAS* 450.2 (June 2015), pp. 1745–1759. DOI: 10.1093/mnras/stv723. arXiv: 1503.08634 [astro-ph.HE].

[320] T. D. Russell et al. "Rapid compact jet quenching in the Galactic black hole candidate X-ray binary MAXI J1535-571". In: *MNRAS* 498.4 (Sept. 2020), pp. 5772–5785. DOI: 10.1093/mnras/staa2650. arXiv: 2008.11216 [astro-ph.HE].

[321] T D Russell et al. "Rapid compact jet quenching in the Galactic black hole candidate X-ray binary MAXI J1535-571". In: *MNRAS* 498.4 (Sept. 2020), pp. 5772–5785. ISSN: 0035-8711. DOI: 10.1093/mnras/staa2650. eprint: https://academic.oup.com/mnras/article-pdf/498/4/5772/33838683/staa2650.pdf. URL: https://doi.org/10.1093/mnras/staa2650.

[322] T. D. Russell et al. "The accretion-ejection coupling in the black hole candidate X-ray binary MAXI J1836-194". In: *MNRAS* 439.2 (Apr. 2014), pp. 1390–1402. DOI: 10.1093/mnras/stt2498. arXiv: 1312.5822 [astro-ph.HE].

[323] George B. Rybicki and Alan P. Lightman. *Radiative processes in astrophysics*. 1979.

[324] Payaswini Saikia et al. "Lorentz Factors of Compact Jets in Black Hole X-Ray Binaries". In: *ApJ* 887.1, 21 (Dec. 2019), p. 21. DOI: 10.3847/1538-4357/ab4a09. arXiv: 1910.01151 [astro-ph.HE].

[325] E. E. Salpeter. "Accretion of Interstellar Matter by Massive Objects." In: *ApJ* 140 (Aug. 1964), pp. 796–800. DOI: 10.1086/147973.

[326] A. Sanna et al. "NICER identification of MAXI J1348-630 as a probable black hole X-ray binary". In: *The Astronomer's Telegram* 12447 (Jan. 2019), p. 1.

[327] Gideon Schwarz. "Estimating the Dimension of a Model". In: *The Annals of Statistics* 6.2 (1978), pp. 461 –464. DOI: 10.1214/aos/1176344136. URL: https://doi.org/10.1214/aos/1176344136.

[328] R. J. Selina et al. "The ngVLA Reference Design". In: *Science with a Next Generation Very Large Array*. Ed. by Eric Murphy. Vol. 517. Astronomical Society of the Pacific Conference Series. Dec. 2018, p. 15. arXiv: 1810.08197 [astro-ph.IM].

[329] P. H. Sell et al. "Shell-shocked: the interstellar medium near Cygnus X-1". In: *MNRAS* 446.4 (Feb. 2015), pp. 3579–3592. DOI: 10.1093/mnras/stu2320. arXiv: 1410.8531 [astro-ph.HE].

[330] F. Seward et al. "Diffuse X-ray emission from the jets of SS433". In: *Nature* 287.5785 (Oct. 1980), pp. 806–808. DOI: 10.1038/287806a0.

[331] N. I. Shakura and R. A. Sunyaev. "Reprint of 1973A&A....24..337S. Black holes in binary systems. Observational appearance." In: *A&A* 500 (June 1973), pp. 33–51.

[332] S. L. Shapiro and S. A. Teukolsky. "The collapse of dense star clusters to supermassive black holes : the origin of quasars and AGNs." In: *ApJ* 292 (May 1985), pp. L41–L44. DOI: 10.1086/184469.

[333] N. Shaposhnikov et al. "GRO J1655-40: Early Stages of the 2005 Outburst". In: *ApJ* 655.1 (Jan. 2007), pp. 434–446. DOI: 10.1086/509755. URL: https://doi.org/10.1086/509755.

[334] A. W. Shaw et al. "Observations of the Disk/Jet Coupling of MAXI J1820+070 during Its Descent to Quiescence". In: *ApJ* 907.1, 34 (Jan. 2021), p. 34. DOI: 10.3847/1538-4357/abd1de. arXiv: 2012.04024 [astro-ph.HE].

[335] Masaru Shibata. *Numerical Relativity*. Vol. 1. World Scientific, 2015.

[336] Masaru Shibata and Stuart L. Shapiro. "Collapse of a Rotating Supermassive Star to a Supermassive Black Hole: Fully Relativistic Simulations". In: *ApJ* 572.1 (June 2002), pp. L39–L43. DOI: 10.1086/341516. arXiv: astro-ph/0205091 [astro-ph].

[337] Masaru Shibata et al. "Constraint on the maximum mass of neutron stars using GW170817 event". In: *Phys. Rev. D* 100.2, 023015 (July 2019), p. 023015. DOI: 10.1103/PhysRevD.100.023015. arXiv: 1905.03656 [astro-ph.HE].

[338] R. Shimomukai et al. "MAXI J1348-630: MAXI/GSC detection". In: *The Astronomer's Telegram* 13459 (Feb. 2020), p. 1.

[339] Gregory J. Sobczak et al. "Complete RXTE Spectral Observations of the Black Hole X-ray Nova XTE J1550-564". In: *ApJ* 544.2 (Dec. 2000), pp. 993–1015. DOI: 10.1086/317229. arXiv: astro-ph/0005599 [astro-ph].

[340] P. Soleri, T. Belloni, and P. Casella. "A transient low-frequency quasi-periodic oscillation from the black hole binary GRS 1915+105". In: *Monthly Notices of the Royal Astronomical Society* 383.3 (Jan. 2008), pp. 1089–1102. ISSN: 0035-8711. DOI: 10.1111/j.1365-2966.2007.12596.x. eprint: https://academic.oup.com/mnras/article-pdf/383/3/1089/3489975/mnras0383-1089.pdf. URL: https://doi.org/10.1111/j.1365-2966.2007.12596.x.

[341] Paolo Soleri and Rob Fender. "On the nature of the 'radio-quiet' black hole binaries". In: *MNRAS* 413.3 (May 2011), pp. 2269–2280. DOI: 10.1111/j.1365-2966.2011.18303.x. arXiv: 1101.1214 [astro-ph.HE].

[342] Robert Soria. "Bridging the gap between stellar-mass black holes and ultraluminous X-ray sources". In: *Ap&SS* 311.1-3 (Oct. 2007), pp. 213–222. DOI: 10.1007/s10509-007-9599-0. arXiv: 0707.2049 [astro-ph].

[343] Maddalena Spada et al. "Internal shocks in the jets of radio-loud quasars". In: *MNRAS* 325.4 (Aug. 2001), pp. 1559–1570. DOI: 10.1046/j.1365-8711.2001.04557.x. arXiv: astro-ph/0103424 [astro-ph].

[344] Joshua S. Speagle. "A Conceptual Introduction to Markov Chain Monte Carlo Methods". In: *arXiv e-prints*, arXiv:1909.12313 (Sept. 2019), arXiv:1909.12313. arXiv: 1909.12313 [stat.OT].

[345] R. E. Spencer. "A radio jet in SS433". In: *Nature* 282.5738 (Nov. 1979), pp. 483–484. DOI: 10.1038/282483a0.

[346] James F. Steiner and Jeffrey E. McClintock. "Modeling the Jet Kinematics of the Black Hole Microquasar XTE J1550-564: A Constraint on Spin-Orbit Alignment". In: *ApJ* 745.2, 136 (Feb. 2012), p. 136. DOI: 10.1088/0004-637X/745/2/136. arXiv: 1110.6849 [astro-ph.HE].

[347] James F. Steiner, Jeffrey E. McClintock, and Mark J. Reid. "The Distance, Inclination, and Spin of the Black Hole Microquasar H1743-322". In: *ApJ* 745.1, L7 (Jan. 2012), p. L7. DOI: 10.1088/2041-8205/745/1/L7. arXiv: 1111.2388 [astro-ph.HE].

[348] James F. Steiner et al. "The Constant Inner-disk Radius of LMC X-3: A Basis for Measuring Black Hole Spin". In: *ApJ* 718.2 (Aug. 2010), pp. L117–L121. DOI: 10.1088/2041-8205/718/2/L117. arXiv: 1006.5729 [astro-ph.HE].

[349] A. M. Stirling et al. "A relativistic jet from Cygnus X-1 in the low/hard X-ray state". In: *MNRAS* 327.4 (Nov. 2001), pp. 1273–1278. DOI: 10.1046/j.1365-8711.2001.04821.x. arXiv: astro-ph/0107192 [astro-ph].

[350] R. A. Sunyaev and L. G. Titarchuk. "Comptonization of X-rays in plasma clouds. Typical radiation spectra." In: *A&A* 500 (June 1980), pp. 167–184.

[351] Y. Tanaka and N. Shibazaki. "X-ray Novae". In: *ARA&A* 34 (Jan. 1996), pp. 607–644. DOI: 10.1146/annurev.astro.34.1.607.

[352] C. Tasse et al. "Faceting for direction-dependent spectral deconvolution". In: *A&A* 611, A87 (Apr. 2018), A87. DOI: 10.1051/0004-6361/201731474. arXiv: 1712.02078 [astro-ph.IM].

[353] C. Tasse et al. "The LOFAR Two-meter Sky Survey: Deep Fields Data Release 1. I. Direction-dependent calibration and imaging". In: *A&A* 648, A1 (Apr. 2021), A1. DOI: 10.1051/0004-6361/202038804. arXiv: 2011.08328 [astro-ph.IM].

[354] Alexander Tchekhovskoy, Ramesh Narayan, and Jonathan C. McKinney. "Efficient generation of jets from magnetically arrested accretion on a rapidly spinning black hole". In: *MNRAS* 418.1 (Nov. 2011), pp. L79–L83. DOI: 10.1111/j.1745-3933.2011.01147.x. arXiv: 1108.0412 [astro-ph.HE].

[355] A. J. Tetarenko et al. "Extreme jet ejections from the black hole X-ray binary V404 Cygni". In: *MNRAS* 469.3 (Aug. 2017), pp. 3141–3162. DOI: 10.1093/mnras/stx1048. arXiv: 1704.08726 [astro-ph.HE].

[356] A. J. Tetarenko et al. "Jet-ISM interactions near the microquasars GRS 1758-258 and 1E 1740.7-2942". In: *MNRAS* 497.3 (Sept. 2020), pp. 3504–3524. DOI: 10.1093/mnras/staa2175. arXiv: 2007.11085 [astro-ph.HE].

[357] A. J. Tetarenko et al. "Mapping jet-ISM interactions in X-ray binaries with ALMA: a GRS 1915+105 case study". In: *MNRAS* 475.1 (Mar. 2018), pp. 448–468. DOI: 10.1093/mnras/stx3151. arXiv: 1712.00432 [astro-ph.HE].

[358] A. J. Tetarenko et al. "Measuring fundamental jet properties with multiwavelength fast timing of the black hole X-ray binary MAXI J1820+070". In: *MNRAS* 504.3 (July 2021), pp. 3862–3883. DOI: 10.1093/mnras/stab820. arXiv: 2103.09318 [astro-ph.HE].

[359] A. J. Tetarenko et al. "Radio frequency timing analysis of the compact jet in the black hole X-ray binary Cygnus X-1". In: *MNRAS* 484.3 (Apr. 2019), pp. 2987–3003. DOI: 10.1093/mnras/stz165. arXiv: 1901.03751 [astro-ph.HE].

[360] B. E. Tetarenko et al. "Strong disk winds traced throughout outbursts in black-hole X-ray binaries". In: *Nature* 554.7690 (Feb. 2018), pp. 69–72. DOI: 10.1038/nature25159. arXiv: 1801.07203 [astro-ph.HE].

[361] B. E. Tetarenko et al. "Thermally driven disc winds as a mechanism for X-ray irradiation heating in black hole X-ray binaries: the case study of GX339-4". In: *MNRAS* 495.4 (July 2020), pp. 3666–3682. DOI: 10.1093/mnras/staa1367. arXiv: 2005.06378 [astro-ph.HE].

[362] B. E. Tetarenko et al. "Understanding X-ray irradiation in low-mass X-ray binaries directly from their light-curves". In: *MNRAS* 480.1 (Oct. 2018), pp. 2–16. DOI: 10.1093/mnras/sty1798. arXiv: 1807.01360 [astro-ph.HE].

[363] B. E. Tetarenko et al. "WATCHDOG: A Comprehensive All-sky Database of Galactic Black Hole X-ray Binaries". In: *ApJS* 222.2, 15 (Feb. 2016), p. 15. DOI: 10.3847/0067-0049/222/2/15. arXiv: 1512.00778 [astro-ph.HE].

[364] S. J. Tingay et al. "Relativistic motion in a nearby bright X-ray source". In: *Nature* 374.6518 (Mar. 1995), pp. 141–143. DOI: 10.1038/374141a0.

[365] Mayu Tominaga et al. "Discovery of the Black Hole X-Ray Binary Transient MAXI J1348-630". In: *ApJ* 899.1, L20 (Aug. 2020), p. L20. DOI: 10.3847/2041-8213/abaaaa. arXiv: 2004.03192 [astro-ph.HE].

[366] John A. Tomsick, Emrah Kalemci, and Philip Kaaret. "Detection of Low-Hard State Spectral and Timing Signatures from the Black Hole X-Ray Transient XTE J1650-500 at Low X-Ray Luminosities". In: *ApJ* 601.1 (Jan. 2004), pp. 439–449. DOI: 10.1086/380484. arXiv: astro-ph/0307458 [astro-ph].

[367] John A. Tomsick et al. "Broadband X-Ray Spectra of GX 339-4 and the Geometry of Accreting Black Holes in the Hard State". In: *ApJ* 680.1 (June 2008), pp. 593–601. DOI: 10.1086/587797. arXiv: 0802.3357 [astro-ph].

[368] John A. Tomsick et al. "X-Ray Jet Emission from the Black Hole X-Ray Binary XTE J1550-564 withChandrain 2000". In: *The Astrophysical Journal* 582.2 (Jan. 2003), pp. 933–944. DOI: 10.1086/344703. URL: https://doi.org/10.1086%2F344703.

[369] E. Tremou et al. "Radio & X-ray detections of GX 339-4 in quiescence using MeerKAT and Swift". In: *MNRAS* 493.1 (Feb. 2020), pp. L132–L137. DOI: 10.1093/mnrasl/slaa019. arXiv: 2002.01522 [astro-ph.HE].

[370] Evangelia Tremou et al. "MeerKAT observations of the new transient MAXI J1848-015". In: *The Astronomer's Telegram* 14432 (Mar. 2021), p. 1.

[371] Roberto Trotta. "Bayesian Methods in Cosmology". In: *arXiv e-prints*, arXiv:1701.01467 (Jan. 2017), arXiv:1701.01467. arXiv: 1701.01467 [astro-ph.CO].

[372] J. Trümper and V. Schönfelder. "Distance Determination of Variable X-ray Sources". In: *A&A* 25 (June 1973), p. 445.

[373] V. Tudor et al. "Disc-jet coupling in low-luminosity accreting neutron stars". In: *MNRAS* 470.1 (Sept. 2017), pp. 324–339. DOI: 10.1093/mnras/stx1168. arXiv: 1705.05071 [astro-ph.HE].

[374] Phil Uttley and Piergiorgio Casella. "Multi-Wavelength Variability. Accretion and Ejection at the Fastest Timescales". In: *Space Sci. Rev.* 183.1-4 (Sept. 2014), pp. 453–476. DOI: 10.1007/s11214-014-0072-4. arXiv: 1501.02117 [astro-ph.HE].

[375] S. V. Vadawale et al. "On the Origin of the Various Types of Radio Emission in GRS 1915+105". In: *ApJ* 597.2 (Nov. 2003), pp. 1023–1035. DOI: 10.1086/378672. arXiv: astro-ph/0308096 [astro-ph].

[376] A Vahdat Motlagh, E Kalemci, and T J Maccarone. "Investigating state transition luminosities of Galactic black hole transients in the outburst decay". In: *Monthly Notices*

of the Royal Astronomical Society 485.2 (Feb. 2019), pp. 2744–2758. ISSN: 0035-8711. DOI: 10.1093/mnras/stz569. eprint: https://academic.oup.com/mnras/article-pdf/485/2/2744/28067409/stz569.pdf. URL: https://doi.org/10.1093/mnras/stz569.

[377] J. van den Eijnden et al. "A new radio census of neutron star X-ray binaries". In: *MNRAS* 507.3 (Nov. 2021), pp. 3899–3922. DOI: 10.1093/mnras/stab1995. arXiv: 2107.05286 [astro-ph.HE].

[378] A. J. van der Horst et al. "Broad-band monitoring tracing the evolution of the jet and disc in the black hole candidate X-ray binary MAXI J1659-152". In: *MNRAS* 436.3 (Dec. 2013), pp. 2625–2638. DOI: 10.1093/mnras/stt1767. arXiv: 1308.4332 [astro-ph.HE].

[379] M. van der Klis. "Rapid X-ray Variability". In: *Compact stellar X-ray sources*. Vol. 39. 2006, pp. 39–112.

[380] H. van der Laan. "A Model for Variable Extragalactic Radio Sources". In: *Nature* 211.5054 (Sept. 1966), pp. 1131–1133. DOI: 10.1038/2111131a0.

[381] J. van Paradijs. "On the Accretion Instability in Soft X-Ray Transients". In: *ApJ* 464 (June 1996), p. L139. DOI: 10.1086/310100.

[382] Evgenii Pavlovich Velikhov. "Stability of an ideally conducting liquid flowing between cylinders rotating in a magnetic field". In: *Journal of Experimental and Theoretical Physics* 9 (1959), pp. 995–998.

[383] D. A. Verner et al. "Atomic Data for Astrophysics. II. New Analytic FITS for Photoionization Cross Sections of Atoms and Ions". In: *ApJ* 465 (July 1996), p. 487. DOI: 10.1086/177435. arXiv: astro-ph/9601009 [astro-ph].

[384] F. M. Vincentelli et al. "Characterization of the infrared/X-ray subsecond variability for the black hole transient GX 339-4". In: *MNRAS* 477.4 (July 2018), pp. 4524–4533. DOI: 10.1093/mnras/sty710. arXiv: 1803.05915 [astro-ph.HE].

[385] Pauli Virtanen et al. "SciPy 1.0: Fundamental Algorithms for Scientific Computing in Python". In: *Nature Methods* 17 (2020), pp. 261–272. DOI: 10.1038/s41592-019-0686-2.

[386] T. Vuillaume, G. Henri, and P. O. Petrucci. "A stratified jet model for AGN emission in the two-flow paradigm". In: *A&A* 620, A41 (Dec. 2018), A41. DOI: 10.1051/0004-6361/201731899. arXiv: 1810.01718 [astro-ph.HE].

[387] X. Y. Wang, Z. G. Dai, and T. Lu. "External Shock Model for the Large-Scale, Relativistic X-Ray Jets from the Microquasar XTE J1550-564". In: *ApJ* 592.1 (July 2003), pp. 347–353. DOI: 10.1086/375638. arXiv: astro-ph/0303370 [astro-ph].

[388] Brian Warner. *Cataclysmic Variable Stars*. 2003. DOI: 10.1017/CBO9780511586491.

[389] B. Louise Webster and Paul Murdin. "Cygnus X-1-a Spectroscopic Binary with a Heavy Companion ?" In: *Nature* 235.5332 (Jan. 1972), pp. 37–38. DOI: 10.1038/235037a0.

[390] Martin C. Weisskopf et al. "Chandra X-ray Observatory (CXO): overview". In: *X-Ray Optics, Instruments, and Missions III*. Ed. by Joachim E. Truemper and Bernd Aschenbach. Vol. 4012. Society of Photo-Optical Instrumentation Engineers (SPIE) Conference Series. July 2000, pp. 2–16. DOI: 10.1117/12.391545. arXiv: astro-ph/0004127 [astro-ph].

[391] Trey V. Wenger et al. "Kinematic Distances: A Monte Carlo Method". In: *ApJ* 856.1, 52 (Mar. 2018), p. 52. DOI: 10.3847/1538-4357/aaaec8. arXiv: 1802.04203 [astro-ph.GA].

[392] D. R. A. Williams et al. "The 2018 outburst of BHXB H1743-322 as seen with MeerKAT". In: *MNRAS* 491.1 (Jan. 2020), pp. L29–L33. DOI: 10.1093/mnrasl/slz152. arXiv: 1910.00349 [astro-ph.HE].

[393] J. Wilms, A. Allen, and R. McCray. "On the Absorption of X-Rays in the Interstellar Medium". In: *ApJ* 542.2 (Oct. 2000), pp. 914–924. DOI: 10.1086/317016. arXiv: astro-ph/0008425 [astro-ph].

[394] Thomas L. Wilson, Kristen Rohlfs, and Susanne Hüttemeister. *Tools of Radio Astronomy*. 2009. DOI: 10.1007/978-3-540-85122-6.

[395] Warwick E. Wilson et al. "The Australia Telescope Compact Array Broad-band Backend: description and first results". In: *MNRAS* 416.2 (Sept. 2011), pp. 832–856. DOI: 10.1111/j.1365-2966.2011.19054.x. arXiv: 1105.3532 [astro-ph.IM].

[396] C. M. Wood et al. "The varying kinematics of multiple ejecta from the black hole X-ray binary MAXI J1820 + 070". In: *MNRAS* 505.3 (Aug. 2021), pp. 3393–3403. DOI: 10.1093/mnras/stab1479. arXiv: 2105.09529 [astro-ph.HE].

[397] S. E. Woosley, A. Heger, and T. A. Weaver. "The evolution and explosion of massive stars". In: *Reviews of Modern Physics* 74.4 (Nov. 2002), pp. 1015–1071. DOI: 10.1103/RevModPhys.74.1015.

[398] Y. X. Wu et al. "Orbital Period and Outburst Luminosity of Transient Low Mass X-ray Binaries". In: *ApJ* 718.2 (Aug. 2010), pp. 620–631. DOI: 10.1088/0004-637X/718/2/620. arXiv: 1006.0057 [astro-ph.HE].

[399] Fu-Guo Xie, Zhen Yan, and Zhongzu Wu. "Radio/X-Ray Correlation in the Mini-outbursts of Black Hole X-Ray Transient GRS 1739-278". In: *ApJ* 891.1, 31 (Mar. 2020), p. 31. DOI: 10.3847/1538-4357/ab711f. arXiv: 1911.06447 [astro-ph.HE].

[400] Fu-Guo Xie and Feng Yuan. "Interpreting the radio/X-ray correlation of black hole X-ray binaries based on the accretion-jet model". In: *MNRAS* 456.4 (Jan. 2016), pp. 4377–4383. ISSN: 0035-8711. DOI: 10.1093/mnras/stv2956. eprint: https://academic.oup.com/mnras/article-pdf/456/4/4377/9386189/stv2956.pdf. URL: https://doi.org/10.1093/mnras/stv2956.

[401] Fu-Guo Xie and Feng Yuan. "Radiative efficiency of hot accretion flows". In: *MNRAS* 427.2 (Dec. 2012), pp. 1580–1586. DOI: 10.1111/j.1365-2966.2012.22030.x. arXiv: 1207.3113 [astro-ph.HE].

[402] J. Yang et al. "A decelerating jet observed by the EVN and VLBA in the X-ray transient XTE J1752-223". In: *Monthly Notices of the Royal Astronomical Society: Letters* 409.1 (Nov. 2010), pp. L64–L68. ISSN: 1745-3925. DOI: 10.1111/j.1745-3933.2010.00948.x. eprint: https://academic.oup.com/mnrasl/article-pdf/409/1/L64/3234582/409-1-L64.pdf. URL: https://doi.org/10.1111/j.1745-3933.2010.00948.x.

[403] F. Yatabe et al. "MAXI/GSC discovery of a new X-ray transient MAXI J1348-630". In: *The Astronomer's Telegram* 12425 (Jan. 2019), p. 1.

[404] Feng Yuan and Wei Cui. "Radio–X-Ray Correlation and the "Quiescent State" of Black Hole Sources". In: *The Astrophysical Journal* 629.1 (Aug. 2005), pp. 408–413. DOI: 10.1086/431453. URL: https://doi.org/10.1086%2F431453.

[405] Feng Yuan and Andrzej A. Zdziarski. "Luminous hot accretion flows: the origin of X-ray emission from Seyfert galaxies and black hole binaries". In: *MNRAS* 354.3 (Nov. 2004), pp. 953–960. ISSN: 0035-8711. DOI: 10.1111/j.1365-2966.2004.08262.x. eprint: https://academic.oup.com/mnras/article-pdf/354/3/953/18659933/354-3-953.pdf. URL: https://doi.org/10.1111/j.1365-2966.2004.08262.x.

[406] L. R. Yungelson et al. "The origin and fate of short-period low-mass black-hole binaries". In: *A&A* 454.2 (Aug. 2006), pp. 559–569. DOI: 10.1051/0004-6361:20064984. arXiv: astro-ph/0604434 [astro-ph].

[407] A. A. Zdziarski and M. Gierliński. "Radiative Processes, Spectral States and Variability of Black-Hole Binaries". In: *Progress of Theoretical Physics Supplement* 155 (Jan. 2004), pp. 99–119. DOI: 10.1143/PTPS.155.99. arXiv: astro-ph/0403683 [astro-ph].

[408] Andrzej A. Zdziarski, Alexandra J. Tetarenko, and Marek Sikora. "Jet Parameters in the Black-Hole X-Ray Binary MAXI J1820+070". In: *arXiv e-prints*, arXiv:2108.10929 (Aug. 2021), arXiv:2108.10929. arXiv: 2108.10929 [astro-ph.HE].

[409] J. Anton Zensus. "Parsec-Scale Jets in Extragalactic Radio Sources". In: *ARA&A* 35 (Jan. 1997), pp. 607–636. DOI: 10.1146/annurev.astro.35.1.607.

[410] L. Zhang et al. "NICER observations reveal that the X-ray transient MAXI J1348-630 is a black hole X-ray binary". In: *MNRAS* 499.1 (Nov. 2020), pp. 851–861. DOI: 10.1093/mnras/staa2842. arXiv: 2009.07749 [astro-ph.HE].

[411] L. Zhang et al. "NICER uncovers the transient nature of the type-B quasi-periodic oscillation in the black hole candidate MAXI J1348-630". In: *MNRAS* 505.3 (Aug. 2021), pp. 3823–3843. DOI: 10.1093/mnras/stab1553. arXiv: 2105.12338 [astro-ph.HE].

[412] Liang Zhang et al. "Re-brightening and decaying of MAXI J1348-630 as observed with NICER". In: *The Astronomer's Telegram* 13465 (Feb. 2020), p. 1.

[413] S. N. Zhang, Wei Cui, and Wan Chen. "Black Hole Spin in X-Ray Binaries: Observational Consequences". In: *ApJ* 482.2 (June 1997), pp. L155–L158. DOI: 10.1086/310705. arXiv: astro-ph/9704072 [astro-ph].

Appendix A

Research paper: "Measuring the distance to the black hole candidate X-ray binary MAXI J1348−630 using H I absorption"

Monthly Notices of the ROYAL ASTRONOMICAL SOCIETY

MNRAS **501,** L60–L64 (2021) doi:10.1093/mnrasl/slaa195
Advance Access publication 2020 December 09

Measuring the distance to the black hole candidate X-ray binary MAXI J1348–630 using H I absorption

J. Chauhan [1★] J. C. A. Miller-Jones [1★] W. Raja,[2] J. R. Allison [3] P. F. L. Jacob,[3] G. E. Anderson [1] F. Carotenuto,[4] S. Corbel,[4,5] R. Fender,[3] A. Hotan,[2] M. Whiting,[2] P. A. Woudt [6] B. Koribalski [2] and E. Mahony[2]

[1]*International Centre for Radio Astronomy Research, Curtin University, GPO Box U1987, Perth, WA 6845, Australia*
[2]*CSIRO Astronomy and Space Science, Australia Telescope National Facility, PO Box 76, Epping, NSW 1710, Australia*
[3]*Sub-Deptartment of Astrophysics, Department of Physics, University of Oxford, Denys Wilkinson Building, Keble Rd., Oxford OX1 3RH, UK*
[4]*AIM, CEA, CNRS, Universiteí Paris Diderot, Sorbonne Paris Citeí, Universiteí Paris-Saclay, F-91191 Gif-sur-Yvette, France*
[5]*Station de Radioastronomie de Nançay, Observatoire de Paris, PSL Research University, CNRS, Univ. Orléans, F-18330 Nançay, France*
[6]*Department of Astronomy, University of Cape Town, Private Bag X3, Rondebosch 7701, South Africa*

Accepted 2020 December 3. Received 2020 December 2; in original form 2020 September 29

ABSTRACT

We present neutral hydrogen (H I) absorption spectra of the black hole candidate X-ray binary (XRB) MAXI J1348–630 using the Australian Square Kilometre Array Pathfinder (ASKAP) and MeerKAT. The ASKAP H I spectrum shows a maximum negative radial velocity (with respect to the local standard of rest) of $-31 \pm 4\,\mathrm{km\,s^{-1}}$ for MAXI J1348–630, as compared to $-50 \pm 4\,\mathrm{km\,s^{-1}}$ for a stacked spectrum of several nearby extragalactic sources. This implies a most probable distance of $2.2^{+0.5}_{-0.6}$ kpc for MAXI J1348–630, and a strong upper limit of the tangent point distance at 5.3 ± 0.1 kpc. Our preferred distance implies that MAXI J1348–630 reached 17 ± 10 per cent of the Eddington luminosity at the peak of its outburst, and that the source transited from the soft to the hard X-ray spectral state at 2.5 ± 1.5 per cent of the Eddington luminosity. The MeerKAT H I spectrum of MAXI J1348–630 (obtained from the older, low-resolution 4k mode) is consistent with the re-binned ASKAP spectrum, highlighting the potential of the eventual capabilities of MeerKAT for XRB spectral line studies.

Key words: black hole physics – ISM: jets and outflows – radio continuum: transients – X-rays: binaries – X-rays: individual: MAXI J1348–630.

1 INTRODUCTION

The distance to an astrophysical object is a key physical parameter, as it provides us with a way to determine physical quantities from observables. For X-ray binaries (XRBs) in our Galaxy, the distance can be directly determined by measuring the parallax to the source, with either very long baseline interferometry (e.g. Miller-Jones et al. 2009; Reid et al. 2011; Atri et al. 2020) or *Gaia* (Gaia Collaboration 2018). XRB distances can also be determined by studying the line features in infrared/optical spectra of the companion star (Jonker & Nelemans 2004), by using the proper motions of the jet ejecta (Mirabel & Rodríguez 1994), or by studying the interstellar extinction (Zdziarski et al. 1998). However, these distances are often poorly constrained, and suffer large uncertainties that in some cases can exceed 50 per cent (Jonker & Nelemans 2004). If the donor star is too faint, or a parallax measurement is not possible, an alternative technique is to use the 21-cm line of neutral hydrogen (H I, e.g. Goss & Mebold 1977; Dickey 1983; Dhawan, Goss & Rodríguez 2000; Chauhan et al. 2019a). The Galactic H I clouds along the line of sight to an XRB are rotating about the centre of the Milky Way, and their Doppler-shifted absorption features allow us to determine the kinematic distance to the source (Gathier, Pottasch & Goss 1986; Kuchar & Bania 1990). While the kinematic distance estimates obtained from this method are fairly accurate (at least for circular rotation) when the source is located beyond the Solar orbit, they suffer ambiguities if the source is located within the Solar circle. Since the rotation curves are then dual-valued, this leads to two distance estimates (near and far) for a single velocity measurement (e.g. Reid et al. 2014; Wenger et al. 2018).

On 2019 January 26, the Monitor of All-sky X-ray Image[1] (*MAXI*; Matsuoka et al. 2009) discovered an uncatalogued XRB at a position RA (J2000) = $13^{\mathrm{h}}48^{\mathrm{m}}12\overset{\mathrm{s}}{.}79 \pm 0.03$ Dec. (J2000) = $-63^{\mathrm{d}}16'28\overset{''}{.}48 \pm 0.04$ (Galactic coordinates $l = 309\overset{\circ}{.}26407$, $b = -1\overset{\circ}{.}10297$; Russell et al. 2019), referred to as MAXI J1348–630 (Yatabe et al. 2019). The optical counterpart of the source was detected by Denisenko et al. (2019), and the outburst was subsequently observed across the electromagnetic spectrum (e.g. Carotenuto et al. 2019; Chauhan et al. 2019b; Kennea & Negoro 2019). The system is believed to harbour a stellar-mass black hole (Russell et al. 2019; Zhang et al. 2020), although the key system parameters are poorly constrained.

★ E-mail: j.chauhan@student.curtin.edu.au (JC), james.miller-jones@curtin.edu.au (JCAM-J)

[1] http://maxi.riken.jp/top/index.html

© 2020 The Author(s)
Published by Oxford University Press on behalf of Royal Astronomical Society

Downloaded from https://academic.oup.com/mnrasl/article/501/1/L60/6029123 by Sapienza Università di Roma user on 30 July 2021

Table 1. Coordinates and 1.42-GHz ASKAP flux densities of MAXI J1348–630 and our extragalactic comparison sources. Positions taken from [1] Russell et al. (2019); [2] Murphy et al. (2007).

Source name	RA (J2000) (hh:mm:ss)	Dec. (J2000) (dd:mm:ss)	Flux density[a] (mJy)
MAXI J1348–630 [1]	13:48:12.79	–63:16:28.48	155 ± 2
MGPS J134353–624941 [2]	13:43:53.13	–62:49:41.4	86 ± 1
MGPS J134551–634755 [2]	13:45:51.50	–63:47:55.7	104 ± 1
MGPS J134559–635023 [2]	13:45:59.85	–63:50:23.1	79 ± 1
MGPS J134625–632600 [2]	13:46:25.73	–63:26:00.7	71 ± 1
MGPS J135145–635836 [2]	13:51:45.91	–63:58:36.8	114 ± 1
MGPS J135236–631600 [2]	13:52:36.51	–63:16:00.0	141 ± 1
MGPS J135401–633032 [2]	13:54:01.09	–63:30:32.1	81 ± 1
MGPS J135546–632642 [2]	13:55:46.25	–63:26:42.5	1181 ± 2

[a] 1σ errors are quoted, calculated by adding in quadrature the error on the Gaussian fit and the rms noise in the image.

In this investigation, we present H I absorption spectra from both ASKAP and MeerKAT observations, and use the Doppler-shifted 21-cm absorption line to constrain the distance to MAXI J1348–630. We further use our distance constraints to estimate the peak X-ray luminosity and the spectral state transition luminosity.

2 OBSERVATIONS AND DATA REDUCTION

2.1 ASKAP

ASKAP (Hotan et al. 2014) observed MAXI J1348–630 on 2019 February 13 for 9.91 h (on source exposure 8.39 h) from 13:22–23:16 UTC, using the full array of 36 dishes, with 36 overlapping beams. The large field of view ($\approx$ 30 deg^2) and high angular resolution ($\sim$25 arcsec) of ASKAP allow us to simultaneously detect the H I absorption towards both MAXI J1348–630 and a set of nearby extragalactic sources (Table 1), enabling a discrimination between near and far kinematic distances. Our observation was performed at a central frequency of 1.34 GHz, with a total bandwidth of 288 MHz divided into 15 368 fine channels, each of which has a frequency resolution of 18.519 kHz (velocity resolution 3.9 km s^{-1}).

For reducing our multiple-beam full array data on MAXI J1348–630, we used the ASKAP data analysis software, ASKAPSOFT.[2] Although our MAXI J1348–630 data have more antennas and beams, we follow a similar calibration procedure to that described in Chauhan et al. (2019a). However, for generating the spectral cube from the calibrated, continuum-subtracted measurement set created by ASKAPSOFT, we used the TCLEAN task in the Common Astronomy Software Application (CASA v5.1.2-4: McMullin et al. 2007) to ensure we could use the same procedure to extract both MeerKAT and ASKAP spectra, and to allow quick optimization of our imaging parameters (e.g. *uv*-range, deconvolution depth, deconvolver), given the demand on supercomputing time to run ASKAPSOFT. We produced a spectral sub-cube of 378 channels centered at the rest frequency (1420.4 MHz) of the H I line using a Briggs weighting parameter (robustness) of 0.5, and adopting a minimum baseline length of 700 m.

From the ASKAP spectral cube, we extracted the H I absorption spectrum for MAXI J1348–630 and the eight extragalactic sources listed in Table 1, by measuring the brightness in each frequency channel at the position corresponding to the peak flux density (determined from the continuum image). We used the IMFIT task in CASA to measure source flux densities and 1σ uncertainties from the continuum images.

[2] http://www.atnf.csiro.au/computing/software/askapsoft/sdp/docs/current/index.html

2.2 MeerKAT

MAXI J1348–630 was monitored as part of the MeerKAT Large Survey Project for slow transients (ThunderKAT; Fender et al. 2017). Here, we use data from 2019 February 9 between 05:08 and 05:23 (UTC), when the source was brightest in the radio (486 ± 2 mJy at 1.42 GHz; Carotenuto et al., in preparation) and therefore most sensitive to H I absorption. MeerKAT provides a field of view of 0.86 deg^2, and a spatial resolution of $\sim$10 arcsec at 1.42 GHz. Our observations were carried out using 60 MeerKAT antennas, at a central frequency of 1284 MHz, with 860 MHz of bandwidth. Only the 4k correlator mode was available, which gave a spectral resolution of 209 kHz, equal to 44 km s^{-1} at 1420.4 MHz.

Spectral line data reduction was carried out using a standard procedure that implemented tasks from MIRIAD (Sault, Teuben & Wright 1995). The data were first converted to FITS format using CASA, selecting only channels in the range 10 MHz either side of 1420.4 MHz (equivalent to radial velocities of $\pm$2000 km s^{-1}). Calibration of the bandpass and flux scale was carried out using PKS B1934–638 (Reynolds 1994), and the time varying antenna gains using PKS B1421–490. To avoid corrupting the calibration solutions with Galactic H I emission and absorption, the central 20 channels ($\pm$400 km s^{-1}) were flagged and then interpolated from neighbouring channels. Further self-calibration of the MAXI J1348–630 data was carried out to correct the time-varying gain phase. After subtraction of the continuum flux density, a spectral cube was formed within 5 arcmin of MAXI J1348–630 using a robustness of 0.5, and a minimum baseline length of 700 m. The final spectrum was extracted from the cube, adopting a similar procedure to that described for ASKAP in Section 2.1.

3 RESULTS

In the left-hand panel of Fig. 1, we present an ASKAP continuum image of the MAXI J1348–630 field created by mosaicing beams 14, 15, 20, and 21. Residual uncertainties remain around the bright (>1 Jy) sources (e.g. extragalactic source MGPS J135546–632642 in Fig. 1) at the level of 1–2 per cent, due to remaining calibration and deconvolution errors.

We detected MAXI J1348–630 in our ASKAP data with a flux density of 155 ± 2 mJy at 1.42 GHz. We also selected eight extragalactic comparison sources in the field, which are listed in Table 1, and also shown in Fig. 1 (left-hand panel). At the time of the ASKAP observation, MAXI J1348–630 was transiting from the hard to the soft X-ray spectral state (Tominaga et al. 2020), where many black hole XRBs undergo transient jet ejection events (Fender, Belloni & Gallo 2004).

To characterize the short-time-scale variability in MAXI J1348–630 during our ASKAP observation, we generated a continuum image for each of the 10 time bins (where 1 time bin $\approx$ 1 h). We present the time-resolved 1.34-GHz light curve of MAXI J1348–630 for beam 20 (for which the source is closest to the centre of the beam) in the right-hand panel of Fig. 1. This shows a short-duration flare, peaking at 252 ± 13 mJy at 15:51:32 (UTC), and then gradually decreasing to 111 ± 6 mJy by 22:53:16 (UTC). The radio flux density of the extragalactic sources in the same ASKAP beam remained constant during the observation, verifying that the variation seen from MAXI J1348–630 is intrinsic to the source.

Downloaded from https://academic.oup.com/mnrasl/article/501/1/L60/6029123 by Sapienza Università di Roma user on 30 July 2021

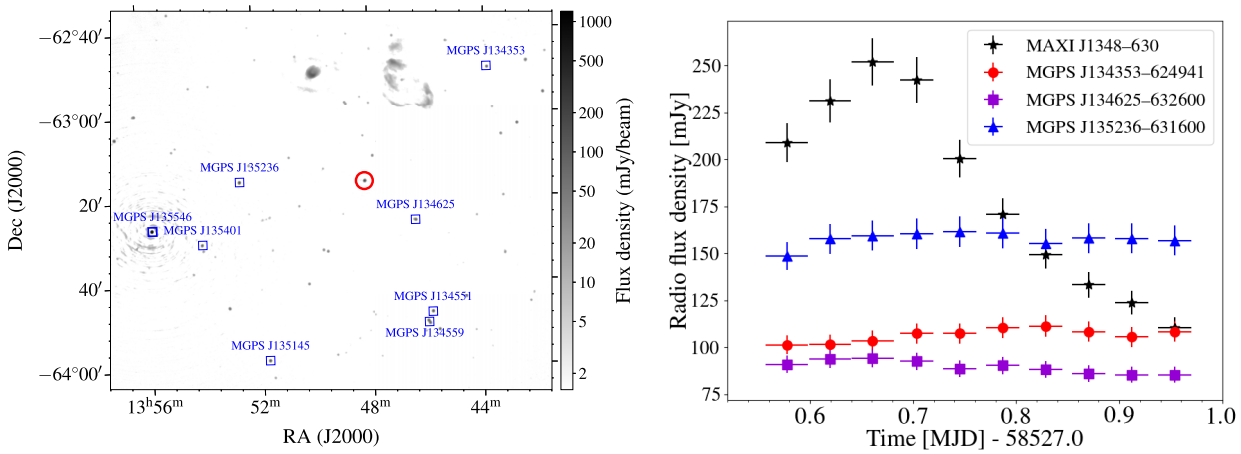

Figure 1. Left-hand panel: A continuum mosaic of the field surrounding MAXI J1348–630, from our 1.34-GHz ASKAP observation on 2019 February 13. The image has a size of 1.7° × 1.5°, centred at RA = $13^{h}49^{m}19\overset{s}{.}78$, DEC. = $-63^{d}20'23\overset{''}{.}93$. The location of MAXI J1348–630 is highlighted with the red circle, and the comparison extragalactic sources (listed in Table 1) are indicated by the blue squares. Right-hand panel: The time-resolved 1.34-GHz ASKAP light curve of MAXI J1348–630 (black stars) and the extragalactic sources, for beam 20 only. The flux density of MAXI J1348–630 varies on a ∼1-h time-scale, whereas the extragalactic sources remain constant within error bars, demonstrating that the variability observed in MAXI J1348–630 is intrinsic to the source.

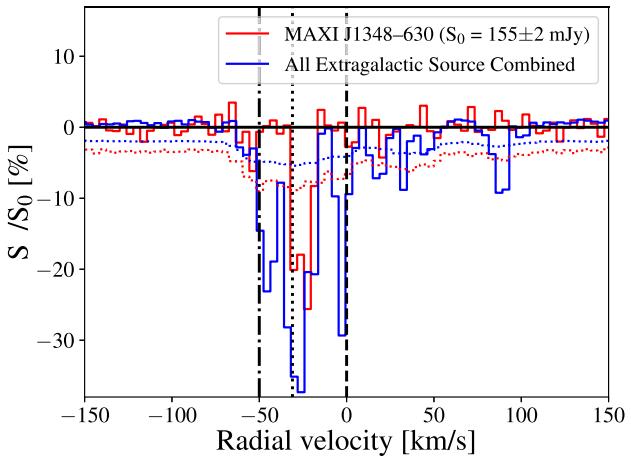

Figure 2. The H I absorption complex observed in the direction of MAXI J1348–630 using our ASKAP observation from 2019 February 13. S_ν is calculated from the spectral cube, whereas S_0 is measured from the continuum image. The red and blue curves show the H I absorption against MAXI J1348–630 and the stack of the eight extragalactic sources (Table 1), respectively. The corresponding dotted lines represent the respective per-channel 3σ noise levels (normalized to the source continuum flux density), taken from nearby source-free regions. The black dashed vertical line represents the rest frequency of the H I line. The dotted ($-31\,\mathrm{km\,s^{-1}}$) and dot–dashed vertical ($-50\,\mathrm{km\,s^{-1}}$) lines highlight the (>3σ significant) maximum negative radial velocities (with respect to the LSR) observed from the spectra of MAXI J1348–630, and the merged extragalactic sources, respectively. The maximum negative velocity of $-31 \pm 4\,\mathrm{km\,s^{-1}}$ towards MAXI J1348–630 determines the most probable distance as $2.2^{+0.5}_{-0.6}$ kpc, whereas the non-detection of more negative velocities sets a stringent upper limit of the tangent point at 5.3 ± 0.1 kpc.

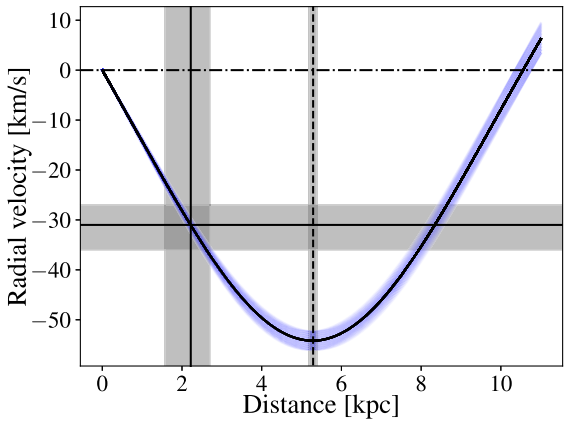

Figure 3. The expected variation of the radial velocity of the local standard of rest in the direction of MAXI J1348–630 with distance from the Sun, calculated using the Monte Carlo approach described by Wenger et al. (2018). The black line represents the expected curve, and the blue shaded region shows the effect of incorporating the 1σ uncertainties on the Galactic rotation parameters from Reid et al. (2014). The horizontal solid line shows the maximum negative radial velocity (with respect to the LSR) measured from the H I absorption spectrum. The solid and dashed vertical lines show the most likely distance and the tangent point distance, respectively. The grey shaded regions show the 1σ uncertainties. The most probable distance of MAXI J1348–630 is the near kinematic distance of $2.2^{+0.5}_{-0.6}$ kpc.

3.1 H I absorption spectra

In Fig. 2, we show the spectrum for MAXI J1348–630, together with a stacked spectrum for all eight extragalactic sources, and the 3σ noise levels measured from nearby regions. We detect significant (>3σ) H I absorption complexes out to maximum negative velocities (with respect to the local standard of rest, or LSR) of -31 ± 4 km $\mathrm{s^{-1}}$ and $-50 \pm 4\,\mathrm{km\,s^{-1}}$ for MAXI J1348–630 and the extragalactic sources, respectively.

To determine the distance to MAXI J1348–630, we computed the Galactic rotation curve for the Galactic longitude of MAXI J1348–630, and determined the variation of the radial velocity (V_{LSR}) of the LSR with distance from the Sun (d). For simplicity, we assumed that the Galactic rotation curve is flat, that the Milky Way is rotating with a circular velocity (V_0) of $240 \pm 8\,\mathrm{km\,s^{-1}}$ (Reid et al. 2014), and that the Sun is located at a distance $R_0 = 8.34 \pm 0.16$ kpc from the Galactic centre (Reid et al. 2014). Fig. 3 shows that the predicted

Downloaded from https://academic.oup.com/mnrasl/article/501/1/L60/6029123 by Sapienza Università di Roma user on 30 July 2021

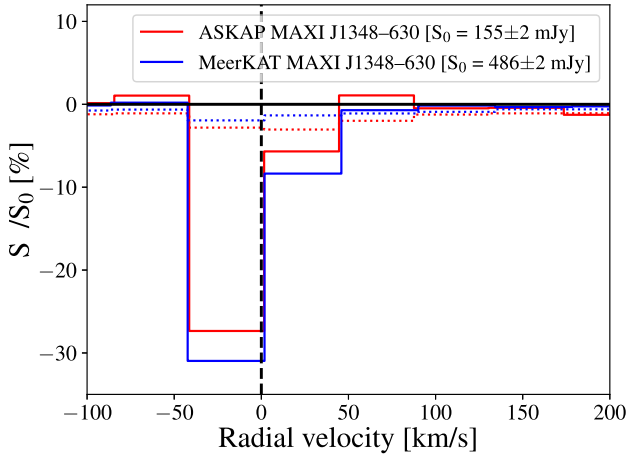

Figure 4. The MeerKAT (blue) and rebinned ASKAP (red) H I absorption spectra towards MAXI J1348–630. The 3σ rms noise levels for both instruments are shown as dotted lines. The two spectra match well within uncertainties.

LSR radial velocities are negative within a few kpc of the Sun, and by comparison with our observed H I spectrum allows us to determine the near distance, the far distance, and the tangent point distance ($R_T = R_0 \cos l \equiv 5.3 \pm 0.1$ kpc) for this line of sight.

To determine robust constraints on the kinematic distance, we adopted the recipes suggested by Wenger et al. (2018), who developed a Monte Carlo approach[3] for inferring kinematic distances and associated uncertainties, using the rotation curve provided by Reid et al. (2014). Using this approach, we determined the near and far distances of MAXI J1348–630 to be $2.2^{+0.5}_{-0.6}$ and $8.4^{+0.6}_{-0.6}$ kpc, respectively. The maximum negative absorption velocity (with respect to the LSR) observed for the extragalactic sources (-50 ± 4 km s^{-1}) is in good agreement with the tangent point velocity (-54 ± 4 km s^{-1}) for this line of sight (within error bars, and calculated using Reid et al. 2014 and Wenger et al. 2018). H I absorption at the tangent point velocity is not observed towards MAXI J1348–630, implying that it must be closer than the tangent point distance of 5.3 ± 0.1 kpc, and thereby most likely placing the source at the near kinematic distance of $2.2^{+0.5}_{-0.6}$ kpc.

3.1.1 Comparison with the MeerKAT spectrum

MeerKAT detected MAXI J1348–630 as a bright point source, of flux density 486 ± 2 mJy at 1.42 GHz (Carotenuto et al., in preparation). In the 4k correlator mode that was used, MeerKAT had a velocity resolution of 44 km s^{-1}, so we rebinned our ASKAP data (with velocity resolution 3.9 km s^{-1}) to match the MeerKAT resolution. The uncertainties on the MeerKAT spectra are smaller, both because the instrument has a lower system temperature, and because MAXI J1348–630 was brighter at the time of the MeerKAT observations than it was during the ASKAP observations (155 ± 2 mJy at 1.42 GHz). Nonetheless, as shown in Fig. 4, the two spectra are consistent within uncertainties.

[3]http://www.treywenger.com/kd/index.php

4 DISCUSSION

4.1 Distance constraint and its implications

Tominaga et al. (2020) studied the complete outburst of MAXI J1348–630 using *MAXI*/GSC data in the 2–20 keV energy range. They found the peak of the outburst to have occurred on 2019 February 9, and the soft-to-hard spectral state transition to have occurred on 2019 April 27 (Tominaga et al. 2020). We used the High Energy Astrophysics Science Archive Research Center tool WebPIMMS[4] to calculate the bolometric X-ray flux in the energy range 0.01–100 keV from the X-ray flux (2–20 keV) and spectral model determined by Tominaga et al. (2020). We derived a peak unabsorbed X-ray flux of $2.8 \pm 0.2 \times 10^{-7}$ erg cm^{-2} s^{-1}, and an unabsorbed flux of $4.2 \pm 0.5 \times 10^{-8}$ erg cm^{-2} s^{-1} for the soft-to-hard X-ray spectral state transition, corresponding to luminosities of $1.6 \pm 0.9 \times 10^{38}$ and $2.4 \pm 1.4 \times 10^{37}$ erg s^{-1}, respectively, at our preferred distance.

If we consider the compact object to be a black hole (Russell et al. 2019; Zhang et al. 2020) of typical mass 8 ± 1 M$_\odot$ (Kreidberg et al. 2012), the peak unabsorbed luminosity corresponds to $0.17 \pm 0.10 L_{\rm Edd}$, where $L_{\rm Edd}$ is the Eddington luminosity. This is in reasonable agreement with the range of $0.2–0.4 L_{\rm Edd}$ found for canonical black hole XRBs (McClintock & Remillard 2009). We further found that the system transitioned from the soft to the hard X-ray spectral state at $0.025 \pm 0.015 L_{\rm Edd}$, consistent with the range of $0.003–0.03 L_{\rm Edd}$ determined by Maccarone (2003), Kalemci et al. (2013), and Vahdat Motlagh, Kalemci & Maccarone (2019) for typical black hole XRBs.

Using the soft-to-hard X-ray spectral state transition luminosity and the measured column density towards the source, Tominaga et al. (2020) placed it in front of the Scutum–Centaurus arm, at <4 kpc. Our measured H I distance is consistent with (albeit more precise than) this estimate, and implies a state transition luminosity towards the lower end of their assumed range. Tominaga et al. (2020) further used their measured inner disc radius in the soft X-ray spectral state to constrain the black hole mass as a function of distance, inclination angle, and black hole spin. Fitting the X-ray data of Tominaga et al. (2020) with the same `kerrbb` model, and leaving the distance free to vary within our 1σ uncertainty range, we find that the lower limit on the inferred black hole mass (for the case of a non-rotating black hole with an inclination angle of 0°) reduces to 3.7M$_\odot$, rising to 5.8M$_\odot$ for an inclination angle of 60°. If the system is at low inclination and slowly rotating, this weakens the evidence for a particularly massive black hole in the system.

4.2 Future X-ray binary monitoring

Over the past year, MeerKAT has conducted weekly XRB monitoring (e.g. Bright et al. 2020; Tremou et al. 2020; Williams et al. 2020) under the large survey project ThunderKAT (Fender et al. 2017). However, the low spectral resolution limited the potential for H I studies. The recent correlator upgrade (providing 32K spectral channels with a velocity resolution of 6.1 km s^{-1}) enables spectral resolution comparable to that of ASKAP. Our data demonstrate the future potential of MeerKAT, which with its high sensitivity will be well placed to routinely provide H I distance estimates for all bright, outbursting XRBs.

[4]https://heasarc.gsfc.nasa.gov/cgi-bin/Tools/w3pimms/w3pimms.pl

Downloaded from https://academic.oup.com/mnrasl/article/501/1/L60/6029123 by Sapienza Università di Roma user on 30 July 2021

The combined temporal coverage of our ASKAP and MeerKAT observations shows that the flare detected by ASKAP (Fig. 1) is a secondary re-brightening, following the peak detected during the MeerKAT observation (Carotenuto et al. 2019). This is not unusual, as multiple jet ejections have been observed in several previous black hole XRB outbursts (e.g. Mirabel & Rodríguez 1994; Brocksopp et al. 2013). In future, the combination of MeerKAT and ASKAP observations, together with higher frequency facilities, will provide high-cadence light curves that can help constrain key parameters such as jet speed, energetics, and geometry (Tetarenko et al. 2017).

5 CONCLUSIONS

We have used ASKAP to detect H I absorption towards MAXI J1348–630 out to a maximum negative radial velocity (with respect to the LSR) of -31 ± 4 km s^{-1}, implying a most probable kinematic distance of $2.2^{+0.5}_{-0.6}$ kpc. By comparison with the absorption towards a stack of the extragalactic sources in the field of view, we place a robust upper limit of 5.3 ± 0.1 kpc, corresponding to the tangent point distance.

Using our preferred distance and assuming a canonical black hole mass of $8 \pm 1 M_{\odot}$, we found that MAXI J1348–630 was accreting at 17 ± 10 per cent of the Eddington luminosity over the peak of the outburst, and the soft-to-hard X-ray spectral state transition happened at 2.5 ± 1.5 per cent of the Eddington luminosity, consistent in both cases with what has been found for other black hole XRBs.

Finally, our study highlights the synergies between ASKAP and MeerKAT, demonstrating the potential for routine H I distance measurements for future black hole XRBs in outburst.

ACKNOWLEDGEMENTS

We thank the referee for their valuable comments. The Australian SKA Pathfinder is part of the Australia Telescope National Facility which is managed by CSIRO. Operation of ASKAP is funded by the Australian Government with support from the National Collaborative Research Infrastructure Strategy. ASKAP uses the resources of the Pawsey Supercomputing Centre. Establishment of ASKAP, the Murchison Radio-astronomy Observatory and the Pawsey Supercomputing Centre are initiatives of the Australian Government, with support from the Government of Western Australia and the Science and Industry Endowment Fund. We acknowledge the Wajarri Yamatji people as the traditional owners of the Observatory site. The MeerKAT telescope is operated by the South African Radio Astronomy Observatory, which is a facility of the National Research Foundation, an agency of the Department of Science and Innovation. JCAM-J and GEA are the recipients of an Australian Research Council Future Fellowship (FT140101082) and a Discovery Early Career Researcher Award (DE180100346), respectively, funded by the Australian Government.

DATA AVAILABILITY

The processed ASKAP data are available in the CASDA archive at https://data.csiro.au/collections/. The uncalibrated MeerKAT visibility data are publicly available, and stored at the South African Radio Astronomy Observatory (SARAO) Archive at https://archive@ska.ac.za.

REFERENCES

Atri P. et al., 2020, MNRAS, 493, L81
Bright J. S. et al., 2020, Nat. Astron., 4, 697
Brocksopp C., Corbel S., Tzioumis A., Broderick J. W., Rodriguez J., Yang J., Fender R. P., Paragi Z., 2013, MNRAS, 432, 931
Carotenuto F., Tremou E., Corbel S., Fender R., Woudt P., Miller-Jones J., 2019, Astron. Telegram, 12497, 1
Chauhan J. et al., 2019a, MNRAS, 488, L129
Chauhan J., Miller-Jones J., Anderson G., Russell T., Hancock P., Bahramian A., Duchesne S., Williams A., 2019b, Astron. Telegram, 12520, 1
Denisenko D. et al., 2019, Astron. Telegram, 12430, 1
Dhawan V., Goss W. M., Rodríguez L. F., 2000, ApJ, 540, 863
Dickey J. M., 1983, ApJ, 273, L71
Fender R. P., Belloni T. M., Gallo E., 2004, MNRAS, 355, 1105
Fender R. et al., 2017, preprint (arXiv:1711.04132)
Gaia Collaboration, 2018, A&A, 616, A1
Gathier R., Pottasch S. R., Goss W. M., 1986, A&A, 157, 191
Goss W. M., Mebold U., 1977, MNRAS, 181, 255
Hotan A. W. et al., 2014, PASA, 31, e041
Jonker P. G., Nelemans G., 2004, MNRAS, 354, 355
Kalemci E., Dinçer T., Tomsick J. A., Buxton M. M., Bailyn C. D., Chun Y. Y., 2013, ApJ, 779, 95
Kennea J. A., Negoro H., 2019, Astron. Telegram, 12434, 1
Kreidberg L., Bailyn C. D., Farr W. M., Kalogera V., 2012, ApJ, 757, 36
Kuchar T. A., Bania T. M., 1990, ApJ, 352, 192
Maccarone T. J., 2003, A&A, 409, 697
McClintock J. E., Remillard R. A., 2009, in Lewin W., van der Klis M., eds, Compact Stellar X-ray Sources. Cambridge Univ. Press, Cambridge, p. 157
McMullin J. P., Waters B., Schiebel D., Young W., Golap K., 2007, in Shaw R. A., Hill F., Bell D. J., eds, ASP Conf. Ser. Vol. 376, Astronomical Data Analysis Software and Systems XVI, Astron. Soc. Pac., San Francisco. p. 127
Matsuoka M. et al., 2009, PASJ, 61, 999
Miller-Jones J. C. A., Jonker P. G., Dhawan V., Brisken W., Rupen M. P., Nelemans G., Gallo E., 2009, ApJ, 706, L230
Mirabel I. F., Rodríguez L. F., 1994, Nature, 371, 46
Murphy T., Mauch T., Green A., Hunstead R. W., Piestrzynska B., Kels A. P., Sztajer P., 2007, MNRAS, 382, 382
Reid M. J., McClintock J. E., Narayan R., Gou L., Remillard R. A., Orosz J. A., 2011, ApJ, 742, 83
Reid M. J. et al., 2014, ApJ, 783, 130
Reynolds J., 1994, ATNF Technical Memos, AT/39.3/040, Available at: https://archive-gw-1.kat.ac.za/public/meerkat/A-Revised-Flux-Scale-for-the-AT-Compact-Array.pdf
Russell T., Anderson G., Miller-Jones J., Degenaar N., Eijnden J. V. d., Sivakoff G. R., Tetarenko A., 2019, Astron. Telegram, 12456, 1
Sault R. J., Teuben P. J., Wright M. C. H., 1995, in Shaw R. A., Payne H. E., Hayes J. J. E., eds, ASP Conf. Ser. Vol. 77, Astronomical Data Analysis Software and Systems IV, Astron. Soc. Pac., San Francisco. p. 433
Tetarenko A. J. et al., 2017, MNRAS, 469, 3141
Tominaga M. et al., 2020, ApJ, 899, L20
Tremou E. et al., 2020, MNRAS, 493, L132
Vahdat Motlagh A., Kalemci E., Maccarone T. J., 2019, MNRAS, 485, 2744
Wenger T. V., Balser D. S., Anderson L. D., Bania T. M., 2018, ApJ, 856, 52
Williams D. R. A. et al., 2020, MNRAS, 491, L29
Yatabe F. et al., 2019, Astron. Telegram, 12425, 1
Zdziarski A. A., Poutanen J., Mikolajewska J., Gierlinski M., Ebisawa K., Johnson W. N., 1998, MNRAS, 301, 435
Zhang L. et al., 2020, MNRAS, 499, 851

This paper has been typeset from a TEX/LATEX file prepared by the author.

Downloaded from https://academic.oup.com/mnrasl/article/501/1/L60/6029123 by Sapienza Università di Roma user on 30 July 2021

Appendix B

Observing proposals

I list here the observing proposals, of which I am Principal Investigator, that have been submitted and accepted over the three years of my PhD.

2021 ***Swift*/XRT ToO 1639** – 7.5 ks
Observations of GX 339−4 in the hard state, to be coupled with a high-cadence ATCA radio monitoring.

***Chandra* Director's Discretionary Time (DDT)** – 30 ks
Observation of MAXI J1348−630 in quiescence, simultaneously to a deep ATCA radio observation to be probe the location of MAXI J1348−630 on the radio/X-ray diagram in quiescence. The observation has been performed, and the results are discussed in Section 6.5.

***Swift*/XRT ToO 15251, 16523** – 1 ks
Two observations of 4U 1755–338 in the soft state.

***Swift*/XRT ToO 16505, 15705** – 10.5 ks
Six observations of MAXI J1803–298 during its 2021 outburst.

2020 **ATCA Proposal C4316 - Semester 2021APRS** – 24 hours on source
Probing the disk/jet connection of a black hole in quiescence
Observation of the MAXI J1348−630 in quiescence, to coupled to a deep *Chandra* X-ray observation in July 2021, with the goal of probing the location of MAXI J1348−630 on the radio/X-ray diagram in quiescence. The observation has been performed, and the results are discussed in Section 6.5.

***XMM–Newton* Proposal 088479 - AO-2020** – 70 ks
Probing the disk-jet connection of a nearby quiescent black hole with XMM-Newton
Observation of the MAXI J1348−630 in quiescence, with the original goal of being coupled to a deep ATCA radio observation in July 2021 in order to probe the location of MAXI J1348−630 on the radio/X-ray diagram in quiescence. The proposal has been accepted with priority C, but the observation has not been scheduled yet.

Joint *Swift*/VLA Proposal VLA/20B-314 - Semester 2020B/2021A
30 ks (*Swift*), 40 hours (VLA)
Constraining black hole accretion-ejection coupling at low accretion rate
Triggered joint *Swift* and VLA proposal for the radio and X-ray monitoring of a new or known black hole transient in outburst in the low flux regime, at the very beginning of the outburst or in the final part of the decay towards quiescence. The proposal has been triggered on the new BH LMXB MAXI J1803–298.

ATCA Proposal C3362 - Semester 2020APRS - Renewed for Semester 2020OCTS and 2021APRS
100 hours
Constraining black hole accretion-ejection coupling at low accretion rate
Triggered ATCA proposal for the radio monitoring of a new or known black hole transient in outburst in the low flux regime, at the very beginning of the outburst or in the final part of the decay towards quiescence. The proposal has not been triggered, but will be renewed for an additional semester.

2019 ***Swift*/XRT ToOs 12526, 13134, 13639** – 16 ks
Observations of MAXI J1348−630 in the hard state, simultaneous with ATCA and MeerKAT